A multi-scale computational investigation of cardiac electrophysiology and arrhythmias in acute ischaemia

Sara Dutta
Balliol College

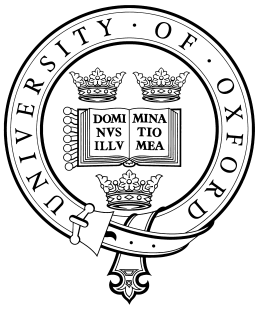

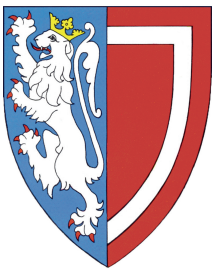

Department of Computer Science
University of Oxford

Trinity Term 2014

This thesis is submitted to the Department of Computer Science, University of Oxford, for the degree of Doctor of Philosophy. This thesis is entirely my own work, and, except where otherwise indicated, describes my own research.

Sara Dutta
Balliol College

Doctor of Philosophy
Trinity Term 2014

A multi-scale computational investigation of cardiac electrophysiology and arrhythmias in acute ischaemia

Abstract

Sudden cardiac death is one of the leading causes of mortality in the western world. One of the main factors is myocardial ischaemia, when there is a mismatch between blood demand and supply to the heart, which may lead to disturbed cardiac excitation patterns, known as arrhythmias. Ischaemia is a dynamic and complex process, which is characterised by many electrophysiological changes that vary through space and time. Ischaemia-induced arrhythmic mechanisms, and the safety and efficacy of certain therapies are still not fully understood. Most experimental studies are carried out in animal, due to the ethical and practical limitations of human experiments. Therefore, extrapolation of mechanisms from animal to human is challenging, but can be facilitated by *in silico* models. Since the first cardiac cell model was built over 50 years ago, computer simulations have provided a wealth of information and insight that is not possible to obtain through experiments alone. Therefore, mathematical models and computational simulations provide a powerful and complementary tool for the study of multi-scale problems.

The aim of this thesis is to investigate pro-arrhythmic electrophysiological consequences of acute myocardial ischaemia, using a multi-scale computational modelling and simulation framework. Firstly, we present a novel method, combining computational simulations and optical mapping experiments, to characterise ischaemia-induced spatial differences modulating arrhythmic risk in rabbit hearts. Secondly, we use computer models to extend our investigation of acute ischaemia to human, by carrying out a thorough analysis of recent human action potential models under varied ischaemic conditions, to test their applicability to simulate ischaemia. Finally, we combine state-of-the-art knowledge and techniques to build a human whole ventricles model, in which we investigate how anti-arrhythmic drugs modulate arrhythmic mechanisms in the presence of ischaemia.

Publications

Below are a list of publications which directly relate to the work described in this thesis.

- **S Dutta**, A Mincholé, P Taggart, T A Quinn, B Rodriguez; Class III drugs in human regionally-ischemic ventricles: anti- or pro-arrhythmic action? *Under Review*
- **S Dutta**, A Mincholé, T A Quinn, B Rodriguez; Electrophysiological properties under varied ischaemic conditions in human ventricular cell action potential models; *In preparation*
- **S Dutta**, A Mincholé, T A Quinn, B Rodriguez; Recent human ventricular cell action potential models under varied ischaemic conditions; *Computing in Cardiology (CinC) 2013*: 695 - 698 (2013)
- **S Dutta**, M Bishop, P Pathmanathan, P Lee, P Kohl, T A Quinn, B Rodriguez; Interpreting optical mapping recordings in the ischemic heart: A combined experimental and computational investigation; *Lecture Notes in Computer Science, Functional Imaging and Modeling of the Heart*: (6666) 20 - 27 (2011)

Conference Presentations

The work described in this thesis was presented at the following international conferences:

- **Cardiostim**, June 2014 in France: *Class III drugs in human regionally-ischemic ventricles: anti- or pro-arrhythmic action?* S Dutta, A Mincholé, P Taggart, T A Quinn, B Rodriguez; (Poster)
- **Computing in Cardiology (CinC)**, September 2013 in Spain: *Recent human ventricular cell action potential models under varied ischaemic conditions*; S Dutta, A Mincholé, T A Quinn, B Rodriguez (Oral)
- **Gordon Research Conference (GRC) on Cardiac Arrhythmia Mechanisms**, February 2013 in USA: *Recent human ventricular cell action potential models under varied ischemic conditions*; S Dutta, A Mincholé, T A Quinn, B Rodriguez (Poster)
- **Functional Imaging and Modeling of the Heart (FIMH)**, May 2011 in USA: *Interpreting optical mapping recordings in the ischemic heart: A combined experimental and computational investigation*; S Dutta, M Bishop, P Pathmanathan, P Lee, P Kohl, T A Quinn, B Rodriguez (Oral)

Contents

Acknowledgements

First and foremost, I would like to thank my supervisors Dr Blanca Rodriguez, Dr Ana Mincholé and Dr T. Alexander Quinn for being the pillars of my PhD. Blanca, gracias por todo lo que me has enseñado, desde como funciona el mundo complicado de isquemia hasta como venderse en el mundo del trabajo, pasando por consejos sobre novios. Encore merci pour 4 années incroyables! Ana, gracias por siempre darme ánimos y alegría, desde alojarme en el 5 estrellas minch'hotel hasta analizar películas de reentradas durante horas. Tea will always be lovely with you Ana! Alex, thanks for providing the different perspective of a biologist and for allowing me to take part in optical mapping experiments, where I saw a real heart for the first time - what an amazing organ!

I would also like to thank Dr Martin Bishop and Dr Pras Pathmanathan, who supervised me at the start of my PhD. Martin, you are a dedicated teacher and mentor who provided the ideal support for the foundations of my PhD. Pras, I couldn't have wished for a better introductory guide to the mysterious Chaste world. I would like to give a special thanks to the rest of the Chaste team, as all of my PhD is based on it and wouldn't have been possible without it: Dr Gary Mirams, Dr Jonathan Cooper, Dr Miguel Bernabeu and Dr Joe Pitt-Francis. Now I think all meetings should be standing and more importantly, everyone must have a lollipop!

I would like to thank my Transfer and Confirmation viva examiners, Prof Kevin Burrage and Dr Gil Bub, for the thought provoking questions and comments. Furthermore, I would like to thank our collaborators for fruitful discussions that resulted in my first reentry after months of failed attempts (Dr Jóse Félix Rodríguez), for enabling me to create cool reentry movies (Dr Ernesto Zacur), for access to HECToR (Prof Peter Coveney and Stefan Zasada) and for inspiring me (Prof Peter Taggart, Prof Yorum Rudy and Prof Pier Lambiase).

I want to dedicate a massive thank you to my 'little' PhD family: the computational biology group. Thanks for all the pub trips led by our one and only concertina/mountain leader, christmas celebrations made magic through Kylie's face picking a name out of Anna J.'s secret santa hat, rounders games, which were fun despite the competitiveness of D&D that always favoured winning over participation and last but not least the Holiday of a Lifetime! Thank you Alfonso and Raf (for sharing your wisdom), Kylie (for all the giggles - 'Ich liebe dich!'), James Mb. (for always checking up on me - Cheers!), Mikael (for believing in my mini-Blanca skills - puss puss), Anna J. (for being the best co-PhD rep and initiating me to the laser tag world), John (for being the perfect Blanca & Balliol mentor), Ely (for all the fruit breaks and Mr Darcy stories), Lorenz (for the best impromptu skiing holiday), Ciara (for making sure 'I'll be Ok' as McFly said), Louie (for letting everyone benefit from your Chaste installation talent), Sophie (for all the girlie chats), Matt (for all your crazy stories), Ollie (our ICT pioneer winner!), Anna M. (for the orchid garden), AJ (for a fun car ride to Wales), Xin (for always smiling) and the rest of the group.

I would also like to thank the rest of the Computer Science Department who made practical aspects of my PhD easy and fun to handle (Julie, John, Manu, Ashish, Terry, Ian, Paul and Barbara). I would also like to thank the organisations that funded my PhD: EPSRC, Blanca's MRC and Wellcome Trust Fellowships, Ana's Marie-Curie Fellowship, Balliol College and the Department of Computer Science.

Work hard, play hard: thanks to Jo (3 years of homie adventures), Phoebe (best dance/running buddy), Rahul (and his endless shoulder tapping game), Hilary (and the delicious dinner parties), Carla & Ines (yum din dins), Martha (efharisto poli!), Sumudu & Simin (the inseparable trio) and many others (Gabi, Seb, Aoife, Indrek, Miroslawa, the Nathans, Friederike, Elisabetta, Natasha, Soraya, Kira, Maga, Solène ...). I would like to thank the whole of Balliol College (especially Tom, Nicky, Yannick, Nick and Jo) for providing the perfect environment for my PhD.

Finally, I would like to thank my family in India and Spain and more importantly my parents for their unconditional love and support. I couldn't have made it without them!

Acronyms

AP Action Potential

APD Action Potential Duration

AT Activation Time

AV Atrioventricular Node

BZ Border Zone

CDI Calcium Dependent Inactivation

CP Creatine Phosphate

CRLP Carro *et al.* 2011 Human Ventricular Action Potential Model

CV Conduction Velocity

ECG Electrocardiogram

ERP Effective Refractory Period

GPB Grandi *et al.* 2010 Human Ventricular Action Potential Model

LV Left Ventricle

ORd O'Hara *et al.* 2011 Human Ventricular Action Potential Model

PRR Post Repolarisation Refractoriness

RT Repolarisation Time

RV Right Ventricle

SAN Sinoatrial Node

TP06 ten Tusscher *et al.* 2006 Human Ventricular Action Potential Model

VDI Voltage Dependent Inactivation

VF Ventricular Fibrillation

VT Ventricular Tachycardia

3D Three-Dimensional (similarly for 1D and 2D)

Nomenclature

$\phi_{\mathbf{i}}$ Intracellular potential

$\phi_{\mathbf{e}}$ Extracellular potential

$\sigma_{\mathbf{i}}$ Intracellular conductivity tensor

$\sigma_{\mathbf{e}}$ Extracellular conductivity tensor

β Cellular surface area to volume ratio

$\mathbf{C_m}$ Membrane capacitance per unit area

$\mathbf{I_m}$ Total transmembrane current

$\mathbf{I_{ion}}$ Total ionic transmembrane current

$\mathbf{I_{K(ATP)}}$ ATP-sensitive potassium channel

$\mathbf{I_{Na}}$ Fast inward sodium channel

$\mathbf{I_{NaCa}}$ Sodium calcium exchanger

$\mathbf{I_{NaK}}$ Sodium potassium pump

$\mathbf{I_{CaL}}$ L-type calcium channel

$\mathbf{I_{Kr}}$ Rapid delayed rectifier potassium current

$\mathbf{I_{Ks}}$ Slow delayed rectifier potassium current

$\mathbf{I_{K1}}$ Inward rectifier potassium current

$\mathbf{I_{to}}$ Transient outward potassium current

$\mathbf{V_m}$ Transmembrane potential

Chapter 1

Introduction

1.1 Motivation

Sudden cardiac death accounts for an estimated 300 000 deaths in the United States and upwards of 60 000 deaths in the United Kingdom, each year [Papadakis et al., 2009]. One of the major causes of cardiac arrest is coronary artery occlusion, reducing the supply of blood to the heart, and resulting in a phenomenon known as acute myocardial ischaemia. In 2008 in the UK, over 12 500 people under the age of 65 died from coronary heart disease, also known as ischaemic heart disease. That is equivalent to about 35 people per day [Scarborough et al., 2010]. Most cardiovascular deaths occur due to arrhythmias, disturbed excitation patterns of the heart. There are different types of arrhythmias, but the most lethal one is ventricular fibrillation (VF), when many chaotic self-sustained rotors of activation occur. Death arises within minutes if left untreated. VF is often preceded by ventricular tachycardia (VT), characterised by an abnormally high heart rate.

Anti-arrhythmic drugs constitute first line therapy for patients suffering from abnormal heart rhythms, often in combination with electrical therapy [Guarnieri et al., 1987; Tacker et al.,

1980; Brode et al., 1997; DiMarco, 2003]. Despite the proven efficacy of anti-arrhythmic drugs in most patients [Wichter et al., 1992], cases of lethal side-effects cannot be ignored. Clinical trials, such as the Survival With ORal D-Sotalol (SWORD) and Cardiac Arrhythmia Suppression (CAST) trials, have demonstrated that administration of certain anti-arrhythmic drugs was associated with increased mortality in certain patients [Waldo et al., 1996; Ruskin, 1989]. Dissecting key underlying mechanisms, particularly in patients with an existing pro-arrhythmic substrate, is urgently needed to improve patient risk stratification, management, and development of improved anti-arrhythmic therapy. One of the possible risk factors is ischaemia, as was shown in a recent study where anti-arrhythmic drugs were prescribed to patients, and the cohort suffering from coronary artery disease displayed increased hospitalisation and death [Steinberg et al., 2014].

Ischaemia increases electrophysiological heterogeneities across the heart and the likelihood of developing cardiac arrhythmias [Kimura et al., 1986]. Ischaemic cells are less excitable due to the mismatch between blood demand and supply. Therefore, their electrophysiological activity is significantly altered. Ischaemic changes vary through time, as the duration of the mismatch increases, and spatially, as a gradient in properties develops between the normal and ischaemic tissue. Various important electrophysiological properties are altered during ischaemia: the time between activation and repolarisation of a cell, referred to as the action potential (AP) duration (APD), the time frame during which the cell cannot be excited, referred to as the effective refractory period (ERP), the time lag between the cell recovering and being able to excite again, referred to as post-repolarisation refractoriness (PRR) and the speed of propagation of the excitation wavefront, also known as conduction velocity (CV). Heterogeneities in repolarisation and refractoriness properties between the normal and ischaemic tissue significantly increase the likelihood of developing arrhythmias, namely VT through a figure-of-eight reentry around the ischaemic region [Janse et al., 1986; Ferrero et al., 2003]. Due to limitations of current methods and the complexity of ischaemia, there is a need to develop new techniques to measure and

characterise the spatio-temporally varying pro-arrhythmic substrate.

Most experimental research on ischaemia has been carried out in animals [Coronel et al., 1988; Fiolet et al., 1985; Furukawa et al., 1991; Downar et al., 1977; Kimura et al., 1986; Weiss and Shine, 1982b,a; Wilensky et al., 1986; Schaapherder et al., 1990; Vermeulen, 1996; Kleber, 1983; Carmeliet, 1999] and data from human is scarce due to ethical and practical reasons [Sutton et al., 2000; Taggart, 2000]. In fact, rabbit hearts are often used to study ventricular electrophysiology and arrhythmias given their similarities to human hearts [Maier, 2000; Hasenfuss, 1998]. Extrapolating our understanding of mechanisms from animal to human is challenging, and computer models can provide a powerful complementary tool to facilitate this process. They consist of AP models describing the ionic current and concentration dynamics occurring at the cell's membrane, which are then coupled in a realistic geometry to reproduce whole heart electrical activity, as shown in Figure 1.1 [Carusi et al., 2012]. These multi-scale models are built and parameterised with experimental data, namely from voltage clamp data at the ionic level to MRI scans at the whole heart level. Studies using *in silico* models have, amongst other discoveries, increased our understanding of specific arrhythmic mechanisms during ischaemia [Tice et al., 2007; Heidenreich et al., 2012; Ferrero et al., 2014; Rodríguez et al., 2006; Trayanova, 2011; Shaw and Rudy, 1997a]. In fact, modelling provides a multi-scale platform to dissect and analyse specific ischaemic processes with high spatio-temporal resolution, not possible to obtain through experiments alone, especially in human.

1.2 Thesis goal

The aim of this thesis is to investigate acute ischaemia-induced electrophysiological changes and arrhythmic mechanisms using the latest cardiac models and computational techniques. It can be divided into these three specific goals:

1. Build a novel method to characterise ischaemia-induced heterogeneities in rabbit hearts

Figure 1.1 Schematic representation of cardiac model development: integrating experimental data from the subcellular to the whole organ level[Carusi et al., 2012].

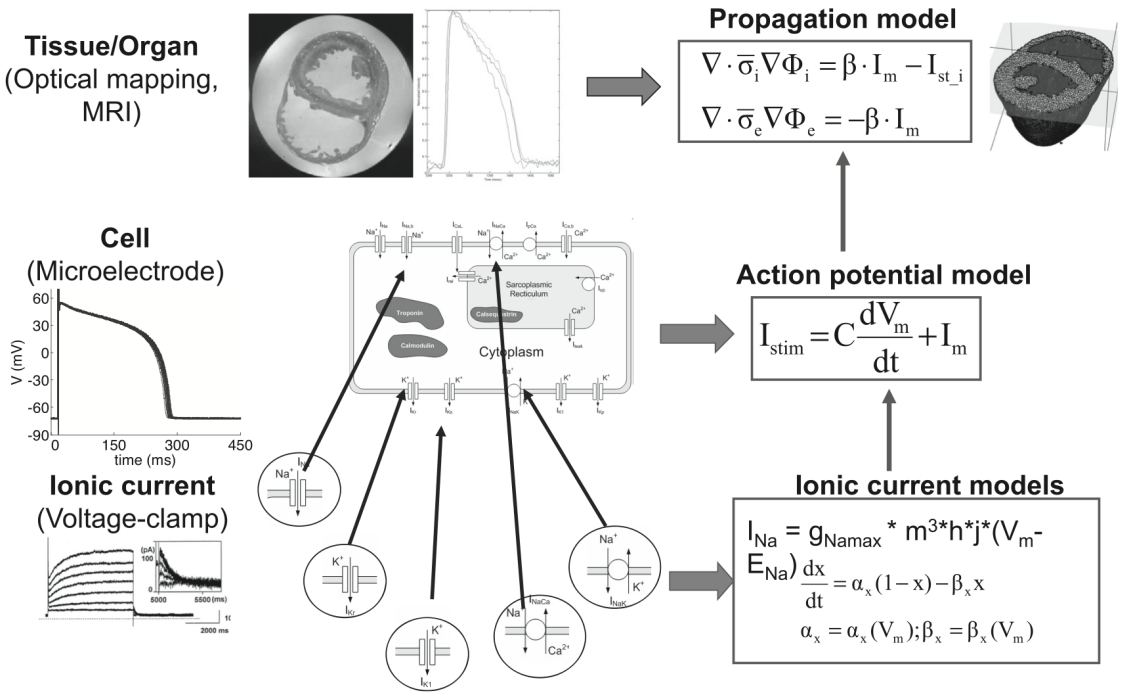

through a combined computational and experimental approach;

2. Examine the response of recent human AP models under varied ischaemic conditions and assess their applicability to simulations of ischaemia;

3. Investigate how ischaemia modulates the safety and efficacy of class III anti-arrhythmic drugs in an anatomically-accurate human whole ventricles model.

The first part of this thesis focuses on using computational and experimental techniques synergistically to investigate ischaemia-induced heterogeneities in rabbit hearts. These heterogeneities play an important role in arrhythmogenesis [Coronel et al., 2009; Coronel, 1994; Costeas et al., 1997; Janse et al., 1979; Ferrero et al., 2003; Bernus et al., 2005b] and therefore, their characterisation is essential and unfortunately limited with current techniques. These experiments are carried out in rabbit due to the ethical and practical challenges of carrying out experiments in human.

The second part of this thesis extends the investigation of ischaemia-induced changes to human by focusing on the four most recent human AP models [ten Tusscher and Panfilov, 2006; Grandi et al., 2010; O'Hara et al., 2011; Carro et al., 2011]. These models are built using data from healthy cells, therefore, in most cases, their use to model ischaemia, when many electrophysiological parameters are modified, has not been investigated systematically. Therefore, this thesis compares recent human AP models under varied ischaemic conditions, to assess their applicability to simulate ischaemia. We vary parameters that play an important role in modulating arrhythmic risk and we cover a range of values to account for the high degree of ischaemic heterogeneities observed both temporally and spatially.

Ischaemic pro-arrhythmic alterations have been investigated in a large number of studies [Wilensky et al., 1986; Coronel et al., 1991; Janse and Wit, 1989; Coronel et al., 1988; Taggart, 2000], but few have looked at how the changes are modulated by pharmacological action [You et al., 2005; Cobbe and Manley, 1987; Steinberg et al., 2014]. The improvement of computational power, with the increased availability and size of high performance computing resources, have played an unprecedented role in enabling the investigation of clinically relevant arrhythmic mechanisms in large human whole ventricles models [Bernabeu et al., 2010a; Niederer et al., 2011]. The model we build, and describe in the final part of this thesis, provides a powerful tool to investigate the efficacy and safety of anti-arrhythmic drugs during ischaemia, with high spatio-temporal resolution, not available with experiments alone. We use this model to dissect mechanisms modulating arrhythmic risk when prescribing anti-arrhythmic drugs to ischaemic patients.

In this thesis, we investigate research questions alongside experiments at a multi-scale level, from the single cell to the whole organ using both rabbit- and human-specific models, as described in Figure 1.2. Information from experiments is integrated into our mathematical models, such as information on ischaemia-induced electrophysiological changes. The models are then coupled together and solved computationally on a given mesh, such as a human whole ventricles

Figure 1.2 Flow chart of cardiac investigation pipeline used to explore research goals.

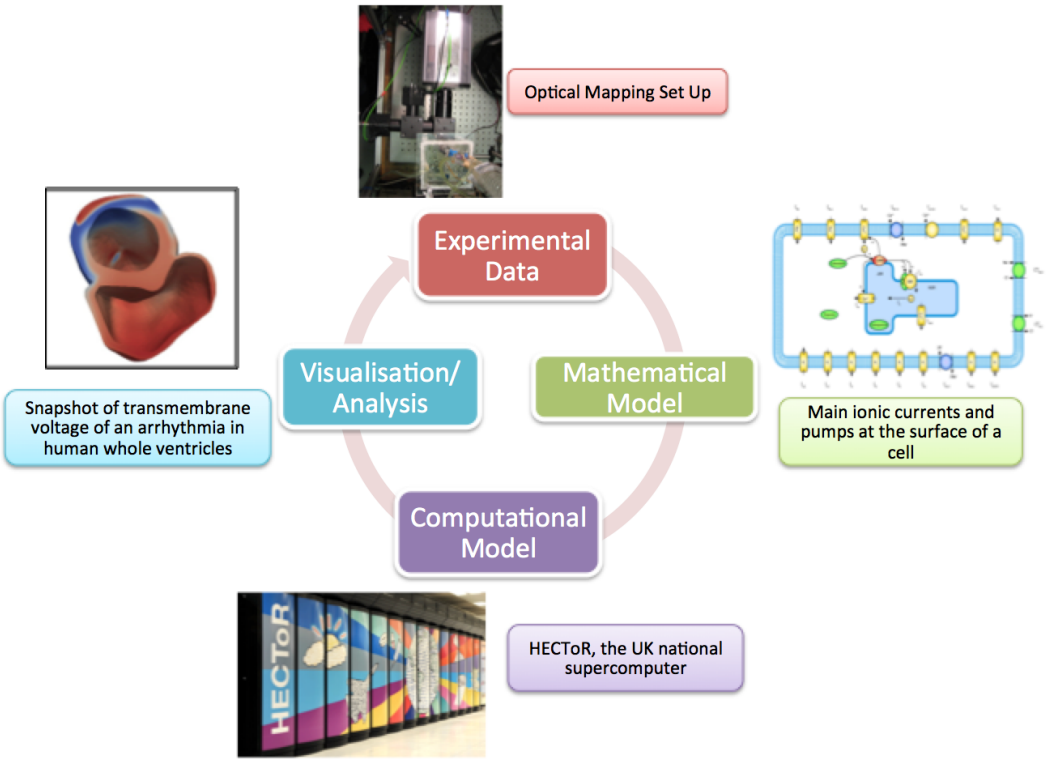

mesh to address the final goal of this thesis. The simulation output is visualised and analysed using the following tools: CMGUI [1], ParaView [2] and Meshalyzer [3]. Results are compared to experimental data in order to lend credibility to the model and, more importantly, to gain insight into new mechanisms and inform future experiments. Namely, results from the final part of this thesis provide new information on how ischaemia modulates anti-arrhythmic drug efficacy and the combined computational and experimental approach developed in the first part of this thesis could be used to test our hypotheses experimentally (as suggested in Section 8.3).

1.3 Thesis outline

We now describe the structure of this thesis by giving a brief overview of each chapter.

[1] http://www.cmiss.org/cmgui
[2] http://www.paraview.org
[3] https://chaste.cs.ox.ac.uk/trac/wiki/ChasteGuides/VisualisationGuides/UsingMeshalyzer

Chapter 2 introduces the biological background underlying the work presented in this thesis. We describe the basic structure and function of the heart. In particular, we discuss the electrical activity of the heart, the role of ion channels in the normal electrical functioning of cardiac cells and the main measures used throughout this thesis to quantify the activity. We also provide evidence of electrophysiological heterogeneities and variability found in hearts. We describe the overall changes that occur during ischaemia and emphasise the main electrophysiological changes that are investigated in this thesis. We then provide a description of the different types of arrhythmias, and specify which are more likely to occur during ischaemia. We present some of the main anti-arrhythmic treatments used, especially anti-arrhythmic drugs which are a main point of focus of this thesis. Finally, we give an overview of the experimental techniques used to investigate arrhythmic mechanisms relevant to this thesis.

Chapter 3 provides a literature review of ischaemia-induced electrophysiological changes. We initially review how these alterations vary temporally and spatially. We then describe the effects of ischaemia on electrophysiological properties that modulate arrhythmic risk. In the next part of this chapter, we present studies that have investigated the use of anti-arrhythmic drugs during ischaemia, namely trials that have shown increased mortality rates associated with anti-arrhythmic drugs. Finally, we give an overview of previous computational studies of ischaemia and arrhythmogenesis.

Chapter 4 introduces the main mathematical and computational modelling techniques used to simulate cardiac electrophysiology. We present the models reproducing the ionic current activity at the single cell level. We provide a description of the main Hodgkin-Huxley equations on which most cell models are based, and review the main ventricular AP models relevant to this thesis. We also provide a description of the ATP-sensitive ionic current included in all our models, as it is activated under ischaemic conditions. We describe the bidomain and monodomain equations of electrical conduction and the algorithms used to solve them on human whole ventricular geometries. Finally, we give a brief overview of the software package used throughout

this thesis to run simulations.

Chapter 5 addresses the first goal of this thesis by presenting our method developed to understand and extract novel information on transmural heterogeneities from optical mapping results in the globally ischaemic rabbit heart. Using our knowledge of light photon scattering and wavelength-dependent tissue penetration, we have computationally investigated how optical mapping can be used to characterise ischaemia-induced heterogeneities. The work is based on close iteration between rabbit optical mapping experiments and computational simulations.

In Chapter 6, we extend our investigation of ischaemia to human by comparing four recent human cardiac cell AP models. Most of these models are built using data from healthy cells and have not been tested under ischaemic conditions. In order to assess their applicability to simulate ischaemia, we examine their behaviour under varied ischaemic conditions in single cell and tissue simulations. We initially analyse ionic current dynamics and formulations, and then assess how electrophysiological properties related to arrhythmias are modulated. Results are also compared to experimental data from human.

In Chapter 7, we construct a human whole ventricles model of regional ischaemia to test the efficacy of class III anti-arrhythmic drugs. We build upon the findings from our previous investigation, which assessed the applicability of the models to simulate ischaemia. Our model offers high spatio-temporal resolution of arrhythmia mechanisms than experiments alone. To lend credibility to our computational simulations, we closely compare it to experimental data from human. Pro- and anti-arrhythmic mechanisms of anti-arrhythmic drugs are dissected in this chapter.

In Chapter 8, we end this thesis with a summary and a discussion of the main contributions of this work. Possible future avenues of the work and concluding remarks are also presented and reviewed.

Chapter 2

Biological background

This chapter introduces basic principles of cardiac physiology and anatomy from the whole organ level (with a description of the functionality of the different compartments of the heart) to the ionic level (with a detailed description of the ionic currents involved in cardiac cell excitation). The main measures used to quantify electrophysiology are presented. Ischaemia-induced alterations are introduced with an emphasis on electrophysiological changes, a central theme of this thesis. Different patterns of arrhythmias and an overview of the main anti-arrhythmic treatments are described. Finally, a brief overview of experimental techniques available to measure in vivo and in vitro electrophysiological properties are given.

2.1 Cardiac anatomy and function

The heart consists of 4 chambers - the right and left atria (RA and LA) and the left and right ventricles (LV and RV). The ventricles generate the force that pushes the blood into the lungs and the rest of the body. The LV wall is thicker than the RV as it needs to push the blood out to the rest of the organs while the RV pushes blood to the neighbouring lungs. The section of tissue in between the two ventricles is referred to as the *septum*, the bottom part of the heart is

known as the *apex* and the top part as the *base*.

Figure 2.1 shows a schematic representation of the blood flow through the heart along with the main chambers and arteries of the heart. The pathway of the de-oxygenated blood is shown by the white arrows in the blue region and the pathway of the oxygenated blood is shown by the white arrows in the red region. The de-oxygenated blood arrives into the heart via the superior and inferior *vena cava* connected to the RA. It then enters the RV through the tricuspid valve. Upon contraction of the heart, the blood in the RV is pushed into the pulmonary arteries past the pulmonary valve. The lungs then re-oxygenate the blood that comes back into the heart through the pulmonary veins and into the LA. Finally, the blood goes into the LV via the mitral valve and upon contraction exits up the aortic valve into the aorta in order to be pumped back out to the rest of the body.

Figure 2.1 Schematic representation of longitudinal cross-section of the heart showing the main structural features. The white arrows indicate the direction of blood flow. The blue-shaded region represents the flow of the de-oxygenated blood coming from the organs through the superior and inferior vena cava and into the lungs along the pulmonary arteries. The red-shaded region represents the flow of oxygenated blood coming from the lungs and into the body via the aorta.

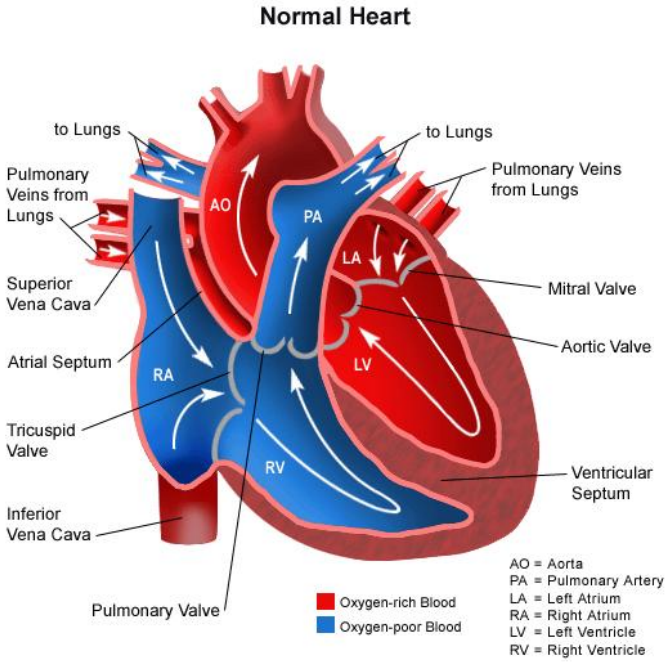

Spread of electrical activation throughout the heart plays a critical role in creating an effective and efficient heart beat, and it is modulated by the structure of the cardiac tissue [Roberts and Scher, 1982; Valderrabano, 2007; Hooks et al., 2002]. The latter, also known as myocardium, is generally thought to be structurally orthotropic [Saffitz et al., 1994; Clerc, 1976]. Figure 2.2 shows a schematic representation of this microstructure. The cardiac cells, also known as myocytes, are arranged into adjacent layers of muscle tissue, of 3 to 4 cells in thickness, separated by cleavage planes, as has been shown by numerous imaging techniques in animal [LeGrice et al., 1995; Young et al., 1998; Sands et al., 2005; Costa et al., 1999]. These muscle layers contain fibre-like structures, formed from longitudinal arrangement of myocytes, that vary in orientation from the outer surface ($+60°$) to the inner surface $-60°$ of the heart.

Figure 2.2 Schematic representation of cardiac microstructure: (a) Fibre orientation along the muscle sheets (b) Sheets of muscle fibres separated by collagen [LeGrice et al., 1995]

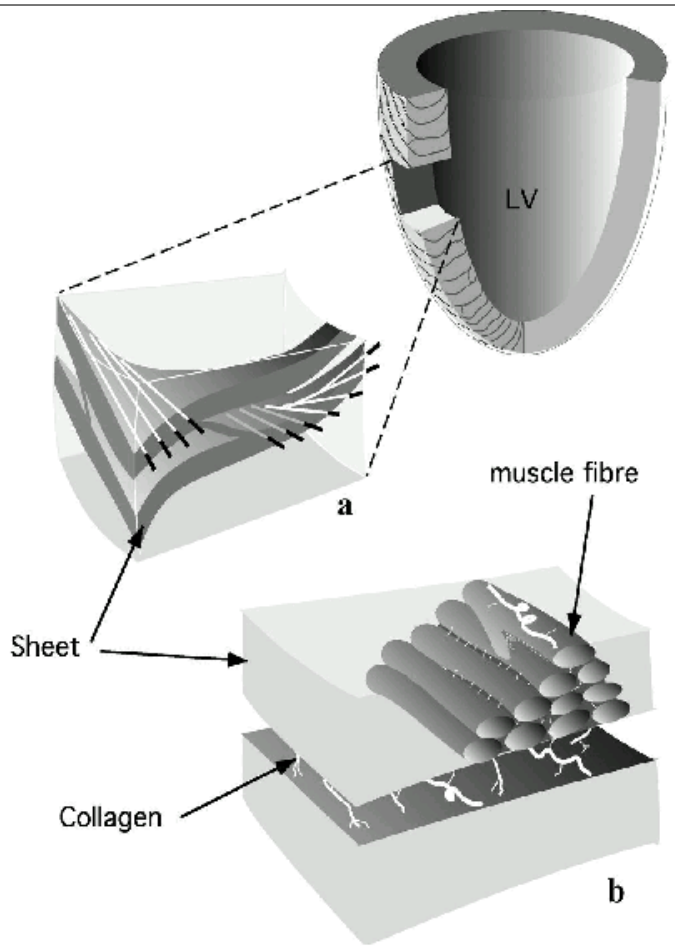

The direction of the cells defines the preferential direction of contraction and electrical conduction. This was shown by many animal studies [Saffitz et al., 1994; Sano et al., 1959; Clerc, 1976], such as the one by Roberts *et al.* in canine ventricles that showed spread of epicardial excitation to be 2.4 times faster parallel to the long axes of the cardiac fibers than perpendicular to them [Roberts et al., 1979]. This allows for quick electrical excitation propagation across the whole heart and an efficient mechanical pump action through a twisting motion along the fibre direction. Discontinuities or changes to the cardiac microstructure can have significant adverse effects on the heart's normal activity, such as increasing the likelihood of arrhythmias [Spach and Dolber, 1986]. However, our knowledge of cardiac microstructure is still being revised, for example, Caldwell *et al.* showed that electrical coupling in pig is not uniform transverse to the local myocyte axis, therefore, conflicting with previously widespread assumption that it was uniform [Caldwell et al., 2009].

2.2 Cardiac cell electrophysiology

The contraction of the heart is triggered by the electrical excitation of the cells. The key players in this conduction system are represented in Figure 2.3. The sinoatrial node (SAN), also known as the sinus node, generates the electrical impulse that regulates the normal heart beat, also known as sinus rhythm. The electrical activity triggered in the SAN excites the rest of the atria until the excitation wave reaches the atrioventricular node (AV), which connects the electrical activity of the atrial and ventricular chambers of the heart. There is a small but crucial delay at the AV node to ensure all of the blood has been pushed into the ventricles before they are excited. The electrical activity propagates quickly through the areas of fast conduction: the bundle of His, the two bundle branches and the Purkinje fibres. This ensures coordinated contraction of the ventricles to maximise the strength and synchronisation of the blood movement. Propagation of membrane activation between cells occurs mostly through diffusion of charged ions through gap junctions at the cell surface that link the cytoplasm of two cells. A gap junction

channel is composed of two connexons, formed of connexin proteins.

Figure 2.3 Schematic representation showing the main players involved in the electrical activation pathway and their approximate excitation rate.

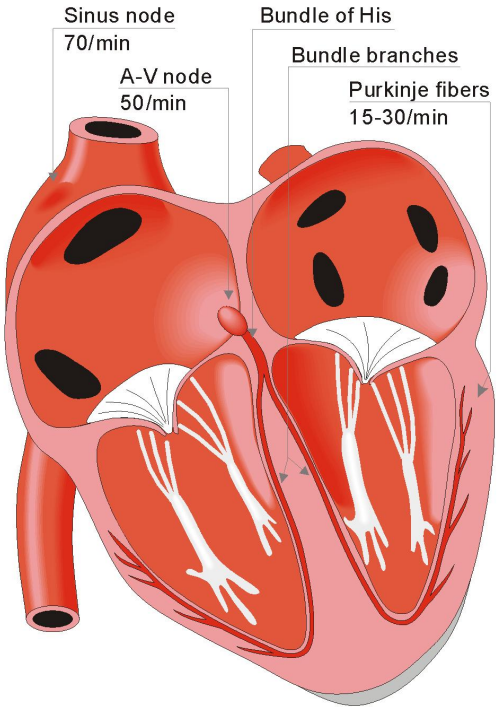

The electrical activity of a cardiac cell is governed by ions moving in and out of the cell through ion channels, exchangers and pumps at the membrane, as shown in Figure 2.5. The difference in potential across the cell membrane, referred to as the transmembrane potential (V_m), is due to different concentrations of positively and negatively charged ions lying inside and outside the cell. When the cell gets excited, usually due to excitation of a neighbouring cell, ion channels at the surface of the cell change their activity in response and trigger cell excitation, represented by the AP, which shows the change in transmembrane potential of the cell. A schematic representation is shown in Figure 2.4. The shape of the AP varies widely between different cell types of the ventricles. However, the ventricular AP can be broadly defined by the following phases:

- **Phase 0 - Initial Upstroke**: During the upstroke phase (phase 0), there is a rapid depolarisation due to an increase in inward flux of sodium ions (Na^+) as the fast inward sodium

channel (I_{Na}) opens.

- **Phase 1 - Initial Repolarisation**: An initial repolarisation occurs once the cell has reached maximum depolarisation and the I_{Na} currents become inactive. The sharp downward deflection of the AP that characterises this phase is often referred to as the *notch*, and it is triggered by the transient outward potassium current (I_{to}) and results in the movement of potassium ions (K^+) out of the cell.

- **Phase 2 - Plateau Phase**: After the initial *notch*, there is a plateau phase governed by the L-type calcium current (I_{CaL}), the slow delayed rectifying potassium current (I_{Ks}) and the sodium calcium exchanger (I_{NaCa}) and sodium potassium pump I_{NaK}. This results in the movement of calcium ions (Ca^{2+}) into of the cell and K^+ ions out of the cell.

- **Phase 3 - Complete Repolarisation**: The cell completely repolarises back to its resting membrane potential by moving K^+ ions out of the cell via the main potassium currents of the cell, the inward rectifying potassium current I_{K1} and the fast delayed rectifying potassium current (I_{Kr}).

- **Phase 4 - Resting Phase**: During the resting phase, the transmembrane voltage (V_m) of the cell is usually between -85 mV and -90 mV for a healthy cell. At resting state, there is a slow and steady intake of potassium ions due to the cell's greater permeability to K^+ through I_{K1} and the I_{NaK} pump.

Under normal conditions there is a gradient in ions across the cell membrane that is modulated and maintained by all of the ionic currents and pumps mentioned above. Under normal conditions, $[K^+]_i$ is high (about 100 mM) and $[K^+]_o$ is low (about 5 mM) [Carmeliet, 1999; Lee and Fozzard, 1975]. The I_{NaK} pump, plays an important role in modulating the activity of K^+ and Na^+, by moving 3 Na^+ ions out of the cell for every two K^+ ions it moves inside. Therefore, this moves one extra positive charge from intracellular to extracellular for each cycle, making $[Na^+]$ high in the extracellular space (about 140 mM) and low in the intracellular space (about

Figure 2.4 Schematic representation of a ventricular cardiac action potential with 4 different phases: upstroke (0), initial repolarisation (1), plateau phase (2), complete repolarisation (3) and resting phase (4). Main ionic currents and pumps involved at each stage are labelled.

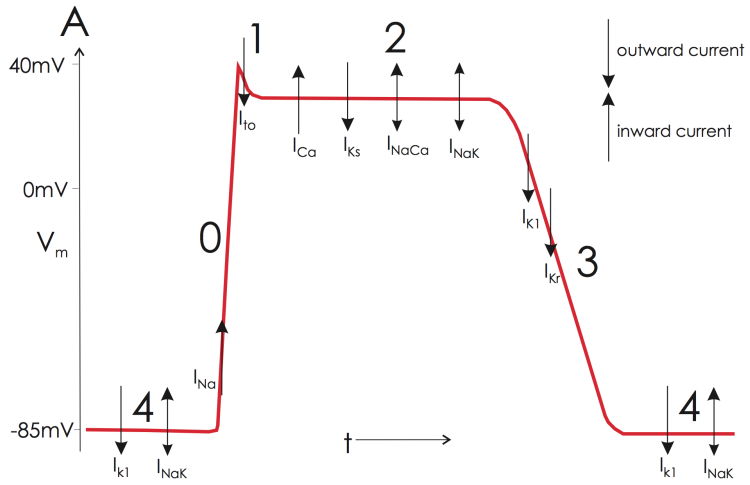

15 mM) [Carmeliet, 1999]. The change in gradient across the cell activates the I_{Na} channel that allows Na^+ back into the cell. Finally the K^+ ions are pushed out of the cell via the outward potassium currents during the repolarisation phase, in order for the cell to get back to its resting state. Furthermore, $[Ca^{2+}]_o$ (about 2 mM) is greater than $[Ca^{2+}]_i$ (approximately 100 nM during diastole and about 400 nM during systole) [Carmeliet, 1999]). During the plateau phase, I_{CaL} opens to let Ca^{2+} ions into the cell, creating the calcium transient that plays an important role in contraction, as described at the end of this section. The main mechanism of calcium extrusion from the cell is through the I_{NaCa} exchanger.

Following each AP, the cardiac cell recovers electrically, and the transmembrane voltage returns to its resting state. The cell can only be excited again once it has repolarised and recovered to its resting state. It is governed partly by the recovery kinetics of the inactivation gates of I_{Na}. A cell which has not recovered is said to be *refractory*, and therefore, not excitable. The normal heart beat is usually much longer than the ERP and the time between the completion of the AP and the onset of the next AP is termed the *diastolic interval*. The refractory period and the CV modulate the *wavelength* of cardiac excitation, which is defined as the distance travelled by the excitation wavefront during the refractory period. The wavelength is a good measure to

Figure 2.5 Schematic representation of a cardiac cell and the major ionic currents that lie at the surface of the cell and at the surface of the sarcoplasmic reticulum. Calmodulin and troponin proteins that are present in the cytoplasm and play a role in calcium cycling are also shown.

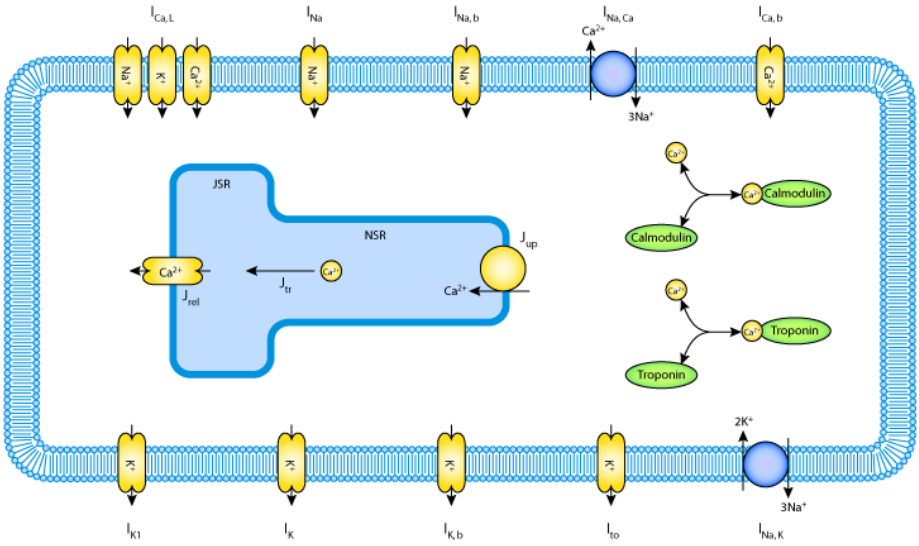

assess the dynamics of arrhythmias. ERP and wavelength play an important role in defining arrhythmic risk, especially when there is heterogeneous distribution of excitable and refractory tissue across the heart. Refractory tissue creates conduction block that may prevent progression of an existing excitation wavefront.

Within the cell, the sarcoplasmic reticulum, represented by a T shape in Figure 2.5, plays an important role in regulating calcium concentration, which is involved in contraction. Calcium concentration ($[Ca^{2+}]$) differs in the cytoplasm, the SR and the mitochondria. The SR acts as a store for Ca^{2+} and modulates contraction and relaxation. The electrical stimulus of each cell drives mechanical contraction in a process referred to as *excitation-contraction coupling*. During the plateau phase of the AP, calcium ions enter the cell through I_{CaL} triggering the subsequent release of Ca^{2+} stored in the SR, in a process referred to as *calcium-induced calcium release*. The free calcium binds to proteins, known as troponin-C, on actin filaments, causing a conformational change that exposes sites on the actin fibres to which myosin can bind, thus, stimulating contraction of the muscle cell. Myosin filaments then slide along actin filaments to

Figure 2.6 Schematic representation of two AP traces showing the AP duration (APD), effective refractory period (ERP) and post repolarisation refractoriness (PRR).

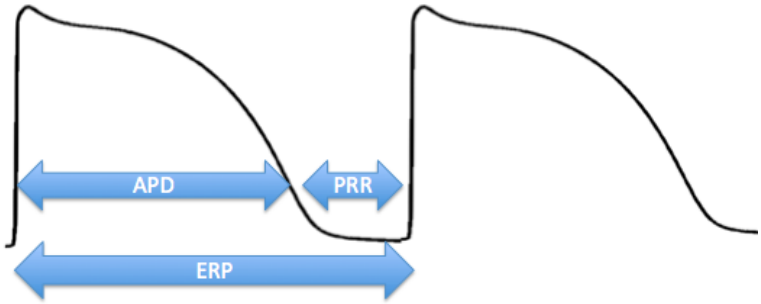

shorten or lengthen the muscle fibre for contraction and relaxation.

2.3 Measuring and quantifying cardiac electrophysiology

This section describes measures often used to quantify the AP and electrical propagation properties of the tissue. They are sometimes referred to as *biomarkers* describing cardiac electrophysiology and are related to arrhythmic risk. The main biomarkers described in this section and investigated in this thesis are: APD, ERP, PRR and CV. Figure 2.6 shows a schematic representation of an APD, ERP and PRR.

APD is defined as the time between activation and repolarisation of the cell. The activation time is usually defined by the point of maximum upstroke velocity, and the repolarisation time by the time point when V_m crosses a certain percentage of maximum AP amplitude (generally specified at 90% repolarisation). The APD is determined by a variety of currents, amongst which are the potassium outward repolarising currents such as I_{Ks} and I_{Kr}. An increased outflux of K^+ decreases the APD (as during ischaemia [Sutton et al., 2000]), and the opposite effect occurs if the outflux is decreased (as during certain anti-arrhythmic therapies). As discussed in Sections 2.7 and 3.3, this marker is significantly altered during ischaemia and anti-arrhythmic drug treatments. It can be approximated non-invasively using electrode recordings or electrocardiograms (ECGs) by calculating the monophasic AP (MAP) [Franz et al., 1986] or the activation-recovery interval (ARI) [Iwata et al., 1999]. The MAP is measured from the exterior of the cell through

contact electrodes and has been shown to accurately reflect transmembrane voltage. The MAP reflects the potential difference between two recording sites, which are recorded by an exploring and a reference electrode. For a unipolar recording, the reference electrode is positioned in nonexcitable tissue at a large distance from the exploring electrode. In contrast, for a bipolar recording, the reference electrode is positioned next to the exploring electrode (millimeter range) in excitable tissue. [Coronel et al., 2006]. ARIs are measured from the unipolar extracellular ECG as the interval between the deflection representing activation of the myocardium and the one representing repolarisation of the ventricles.

The ERP is the time during which a cell is refractory and cannot be excited again. Under normal conditions it is normally equal to the APD. As soon as the cell repolarises it is ready to fire another AP. This is governed by the recovery kinetics of the I_{Na} current inactivation gates [Ferrero et al., 1999, 2003]. However, under diseased conditions (such as ischaemia) there is a time lag between the cell repolarising and being excitable again [Coronel et al., 2012]. The cell's excitability is mostly governed by the inactivation gates of I_{Na}, which in turn is affected by the resting V_m of the cell, both properties are significantly altered during ischaemia.

The time lag between the cell repolarising and being excitable again is referred to as the PRR. Under normal conditions the PRR is approximately 0, but under certain diseased conditions, such as ischaemia, this can be altered [Coronel et al., 2012]. The PRR is calculated as the difference between ERP and APD. Therefore, it is affected by the same electrophysiological changes as these two biomarkers.

CV is defined as the speed of the activation wave. Given two points, it is calculated as the distance between the two points divided by the time taken for the excitation wave to go from the first to the second point. The main ionic current affecting CV is I_{Na}, which is affected by ischaemia [Carmeliet, 1999; Taggart, 2000].

Another important marker used in numerous studies is the APD restitution curve [Franz, 2003].

The curve describes the relationship between APD and the preceding diastolic interval. It is calculated by pacing at varying coupling intervals. There are two types of restitution curves: dynamic restitution is calculated by pacing to steady state as the basic cycle length is decreased, while S1S2 restitution is calculated by applying a premature (S2) beat following a series of paced (S1) beats. The dynamic restitution curve is a measure of steady-state response, while S1S2 restitution is a measure of the immediate response to a change in cycle length.

Similar restitution properties are calculated for CV, as they play an important role in modulating conduction block and wavefront propagation [Banville and Gray, 2002; Qu et al., 1999; Cao et al., 1999; Cherry and Fenton, 2004]. All of these restitution curves usually display a plateau phase for long DIs and a steep phase for shorter DIs. They play an important role in characterising dynamics of arrhythmias [Weiss et al., 2002; Qu et al., 1999; Keldermann et al., 2010]. Many studies have argued that a restitution slope greater than 1 has increased likelihood of generating arrhythmias through alternans and spiral wave breakup, compared to a restitution slope smaller than 1 [Karma, 1993; Fenton et al., 2002]. Furthermore, studies have shown that the flattening of the curve terminates fibrillation [Garfinkel et al., 2000; Riccio et al., 1999]. How these biomarkers are affected under ischaemia will be discussed in the following chapter.

Triangulation of the AP is also used as a biomarker of arrhythmic risk. It is usually measured as the ratio of APD at 30 or 50% and APD at 90% repolarisation [Hondeghem et al., 2001]. Triangulation refers to the shape of the AP and is mostly modulated by the plateau phase. Studies have shown a positive correlation between triangulation and pro-arrhythmia [Guo et al., 2007; Hondeghem et al., 2001; Lu et al., 2002]. AP alternans often appear as a precursor to arrhythmias [Watanabe et al., 2001; Laurita and Rosenbaum, 2008; Pastore et al., 1999; Lakireddy et al., 2005; Rosenbaum et al., 1994]. They can be defined as a beat-to-beat oscillation in AP amplitude and are usually characterised by two consecutive APs, the first one with a normal APD and the second one with a much smaller APD. They often appear in pathological conditions and as a precursor to arrhythmias. Other biomarkers such as AP amplitude, upstroke

velocity or resting membrane potential can also be related to arrhythmic risk. During ischaemia the AP amplitude and the upstroke velocity are decreased and the resting membrane potential is increased [Carmeliet, 1999].

2.4 Electrophysiological heterogeneities and variability

Myocardial tissue is highly heterogeneous. The outer surface of the heart is referred to as the *epicardium*. The interior surface of the ventricles is referred to as the *endocardium*. The regions of myocardium close to the epicardium and endocardium are often referred to as the *subepicardium* and *subendocardium* respectively. The rest of the myocardium is referred to as the *midmyocardium*. An example of the differences in AP from epi- to endocardium are shown in Figure 2.7, which are taken from human heart tissue experiments carried out by Igor Efimov's group [Glukhov et al., 2010]. The cells close to the *endocardium*, denoted as subendocardium, have the longest APD (shown in red), while the cells close to the *epicardium*, denoted as subepicardium, have the shortest APD. However, certain studies have shown a different transmural APD pattern with the existence of midmyocardial cells that display an APD significantly longer than the endocardial cells, they are often referred to as M cells [Antzelevitch et al., 1991].

Figure 2.7 Results from experiments carried out by Efimov's group showing the transmural differences in action potential in human cardiac tissue [Glukhov et al., 2010]

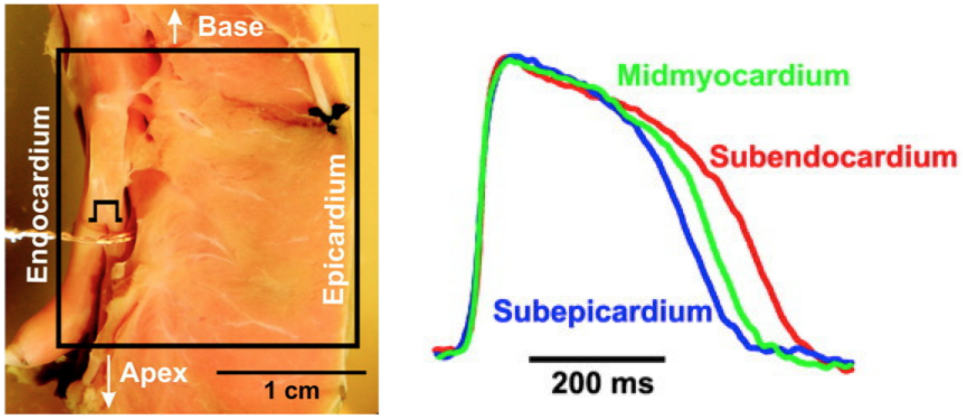

Differences in electrophysiological properties have also been reported between the LV and RV

and between the apex and the base of the heart, with a longer APD in LV and apex compared to the RV and base respectively [Verduyn et al., 1997; Cheng et al., 1999]. Ramanathan *et al.* carried out a human *in vivo* study that shows a mean LV apex-to-base ARI of 42 ms and an average 32 ms greater ARI in the LV compared to the RV [Ramanathan et al., 2006]. Bueno-Orovio *et al.* also suggested a longer APD in the LV compared to the RV in their *in vivo* electrogram study [Bueno-Orovio et al., 2012]. Voulders *et al.* showed that these differences may be due to a larger density of the repolarising current I_{Ks} found in dog hearts [Volders et al., 1999]. Finally, Cheng *et al.* also found an APD 40 ms longer in the apex compared to the base during *in vitro* single rabbit myocyte studies [Cheng et al., 1999].

Furthermore, we are all different and these differences are a multi-scale phenomenon, occurring from the sub-cellular to the whole organ level. This variability, which is being investigated computationally, can be inter-subject [Britton et al., 2013; Sarkar and Sobie, 2011] or from one beat to another within the same cell [Dangerfield et al., 2012; Pueyo et al., 2011; Johnson et al., 2010], and depends on differences in underlying ionic activity and the circadian rhythm, which modulates electrophysiological activity throughout the day [Portaluppi and Hermida, 2007].

2.5 Ischaemia

The blood is perfused to the heart through coronary arteries, the main ones are shown in Figure 2.8a. However, in some cases, tissue can become ischaemic, *i.e.* mismatch between oxygen and nutrients supply and demand. Ischaemia may occur due to increased demand caused, for example, by exercise, or to a restriction in the arteries causing part of the tissue to be poorly perfused, as represented in Figure 2.8b. Some of the causes may be wall thickening of the artery or blood clot formation [Davies and Thomas, 1984; Davies, 1990]. Occlusion of the left anterior descending (LAD) or the circumflex coronary artery has been been reported to be life-threatening [Mazhari et al., 2000; McDonald et al., 1986; Knopf et al., 1988; Reimer et al., 1977; Ma and Wang, 2007; Mazhari et al., 2000]. Size of the ischaemic region can vary widely

from patient to patient and in span (13 to 72%) of the myocardium, as shown in a human study by Lee *et al.* [Lee et al., 1981]. The tissue state changes following occlusion of an artery are very dynamic.

If ischaemia persists for a long period of time (over 2-4h) it leads to cell death and myocardial infarction (MI). After the onset of ischaemia, cell death is not immediate, it varies through time starting from about 20-40 min in animal experiments [Reimer et al., 1977; Thygesen et al., 2007]. The extent of the MI region depends on the size of the ischaemic zone, the extent of collateral blood flow that may still be able to provide limited perfusion to the affected region, variability in myocyte and individual demand and pre-conditioning (preparing the cells with short bursts of occlusion). Once the tissue becomes necrotic it can no longer contract, ventricular remodelling takes place due to the changes in the stresses and strains of the surrounding healthy tissue. The study of ischaemia in this thesis does not extend to MI, however studies that will be referenced may focus on MI due to its close link to ischaemia.

The incidence of arrhythmias critically depends on the duration of the preceding ischaemic period, the greatest risk occurs during the early stages of ischaemia up to 15 min, a phase often referred to as acute ischaemia. The risk of arrhythmias then deacreases as the tissue becomes more necrotic [Balke et al., 1981; Corr and Witkowski, 1983; Manning and Hearse, 1984; Penny and Sheridan, 1983]. The propensity to arrhythmias during ischaemia is often divided into three phases post-occlusion: the first 30 min (phase I), up to 72h (phase II) and the chronic stage after an infarct (phase III) [Smith et al., 1995]. Two distinct phases of ventricular arrhythmias occur during the first 30 minutes after induction of regional ischaemia by acute occlusion of a coronary artery in canine and porcine hearts and were termed Ia and Ib [Horacek et al., 1984; Hirche et al., 1980; Kaplinsky et al., 1979]. Type Ia arrhythmias occur 2 to 10 min after the onset of ischaemia and the frequency peaks 5 to 6 min post-occlusion. The second wave of arrhythmias, type Ib, occurs later, peaking 12 to 30 minutes after coronary artery ligation. In this thesis we focus on simulating 10-15 min of ischaemia post-occlusion, the last stages of

phase Ia, when the likelihood of developing disturbed arrhythmias is high [Rodríguez et al., 2004a; Tice et al., 2007; Russell et al., 1984].

In some cases, ischaemia is only transient, for example the blood clot may get dissolved or moved, or the demand for blood will decrease, which will allow blood flow to regain its normal route, reperfusing the tissue. Despite the benefits of reperfusion, it may trigger arrhythmias as the sudden change in electrophysiological properties may result in inflammation and oxidative damage rather than restoration of normal function, this phenomenon is known as *reperfusion injury* [Balke et al., 1981; Corr and Witkowski, 1983; Penny and Sheridan, 1983; Yellon and Hausenloy, 2007]. If reperfusion occurs after 30 min the tissue is usually not able to recover. This thesis does not extend to the study of reperfusion.

Figure 2.8 Perfusion system of the heart and example of an ischaemic region.

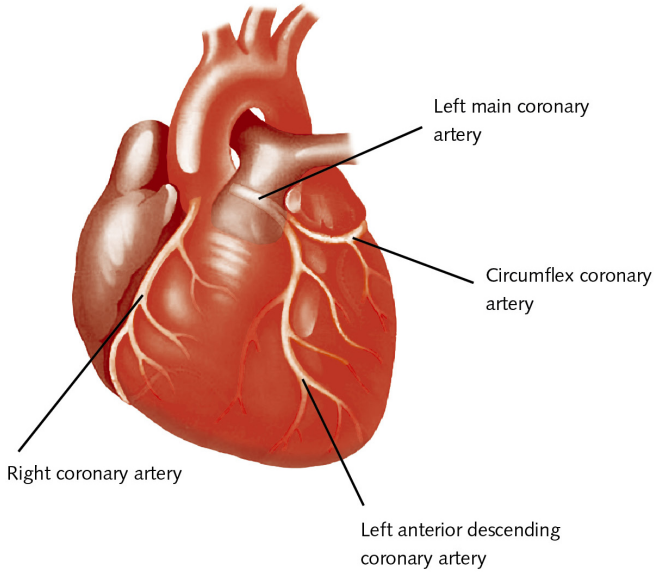

(a) Schematic representation showing the main arteries perfusing the heart.

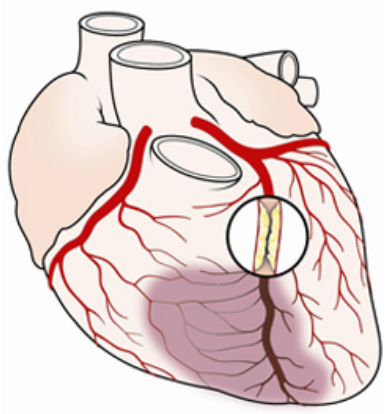

(b) Schematic representation of an occluded artery and the corresponding ischaemic region.

In this thesis, we focus on the main changes that occur during the first 10 min of ischaemia, when permanent cell damage is still not present and the arrhythmic risk is the highest. The main electrophysiological changes that occur are hyperkalaemia, acidosis and hypoxia [Kodama et al., 1984; Moréna et al., 1980; Gilmour and Zipes, 1980]. At the ionic level this is reflected

by an increase in extracellular potassium concentration ($[K^+]_o$) [Pandit et al., 2010; Watanabe et al., 1997; Weiss and Shine, 1982b; Schaapherder et al., 1990], decreased conductance of I_{Na} and I_{CaL} [Yatani et al., 1984; Irisawa and Sato, 1986; Sato et al., 1985] and activation of the ATP-sensitive potassium current $I_{K(ATP)}$ [Van Wagoner and Lamorgese, 1994; Weiss et al., 1992]. These alterations trigger the main AP morphology modifications that are observed under ischaemic conditions (see Figure 2.9): an increase in resting V_m [Kleber, 1983; Janse and Kléber, 1981], a slower upstroke [Kagiyama et al., 1982; Janse and Kléber, 1981] and a shorter APD [Sutton et al., 2000].

Figure 2.9 Schematic representation of a normal AP (black) and an ischaemic AP (red) resulting from changes in I_{Na}, I_{CaL}, which reproduces acidosis and decreases the upstroke velocity and AP amplitude, $I_{K(ATP)}$, which reproduces hypoxia and shortens the APD, and $[K^+]_o$, which reproduces hyperkalaemia and increases resting membrane potential.

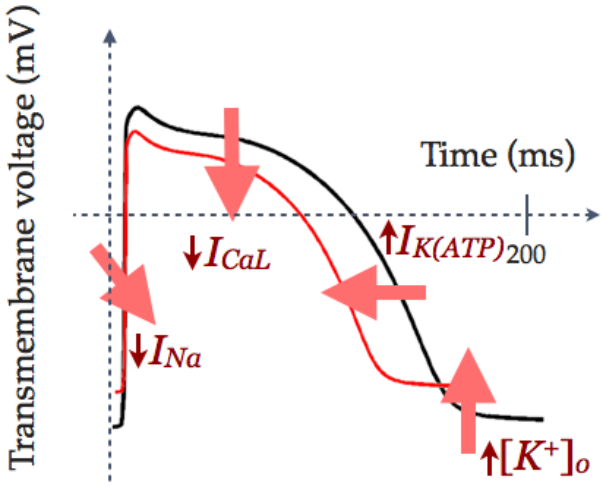

The ionic level modifications described above have been used extensively to investigate ischaemia-induced electrophysiological mechanisms computationally [Tice et al., 2007; Ferrero et al., 2003; Shaw and Rudy, 1997a; Rodríguez et al., 2004a; Ferrero et al., 1996]. Due to the lack of oxygen, the cells have to switch to anaerobic respiration, which produces lactic acid and decreases the pH of the cell as protons are produced during hydrolysis of ATP. The fall of ATP, in turn inhibits energy-dependent regulation of transmembrane ion gradients, such as the sodium potassium pump (I_{NaK}) and sarcoplasmic reticulum Ca^{2+} cycling. Therefore, a net accumu-

lation of intracellular sodium ($[Na^+]_i$) and calcium ($[Ca^{2+}]_i$) occurs. Measurements of $[Na^+]_i$ vary from 5 to 16 mM for different animal species [Baartscheer, 1997; Yao et al., 1998]. An increase in $[Na^+]_i$ promotes the reversed mode of I_{NaCa}, whereby Ca^{2+} is entering the cell and Na^+ is removed [Haigney et al., 1994; Smith and Allen, 1988; Tani and Neely, 1989]. Furthermore, I_{NaCa} is very sensitive to pH and strongly inhibited by acidosis [Doering and Lederer, 1993; Philipson et al., 1982]. All mechanisms responsible for an increase in $[Na^+]_i$ thus also contribute to the increase in $[Ca^{2+}]_i$ via the I_{NaCa} exchanger. At the AP level, the decrease in I_{NaCa} activity induces a reduction of upstroke velocity, prolonged refractoriness and slowed conduction.

After 10-15 min of ischaemia, free magnesium concentration ($[Mg^{2+}]$) increases from 0.5-0.8 mM to 2-6 mM [Kirkels, 1989; Murphy et al., 1989; Schreur, 1993]. In the cytoplasm, only about one-tenth of the total Mg^{2+} is free; the rest is bound to ATP and proteins. The main mechanism for the increase in $[Mg^{2+}]$ during ischaemia is the net hydrolysis of ATP to which Mg^{2+} was bound. The increase in $[Mg^{2+}]$ affects the main depolarisation and repolarisation currents: I_{Na}, I_{CaL}, I_{K1}, and I_{Ks}. Although not as well studied, Cl^- channels are also affected by ischaemia and may contribute to regulation of cell volume and cellular K^+ loss [Cascio, 2001].

During acute ischaemia, numerous electrophysiological properties are altered. PRR is increased [Sutton et al., 2000; Coronel et al., 2012] and CV is decreased [Janse and Wit, 1989], due to decreased excitability of the ischaemic cells. This mechanism is modulated by the decrease in Na^+ channel activity as the inactivation gates take longer to recover and the AP upstroke is slower [Coronel et al., 2012; Papadatos et al., 2002; Carmeliet, 1999]. This plays an important role in arrhythmic risk as the difference between the healthy and ischaemic tissue creates a heterogeneous path for the excitation wavefront. The ERP shows both no changes or an increase depending on parameters such as the stimulus amplitude [Sutton et al., 2000].

The ischaemia-induced electrophyisological changes that occur are spatially heterogeneous.

The area surrounding the ischaemic region, referred to as the border zone (BZ), has been shown to play an important role in the initiation and maintenance of ischemia-induced rhythm disturbances [Bernus et al., 2002; Coronel et al., 2002; Ferrero et al., 2003]. Steep gradients of metabolic and ionic changes are present at the ischaemic boundaries due to diffusion to and from the neighbouring healthy tissue or blood from the ventricles [Cascio, 2001]. These spatial changes will be discussed further in the following chapter.

Arrest of perfusion causes a shrinkage of the extracellular compartment and an increase in the extracellular electrical resistance by 25% to 50% and it may slowly increase further as ischaemic cells swell and compress the interstitial space. Due to the cell becoming less excitable, the ischaemic region may contract differently than the normal tissue, therefore, extra stresses and strains will be applied. Furthermore, swelling of the cell will also add new stretches and strains. These will in turn modulate ionic currents that are stretch-sensitive such as I_{CaL} or even $I_{K(ATP)}$ [Hu, 1997]. These mechanical changes start appearing in later stages of ischaemia, after 30 min or 1h. Therefore, the changes are not relevant to the first 10-15 min period investigated in this thesis.

2.6 Arrhythmias

Abnormal heart rhythms, known as arrhythmias, can be lethal. There are different types of arrhythmias, where the heart beat becomes faster, slower or irregular. There are arrhythmias that affect only the atria and others that affect only the ventricles. Patients can survive longer with atrial arrhythmias than with ventricular arrhythmias as the ventricles are essential for pumping blood to the body [Nattel, 2002]. Some arrhythmias can be asymptomatic, while others can be lethal within minutes, such as ventricular fibrillation (VF) [Jalife, 2000; Gray et al., 1998; Pandit and Jalife, 2013]. During ventricular tachycardia (VT) there is a faster wave of activation that self-perpetuates and overrides the normal sinus rhythm regulated by the SAN node [Wichter et al., 1992]. This wave of activation usually consists of a single rotor. During VF, the heart beat

is completely unsynchronised and does not allow the heart to carry out its normal mechanical pump function effectively. The pattern of electrical activity is formed by multiple reentrant wavelets and rotors. VF is often preceded by VT, this occurs when the main reentrant spiral-wave pattern breaks into multiple fractioned wavefronts [Huikuri et al., 2001; Weiss et al., 1999]. Figure 2.10 shows results from Cherry and Fenton's group, that demonstrate VT and VF principles with a single spiral-wave reentry and multiple wavelets in a three-dimensional (3D) slab of cardiac tissue [Cherry and Fenton, 2008].

Figure 2.10 Simulation results from Cherry and Fenton showing (a) tachycardia and (b) fibrillation under different conditions [Cherry and Fenton, 2008].

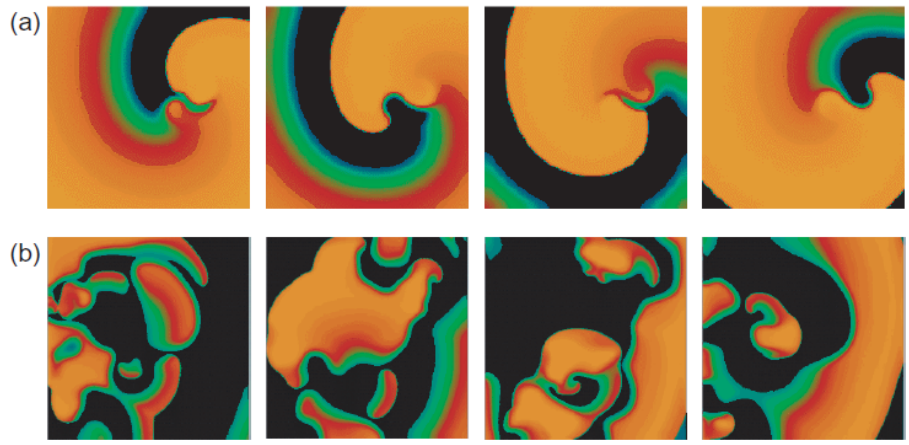

Dispersion of repolarisation is a normal physiological factor that exists in healthy hearts [Antzelevitch et al., 1991; Clark et al., 1993], but becomes especially prominent during regional ischaemia and has been shown to increase the likelihood of arrhythmias [Gettes et al., 1991; Kimura et al., 1990]. Numerous studies have shown the importance of the border zone area, where the ischaemic tissue meets the normal tissue, in modulating arrhythmic risk [Janse et al., 1979; Zaitsev et al., 2003; Bernus et al., 2005b]. An example of this, is the injury current that flows between the normal and ischaemic tissue that occurs both during diastole because of the difference in resting V_m and systole due to the differences in APD and delays in activation as shown by Janse *et al.* in isolated porcine and canine hearts [Janse et al., 1980]. Ischaemia-induced electrophysiological heterogeneities play an important role in arrhythmogenesis, how-

ever many mechanisms remain unknown due to the scarcity of experimental data in human and the high degree of spatio-temporal resolution needed to investigate these mechanisms.

Numerous mechanisms underlie VT and VF, but one of the main causes is ischaemia [Costeas et al., 1997; Coronel et al., 2002; Bradley et al., 2011]. The increase in electrophysiological heterogeneities can create a second conduction pathway that disrupts the normal SAN node rhythm. The ischaemic tissue, has a slower CV and a longer ERP, as shown in the lighter blue circle in Figure 2.11 from computer simulations carried out by Ferrero *et al.* [Ferrero et al., 2003]. As the wave of activation reaches the ischaemic region, a conduction block occurs as the tissue is still refractory. By the time the excitation wave reaches the distal part of the ischaemic region, the latter has recovered. The wave can then reenter the ischaemic tissue and the normal tissue where the excitation wave initially met the conduction block. This pattern of activation, often referred to as *figure-of-eight reentry*, can become self-sustained, as described experimentally in pig hearts by Janse *et al.* [Janse and Wit, 1989]. This can lead to VF and death within minutes if a defibrillation shock or cardiopulmonary resuscitation (CPR) is not performed.

Figure 2.11 Snapshots at different times of simulation results from Ferrero *et al.* showing mechanisms of reentry during ischaemia [Ferrero et al., 2003].

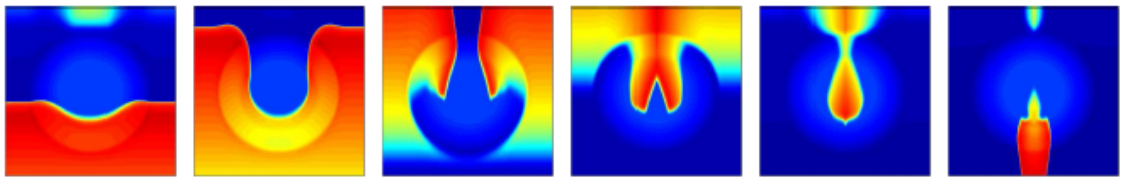

2.7 Anti-arrhythmic treatment

Both electrical therapy through internal cardioverter defibrillators (ICDs) and/or pharmacological therapies are administered against sudden cardiac death. ICDs are usually implanted in patients with low LV ejection fraction (LVEF $< 30\%$) but the majority of sudden cardiac deaths occur in patients with LVEF $> 30\%$, and therefore, classified as low risk [Van Herendael et al.,

2010]. Implanted pacemakers act by detecting an abnormal heart rhythm and pacing the heart back into a normal rhythm, while defibrillators, act by applying an electrical shock when the heart goes into fibrillation [DiMarco, 2003; Brode et al., 1997].

Anti-arrhythmic drugs constitute first line therapy for patients suffering from abnormal atrial and ventricular rhythms [Wazni et al., 2005], often in combination with electrical therapy [Van Herendael et al., 2010]. Anti-arrhythmic drugs go through a long series of tests and milestones before they are available on the market. It is a lengthy and expensive process. Numerous studies have shown their efficacy in suppressing arrhythmias [Nademanee et al., 1985; Myburgh et al., 1979]. Unfortunately, certain drugs display lethal side-effects and have to be removed from the market, as was shown in the SWORD and CAST clinical trials [MacNeil, 1997; Waldo et al., 1996]. The underlying mechanisms behind this paradox remain unclear. Thus, cardiac drug toxicity is a major concern for society and has a huge socio-economic impact [Corrias et al., 2010; DiMasi et al., 2003; Brennan et al., 2009].

There are numerous anti-arrhythmic drugs and they can be grouped into 5 classes according to the Singh Vaughan Williams classification [Williams, 1984], as summarised in Table 2.1. Class I drugs act by blocking I_{Na} channels and therefore slowing CV, they are divided into three subgroups according to the kinetics of drug action. Class II drugs, also known as beta-blockers, act by blocking the beta receptors which are part of the sympathetic nervous system and help regulate the heart rate. Class III drugs act by blocking I_{Kr} channels, which prolongs the APD. Class IV drugs mainly act by blocking Ca^{2+} channels, therefore slowing the plateau phase of the AP. Finally, class V drugs act by other or unknown mechanisms. Certain compounds such as amiodarone and sotalol, which are classified as Class III anti-arrhythmic drugs, also display properties from other classes. This thesis focuses on class III anti-arrhythmic drugs, which act by increasing the wavelength of reentry, therefore increasing the likelihood the excitation wave will encounter refractory tissue [Nademanee et al., 1985]. Little is known about how the efficacy and safety of anti-arrhythmic compounds is modulated by myocardial ischaemia, a

common and dangerous phenomenon that many of these patients suffer from [Steinberg et al., 2014].

2.8 Experimental and clinical electrophysiological recording techniques

Numerous experimental and clinical techniques are used to investigate arrhythmogenic mechanisms during ischaemia. Here we describe the main ones used in this thesis, such as electrocardiograms from *in vivo* human open chest surgery and optical mapping from *in vitro* animal experiments.

2.8.1 Electrocardiogram

The main clinical tool used to examine the heart's electrical activity through time in human patients is the electrocardiogram (ECG). It is widely used as it is not only useful for the study of cardiac pathologies, but also relatively simple, cheap and non-invasive. The signal is recorded from electrodes on the body surface. ECGs have played a pivotal role in shaping our knowledge of cardiac electrophysiology, with the first electrocardiogram being recorded in the 1800s [Lüderitz, 2009].

The different phases of the cardiac cycle can be observed on the ECG, as shown in Figure 2.12. The depolarisation of the atria is reflected by the positive P wave. The QRS complex, composed of the Q, R and S waves, defines the depolarisation of the ventricles. The amplitude of the QRS complex is larger than the P wave due to the ventricles being much larger than the atria. Finally, the T wave represents the repolarisation of the ventricles. An important ECG measurement that is widely used in the diagnosis of pathologies is the QT interval, the time between the onset of the QRS complex (ventricle depolarisation) and the end of the T wave (ventricle repolarisation). Prolongation of the QT interval is thought to indicate arrhythmic risk, and many drug

Table 2.1 Singh Vaughan Williams classification of anti-arrhythmic drugs [Rang et al., 2003].

Class	Mechanism	Compounds	Clinical Use
Ia	I_{Na} channel blocker	• Quinidine • Procainamide, • Disopyramide	ventricular arrhythmias
Ib	I_{Na} channel blocker (fast kinetics)	• Lidocaine • Phenytoin • Mexiletine • Tocainide	ventricular tachycardia
Ic	I_{Na} channel blocker (slow kinetics)	• Encainide • Flecainide • Propafenone • Moricizine	atrial fibrillation and recurrent tachyarrhythmias
II	beta blockers	• Propranolol • Esmolol • Timolol	decrease myocardial infarction and prevent tachyarrhythmias
III	K^+ channel blockers	• Amiodarone • Sotalol • Dofetilide • Dronedarone	ventricular tachycardias and atrial fibrillation
IV	Ca^{2+} channel blockers	• Verapamil • Diltiazem	atrial fibrillation
V	other or unknown mechanisms	• Adenosine • Digoxin	atrial fibrillation

Figure 2.12 Schematic representation of an electrocardiogram (ECG) with annotated phases: P wave represents atrial depolarisation, QRS complex represents the ventricle depolarisation and the T wave represents repolarisation of the whole ventricles.

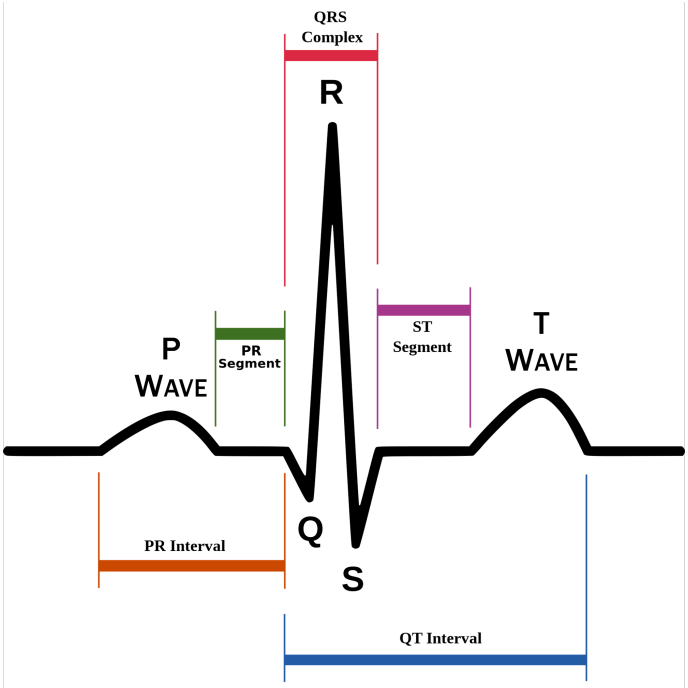

compounds fail to reach the market during the final stages of testing due their prolonged QT effects. However, studies have shown that the QT interval prolongation is not a sufficient measure of arrhythmogenesis. Indeed, class III anti-arrhythmic drugs have proven their efficacy in reducing arrhythmias and act by prolonging the refractory period and therefore the QT interval [Lawrence et al., 2005; Hondeghem, 2006]. Furthermore, ischaemia has been shown to modulate ECG morphology, by decreasing the QT interval and by ST segment elevation [Gima and Rudy, 2002; Sporton et al., 1997; Kléber, 2000; Taggart et al., 1979].

2.8.2 Electrode recordings

To record the electrical activity of cardiac cells, the first techniques used microelectrodes, which were placed on the surface of the heart or inserted intramurally into the tissue to obtain AP measurements of the cells under the electrode surface [Franz et al., 1986; Coronel et al., 1988; Kadish, 2004; Efimov et al., 2004]. The need to cover a bigger region of tissue led to the

development of microelectrode arrays or sock of electrodes. Measurements of cardiac electrical activity have been taken *in vivo* human hearts during open chest surgeries to investigate changes induced by ischaemia [Taggart, 2000; Sutton et al., 2000]. Ionic concentrations can also be recorded using ion sensitive electrodes [Wilensky et al., 1986; Coronel et al., 1988]. This is especially important during ischaemia when various ion concentrations, such as $[K^+]_o$ are significantly altered as a function of time post-occlusion.

Current-voltage relationships can be measured through voltage clamp experiments, which consist of two electrodes that control the transmembrane voltage of the cell and measure how the changes modulate ionic current activity [Deck et al., 1964; Johnson et al., 1999]. Therefore, the membrane voltage can be manipulated independently of the ionic currents. This method has been refined to record the currents of single ion channels. This technique is known as patch clamping and uses a glass micropipette as a an electrode that suctions the membrane surface area of interest, which often contains just one or few ion channels [Hamill et al., 1981]. Applying channel blocking drugs allows the isolation of particular ionic current effects.

2.8.3 Optical mapping

Optical mapping overcomes many of the limitations of electrode recordings such as: the electrodes damaging the tissue during insertion [Knisley and Smith, 1996], the challenges of maintaining the electrodes in the tissue as well as obtaining a stable recording, the recorded signal being only local to the area under the electrode [Arora et al., 2003; Rosenbaum and Jalife, 2001]. During arrhythmias there are numerous spatio-temporal events occurring and the need to record them more accurately led to the development of optical mapping. It can provide information on the whole surface of the *ex vivo* Langendorff-perfused heart. The heart is stained with voltage sensitive dyes, which upon excitation emit fluorescence that changes as a function of the transmembrane voltage of the cell they are attached to. Ion specific dyes also exist which can calculate the change in concentration of specific ions [Himel et al., 2009; Lakireddy

Figure 2.13 Schematic representation of an optical mapping experimental setup (diagram provided by Igor Efimov's group).

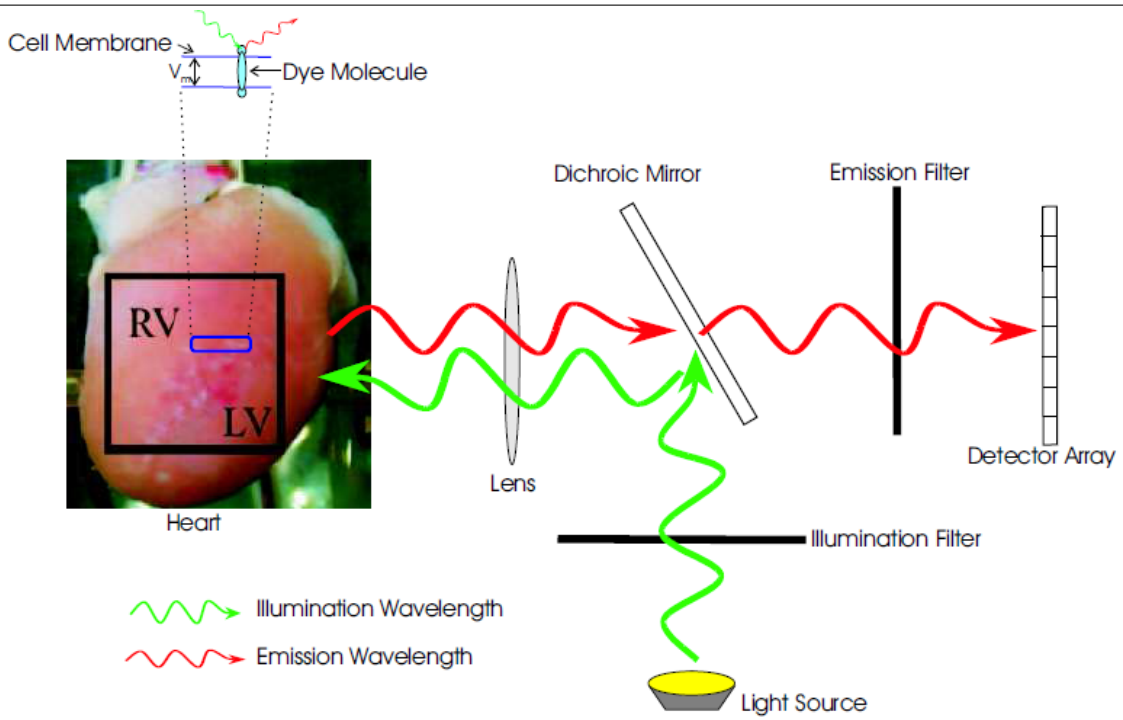

et al., 2005; Bishop et al., 2011]. A schematic representation of the setup is shown in Figure 2.13. Dichroic mirrors are used to guide the illuminating and emitting wavelengths in the right direction. The emission and illumination filter only let the corresponding wavelength of light through and the detector array records the signal emitted.

Optical mapping studies have provided important understanding of activation and repolarisation patterns in cardiac tissue and arrhythmogenesis during ischaemia [Yang et al., 2007; Efimov et al., 1994; El-Sherif et al., 2009]. Due to the high scattering and low absorption properties of biological tissue, the excitation light can penetrate the tissue up to a few millimetres. Studies have shown that the signal distortion is reflected by a significantly prolonged upstroke of the optical AP [Girouard et al., 1996; Gray, 1999]. Furthermore, the exact depth the fluorescent signal reaches varies from one study to another, depending on the techniques and species used [Ding et al., 2001; Cheong et al., 1990; Knisley, 1995; Baxter et al., 2001].

Recent studies have shown that the depth of penetration of the illuminating light into the tissue

is dependent on the wavelength [Walton et al., 2010]. Near-infrared (NIR) light is less absorbed and scattered in tissue than blue-green light, thus allowing for increased depth penetration of the optical signal. Lee *et al.* have developed a novel affordable and effective technique to record these two signals quasi-simultaneously [Lee et al., 2011]. In their most recent study they measured transmembrane voltage and intracellular free calcium at two wavelengths, suitable for ratiometric mapping of these parameters. The framework developed by Lee *et al.* is simpler than previous set ups as it uses a single recording camera compared to 2 or 4 which were used in previous dual voltage-calcium optical mapping recordings [Omichi et al., 2004; Wu et al., 2005; Choi and Salama, 2000; Fast, 2005; Laurita and Singal, 2001].

Computer simulations have been used to understand the underlying physical processes involved in the production of the voltage-sensitive signal during an optical mapping experiment. The first computational modelling study of optical mapping signals was performed by Ding *et al.* [Ding et al., 2001]. Hyatt *et al.* later extended the computational study to include effects of three-dimensional photon scattering in cardiac tissue [Hyatt, 2003]. However, these models could not capture the three-dimensional photon scattering effects in complex realistic ventricular geometry and heterogeneity present during whole-heart recordings. Bishop *et al.* addressed these limitations by developing a model of panoramic optical signal synthesis over a three-dimensional realistic anatomically-based ventricular model [Bishop et al., 2007a]. Three-dimensional photon transport within the tissue is modelled using a finite element solution to the photon diffusion equation. The combination of experimental and computational models have helped interpret optical mapping recordings, especially during arrhythmias and defibrillation [Bishop et al., 2007b; Baxter et al., 2001; Efimov et al., 1999; Bray and Wikswo, 2003].

2.8.4 Species of animals

Many different types of species such as dog [Harken et al., 1981; LeGrice et al., 1995; Cobbe et al., 1983; Magyar et al., 2002; Janse et al., 1985; Zicha et al., 2004], pig [Harken et al., 1981;

Dean and Lab, 1990; Janse et al., 1979, 1985; Downar et al., 1977], rabbit [Harken et al., 1981; Maier, 2000; Fedida and Giles, 1991; Weiss and Shine, 1982b; Wilde et al., 1988; Bersohn et al., 1982; Vermeulen, 1996] and rat [Maier, 2000; Murphy et al., 1989; Clark et al., 1993; Ju et al., 1996; Malloy et al., 1990] are used as models to investigate electrophysiological arrhythmic mechanisms and pathologies. Every model offers its own advantages and disadvantages. Rat and rabbit models are relatively inexpensive compared to bigger animals such as dogs or cats which are costlier to maintain due to their greater size and maintenance requirements [Harken et al., 1981]. Rat models are limited in their AP morphology, as it is significantly different to the human AP, with a very short APD due to a lack of a plateau phase and a resting heart rate 5 times faster than humans [Bers, 1993; Shattock and Bers, 1989]. Furthermore, Harken *et al.* compared patterns of myocardial ischaemia in rabbit, dog, pig and monkey hearts [Harken et al., 1981], showing that the pattern of perfusion in dog is different from other species, leading to a better perfusion of the ischaemic zone compared to the other 3 species.

Rabbits offer a good model as they are both affordable (smaller than bigger animals such as dog and pig) and share important similarities with human cardiac electrophysiology. They are able to reproduce pathological properties such as heart failure, as described by Hasenfuss in [Hasenfuss, 1998]. Panfilov compared patterns of VF in rabbit, rat, guinea-pig and mouse hearts and found that patterns displayed in human are similar to those in the rabbit heart due to the comparable effective size of both hearts. On the other hand, patterns of VF displayed in pig and dog have a more complex organisation [Panfilov, 2006]. Furthermore, rabbit and human show similar calcium dynamics, as described by Maier *et al.* [Maier, 2000], and similar repolarising current activity, such as I_{Kr}, as described in [Virág et al., 2001]. The first part of this thesis focuses on the rabbit model due to its similarities to human hearts and due to the ethical and practical limitations of human experiments.

Chapter 3

Literature review of ischaemia-induced electrophysiological changes

This section will focus on the main ischaemia-induced electrophysiological changes investigated in this thesis by presenting a review of the literature, carried out both experimentally and computationally. We provide a detailed description of previous studies showing how the main ischaemia-induced electrophysiological changes vary spatially and temporally. We also present important clinical studies showing how acute ischaemia affects the main arrhythmic biomarkers. We review drug safety and efficacy during ischaemia, focusing on class III anti-arrhythmic drugs. Finally, the main computational studies of acute ischaemia and their investigations of arrhythmic mechanisms will be presented.

3.1 Temporal changes of ischaemia-induced electrophysiological changes

In this section we review the literature describing how the main ischaemia-induced electrophysiological changes (hyperkalaemia, acidosis and hypoxia) and biomarkers vary through time during acute ischaemia.

Figure 3.1 Extracellular potassium concentration ($[K^+]_o$) after the onset of ischaemia (min) in Langendorff perfused rat and rabbit hearts with (open squares) and without (closed squares) pacing [Wilde and Aksnes, 1995; Wilde et al., 1990].

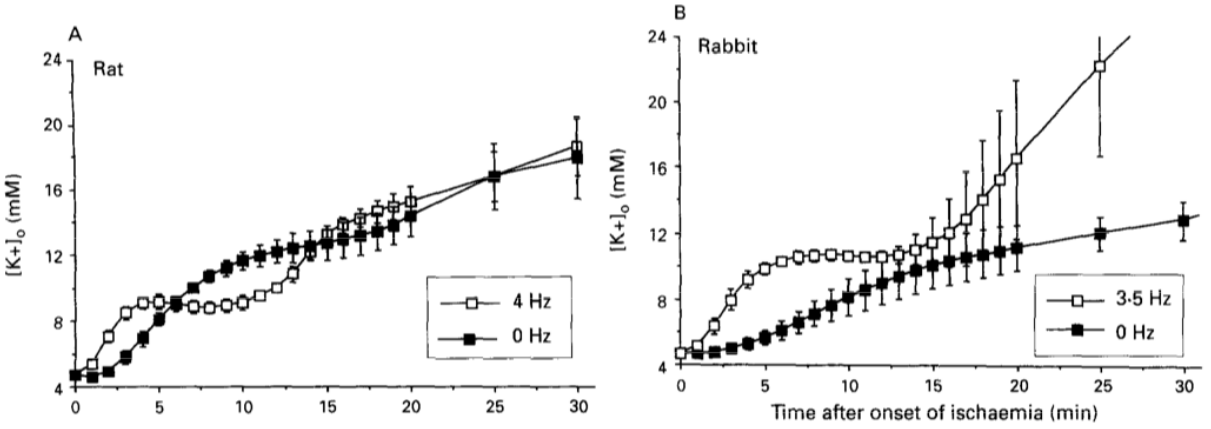

(a) Rat **(b)** Rabbit

During ischaemia, the K^+ equilibrium across the cell membrane is broken and external K^+ accumulates. It usually occurs within 3 phases: there is a fast accumulation of K^+ in the extracellular space during the first 20 s. It then reaches a plateau phase after 3-10 min and finally a third slower increase after 15 and 30 min [Wilde and Aksnes, 1995; Cascio, 2001]. Results found by Wilde *et al.* in isolated Langendorff perfused rabbit and rat hearts are presented in Figure 3.1, where we can clearly see the three stages with 4 and 3.5 Hz pacing [Wilde et al., 1990]. A study by Vermeulen *et al.* in isolated rabbit and rat hearts showed that $[K^+]_o$ increases steadily up until 6 min of ischaemia after which it more or less plateaus around a value of 11 mM for failing hearts and 9 mM for control hearts, as shown in Figure 3.2.

The values reached and the exact dynamics are dependent on the species, the experimental preparation and pacing frequency. Furthermore, the changes are not homogeneous; higher levels of $[K^+]_o$ are present in the subepicardium compared with the subendocardium [Schaapherder et al., 1990]. The main mechanisms responsible for the change in $[K^+]_o$ are the shrinkage of the extracellular space due to the swelling of the cell, decrease of active K^+ influx (due to a decrease in I_{NaK} pump activity) and increase of passive K^+ efflux, due to $I_{K(ATP)}$ current [Carmeliet, 1999].

Figure 3.2 Extracellular potassium concentration ($[K^+]_o$) and pH through time after the onset of ischaemia (min) in Langendorff perfused rabbit control (white squares) and failing hearts (black squares) [Vermeulen, 1996].

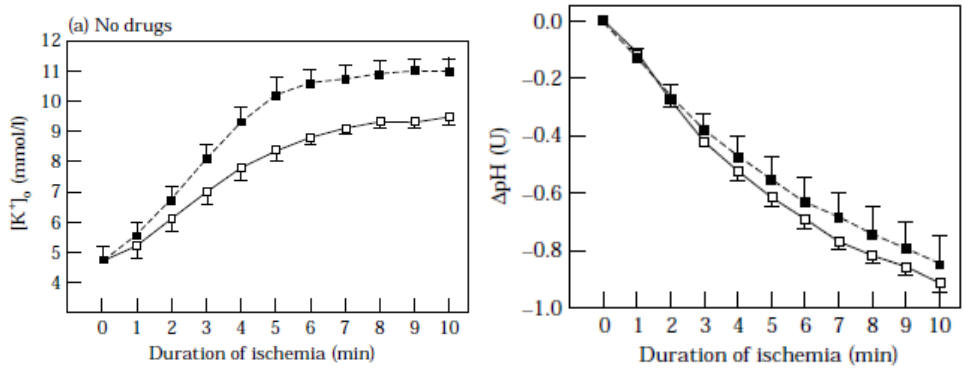

After occlusion, external pH changes rapidly and monotonically from 7.4 to values as low as 6.0 [Clarke et al., 1993]. Intracellular pH changes from control values of 7.15 to 6.5 after approximately 4 min and 6.2-6.0 after 10-20 min (rat [Camacho et al., 1993; Clarke et al., 1993; Tani and Neely, 1989; Wagner et al., 1990]; ferret [Marban et al., 1990], rabbit [Mohabir et al., 1991]). A small delay of 1 min before the decline in intracellular pH has been observed by Vandenberg *et al.* in Langendorff perfused ferret hearts [Vandenberg et al., 1993]. The fall in pH is caused by an increased production and insufficient removal of protons [Dennis, 1991]. The study by Vermeulen *et al.* reported a steady and constant decrease in pH throughout 10 min of ischaemia, as shown in Figure 3.2. After 10 min of ischaemia, the decrease in pH was of about 0.8 compared to the pH at 0 min, in both control and failing hearts [Vermeulen, 1996].

Figure 3.3 Creatine phosphate (CP) and adenosine triphosphate (ATP) levels during 30 min of ischaemia in isolated pig hearts [Moréna et al., 1980].

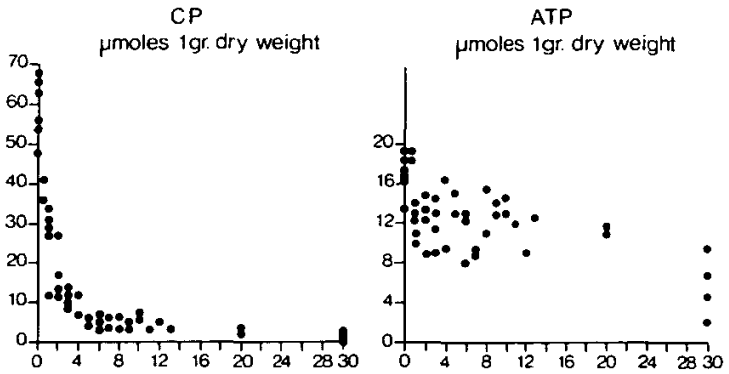

Moréna *et al.* investigated creatine phosphate (CP) and adenosine triphosphate (ATP) levels, measures of oxygen availability, post-occlusion in isolated pig hearts [Moréna et al., 1980]. Both measurements provide a good approximation of the decrease in oxygen during ischaemia. Figure 3.3 shows an abrupt decrease of about 60 μM per 1g dry in CP during the first 2 min of ischaemia, which then steadily goes down to 0 at 30 min. Decrease in ATP displays a more constant linear decrease throughout the 30 min of ischaemia, going from 20 μM per 1g dry at 0 min to 2 at 30 min.

Figure 3.4 Experimental results carried out by Vermeulen *et al.* showing CV and APD_{80} in isolated rabbit control (white squares) and failing (black squares) hearts during 10 min of ischaemia [Vermeulen, 1996].

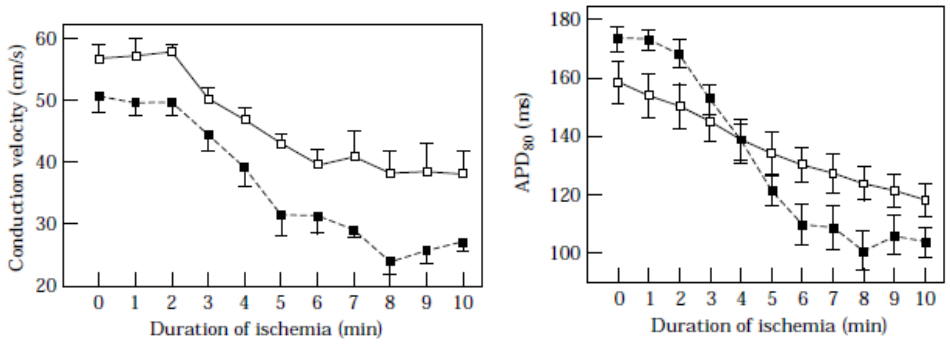

The study by Vermeulen *et al.* in Langendorff perfused rabbit hearts reported changes in APD and CV after 10 min of ischaemia in normal and failing hearts [Vermeulen, 1996]. Their results, showing changes through time for CV, APD at 80% repolarisation (APD_{80}), pH and $[K^+]_o$ are summarised in Figure 3.4. There is a decrease in CV of 27% in control hearts and 50% in failing hearts during the first 10 min of ischaemia. CV is constant for the first 2 min of ischaemia and then starts decreasing linearly after 3 min until it reaches a second plateau phase in the control hearts after 6 min. APD_{80} decreased by about 25% in normal hearts and about 41% in failing hearts after 10 min of ischaemia. The rate of decrease of APD in normal hearts appears to follow a constant linear gradient. However, in failing hearts, the APD decrease is more pronounced between 3 and 6 min of ischaemia. A study by Watanabe *et al.* in porcine hearts showed

a prolongation of APD of about 31 ms during the first 2 min of ischaemia followed by the expected shortening of APD [Watanabe et al., 1997].

3.2 Spatial heterogeneities at the border of the ischaemic region

The central ischaemic zone around the occluded artery experiences the most severe ischaemic conditions, however due to diffusion to and from the normal tissue surrounding the ischaemic region, a gradient in ischaemic properties exists. Coronel *et al.* showed spatial dispersion of $[K^+]_o$ around the occluded artery in isolated dog heart experiments [Coronel, 1994]. Lateral heterogeneities in the tissue surrounding the area of regional ischaemia were also found by Janse *et al.* and Rumsey *et al.* in perfused pig hearts [Janse et al., 1979; Rumsey et al., 1994].

The severity of ischaemic changes varies transmurally through the ischaemic region. Extracellular K^+ accumulation is faster in the subendocardium than in the subepicardium while APD shortening due to $I_{K(ATP)}$ activation is more pronounced in the subepicardium [Hill and Gettes, 1980; Gilmour and Zipes, 1980; Kimura et al., 1986; Schaapherder et al., 1990; Furukawa et al., 1991]. Pandit *et al.* showed how $I_{K(ATP)}$ determines LV-RV APD gradients during global ischaemia in Langerdorff-perfused guinea pig hearts and computational models [Pandit et al., 2011]. These results agree with the study by Komniski *et al.* in rat hearts showing that LV cells are able to maintain a better ATP level than RV cells during hypoxia [Komniski et al., 2011]. More acidic conditions are found in the subendocardial regions [Watson et al., 1984]. Delayed activation is especially prominent in the subepicardium, whereas activation of the subendocardial layers is relatively unaffected. This may be related to a relatively elevated O_2 tension in the subendocardial layers, due to diffusion from the cavity [Wilensky et al., 1986]. Schaapherder *et al.* carried out experiments in isolated rat hearts in different gaseous environments: 100% O_2, 100% CO_2 and 100% N_2 [Schaapherder et al., 1990]. Figure 3.5 shows how CP (defined as CrP in the Figure) varies depending on the distance from the epicardium in rat hearts after

10 min of ischaemia. The 100% O_2 gaseous environment is the closest approximation to the metabolic dynamics of the tissue surrounding the ischaemic region. In which case the amount of CP drops off quite quickly after 0.2 mm from the epicardium.

Figure 3.5 Subepicardial creatine phosphate (CrP) after 10 min of global ischaemia at difference distances from the epicardium (x-axis in mm) in a 100% O_2 (open circles), 100% CO_2 (open triangles) and 100% N_2 (closed circles) environment. [Schaapherder et al., 1990]

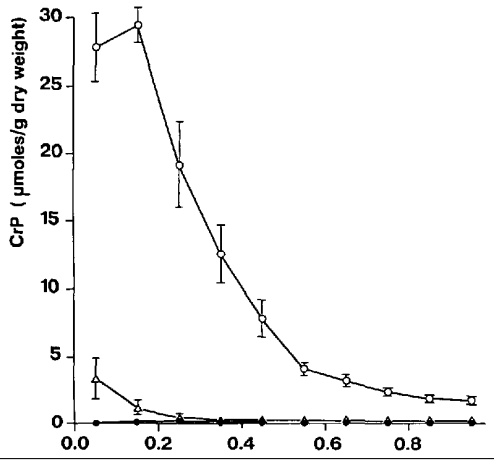

A thin layer of tissue, referred to as the border zone, of approximately 1 - 2 mm at the surface of the ischaemic tissue, receives nutrients and oxygen from blood in the cavities and the medium surrounding the heart, thus remaining viable over the course of acute ischaemia [Wilensky et al., 1986; Darsee et al., 1981; Peters et al., 1997; Ursell et al., 1985]. Therefore, the first few layers of cells at the surface of the heart are not in fully ischaemic conditions. The border zone can be represented by a gradient in electrophysiological properties and by differences in AP morphology and duration. The depth of the border zone (i.e. the region over which there exists a gradient in electrophysiological parameters) varies for the different parameters and experimental setups. A study carried out by Wilensky *et al.* in isolated preparations of rabbit interventricular septum showed how electrophysiological changes vary spatially after 10 to 12 min of ischaemia [Wilensky et al., 1986]. The table shown in Figure 3.6 summarises their findings. Values of various electrophysiological characteristics and different depths below the endocardium are reported, up to 650 μm and deeper than 650 μm. Their results show a

decrease of 27% in resting membrane potential, a decrease of 46% in AP amplitude, a decrease of 12% in APD, an increase of 44% in $[K^+]_o$, a decrease of 6% in pH and a decrease of 80% in phosphocreatine, a measure of how much oxygen is available. This gradient is due to the surrounding healthy tissue or blood lying in the ventricles. Transmural inhomogeneities were also reported by Schaapherder *et al.* in isolated rat hearts [Schaapherder et al., 1990].

Figure 3.6 Electrophysiological characteristic of different layers below the epicardium after 10 to 12 min of global ischaemia[Wilensky et al., 1986]

Depth below endocardium	Resting membrane potential (mV)	Action potential amplitude	Action potential duration	Extracellular [K⁺] (mM)	pH	Phospho-creatine (μmol/g dry weight)
To 650 μm	73 ± 3	81 ± 13	116 ± 42	7.68 ± 2.08	6.81 ± 0.27	18.01 ± 8.34
Deeper than 650 μm	53 ± 4	44 ± 11	102 ± 42	11.09 ± 1.81	6.36 ± 0.32	3.72 ± 2.56
p value (two-tailed Student's t test)	p<.01	p<.01	NS	p<.05	p<.05	p<.01

3.3 Effects on arrhythmic electrophysiological properties

As described earlier in 2.6, during ischaemia, the difference in refractory period creates a *figure-of-eight* reentry around the ischaemic region. As was reported in porcine hearts by Janse *et al.* [Janse and Wit, 1989]. The longer refractory period of the ischaemic region creates a conduction block when the excitation wave first reaches it. As the wave circumvents the ischaemic region and reaches the distal area, the ischaemic tissue recovers and is re-excited again, reaching the proximal normal tissue and self-sustaining the figure-of-eight reentry.

Other studies have shown that the spatial differences in refractory period favour the occurrence of arrhythmias [Nademanee et al., 1985; Russell and Oliver, 1978; Zaitsev et al., 2003]. Kuo *et al.* showed that a ventricular premature beat could lead to sustained arrhythmias under certain degrees of dispersion of repolarisation in canine hearts [Kuo et al., 1983]. Studies have emphasised the importance of timing of activation, repolarisation and dispersion of repolarisation in the initiation and maintenance of reentrant ventricular arrhythmias [Hanson et al., 2009;

Janse et al., 1985; Farid et al., 2011; Banville and Gray, 2002]. All these factors are altered during ischaemia [Carmeliet, 1999]. Regional ischaemia increases heterogeneities across the tissue which augments the likelihood of arrhythmias [Janse et al., 1986; Coronel et al., 2009; Kuo et al., 1983]. Furthermore, Bradley *et al.* showed that global ischaemia increased the complexity of electrical activation during VF in human patients during open chest surgery [Bradley et al., 2011].

During ischaemia the extent of heterogeneities increases, mainly due to differences between the ischaemic and healthy tissue, but also due to spatial differences at the border of the ischaemic regions (as described in the previous section). Coronel showed how the increased heterogeneity in $[K^+]_o$ during ischaemia is pro-arrhythmic, due to its effect on CV, excitability and refractoriness which in turn promote the initiation and maintenance of arrhythmias [Coronel, 1994]. Furthermore, a study by Janse *et al.* during the first 10 min of ischaemia in canine hearts demonstrated that arrhythmias originated from premature beats occurring in the subendocardial border zone [Janse et al., 1986]. Similar results showing the importance of intramural reentry in the subendocardial border zone during mechanisms of VT and VF were shown by Pogwidz *et al.* in feline hearts [Pogwizd and Corr, 1987b, 1990].

A review by Coronel *et al.* describes the importance of PRR in modulating arrhythmic risk; the increased dispersion of PRR creates a substrate for reentry to occur [Coronel et al., 2012]. Sutton *et al.* and Taggart *et al.* calculated important biomarkers (APD, ERP, PRR and CV) during the first 3 min of global ischaemia in human during open chest surgery, using a pressure contact electrode they placed on the endocardium and intramural electrodes [Sutton et al., 2000; Taggart, 2000]. Their experiments provide unique *in vivo* human data during the first few minutes of ischaemia. Their results are summarised in Figure 3.7. APD decreased by approximately 60 ms after 3 min of ischaemia. As shown in Figure 3.7b, ERP depends on the amplitude of the stimulus, as differences were observed between the two groups: group 1 was applied a greater stimulus amplitude than group 2. The ERP increased by only 10 ms in group 1 compared to

about 100 ms in group 2. Figure 3.7c shows an increase in PRR from 0 ms to approximately 40 ms and 140 ms for the first and second group respectively after 3 min of ischaemia. Finally Figure 3.7d shows a decrease in LV transmural CV from approximately 55 cm/s at 0 min to 25 cm/s at 3 min of ischaemia.

Ischaemia can also be reflected at the ECG level. Changes to the ECG can potentially allow the clinician to estimate the timing of occlusion, the infarct-related artery, and the size of the affected tissue [de Lemos et al., 2000; Thygesen et al., 2007]. The main changes triggered by ischaemia are increased ST segment elevation due to a higher resting membrane potential, a prolonged QRS interval due to slower conduction and an increased width of the T wave due to increased dispersion of repolarisation times [Thygesen et al., 2007; Gima and Rudy, 2002; Kléber, 2000].

However, many of the changes observed at the ECG level during ischaemia are also observed in other conditions such as pericarditis, LV hypertrophy, left bundle branch block and Brugada syndrome [Thygesen et al., 2007]. Furthermore, Taggart *et al.* found similar symptoms in asymptomatic patients with normal coronary arteriograms [Taggart et al., 1979]. Schang *et al.* carried out a study in 20 patients with coronary heart disease and showed that only 25% of the ST elevation episodes were associated with angina [Schang and Pepine, 1977].

3.4 Drug cardiotoxicity

Many studies have investigated ischaemia-induced arrhythmic mechanisms, both experimentally [Bradley et al., 2011; Ma and Wang, 2007; Russell et al., 1984; Coronel et al., 1991, 2002; Janse and Wit, 1989; Pogwizd and Corr, 1990; Janse et al., 1979, 1980, 1986; Zaitsev et al., 2003; Pogwizd and Corr, 1987b] and computationally [Jie et al., 2009; Shaw and Rudy, 1997b; Ferrero et al., 2003; Jie et al., 2005; Tice et al., 2007]. However, most studies on anti-arrhythmic treatments have been carried out in non-ischaemic hearts, such as investigations on

Figure 3.7 APD, ERP and PRR and CV in patients after one, two and three minutes of global ischaemia. Group 1 was given a higher stimulus amplitude than Group 2 [Sutton et al., 2000; Taggart, 2000].

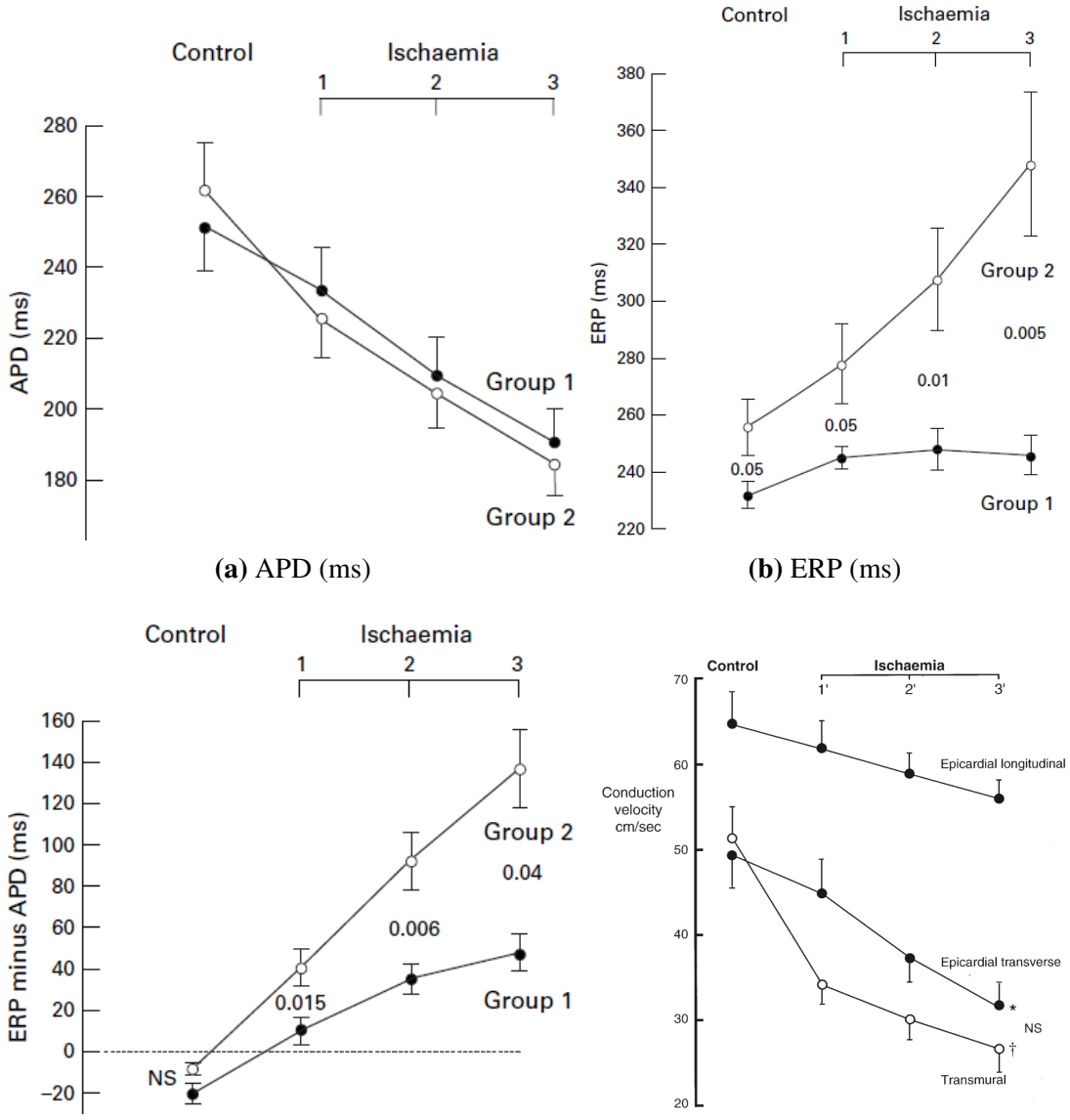

(a) APD (ms)

(b) ERP (ms)

(c) ERP minus APD (ms), equivalent to the PRR

(d) CV (cm/sec)

anti-arrhythmic drug effects [Moreno et al., 2011; van Opstal et al., 2001; Nademanee et al., 1985; Suttorp et al., 1991; Drouin et al., 1998; Brennan et al., 2007; Cobbe et al., 1983; Brennan et al., 2009; Zemzemi et al., 2013] and defibrillation therapy [Efimov et al., 2000, 1998; Trayanova et al., 2002; Chen et al., 1986; Hwang et al., 1994; Skouibine et al., 2000; Rodríguez and Trayanova, 2003], both of which are often used in conjunction to improve the success of treatment [Tacker et al., 1980; Guarnieri et al., 1987; Brode et al., 1997].

Numerous studies have shown efficacy of class III anti-arrhythmic drugs in treating patients suffering from arrhythmias. A clinical study carried out by Myburgh *et al.* showed that sotalol, a beta-adrenergic blocking agent with class III anti-arrhythmic properties, suppressed ventricular ectopic beats in 20 patients suffering from ischaemic heart disease [Myburgh et al., 1979]. Another clinical trial by Nademanee *et al.* also showed the efficacy of sotalol in treatment for life-threatening arrhythmias for both short- and long-term treatments [Nademanee et al., 1985]Nademanee1985Electrophysiologic. It was prescribed to 37 patients with recurrent VT/VF. Their results show that the drug caused an increase in ERP of 14.9% in the ventricles. In the short term, the drug prevented reinduction of VT/VF in 15 patients, was ineffective in 7 and increased likelihood of VT/VF in 1. In the long term, it reduced premature ventricular beats by 85% and the incidence of tachycardiac beats by 90% in 52% of the patients (the rest of the group showed no significant changes). Sotalol, is also often prescribed for the treatment of atrial fibrillation, as shown by Suttorp *et al.* in 300 patients, therefore understanding its interaction with potential transient ischaemia in the ventricles is important [Suttorp et al., 1991].

Many patients in need of anti-arrhythmic treatment are prone to ischaemia [Steinberg et al., 2014; Waldo et al., 1996] and few studies analyse the interplay between anti-arrhythmic pharmacological treatment and ischaemia computationally [Wilhelms et al., 2012] or experimentally [You et al., 2005]. However, class III anti-arrhythmic drugs can have pro-arrhythmic effects, as shown in clinical trials such as SWORD [Waldo et al., 1996], in patients with myocardial infarction (MI) (resulting from an extended period of ischaemia) and a recent study by Steinberg

et al. carried out in patients with coronary artery disease (also known as ischaemic heart disease) [Steinberg et al., 2014]. Both studies resulted in increased mortality and rehospitalisation in patients taking class III anti-arrhythmic drugs compared to placebo. Mechanisms underlying the increased risk of death are not understood and will be investigated in Chapter 7.

3.5 Computational studies

3.5.1 Electrophysiological parameters modified to simulate ischaemia

The first 10-15 min of ischaemia are often simulated by incorporating effects of hyperkalaemia, acidosis, and anoxia in computational models [Moréna et al., 1980; Kodama et al., 1984]. These changes are implemented at the ionic level through the following changes: an increase in $[K^+]_o$ to 8-12 mM [Weiss and Shine, 1982a; Weiss et al., 1992], a decreased maximum conductance of I_{Na} and I_{CaL} usually by 25% [Kagiyama et al., 1982; Sato et al., 1985; Irisawa and Sato, 1986], and an activation of the $I_{K(ATP)}$ [Shaw and Rudy, 1997b,a; Ferrero et al., 1996]. Ferrero *et al.* and Shaw and Rudy [Ferrero et al., 1996; Shaw and Rudy, 1997a,b] demonstrated using computer simulations that these changes account for the most significant alterations in AP morphology and wave propagation over the course of ischaemia. Numerous studies have shown that the increase in $[K^+]_o$ above 8 mM causes severe depolarisation at rest, which results in reduced availability of Na^+ current and thus in slow AP upstroke and decreased CV [Shaw and Rudy, 1997a; Rodríguez et al., 2004a,b]. While under normal conditions AP upstroke velocity is mainly determined by I_{Na}, after 10-15 min of occlusion AP upstroke becomes biphasic, with the first phase corresponding to the decreased influx of Na^+ current and the second component being Ca^{2+} driven [Shaw and Rudy, 1997a; Downar et al., 1977; Kléber et al., 1978; Pogwizd and Corr, 1987a; Ferrero et al., 2003]. Simulation studies have demonstrated that, under these conditions, Ca^{2+} current plays a critical role in the occurrence of propagation block and the development of alternans in the ischaemic region, both phenomena being precursors of reentrant

activity in ischaemia [Shaw and Rudy, 1997a; Ferrero et al., 2003; Tice et al., 2007; Bernus et al., 2005b].

The high degree of electrophysiological detail provided by computer simulations allows examination of the contribution of each ischaemic change at the ionic level to the electrophysiological alterations in AP and propagation following coronary occlusion. Some of the first simulations of ischaemia were carried out by Ch'en *et al.* [Ch'en et al., 1998] who induced ATP depletion and fall in pH to investigate calcium-overload arrhythmias during ischaemia and reperfusion-induced arrhythmias. Early simulations of myocardial energy metabolism during ischaemia were also carried out and effectively predicted the changes in energy production [Zhou et al., 2005; Cabrera et al., 2005].

As described earlier, $[K^+]_o$ increases quickly following coronary occlusion, reaching a plateau level of 6-11 mM above its normal value of 5.4 mM at 10-15 min post-occlusion [Gasser and Vaughan-Jones, 1990; Weiss and Shine, 1982b,a; Wilde and Aksnes, 1995; Weiss and Shine, 1986; Wilde et al., 1990; Yan et al., 1996]. Mechanisms by which K^+ accumulates in the extracellular space are still not fully understood, due to the challenges of simultaneously recording all ionic currents and concentrations in experiments. Therefore, Rodríguez *et al.* used computational modelling to investigate mechanisms of extracellular K^+ accumulation in ischaemia [Rodríguez et al., 2002]. The model included ion fluxes between the intracellular medium, the interstitial cleft and the extracellular medium. Membrane kinetics were represented using the Luo-Rudy AP model [Luo and Rudy, 1994; Zeng et al., 1995] with an added $I_{K(ATP)}$ formulation described in [Ferrero et al., 1996]. Interruption of coronary flow was simulated by increasing the time constant of diffusion between the extracellular medium and the interstitial clefts from its normoxic value to infinity. Experimental results suggest that three mechanisms could be responsible for the increase in $[K^+]_o$ in acute ischaemia: inhibition of the I_{NaK} pump [Wilde et al., 1988; Bersohn et al., 1982], activation of the $I_{K(ATP)}$ current [Wilde and Aksnes, 1995; Noma, 1983], and activation of an inward Na^+ current [Wilde and Aksnes, 1995;

Shivkumar et al., 1997; Hartmann et al., 1998; Ju et al., 1996]. The simulations carried out by Rodriguez *et al.*, suggest that the ischaemic cellular K^+ loss is mainly due to an increase in the K^+ efflux via the time-independent K^+ current and $I_{K(ATP)}$, rather than to a decrease in K^+ influx via the Na^+/K^+ pump [Rodríguez et al., 2002]. These results are an important stepping stone in understanding the pathophysiology of ischaemia and were followed up in studies led by Smith and Crampin [Smith and Crampin, 2004; Terkildsen et al., 2007].

3.5.2 Arrhythmic mechanisms during ischaemia

As described earlier, ischaemic impact on the myocardium is characterised by a high degree of heterogeneity. Electrophysiological properties vary not only with time post-occlusion, but also spatially. Ferrero *et al.* used data from experimental measurements to construct a two-dimensional (2D) model of regional ischaemia which included the a detailed model of the BZ [Ferrero et al., 2003]. They illustrate mechanisms of figure-of-eight reentry following application of a premature stimulus, which is similarly described experimentally [Janse et al., 1980; Janse and Kléber, 1981; Kléber, 1987; Costeas et al., 1997]. Their results show that the degree of activation of $I_{K(ATP)}$ plays an important role in arrhythmogenesis, in agreement with simulation results by Trénor *et al.* [Ferrero et al., 2003; Trénor et al., 2005].

Tice *et al.* present a physiologically accurate model of phase 1A regional ischaemia in a 2D slab of rabbit ventricular tissue to study the effect of the transmural ischaemia-induced heterogeneities on the vulnerability to arrhythmia [Tice et al., 2007]. Figure 3.8 shows a diagram of the ischaemia-induced spatial heterogeneities included in their model. The left panel shows the location of the ischaemic region and its border zone on a cross-section of the rabbit heart. The right panel shows the gradient of electrophysiological parameters varied in the epicardial and endocardial border zones. Ischaemic substrate was represented by progressive changes in membrane dynamics due to hyperkalaemia, acidosis, and hypoxia corresponding to 2-10 min post-occlusion. The model, illustrated in Figure 3.8, includes realistic ischaemic parameters and

border zone heterogeneities. The LV wall was paced at 200 ms basic cycle length and premature stimulation was applied to the RV endocardium over a range of varying interval lengths, often referred to as coupling intervals. The simulation results show that a premature stimulus is more likely to initiate arrhythmia at 7-8 min post-occlusion, when refractoriness in the normal tissue and the ischaemic region differs the most. Arrhythmia induction is then initiated by alternans in the border zone. Halving the border zone decreases the safety factor for propagation, resulting in a 58.8% decrease in reentry initiation. Their results show that the increased likelihood of arrhythmogenesis in regional ischaemia is caused by increased dispersion of refractoriness and CV in the ischaemic BZ. They also notice that the absence of a transmural gradient in $I_{K(ATP)}$ activation in the central ischaemic region drastically reduces the number of sustained reentries. However, this study is two-dimensional, therefore, the role of transmural heterogeneities may be different in a three-dimensional model.

Figure 3.8 (A) Ischaemic region and surrounding border zone shown in white and grey on a cross section of the ventricles. (B) Gradient of main ischaemic electrophysiological parameters varied across the epicardial and endocardial border zones [Tice et al., 2007].

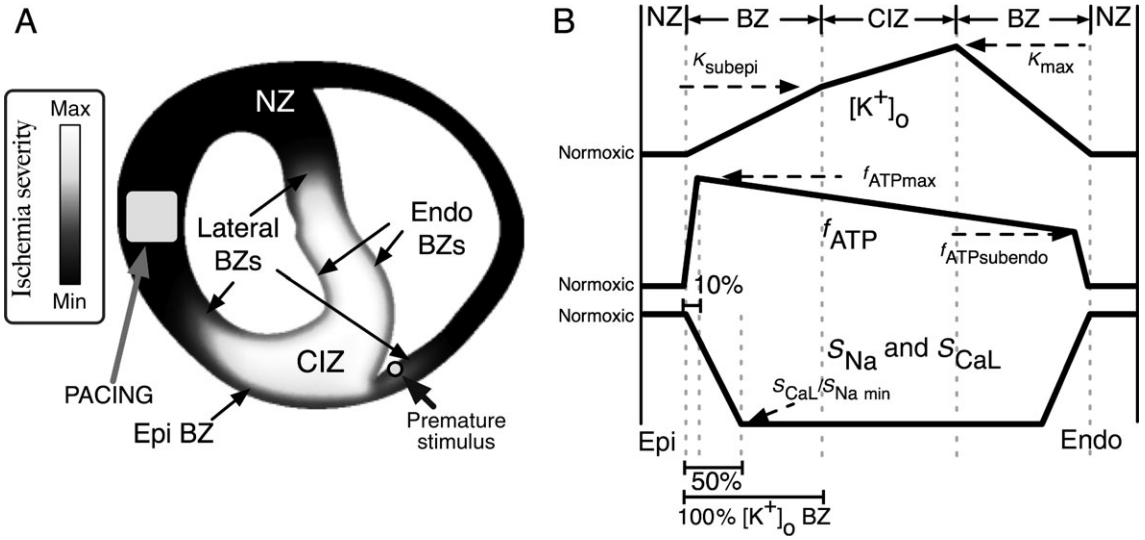

Bernus *et al.* also show the importance of the BZ in 3D slabs of ventricular tissue using the LRd model. They show that arrhythmias could be triggered through alternating conduction blocks in the ischaemic BZ which lead to intramural reentry and APD alternans, alternating variations of

AP amplitude over successive cardiac cycles [Bernus et al., 2005b].

Clayton *et al.* carried out experimental and computational studies in human hearts to investigate the effects of ischaemia on fibrillation [Clayton et al., 2011b]. Their results indicate that cardiac ischaemia slows conduction, shortens APD, flattens APD restitution, prolongs refractoriness and increases dispersion of CV, APD and ERP. They also show that these effects result in slower reentrant activity. While the simulations show that the flattening of the restitution curve leads to the collapse of many reentrant waves, this is not seen in the experimental results. This discrepancy implies that there are other factors, such as functional heterogeneities, that may play an important role in sustaining wavebreak during human VF. Furthermore, this study is a good example of computational models and experimental results being used synergistically.

Chapter 4

Computational cardiac electrophysiology methods

In this chapter, we present the methods used to simulate cardiac electrical conduction computationally. The first part of this chapter describes the models that simulate the action potential of a cell by reproducing the ionic current level activity. A brief overview of the Hodgkin-Huxley equations, on which most other ionic models are based, is given. The main ventricular action potential models and the parameters modified to simulate ischaemia are detailed. Coupled ODE solvers are also reviewed. The second part of this chapter describes the equations underlying the electrical activity propagation in tissue, which are known as the bidomain and monodomain equations. The numerical methods used to solve these equations, known as semi-implicit time stepping and finite element method are also reported. The third part of this chapter presents an overview of the simulation software package Chaste, which contains the code that was developed and used to run most of the simulations presented in this thesis.

Computational models have provided insights into cardiac electrophysiology since the first model was built over 50 years ago, these have been described in various reviews [Noble, 2002; Rodríguez et al., 2006; Trayanova, 2011; Clayton et al., 2011a]. They have been extensively

used for research and recently these models have been put in the spotlight for industrial and regulatory applications by the FDA-led initiative CiPA [Sager et al., 2014]. They provide an ideal framework within which hypothesis and ideas can be tested. Current models have undergone many iterations between experiments and theory, experimental and clinical data are first used to build and then verify the computational model and its findings, as described briefly in Chapter 1. Examples of iteration between experiments and simulations are presented in a review by Quinn *et al.* and Carusi *et al.* [Quinn and Kohl, 2013; Carusi et al., 2012]. Furthermore, these models integrate information at a multi-scale level and draw information from multiple fields: molecular biology, physiology, anatomy, cardiology, applied mathematics, engineering, physics and computer science [Clayton, 2001]. They are able to overcome experimental limitations by providing high spatio-temporal resolution and a framework within which parameters can be easily modified. At the same time, their findings help us discover new mechanisms and ideas that can then be tested experimentally. The computational studies presented in this thesis identify key mechanisms underlying the response of the heart to drugs and disease and they illustrate the state-of-the art in computational modelling and simulation of human electrophysiology.

4.1 Modelling transmembrane ionic current

The biophysical activity of the ionic currents and concentrations across the cell membrane are modelled by a set of ODEs, referred to as the action potential models. Here we present the Hodgkin-Huxley model, which forms the basis of most action potential models. The main ventricular models relevant to this thesis are also presented. The formulation of the $I_{K(ATP)}$ current, which is included in all the AP models used in this thesis in order to simulate hypoxia during ischaemia is introduced. Finally, we briefly review the forward and backward Euler methods used to solve the ODEs.

4.1.1 Hodgkin-Huxley model

The Hodgkin-Huxley Nobel prize winning model forms the basis for many other action potential models that have been developed since then [Hodgkin and Huxley, 1952]. The model represents the electrical activity of a squid axon modulated by 3 ionic currents, the sodium channel I_{Na}, the potassium channel, I_K and the leakage channel made up of other ions I_l. Each current is defined as follows:

$$\begin{aligned} I_{Na} &= g_{Na}(V_m - E_{Na}) \\ I_K &= g_K(V_m - E_K) \\ I_l &= g_l(V_m - E_l), \end{aligned} \tag{4.1}$$

where E_{Na}, E_K and E_l and g_{Na}, g_K and g_l are the membrane potentials and conductances for the respective ions. The conductance of I_l is constant, however the conductances of the two other currents follow more complicated patterns as shown in Figure 4.1 for g_K.

Figure 4.1 Potassium conductance of axon squid through time [Hodgkin and Huxley, 1952]

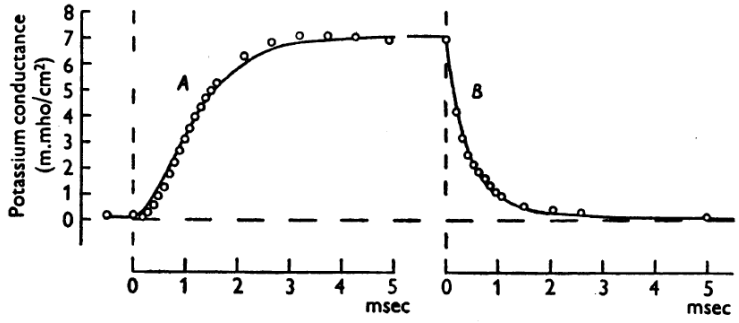

Both of these conductances were described by the following equations

$$\begin{aligned} g_{Na} &= \bar{g}_{Na} m^3 h \\ g_K &= \bar{g}_K n^4, \end{aligned} \tag{4.2}$$

where $\bar{g}_{Na}$ and $\bar{g}_K$ are constants with dimensions of conductance/cm^2 and m, h and n are gating

variables that can vary between 0 and 1 to represent the open and closed states of each ionic channel respectively. Each gating variable follows a time-dependent equation:

$$\frac{dx}{dt} = \alpha_x(1-x) - \beta_x x, \tag{4.3}$$

where x represents the gating variables (m, h and n), and α_n determines the rate of opening of the gates while β_n determines the rate of closing of the gates. The equations underlying these variables were fitted to reproduce experimental data and are as follows:

$$\begin{aligned}
\alpha_m &= 0.1\frac{25-V_m}{e^{\frac{25-V_m}{10}}-1}, & \beta_m &= 4e^{-\frac{V_m}{18}} \\
\alpha_h &= 0.07e^{-\frac{V_m}{20}}, & \beta_h &= \frac{1}{e^{\frac{30-V_m}{10}}+1} \\
\alpha_n &= 0.01\frac{10-V_m}{e^{\frac{10-V_m}{10}}-1}, & \beta_n &= 0.125e^{-\frac{V_m}{80}}
\end{aligned}$$

4.1.2 Ventricular action potential models

The first cardiac cell model was built over 50 years ago by Denis Noble [Noble, 1960]. It was derived from the Hodgkin-Huxley model, described earlier [Hodgkin and Huxley, 1952]. The main change between the models was the potassium sensitive currents that allowed for a plateau phase, which meant a longer repolarisation time. A review by Noble and Rudy describes how iteration between models and experiments played an important role in discovering new ionic channels and pumps involved in different stages of the AP [Noble and Rudy, 2001]. There are now a wide variety of ventricular cardiac cell models that can be used to simulate different species such as rabbit [Mahajan, 2008; Shannon et al., 2004], dog [Decker et al., 2009; Hund and Rudy, 2004], rat [Niederer and Smith, 2007; Pandit et al., 2001] and human [Bernus et al., 2002; Priebe and Beuckelmann, 1998; Iyer et al., 2004; ten Tusscher and Panfilov, 2006; Grandi et al., 2010]. Here we give an overview of the models used and referenced throughout this thesis:

from animal to human models. It is important to note that differences between models of the same species have been reported in numerous studies, as has been shown in previous studies [Cherry and Fenton, 2007; Bueno-Orovio et al., 2008; Cherry and Evans, 2008; ten Tusscher et al., 2006; Gemmell et al., 2014; Romero et al., 2011].

A model that has been widely used in the study of ischaemia is the Luo-Rudy dynamic (LRd) model of mammalian ventricular AP [Luo and Rudy, 1991, 1994]. The model was built using single cell and single channel recordings from different species that were taken using methods that overcame some of the limitations of previous techniques. It has been widely used to investigate arrhythmic mechanisms during ischaemia and is used as a basis for many other mammalian AP models [Shaw and Rudy, 1997b; Bernus et al., 2005b; Ferrero et al., 1996; Rodríguez et al., 2002; Trénor et al., 2005; Ferrero et al., 2003].

The Shannon *et al.* 2004 model was derived from the LRd model and rabbit specific data on calcium homeostasis [Shannon et al., 2004]. The Mahajan *et al.* 2008 model (used in Chapter 5) was based on the Shannon *et al.* model with a reformulated I_{CaL} current and calcium cycling [Mahajan, 2008]. These models are used to simulate different conditions that were not necessarily tested when they were initially developed. Therefore, studies such as the ones by Romero *et al.* and Gemmell *et al.*, performing sensitivity analysis and comparisons of these two models by varying various parameters are important [Romero et al., 2011; Gemmell et al., 2014]. The study by Romero *et al.* suggests that the Shannon *et al.* model reproduces rabbit electrophysiology more accurately at normal pacing rates, while the Mahajan *et al.* does so at faster pacing rates.

Every model is based on different sets of experimental data, and this is important to take into account when selecting the model's applicability to a specific research question. This was shown in a study by ten Tusscher *et al.* that compared 4 human models: the reduced Priebe and Beuckelmann (PB) 1998 model [Priebe and Beuckelmann, 1998] presented by Bernus *et al.* (redPB) [Bernus et al., 2002], the ten Tusscher *et al.* (TNNP) 2004 model and the Iyer *et al.* (IMW)

2004 model [Iyer et al., 2004]. Each model displayed slightly different electrophysiological dynamics, for example a broad range of variation in APD values (270-360 ms) was seen. These differences may be due to many factors such as inter-subject variability or the experimental preparations used [Sarkar and Sobie, 2011; Britton et al., 2013]. This thesis focuses on simulating ischaemia, when major electrophysiological changes are imposed. Therefore, we analyse and compare 4 recent human models under ischaemic conditions. We now review some of the latest human ventricular AP models that have been developed and are analysed in Chapter 6.

The ten Tusscher *et al.* 2006 human ventricular model

The most widely used and studied is the model developed by ten Tusscher *et al.* in 2006 (TP06) [ten Tusscher et al., 2006], whose transmembrane currents are based on a previous model from the same group [ten Tusscher et al., 2004]. Both of these models used human experimental data for most of the main ionic current formulations. The TP06 model included an improved description of calcium dynamics, allowing for the study of alternans, often a precursor or characteristic of arrhythmias. The updated Ca^{2+} handling description incorporates a subsarcolemmal space describing calcium-induced calcium release (CICR) with a Markov-state model for the ryanodine receptor (with reduced dimensionality using quasi-steady-state assumptions). The Ca^{2+} handling model is a reduced version of the model developed by Shannon *et al.* and Stern *et al.* [Shannon et al., 2004; Stern et al., 1999]. The I_{CaL} current simulates both the fast and slow voltage inactivation as shown experimentally [Li and Nattel, 1997; Magyar et al., 2002; Pelzmann et al., 1998]

The authors carried out extensive single cell, tissue, and whole organ simulations under normal and arrhythmic conditions [ten Tusscher et al., 2007]. This model has been widely used and investigated under different conditions such as fibrillation and ischaemia [Clayton et al., 2011b; Heidenreich et al., 2012]. Importantly, the authors were concerned with computational efficiency to ensure these models could be used in multi-scale simulations (from single cell to whole organ). Another advantage of the model, compared to its predecessors, is its ability to

reproduce APD restitution curves [Carro et al., 2011].

The Grandi *et al.* 2010 and Carro *et al.* 2011 human ventricular models

Another recent human AP model is the Grandi *et al.* 2010 model (GPB) [Grandi et al., 2010], which is based on the 2004 rabbit cell model described by Shannon *et al.* [Shannon et al., 2004]. It provides a detailed description of the subsarcolemmal space, which is incorporated into the main ionic current formulations. Ionic current densities and kinetics were updated according to recent experimental data on human myocytes. This model improved the AP response to frequency changes and offered a better performance during block of K^+ currents with respect to the TP06 model. However, the GPB model does not adequately reproduce APD restitution properties or APD rate adaptation dynamics [Carro et al., 2011]. Based on their analysis of these shortcomings, Carro *et al.* (CRLP) modified and reformulated various currents, such as I_{CaL} and I_{K1} [Carro et al., 2011]. They carried out an extensive single cell and one-dimensional (1D) tissue simulation study, and compared their results to those obtained using the GPB and TP06 models described above. Various biomarkers such as ERP, APD, and CV restitution properties were used to compare the models. The authors also performed a parameter sensitivity analysis and investigated the effect of potassium current block and hyperkalaemia on model outputs and concluded that their model adequately reproduced the expected behaviour.

The O'Hara *et al.* 2011 human ventricular model

Despite the many strengths of the models described above, they still suffer from many limitations, the main one being their ability to reproduce calcium dynamics. These shortcomings are addressed in the most recent human cell model, the O'Hara *et al.* 2011 (ORd) model [O'Hara et al., 2011]. Compared to the models described above, it was created based on the most consistent set of experimental human data, obtained from over 100 undiseased human hearts. The model incorporates the effects of Ca^{2+}/calmodulin-dependent protein kinase II (CAMKII) on known ionic currents.

O'Hara *et al.* gathered data from new measurements of human I_{CaL}, K^+ currents and the Na^+/Ca^{2+} exchanger current, as data in human is scarce for these currents. All equations for currents and fluxes were reformulated with the exception of Ca^{2+} buffers, CaMKII kinetics and background currents, for which the detailed Decker canine model formulations with adjusted conductances were used [Decker et al., 2009]. Transmural heterogeneities were included by incorporating mRNA and protein expression changes in epicardial, mid-myocardial and endocardial cells. The ORd model reproduced early after depolarisation (EADs), which were not reproducible by the other models.

4.1.3 Main ionic current formulations

In this section we provide an overview of the main ionic current formulations in the TP06, GPB, CRLP and ORd models:

- I_{Na} current that plays an important role during the upstroke of the AP and modulates the cell's excitability and refractoriness.
- I_{CaL} current that plays an important role during the plateau phase of the AP.
- I_{to} current that plays an important role in the initial small repolarisation the precedes the plateau phase
- I_{Kr}, I_{Ks} and I_{K1} that play an important role in modulating the complete repolarisation phase of the AP.

We chose to describe these currents as they play the main role in modulating the action potential morphology. In the following equations, V_m represents the transmembrane voltage of the cell, S represents the ion selectivity of the current, G_S represents the conductance of the current and E_S the reversal potential. Finally, R, T and F represent the gas constant, temperature and Faraday constant, respectively.

The ten Tusscher *et al.* 2006 human ventricular model

The following equation describes the fast inward sodium current:

$$I_{Na} = G_{Na} m^3 hj(V_m - E_{Na}), \tag{4.4}$$

where m is the activation gate, h is the fast inactivation gate, and j is the slow inactivation gate. The steady state activation (m_∞^3) and inactivation ($h_\infty \times j_\infty$) are fitted to data on steady-state activation of wild-type human Na^+ channels from Nagatomo *et al.* and extrapolated to 37° [Nagatomo et al., 1998]. The peak conductance, G_{Na}, was fitted to reproduce a maximum upstroke velocity of $dV_m/dt_{max} = 260mV/ms$ as found experimentally by Drouin *et al.* [Drouin et al., 1998].

The following equation describes the L-type calcium current:

$$I_{CaL} = G_{CaL} df f_2 f_{cass} 4 \frac{(V_m - 15)F^2}{RT} \frac{0.25 Ca_{ss} e^{2(V_m-15)F/RT} - Ca_o}{e^{2(V_m-15)F/RT} - 1}, \tag{4.5}$$

where d is the voltage-dependent activation gate, f and f_2 are the fast and slow voltage inactivation gate, f_{cass} is the fast subspace Ca^{2+} inactivation gate, Ca_{ss} is the Ca^{2+} concentration in the subspace, Ca_o is the extracellular Ca^{2+} concentration and the energy required to move ions along the channel, often referred to as the *driving force*, is modelled with a Goldmann-Hodgkin-Katz equation. Steady-state activation d_∞ and inactivation f_∞ gates are fitted to experimental data from human ventricular myocytes [Mewes and Ravens, 1994; Bénitah et al., 1992; Pelzmann et al., 1998; Magyar et al., 2002; Li and Nattel, 1997]. Since there is little data available in human, the d gate activation time constant of I_{CaL}, τ_d, was given a value based on the Luo-Rudy dynamic model [Luo and Rudy, 1994]. Time constant values of f_{Ca} and f, $\tau_{f_{Ca}}$ and τ_f, were taken from human atrial and ventricular experimental data [Beuckelmann et al., 1991; Bénitah et al., 1992; Mewes and Ravens, 1994; Magyar et al., 2002; Pelzmann et al., 1998; Sun et al., 1997; Li and Nattel, 1997].

The following equation describes the transient outward potassium current:

$$I_{to} = G_{to} r s (V_m - E_K), \tag{4.6}$$

where r and s are the voltage-dependent activation and inactivation gates. The steady-state activation and inactivation curves (r_∞ and s_∞) are fitted to data from human ventricular myocytes carried out by Näbauer *et al.* [Näbauer et al., 1996]. Endocardial and epicardial cells are defined by different steady-state inactivation properties, and peak conductance G_{to}. Time constants were fitted to experimental data from human carried out by Wettwer *et al.* [Wettwer et al., 1994].

The following equation describes the slow delayed rectifier potassium current:

$$I_{Ks} = G_{Ks} x_s^2 (V_m - E_{Ks}), \tag{4.7}$$

where x_s is the activation gate and E_{Ks} is the reversal potential determined by a large permeability to K^+ and a small permeability to Na^+ ions. The steady-state activation curve ($x_{s\infty}^2$) and activation times are fitted to activation data from human ventricular myocytes [Li et al., 1996; Virág et al., 2001; Wang et al., 1994]. The maximal conductance, G_{Ks}, was not fit to voltage-clamp data because it caused discrepancies in APD values, which was suggested to be due to sensitivity of channels to the cell isolation procedure, so the conductance was fitted to reproduce APD measurements.

The following equation describes the rapid delayed rectifier potassium current:

$$I_{Kr} = G_{Kr} \sqrt{\frac{[K^+]_o}{5.4}} x_{r1} x_{r2} (V_m - E_K), \tag{4.8}$$

where x_{r1} and x_{r2} are the activation and inactivation gates and $\sqrt{[K^+]_o/5.4}$ represents $[K^+]_o$ dependence. The steady-state activation curve x_{r1}^∞ and activation and inactivation times are fitted to data on the expression of hERG channels from human, hamster and frog [Zhou et al., 1998; Johnson et al., 1999; Smith and Yellen, 2002]. As in I_{Ks}, the conductance was fitted to reproduce expected APD values.

The following equation describes inward rectifier potassium current:

$$I_{K1} = G_{K1}\sqrt{\frac{K_o}{5.4}}x_{K1\infty}(V_m - E_K), \tag{4.9}$$

where $x_{K1\infty}$ is the time-independent and voltage-dependent inward rectification factor. The formulation used is based on the previous Priebe and Beuckelmann human cardiac AP model [Priebe and Beuckelmann, 1998] with peak conductance G_{K1} increased by a factor of 2 to account for the larger current densities found by Koumi *et al.* in human cardiac myocytes [Koumi et al., 1995].

Transmural heterogeneities were simulated by developing three different cell types (epicardial, endocardial and midmyocardial cells) that displayed different transient outward K^+ current, I_{to}, and the slow delayed rectifier K^+ current current, I_{Ks}, properties based on experimental data.

The Grandi *et al.* 2010 and Carro *et al.* 2011 human ventricular models

The following equation describes the fast inward sodium current:

$$\begin{aligned} I_{Na_{junc}} &= F_{junc}G_{Na}m^3hj(V_m - E_{Na_{junc}}), \\ I_{Na_{sl}} &= F_{sl}G_{Na}m^3hj(V_m - E_{Na_{sl}}), \\ I_{Na} &= I_{Na_{junc}} + I_{Na_{sl}}, \end{aligned} \tag{4.10}$$

where $F_{junc} = 0.11$ and $F_{sl} = 1 - F_{junc}$ represent the density of the current in the junctional cleft and subsarcolemmal space, m, h and j represent the activation and inactivation gates which are modelled as in TP04 [ten Tusscher et al., 2004] and $E_{Na_{junc}}$ and $E_{Na_{sl}}$ represents the Nernst potential of I_{Na} in the junctional cleft and subsarcolemmal space. The conductance, G_{Na}, was chosen to reproduce AP amplitude and upstroke velocity found in experimental human data [Näbauer et al., 1996; Li et al., 1998, 1999; Péréon et al., 2000].

The following equation describes the L-type calcium current:

$$\begin{aligned} I_{Ca_{junc}} &= F_{junc_{CaL}} \bar{I}_{Ca_j} df (1 - f_{Ca_{B_j}}) \\ I_{Ca_{sl}} &= F_{sl_{CaL}} \bar{I}_{Ca_{sl}} df (1 - f_{Ca_{B_{sl}}}) \\ I_{Ca} &= I_{Ca_{junc}} + I_{Ca_{sl}} \\ I_{Ca_K} &= \bar{I}_K df (F_{junc_{CaL}} (1 - f_{Ca_{B_j}}) + F_{sl_{CaL}} (1 - f_{Ca_{B_{sl}}})) \\ I_{Ca_{Na_{junc}}} &= F_{junc_{Ca_L}} \bar{I}_{Na_j} df (1 - f_{Ca_{B_j}}) \\ I_{Ca_{Na_{sl}}} &= F_{sl_{Ca_L}} \bar{I}_{Na_{sl}} df (1 - f_{Ca_{B_{sl}}}) \\ I_{Ca_{Na}} &= I_{Ca_{Na_{junc}}} + I_{Ca_{Na_{sl}}} \\ I_{CaL} &= I_{Ca} + I_{Ca_K} + I_{Ca_{Na}}, \end{aligned} \tag{4.11}$$

where $F_{junc_{CaL}} = 0.9$ and $F_{sl_{CaL}} = 0.1$ represent the proportion of currents in the junctional cleft and subsarcolemmal space, d and f represent the activation and inactivation gates and f_{Ca_B} is the fraction of Ca-bound Ca-dependent inactivation sites in the respective compartments. The current is permeable to 3 types of ions Ca^{2+}, K^+ and Na^+.

$\bar{I}_S$ for ion S represents ion dynamics in the respective compartments given by the following equation described by Campbell *et al.*, used in various computational models, which is based on the constant field theory [Campbell et al., 1988; Luo and Rudy, 1994; Shannon et al., 2004; Grandi et al., 2010]:

$$\bar{I}_S = P_S z_S^2 \frac{EF^2}{RT} \frac{[S]_i e^{Z_S EF/RT} - [S]_o}{e^{z_s EF/RT} - 1}, \tag{4.12}$$

where P_S is the permeability coefficient of ion S (cm/s), z_S^2 is the valence of ion S, $[S]_i$ and $[S]_o$ are the intracellular and extracellular concentrations of S, and E is the membrane potential.

The following equation describes the transient outward potassium current:

$$\begin{aligned} I_{to_s} &= G_{to_s} x_{to_s} y_{to_s} (V_m - E_K) \\ I_{to_f} &= G_{to_f} x_{to_f} y_{to_f} (V_m - E_K) \\ I_{to} &= I_{to_s} + I_{to_f} \end{aligned} \tag{4.13}$$

where x and y represent the activation and inactivation gates of the fast and slow components. I_{to} has been divided into a fast I_{to_f} and slow I_{to_s} component as described experimentally [Näbauer et al., 1996; Wettwer et al., 1994].

The following equation describes the slow delayed rectifier potassium current:

$$\begin{aligned} I_{Ks_{junc}} &= F_{junc} G_{Ks_{junc}} x_{Ks}^2 (V_m - E_{Ks_{junc}}) \\ I_{Ks_{sl}} &= F_{sl} G_{Ks_{sl}} x_{Ks}^2 (V_m - E_{Ks_{sl}}) \\ I_{Ks} &= I_{Ks_{junc}} + I_{Ks_{sl}}, \end{aligned} \tag{4.14}$$

where x is the activation gate and $F_{junc} = 0.11$ and $F_{sl} = 1 - F_{junc}$ represent the proportion of current in the junctional cleft and subsarcolemmal space. The current was based on experimental data carried out by Virág *et al.* [Virág et al., 2001].

The following equation describes the fast delayed rectifier potassium current:

$$I_{Kr} = G_{Kr} x_{Kr} r_{Kr} (V_m - E_K), \tag{4.15}$$

where x_{Kr} and r_{Kr} are the activation and inactivation gates. The current was formulated based on experimental data in human and a cell line derived from hamster [Zhou et al., 1998; Johnson et al., 1999; Iost et al., 1998].

The following equation describes the inward rectifier potassium current:

$$I_{K1} = 0.35 \sqrt{\frac{[K^+]_o}{5.4}} K1_{ss} (V_m - E_K), \tag{4.16}$$

where $K1_{ss}$ represents the gating variable. We were not able to find an explanation for the 0.35 factor that appears in the equation and is not present in the Shannon *et al.* model. We assume it is used to better fit the human experimental data the authors compare it to [Magyar et al., 2000].

The transmural heterogeneities in electrophysiological properties are defined by the epicardial cells having a dominant I_{to_s} component, comprising 88% of I_{to} as opposed to only 3.6% in endocardial cells [Näbauer et al., 1996].

The CRLP model attempts to overcome the shortcomings of the GPB model by modifying certain ionic formulations, such as I_{CaL}, $I_{Na,K}$ and I_{K1}. The CRLP model improved gating kinetics of I_{CaL} by introducing both fast and slow voltage-dependent inactivation gates, as in the TP06 model. The I_{CaL} current activation gates are divided into the fast and slow component, while keeping the rest of the formulation identical to Equation (4.11). The CRLP formulation includes an f_2 gate next to the f gate which defines the slow component of the inactivation gate. Furthermore, the scaling factor of I_{K1} in the Equation (4.16) was modified from 0.35 to 0.5715 to better fit data by Fink *et al.* on ion current dynamics in human tissue [Fink et al., 2008]. Finally, maximal $I_{Na,K}$ was reduced by 45% to better match the experimental APD_{90} rate adaptation based on a sensitivity analysis for the slow time constant. The model was made more excitable by increasing intracellular K^+ concentration ($[K^+]_i$) which increased the availability of Na^+ channels. Maximal G_{Na} was reduced to reproduce more physiological values for the maximal upstroke velocity [Drouin et al., 1995].

The O'Hara *et al.* 2011 human ventricular model

In the following equations, $\Phi_{S,CaMK}$ represents the proportion of channels of type S phosphorylated by CaMK. I_{Na} was constructed based on data from Sakakibara *et al.* and Nagatomo *et al.* to adjust for temperature differences [Sakakibara et al., 1993; Nagatomo et al., 1998]. CaMKII effects were incorporated based on data from Wagner *et al.* [Wagner et al., 2006]. Late sodium current ($I_{Na,late}$), which is not modelled in the TP06 or GPB models, was based on data from Maltsev *et al.*. The current persists 200 ms after the onset of depolarisation and is characterised by a slow voltage-independent inactivation and reactivation [Maltsev et al., 1998].

$$
\begin{aligned}
I_{Na,fast} &= G_{Na,fast}(V_m - E_{Na})m^3((1-\Phi_{INa,CaMK})hj + \Phi_{INa,CaMK}h_{CaMK}j_{CaMK}) \\
I_{Na,late} &= G_{Na,late}(V_m - E_{Na})m_L((1-\Phi_{INaL,CaMK})h_L + \Phi_{INaL,CaMK}h_{L,CaMK}) \\
I_{Na} &= I_{Na,fast} + I_{Na,late}
\end{aligned}
\tag{4.17}
$$

where m, h and j represent the activation and inactivation gates of the slow and fast components of the current.

O'Hara *et al.* carried out new recordings where Ca^{2+} is used as a charge carrier that allows both Ca^{2+} and voltage dependent inactivation (CDI and VDI respectively) to be recorded. Similar models of I_{CaL} are presented in the Mahajan *et al.* rabbit model and the Decker *et al.* canine model [Mahajan, 2008; Decker et al., 2009].

$$\begin{aligned} I_{CaL} &= \bar{I}_{CaL} d(1-\Phi_{ICaL,CaMK})(f(1-n)+f_{Ca} n j_{Ca}) \\ &+ \bar{I}_{CaL,CaMK} d\Phi_{ICaL,CaMK}(f_{CaMK}(1-n)+f_{Ca,CaMK} n j_{Ca}) \end{aligned} \tag{4.18}$$

where $\bar{I}_{CaL}$ represents the maximum current carried through the ion channel, defined similarly as above in Equation (4.12), d and f are the activation and inactivation gates, n is the fraction in Ca^{2+} dependent inactivation mode and j_{Ca} represents recovery from Ca^{2+} dependent inactivation.

I_{to} was formulated based on newly measured data by O'Hara *et al.* due to the limited data available in human. CaMKII effects were incorporated based on experimental data carried out by Tessier *et al.* in human and Wagner *et al.* in rabbit and mice [Tessier et al., 1999; Wagner et al., 2009]. CaMKII shifted the voltage dependence of steady state activation by 10 mV in the depolarisation direction and the time constant for development of inactivation was increased.

$$I_{to} = G_{to}(V_m - E_K)((1-\Phi_{Ito,CaMK})ai + \Phi_{Ito,CaMK} a_{CaMK} i_{CaMK}), \tag{4.19}$$

where a and i are the activation and inactivation gates.

I_{Kr} and I_{K1} were also constructed using newly generated experimental data by O'Hara *et al.* due to the limited data available in human. They showed that I_{Kr} was voltage dependent, but not pacing rate dependent. The conductance was scaled to obtain physiological APD_{90} values. I_{K1} included inactivation gating and detailed $[K^+]_o$ dependence according to experimental data

from human[Bailly et al., 1998; Konarzewska et al., 1995]. Finally, I_{Ks} was constructed based on experimental data from Virág *et al.* in human [Virág et al., 2001]. The conductance was calculated based on I_{Ks} drug block experiments and Ca^{2+} dependence was based on data from Tohse *et al.* in guinea pig [Tohse, 1990].

$$\begin{aligned} I_{Ks} &= G_{Ks}\left(1+\frac{0.6}{1+\left(\frac{3.8\cdot10^{-5}}{[Ca^{2+}]_i}\right)^{1.4}}\right)x_{s1}x_{s2}(V_m-E_{Ks}) \\ I_{Kr} &= G_{Kr}\sqrt{\frac{[K^+]_o}{5.4}}x_{Kr}R_{Kr}(V_m-E_K) \\ I_{K1} &= G_{K1}\sqrt{[K^+]_o}x_{K1}R_{K1}(V_m-E_K) \end{aligned} \tag{4.20}$$

where $[Ca^{2+}]_i$ is the intracellular Ca^{2+} concentration, x_{s1}, x_{s2} represent the activation and deactivation gates of I_{Ks}, R_S represents the instantaneous rectification gate of current S, x_S represents the time dependent inactivation gate, and 5.4 is the value of $[K^+]_o$ under normal conditions.

4.1.4 ATP-sensitive potassium current model

The $I_{K(ATP)}$ current gets activated when there is a lack of oxygen, which leads to a depletion of ATP and an increase in ADP. The current plays a major role in the APD shortening that is seen. It is usually inactive in a normal cell and ventricular AP models used in this thesis do not include an $I_{K(ATP)}$ current. Therefore, to simulate ischaemia, the current was added to the AP models. Here we discuss the latest models of $I_{K(ATP)}$. Ferrero *et al.* developed a model they included in the LRd model [Ferrero et al., 1996]. Their results showed that 0.6% of $I_{K(ATP)}$ accounted for a 50% reduction in APD. Shaw and Rudy also developed their own $I_{K(ATP)}$ model [Shaw and Rudy, 1997b]. Their model includes the current's dependence on $[K^+]_o$. The most recent model was developed by Michailova *et al.* in 2005, which includes dependencies on Mg^{2+}, MgADP and MgATP [Michailova et al., 2005]. They used their model to test various hypotheses about

the exact mechanisms of action of its subunits and different components. In this thesis we used a simplified version of the Michailova *et al.* model, which does not include the dependence on the concentration of ATP, and MgADP [Dutta et al., 2011, 2013]. Therefore, in this thesis we replace their formulation of $f_{K(ATP)}$ by a scaling factor in the following $I_{K(ATP)}$ current formulation:

$$I_{K(ATP)} = G_{K(ATP)} f_{K(ATP)} \left(\frac{[K^+]_o}{[K^+]_{o,n}} \right)^{0.24} (V_m - E_K), \tag{4.21}$$

where $[K^+]_{o,n}$ is the normal extracellular potassium concentration, V_m is the transmembrane voltage of the cell, E_K is the reversal potential of potassium, $f_{K(ATP)}$ is a scaling factor to vary peak $I_{K(ATP)}$ conductance and $G_{K(ATP)}$, is the channel conductance described by Michailova *et al.*, which has a value of 0.05 $mS.\mu F^{-1}$ [Michailova et al., 2005].

4.1.5 Overview of parameters used to simulate ischaemia

In order to simulate ischaemia, we assessed which parameters were modified in previous computational studies that are referenced throughout this thesis (some of which are introduced in Section 3.5). Our study investigates acute ischaemia, the time of greatest arrhythmic risk (Section 2.5), both in a 3D slab of rabbit tissue (Chapter 5) and human whole ventricles (Chapter 7). Therefore, we compared a range of studies that cover similar cases, as shown in Table 4.1. In cases where ischaemia is simulated at various stages or with spatial heterogeneities, such as the study carried out by Tice *et al.* [Tice et al., 2007], we chose to show only the maximum values used as well as the maximum time post-occlusion simulated (fifth column). Furthermore, changes in the $I_{K(ATP)}$ current are often controlled through changes in [ATP] and [ADP] concentration, which translate into % change in $I_{K(ATP)}$ maximum conductance. However, in some models the % change is not explicitly stated, so we approximated the value given the changes in concentrations stated in the study. Most studies described in the table use the LRd model of guinea pig ventricular myocytes [Luo and Rudy, 1994] or the TP06 model of human

ventricular myocytes [ten Tusscher and Panfilov, 2006] to represent membrane kinetics. Furthermore, the studies described in the table simulate the first 10-12 min of ischaemia apart from Wilhelms *et al.* that simulate up to 30 min of time post-occlusion [Wilhelms et al., 2011] with more pronounced ischaemic parameters.

Table 4.1 List of parameters used to simulate ischaemia in various studies. For each model (first column), we describe the extracellular potassium concentrations $[K^+]_o$ (second column), the % of I_{Na} and I_{CaL} maximum conductance (third column), % increase in $I_{K(ATP)}$ (fourth column), time post-occlusion in min (fifth column), the mesh specification (sixth column) and which AP model was used.

Computational Study	$[K^+]_o$ (mM)	I_{Na}, I_{CaL} (%)	$I_{K(ATP)}$ (%)	Time (min)	Mesh	AP model
[Shaw and Rudy, 1997a]	15	75	0.69	10	1D fiber	LRd
[Ferrero et al., 2003]	12.5	70	0.9	12	2D tissue	LRd
[Tice et al., 2007]	17	75	0.63	10	2D tissue	LRd
[Rodríguez et al., 2004b]	10.4	81.25	1.0	10	rabbit whole ventricles	LRd
[Heidenreich et al., 2012]	9.9	75	0.55	10	human whole ventricles	TP06
[Trénor et al., 2005]	12.5	75	0.6	10	2D tissue	LRd
[Wilhelms et al., 2011]	15	50	0.1	30	human whole ventricles	TP06
[Clayton et al., 2011b]	9.5	80	0.1	6	2D tissue	TP06

4.1.6 Ordinary differential equation solvers

A common method used to solve the set of coupled ODEs constituting the action potential models is the Euler method. They involve approximating the derivative of a function $y(t)$ as follows:

$$y'(t) \approx \frac{y(t+\delta t) - y(t)}{\delta t}, \tag{4.22}$$

where δ t is the time-step size taken. Rearranging the Equation 4.22 we can get the following equation:

$$y(t + \delta t) \approx y(t) + y'(t)\delta t. \tag{4.23}$$

If we know the initial conditions of the function, $y(t_0)$ and we assume that the gradient can be defined by another function dependent on t and y, $f(t, y)$, we can now use a progressive formula to the value of y at the following time step:

$$y_{n+1} = y(t_n) + f(t_n, y_n)\delta t, \tag{4.24}$$

where $\delta t = t_{n+1} - t_n$. This is an *explicit method*, known as the *forward Euler method*, which can be numerically unstable especially for stiff problems as the ones encountered in modelling cardiac electrophysiology. A more stable approach is the *backward Euler method*, an *implicit method* that uses the values of $y(t + \delta t)$ to calculate the gradient of y, which gives the following formula:

$$y_{n+1} = y(t_n) + f(t_{n+1}, y_{n+1})\delta t. \tag{4.25}$$

Since *implicit methods* are more stable, they can be run with larger time steps than with explicit methods. They are usually computationally less intensive given the larger time step, despite having a higher computational cost at each step due to the extra equation being solved. This thesis uses the backward Euler method to solve the ODEs describing cardiac electrophysiology.

4.2 Modelling cardiac electrical conduction

Single cell simulations provide a good platform to easily and quickly test various hypothesis, due to their short computational time and flexibility in accessing and modifying parameters. Despite the many advantages of single cell simulations, they do not include the effects of tissue coupling, such as wavefront dynamics during arrhythmias. Therefore, these models are often

integrated into tissue or whole organ simulations to further investigate arrhythmic mechanisms. With advances in computational power, it is now feasible to simulate whole human ventricles of 14M tetrahedral elements on supercomputers [Heidenreich et al., 2012; Zemzemi et al., 2013].

In this section we present the framework used for tissue level simulations in which the action potential models described earlier are coupled together into 2D or 3D geometries. We start by presenting the whole ventricle geometry used in the last chapter of this thesis. We then describe the bidomain and monodomain equations which approximate electrical conduction. Finally, we present the methods used to solve these equations, the main one being the finite element method.

4.2.1 Anatomically-based models of the heart

The human whole ventricle mesh used in this thesis (Chapter 7) was developed by Bernabeu *et al.* [Bernabeu et al., 2010a]. The mesh was generated from computed tomography (CT) images provided by the CISTIB group of the Pompeu Fabra University, Spain. The version of the mesh used has an average edge length of 400 μm and consists of 2.5M nodes and 14.2M elements. It took 6h to simulate 800 ms of electrical activity on 1024 HECToR processors.

All 3D meshes used in this thesis (3D slab of tissue in Chapter 5 and whole ventricle geometry in Chapter 7) include realistic fibre and sheet orientation (Section 2.1). The anisotropic orientation of the myocardial cells is defined by 3 axes defined as follows: i) the fibre direction; ii) the sheet direction perpendicular to the fibre; iii) the sheet-normal direction perpendicular to both fibres and sheets. Electrical activity propagates preferentially along the fibre direction, then along the sheet direction and is reduced in the sheet-normal direction.

4.2.2 Bidomain model

The bidomain model is used to describe the electrical activity of the myocardium. Parabolic and elliptic partial differential equations (PDEs) describe the electrical activity in the extracellular and intracellular spaces of the tissue. These two domains are connected, at each point in space, via the cell membrane, which is defined by the cardiac ventricular AP models. The electrical potential in each domain is assumed to be continuous, connected via the gap junctions that allow the passage of ions directly from one cell to the next. The cell membrane is considered to be a resistor and barrier between the two domains, creating a potential difference between the two domains. Ions may flow across the membrane in response to changes in the transmembrane potential, creating a current between the two domains. Here we describe the main equations underlying the bidomain model.

The transmembrane potential, V_m (in V), is defined by the following equation

$$V_m = \phi_i - \phi_e, \tag{4.26}$$

where ϕ_i and ϕ_e represent the potential in the intracellular and extracellular domains respectively.

The conservation of current across the membrane leads to the following relationship between current and potential:

$$\begin{aligned} J_i &= -\sigma_i \nabla \phi_i \\ J_e &= -\sigma_e \nabla \phi_e, \end{aligned} \tag{4.27}$$

where J_i and J_e are the current densities (in Am^{-2}) flowing into the intracellular and extracellular spaces, and σ_i and σ_e are the conductivities (in Sm^{-1}) associated with the two domains.

Considering the conservation of current and charge [Clerc, 1976; Weidmann, 1970], and assuming all sources in the two domains are related to the membrane, we can write the following divergence equations, which state that the outward flux of vector field, in this case the transmembrane current I_m (in Am^{-3}), through a closed surface is equal to the integral of the divergence over the region inside the surface:

$$\begin{aligned} \beta I_m &= \nabla \cdot (\sigma_i \nabla \phi_i) \\ \beta I_m &= -\nabla \cdot (\sigma_e \nabla \phi_e), \end{aligned} \tag{4.28}$$

where β is the cellular membrane surface to volume ratio (in m^{-1}) and I_m is composed of a capacitive component, I_c (in Am^{-2}), resulting from the semi-permeable nature of the cell membrane, and an ionic component, I_{ion} (in Am^{-2}), resulting from the current flow through the ion channels, pumps and exchangers. These components are described by the following equations:

$$\begin{aligned} I_m &= I_c + I_{ion} \\ I_c &= C_m \frac{\partial V_m}{\partial t} \end{aligned} \tag{4.29}$$

where C_m represents the cell membrane capacitance (in Fm^{-2})

Replacing I_m in equations 4.28 by equations 4.29 we obtain the bidomain equations:

$$\begin{aligned} \nabla \cdot (\sigma_i \nabla \phi_i) &= \beta (C_m \frac{\partial V}{\partial t} + I_{ion}) \\ \nabla \cdot (\sigma_e \nabla \phi_e) &= -\beta (C_m \frac{\partial V}{\partial t} + I_{ion}). \end{aligned} \tag{4.30}$$

We assume that any current entering at the boundaries can only enter through the extracellular space. Therefore the boundary conditions can be defined as follows:

$$\begin{aligned} \mathbf{n} \cdot (\sigma_i \nabla \phi_i) &= 0 \\ \mathbf{n} \cdot (\sigma_e \nabla \phi_e) &= I_e, \end{aligned} \tag{4.31}$$

where I_e is the extracellular current applied per unit area across the boundary and $\mathbf{n}$ is the outward facing unit normal. The bidomain equations are particularly useful for simulations where the extracellular space is important, such as investigations of defibrillation shocks [Trayanova, 2006; Bernabeu et al., 2010a]. The bidomain equations were used in Chapters 5 and 6 of this thesis.

4.2.3 Monodomain model

The monodomain model, involves solving a single parabolic PDE by taking the bidomain equations and assuming that the extracellular potentials are negligible or that the anisotropy ratios are equal in both the intracellular and extracellular space [Keener and Sneyd, 1998]. Therefore, the monodomain model is computationally less expensive than the bidomain model, as it takes less processing time. This model was used in Chapter 7 when simulating electrical activity on the 2.5M node human whole ventricle mesh. Assuming that the extracellular conductivity is negligible we can reduce the bidomain equations (4.30) to:

$$\nabla \cdot (\sigma \nabla V_m) = \beta (C_m \frac{\partial V}{\partial t} + I_{ion}), \tag{4.32}$$

where σ is the intracellular conductivity, V_m is equal to ϕ_i and the boundary condition is 0.

4.2.4 Semi-implicit time stepping

To solve the monodomain and bidomain models we first need to establish a discretisation in time using a semi-implicit time discretisation. Here we briefly describe the process for the monodomain equations and in the following section we describe how we solve the resulting

time-discrete equations. If v is a function satisfying equation Equation (4.32) on a domain Ω and its boundary $\delta\Omega$ respectively, we have:

$$\begin{aligned} \nabla \cdot (\sigma \nabla v) &= \beta(C_m \frac{\partial v}{\partial t} + I_{ion}) \text{ in } \Omega, \\ \mathbf{n} \cdot (\sigma \nabla v) &= 0 \text{ on } \delta\Omega. \end{aligned} \tag{4.33}$$

Each time step is defined as follows: $\Delta t^n = t^n - t^{n-1}$. We define $v^n = v(\mathbf{x}, t^n)$ and get the following discrete-time approximation to Equation (4.33):

$$\begin{aligned} \nabla \cdot (\sigma \nabla v^n) &= \beta(C_m \frac{v^n - v^{n-1}}{\Delta t} + I_{ion}^{n-1}) \text{ in } \Omega, \\ \mathbf{n} \cdot (\sigma \nabla v^n) &= 0 \text{ on } \delta\Omega, \end{aligned} \tag{4.34}$$

where I_{ion}^{n-1} denotes the ionic current calculated at the previous time step.

4.2.5 Finite element method

The Finite Element Method (FEM) is used to numerically solve the bidomain and monodomain equations by discretising spatially Equation (4.34) [Pathmanathan et al., 2010a; Vigmond et al., 2008]. FEM is used in a wide array of fields from aeronautical to civil engineering. The method divides the continuous domain into discrete sub-domains called elements, usually tetrahedra. Inside each element, the solution is approximated by an interpolation function. This method makes it easier to solve the PDEs over a complex and irregular mesh such as the heart compared to other methods such as the finite difference method [Cherry et al., 2003] and the spectral method [Bueno-Orovio et al., 2006], although it cannot be solved analytically.

Weak formulation

In the FEM, the differential equations are reformulated as equations containing integrals over the domain that must hold for a specific class of *test functions* from infinite-dimensional function

spaces. By approximating these functions by functions from finite-dimensional function spaces we obtain an integral over a finite-dimensional space that can be rewritten as a linear matrix problem and solved numerically. This integral form of the equations is known as the *weak form*.

For any continuous and once differentiable function u, referred to as a *test function*, defined on Ω we have,

$$\nabla \cdot (\sigma \nabla v^n) u = (\beta (C_m \frac{v^n - v^{n-1}}{\Delta t} + I_{ion}^{n-1})) u. \tag{4.35}$$

Integrating this equation gives

$$\int_\Omega \nabla \cdot (\sigma \nabla v^n) u \, \mathrm{d}\Omega = \int_\Omega (\beta (C_m \frac{v^n - v^{n-1}}{\Delta t} + I_{ion}^{n-1})) u \, \mathrm{d}\Omega. \tag{4.36}$$

If we apply the divergence theorem to the left hand side of Equation (4.36) and use the fact that boundary conditions $n \cdot (\sigma \nabla v) = 0$ on $\delta\Omega$

$$\begin{aligned} \int_\Omega \nabla \cdot (\sigma \nabla v^n) u \, \mathrm{d}\Omega &= - \int_\Omega (\sigma \nabla v^n) \cdot \nabla u \, \mathrm{d}\Omega + \int_{\delta\Omega} u \sigma \nabla v^n \cdot \mathbf{n}, \\ &= - \int_\Omega (\sigma \nabla v^n) \cdot \nabla u \, \mathrm{d}\Omega. \end{aligned} \tag{4.37}$$

Rearranging Equation (4.37),

$$\int_\Omega (\sigma \nabla v^n) \cdot \nabla u + (\beta (C_m \frac{v^n - v^{n-1}}{\Delta t} + I_{ion}^{n-1})) u \, \mathrm{d}\Omega = 0. \tag{4.38}$$

Basis functions

In the field of cardiac electrophysiology, the spatial discretisation generally takes the form of triangulation. Points in the domain, referred to as nodes, are selected to form triangles in two dimensions or tetrahedra in three dimensions. The combined nodes and elements form the mesh. On each element we define linear functions for each node that take a value of 1 at the

corresponding node and 0 at the others as described the Lagrange linear basis function shown in Figure 4.2.

Figure 4.2 One dimensional Lagrange linear basis function of Node A. Nodes are indicated by the black dots on the x-axis.

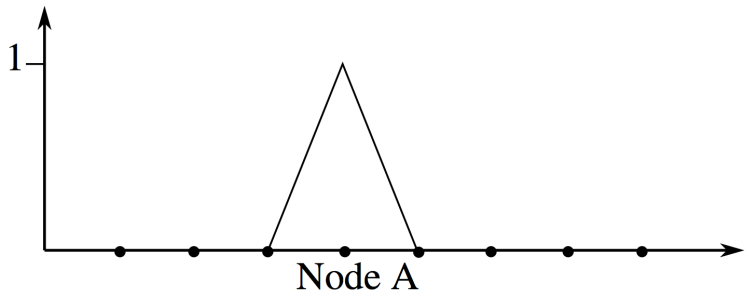

For example, given a triangle with the following coordinates: (0,0), (1,0) and (0,1), the basis functions are as follows:

$$\begin{aligned} f_1(x,y) &= x, \\ f_2(x,y) &= y, \\ f_3(x,y) &= 1 - x - y. \end{aligned} \tag{4.39}$$

These functions are piecewise linear, as shown in Figure 4.3 in red.

Figure 4.3 A function (blue) and its piecewise linear approximation (red) with nodes from x_0 to x_5.

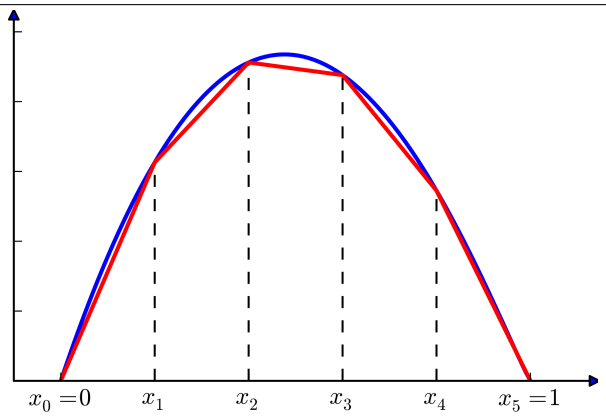

We define the nodes as a set of points $\{\mathbf{x}_i \in \Omega_0, i = 1, \ldots, N\}$. Therefore for each node in the mesh we have the following Lagrange basis function

$$\psi_i(\mathbf{x}_j) = \delta_{ij} = \begin{cases} 1 & \text{if } i = j, \\ 0 & \text{otherwise.} \end{cases} \tag{4.40}$$

These basis functions define the finite dimensional subspace over which the weak formulation is solved such that $V^n = span\{\psi_1, \ldots, \psi_N\}$. The approximation to the function may then be defined in terms of coefficients to these basis function as follows

$$\tilde{v}^n = \sum_{i=1}^{N} \alpha_i^n \psi_i. \tag{4.41}$$

System assembly

Substituting into Equation (4.38) we get

$$\int_\Omega (\sigma \nabla \tilde{v}^n) \cdot \nabla \psi_j + (\beta (C_m \frac{\tilde{v}^n - \tilde{v}^{n-1}}{\Delta t} + I_{ion}^{n-1})) \psi_j \, \mathrm{d}\Omega = 0, \forall \psi_j \in V^n. \tag{4.42}$$

By substitution of Equation (4.41) into Equation (4.42) and linearity we get

$$\begin{gathered} \sum_{i=1}^{n} \alpha_i^n \int_\Omega ((\sigma \nabla \psi_i) \cdot \nabla \psi_j) + \beta C_m \frac{1}{\Delta t} \left(\sum_{i=1}^{n} \alpha_i^n \int_\Omega \psi_i \psi_j - \sum_{i=1}^{n} \alpha_i^{n-1} \int_\Omega \psi_i \psi_j \right) + \ldots \\ \int_\Omega \beta I_{ion}^{n-1} \psi_j = 0, \forall \psi_j \in V^n. \end{gathered} \tag{4.43}$$

If we define mass matrix $\mathbf{M} = \left(\int_\Omega \psi_i \psi_j\right)$, the stiffness matrix $\mathbf{S} = \left(\int_\Omega (\sigma \nabla \psi_i \cdot \nabla \psi_j\right)$, $\mathbf{I}^{n-1} = \left(\int_\Omega \beta I_{ion}^{n-1} \psi_j\right)$ and $\boldsymbol{\alpha}^n = \alpha_i^n$ we get the following matrix-vector equation system,

$$\mathbf{S}\boldsymbol{\alpha}^n + \beta C_m \frac{1}{\Delta t} \mathbf{M}(\boldsymbol{\alpha}^n - \boldsymbol{\alpha}^{n-1}) + \mathbf{I}^{n-1} = 0, \tag{4.44}$$

and rearranging gives the following linear system that is solved for each time step n

$$(\Delta t\mathbf{S} + \beta C_m \mathbf{M})\boldsymbol{\alpha}^n = \beta C_m \mathbf{M}\boldsymbol{\alpha}^{n-1} - \Delta t \mathbf{I}^{n-1}. \tag{4.45}$$

Iterative methods such as GMRES [Saad and Schultz, 1986] and conjugate gradients [Hestenes and Stiefel, 1952] are then used in Chaste to solve the linear system [Pathmanathan et al., 2010a; Bernabeu et al., 2014].

4.3 Simulation software Chaste

The Cancer, Heart and Soft Tissue Environment (Chaste) is a software environment developed by the Computational Biology Group at the Department of Computer Science, University of Oxford. All of the tissue simulations in this thesis were run using Chaste. Its aim is to solve complex multi-scale biological problems that are computationally demanding [Pitt-Francis et al., 2009]. Main areas of focus include cancer and heart modelling. The code is open-source and developed using agile-programming techniques and test-driven implementation. Therefore, test development precedes code functionality, and tests suites are run automatically daily, nightly or weekly. It is written in C++ as it is a fast, flexible and object-oriented language.

The cardiac AP models are all included in CellML format [Lloyd et al., 2004] and converted in compile time to C++ code using PyCml [Cooper et al., 2006, 2011]. Resource Description Framework (RDF) is used to tag parameters in the cell model that you wish to vary. The output is written out in HDF5 format and then converted to specific formats that are requested such as Meshalyzer, Cmgui and VTK for Paraview [Schroeder et al., 2000; Cedilnik et al., 2006]. All three visualisation softwares were used in this thesis. Some of the code that we developed in order to run the simulations presented in this thesis is described in Appendix A.

Figure 4.4 Structure of Chaste's code showing the main components that constitute the *core* used to solve *heart* and *cancer* modelling problems. Arrows show dependencies between components. Image from [Pitt-Francis et al., 2008].

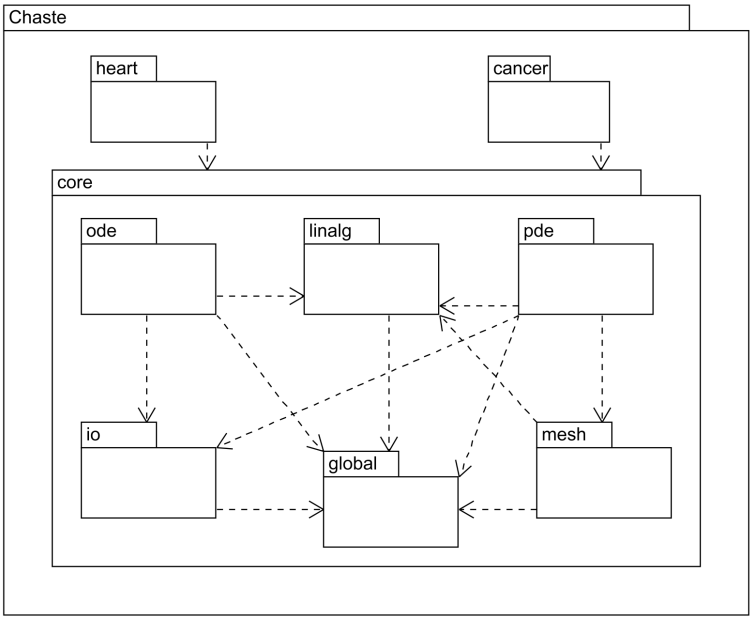

4.3.1 Overall structure

A schematic representation of the overall structure of the code can be seen in Figure 4.4. Both sections involved in solving heart and cancer problems depend on the *core*, constituted by the following domains:

- *mesh*: generates and defines accurate representations of complex, realistic geometry provided mainly through unstructured finite-element meshes
- *pde*: uses FEM to solve the PDEs describing the problem
- *linalg*: computes iterative solution of large sparse systems using PETSc
- *ode*: computes numerical solution of ODEs using an array of solvers such as the finite difference scheme and the Sundials CVODE solver.
- *global*: initialises and calls PETSc when needed
- *io*: handles input and output via HDF5 functionality

PETSc [1] is used for parallel linear algebra and ParMETIS [2] for mesh distribution on high-performance computing facilities [Pitt-Francis et al., 2008]. A scalability study by Bernabeu *et al.* showed linear speedup (optimal scalability) for up to 512 cores for solving a cardiac electrophysiology problem using the bidomain equations [Bernabeu et al., 2014]. This improvement in parallelisation has allowed us to run state-of-the-art whole human ventricle simulations on HECToR using 1024 processors. HECToR is the UK's national high-performance computing service, which is provided by UoE HPCx Ltd at the University of Edinburgh, Cray Inc and NAG Ltd, and funded by the Office of Science and Technology through EPSRC's High End Computing Programme. Smaller simulations were also run using the Advanced Research Computing (ARC) in Oxford.

[1] http://www.mcs.anl.gov/petsc/

[2] http://glaros.dtc.umn.edu/gkhome/metis/parmetis/overview

Chapter 5

Characterising ischaemia-induced heterogeneities using dual wavelength optical mapping experiments in isolated rabbit hearts

In this chapter we describe a novel framework developed to improve the interpretation and understanding of optical mapping recordings in the ischaemic heart. The main results were published in LNCS, as the conference proceedings of the Functional Imaging and Modeling of the Heart conference [Dutta et al., 2011]. Optical mapping is widely used by experimentalists to visualise the heart's surface electrical activity. However, it suffers from signal distortion due to fluorescent photon scattering within the biological tissue. Using a combination of experimental dual wavelength optical mapping experiments and computational simulations, we investigate how photon scattering, in the presence of ischaemia-induced spatial heterogeneities, affects optical mapping recordings. Therefore, the framework presented here can allow us to characterise spatial and temporal properties of ischaemia, which play an important role in arrhythmogenesis.

5.1 Introduction

As described earlier in Section 2.5, the AP displays significant morphological changes during acute ischaemia: a decrease in upstroke velocity, AP amplitude and duration, and a depolarisation of the resting membrane potential. These changes are mainly due to an increase in $[K^+]_o$, a decrease in conductance of I_{Na} and I_{CaL} and an increase in conductance of $I_{K(ATP)}$ [Carmeliet, 1999]. However, as discussed in Section 3.2, a layer of cells between poorly- and well-perfused tissue, referred to as the BZ, does not display fully ischaemic APs [Fiolet et al., 1985; Schaapherder et al., 1990], and the resulting electrophysiological heterogeneities increase the likelihood of developing disturbed excitation patterns and cardiac arrhythmias.

Optical mapping, briefly introduced in Section 2.8.3, utilises voltage-sensitive fluorescent dyes to visualise the electrical activity of the heart. Upon excitation at a specific illumination wavelength, dye molecules transduce differences in membrane potential (V_m) into changes in emitted fluorescence. However, penetration of the illuminating light into the tissue (with depth dependent on illumination wavelength [Walton et al., 2010]) and scattering of the emitted fluorescent photons, means that the detected signal represents a weighted-average of V_m levels from within a volume of tissue beneath the surface recording site. Such effects have been shown in modelling studies to distort optical recordings [Bishop et al., 2006; Hyatt, 2003], in particular causing a prolongation of the AP upstroke.

In this chapter, we combine experiments and computational modelling to investigate how optical mapping recordings are affected by ischaemia-induced transmural electrophysiological heterogeneity at the surface of the heart and photon scattering. We hypothesise that optical signals are significantly distorted relative to actual epicardial APs due to the collection of signals from a depth of tissue containing the BZ and fully ischaemic myocardium. Preliminary dual-wavelength optical mapping experiments were performed on no-flow globally ischaemic rabbit hearts. Two excitation wavelengths were used to investigate whether differences between the

respective emitted optical signals appear with time, assuming ischaemia-induced transmural heterogeneities become more pronounced. Computational simulations, representing both the BZ and the effects of photon scattering on optical mapping signals, were performed to assist interpretation of experimental data.

5.2 Methods

5.2.1 Optical mapping experiments

Figure 5.1 Diagram of the dual-wavelength optical mapping setup. Figure (a) presents a schematical representation of the setup with the path of the two illumination lights, blue and red, reaching the heart chamber and guided by the two dichroics. The emission wavelength of the two lights is represented by the thicker arrows reaching the filter and the camera. Figure (b) shows a picture of the optical mapping setup taken from above, the respective components are positioned in the same order as in the schematical representation

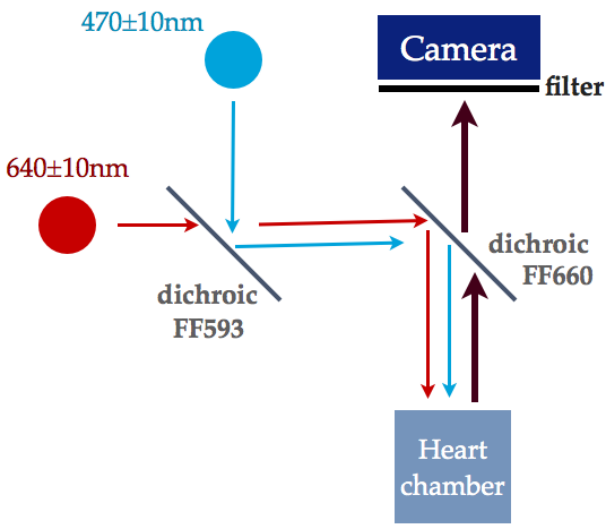

(a) Schematical representation of the optical mapping setup

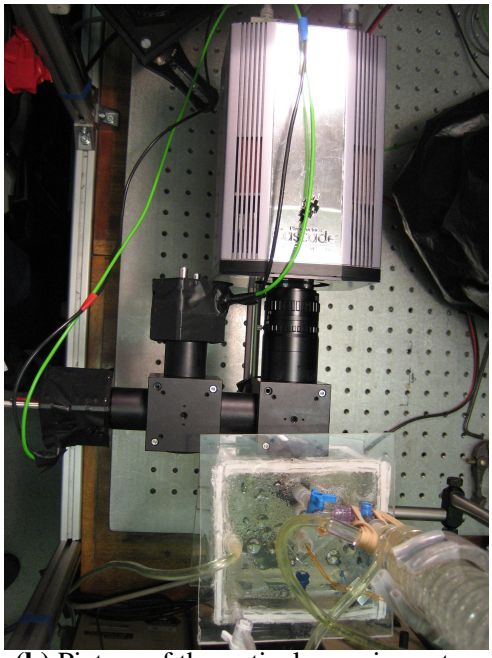

(b) Picture of the optical mapping setup taken from above

Optical mapping experiments were performed on isolated rabbit hearts (1 kg females, n=3), Langendorff-perfused with 37°C Krebs-Henseleit solution bubbled with 95% O_2 / 5% CO_2, and maintained in a heated imaging chamber filled with perfusate. Hearts were stained with

voltage-sensitive dye (20 μL bolus of 27.3 mM di-4-ANBDQPQ), excitation-contraction uncoupled to eliminate motion-induced imaging artefacts (10 μM blebbistatin), paced at the apex (2 ms, 8 V bipolar pulse at 1.25 Hz, to ensure maintained capture and avoid alternans during ischaemia), and subjected to no-flow global ischaemia. Fluorescence was excited using camera frame-synchronised LED illumination, alternating wavelengths of 470 $\pm$ 10 nm (shallow penetration) and 640 $\pm$ 10 nm (deep penetration), and acquired with a 690 nm long-pass filter (which effectively cuts out excitation light) at 922 Hz (64 x 64 pixel 16-bit CCD camera resulting in 300 μm/pixel resolution). This allowed paired comparison of short and long wavelength excitation. This technique was developed by Lee *et al.* [Lee et al., 2011]. A schematical representation of the setup can be seen in Figure 5.1. The two dichroics reflect illumination lights below a certain threshold (593 nm and 660 nm respectively) and let through light above the threshold.

5.2.2 Modelling ischaemia

We constructed a cuboid ventricular segment model (5 mm x 5 mm x 5 mm) of global ischaemia, including transmurally-rotating fibre architecture and a rabbit ventricular cell membrane dynamics model [Mahajan, 2008], with an added $I_{K(ATP)}$ current [Michailova et al., 2005] shown in Equation (4.21).

We chose to model the cardiac tissue after 10 min of ischaemia, as the electrophysiological differences between the healthy and ischaemic tissue are assumed to be greatest at that time [Tice et al., 2007]. The BZ, as shown in Figure 5.2, was represented by a transmural gradient in the main ischaemia-induced changes. These were modelled respectively through an increase in $[K^+]_o$, a decrease in the conductance of I_{Na} and I_{CaL} (S_{Na}, S_{CaL}) and an increase in the conductance of $I_{K(ATP)}$ ($S_{K(ATP)}$) [Tice et al., 2007].

Bidomain simulations, solved using the finite element method within the Chaste environment [Pitt-Francis et al., 2009], were used to simulate propagation of electrical excitation through the tissue following a supra-threshold stimulus applied to the bottom plane of the cube, horizontally

Figure 5.2 Diagram of varying ischaemic electrophysiological parameters of the cardiac tissue model with a BZ. $[K^+]_o$, S_{Na}, S_{CaL}, and $S_{K(ATP)}$ define a BZ of 1mm, 0.5mm, and 0.1mm, respectively.

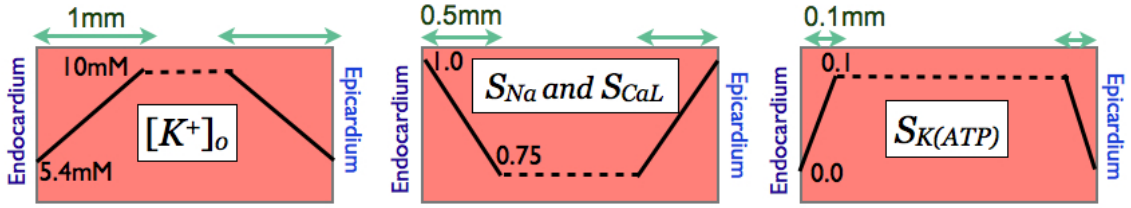

aligned to the transmural section. To assess the effects of the BZ, models with and without ischaemia-induced spatial heterogeneities were considered. A schematic representation of our mesh is shown in Figure 5.3 with blue arrows showing the stimulus direction and a yellow arrow representing the uniform illumination applied on the epicardium to excite the dye-molecules during optical mapping.

Figure 5.3 Diagram of slab of cardiac tissue represented in our model

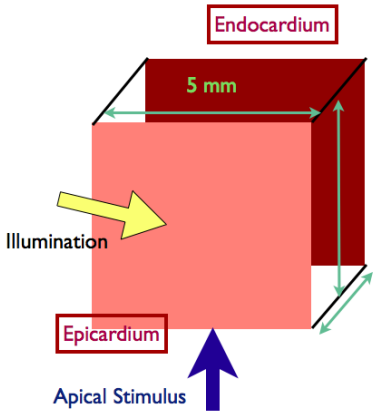

5.2.3 Optical mapping model

Optical mapping signals were simulated using the model presented by Bishop *et al.* [Bishop et al., 2006], as shown schematically in Figure 5.4. Briefly, the steady-state photon diffusion equation was solved using the finite element method in the Chaste environment to calculate the distribution of photon density (Φ) throughout the tissue following both uniform epicardial illumination ($\Phi = \Phi_{illum}$) and the resulting fluorescent photon emission ($\Phi = \Phi_{em}$), both of

which satisfy:

$$D\nabla^2\Phi - \mu_a\Phi = -w, \tag{5.1}$$

where the optical diffusivity (D) and absorptivity (μ_a) were taken at the illumination/emission wavelength (488/669 nm) to be 0.18/0.36 mm and 0.52/0.10 mm^{-1} respectively [Bishop et al., 2006]. Zero boundary conditions were used throughout, except during illumination, where the source term w was set to an arbitrary value of 1 on the epicardial surface; during emission, w was defined to be a function of Φ_{illum} and V_m, as obtained from the bidomain simulations, at each point in the tissue. The recorded optical signal, V_{opt}, was then calculated as the outward flux of Φ_{em} at each time step across the epicardial surface by applying Fick's Law:

$$V_{opt} = -D^{em}\nabla\Phi_{em} \cdot \mathbf{n}, \tag{5.2}$$

where $\mathbf{n}$ is the normal to the epicardial surface.

The degree of distortion due to photon scattering depends highly on the effective optical penetration depth ($\delta = \sqrt{D/\mu_a}$) at both the illumination and emission wavelengths [Bishop et al., 2006]. Therefore, we analysed the effects of high/default/low values of δ at illumination wavelength (2.45/0.59/0.18 mm) and emission wavelength (3.20/1.90/0.18 mm) to represent high and low wavelength penetration depths.

5.2.4 Data analysis

The results presented are taken from normalised V_m and V_{opt} values of a node at the center of the epicardium: V_m^* and V_{opt}^*. We calculate the APD as the time difference between the upstroke reaching 0 mV and 90% depolarisation and upstroke duration as the time between V_m reaching 10% and 90% repolarisation. We define τ_{opt} as the ratio of V_{opt}^* and V_m^*.

Figure 5.4 Schematic representation of the algorithm of the panoramic optical mapping signal synthesis model [Bishop et al., 2006]

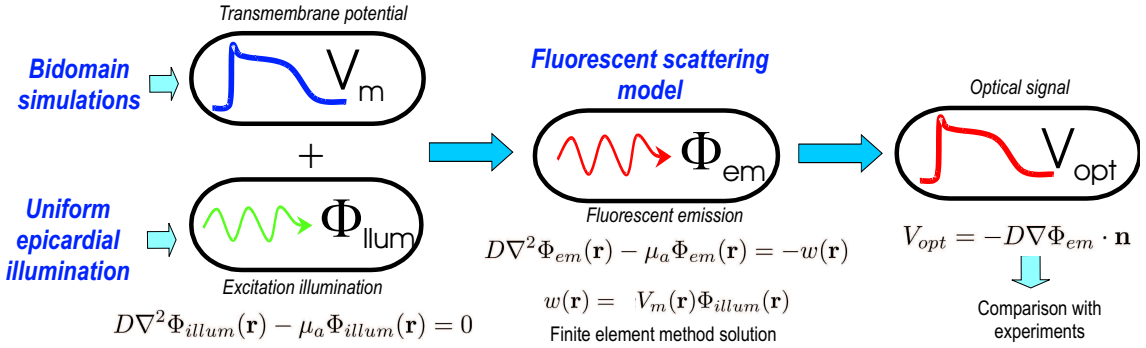

5.3 Results

5.3.1 Optical mapping experiments

Experiments were performed in isolated rabbit hearts to investigate changes in optical mapping signals during no-flow global ischaemia. Normalised voltage signals, showing the activation wavefront at different times following apical stimulation can be seen in Figure 5.5a. Upstrokes from a 2 x 2 pixel area on the left ventricular free wall for the two excitation wavelengths at different times of ischaemia are shown in Figure 5.5b. Differences between the respective emitted optical signals increase with time, showing a prolongation in upstroke duration and a reduced upstroke velocity recorded with 640 nm compared to 470 nm excitation. We hypothesise that the deeper penetrating wavelength (640 nm) displays more ischaemic features, as it gathers information from a larger volume that includes more ischaemic cells than the shallower penetrating wavelength (470 nm). To investigate the source of these differences, we subsequently performed a simulation study.

It is important to bear in mind that the experimental optical signal shown here has been filtered by a 50 Hz low-pass temporal filter and averaged over a 2x2 camera pixel region in order to increase the speed for single camera dual wavelength imaging [Lee et al., 2011]. However, this post-processing pipeline was not applied to the optical signal simulated as this was not the focus of this study, therefore significant differences in upstroke duration appear when comparing

experiments to simulations.

Figure 5.5 (a) Images of normalised fluorescence emitted from the left ventricle of the rabbit heart at different times after apical stimulation. (b) Normalised voltage upstroke after 0, 5 and 10 min of ischaemia for 470 nm ± 10 nm and 640 ± 10 nm excitation with the respective upstroke durations.

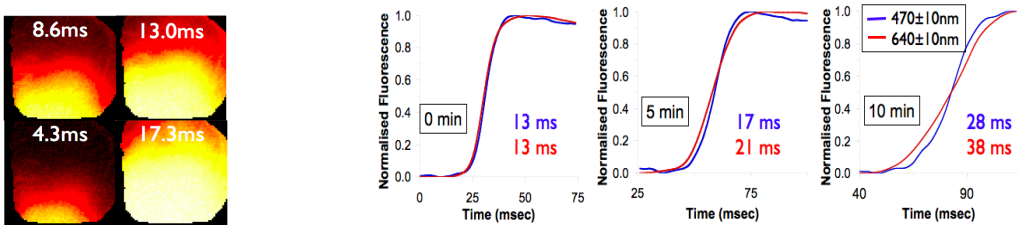

(a) (b)

5.3.2 Border zone effects on simulated epicardial transmembrane potential

Figure 5.6a shows the distribution of simulated V_m transmurally for the two types of tissue: with and without a BZ. We notice that the repolarisation wavefront shapes are significantly different in the two types of tissue. Cells close to the epicardium and endocardium depolarise faster and take longer to repolarise in the tissue with a BZ, than in the homogeneously ischaemic tissue.

Figure 5.6b shows that the AP (sampled from the epicardium) of the fully ischaemic tissue (without a BZ) displays all of the expected ischaemia-induced morphological changes. In the presence of a BZ, the AP displays an upstroke duration 22% shorter and an APD 11% longer than the homogeneously ischaemic tissue, characteristics of an AP from less ischaemic tissue.

5.3.3 Optical signal and transmembrane potential comparison

Figure 5.7a shows the corresponding V^*_{opt} surface optical APs with/without a BZ, whilst Figure 5.7b compares differences in upstroke duration and APD relative to the V^*_m traces of Figure 5.6b. As has been shown in previous optical mapping studies, the emitted signal represents the transmembrane potential of a weighted average volume of myocardium, due to photon scatter-

Figure 5.6 (a) Snapshots of V_m for tissue with and without a BZ during tissue depolarisation (29 ms) and repolarisation (139 ms) following apical stimulation (b) V_m^* with and without a BZ, including APD and upstroke duration values.

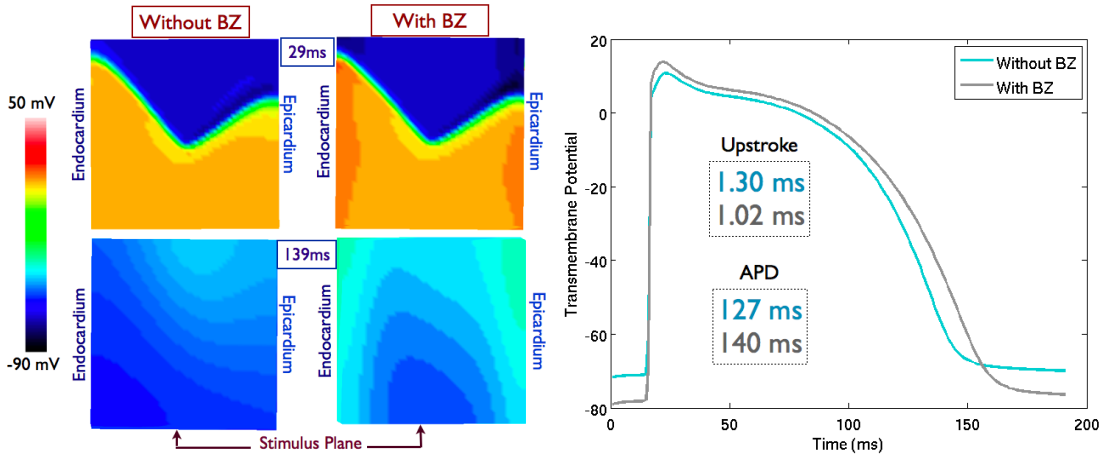

ing [Bishop et al., 2006; Hyatt, 2003]. These effects are more noticeable in the upstroke than the APD, as shown in Figure 5.7b, even in the homogeneously ischaemic tissue. This is caused by the narrow and fast wavefront that occurs during depolarisation, such that as it crosses the scattering volume, some cells are in their resting state while others are excited. This is not the case during the slower repolarisation phase, where most of the cells in the scattering volume will have a similar transmembrane potential. In fact, $\tau_{opt(APD)}$ values are close to 1 while $\tau_{opt(upstroke)}$ values are of 2.92 or greater. Therefore, differences in APD seen in Figure 5.7a are mainly due to the BZ as opposed to photon scattering.

Figure 5.7b shows that τ_{opt} values move away from 1 in the presence of a BZ for both APD and upstroke duration. This arises from the increase in heterogeneities, which lead to differences in AP morphology, in conduction velocity and wavefront propagation. In the presence of a BZ, V_{opt}^* gathers information from cells exposed to different degrees of ischaemia, while V_m^* represents the less ischaemic cells at the epicardium. Differences in upstroke duration and APD for simulations with and without a BZ are attenuated in V_{opt}^* (Figure 5.7a) compared to V_m^* (Figure 5.6b) due to the optical signal representing a weighted average volume of tissue.

Figure 5.7 (a) Simulated V^*_{opt} with and without a BZ. APD and upstroke duration values are shown for the respective APs. (b) Photon scattering effects, represented by τ_{opt}, on APD and upstroke duration for simulations run on a tissue with and without a BZ.

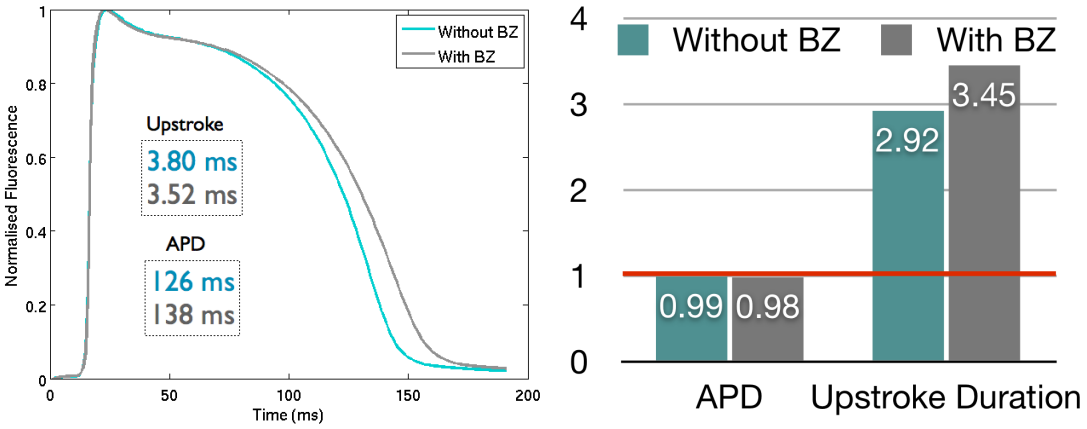

(a) **(b)**

5.3.4 Varying optical mapping penetration depth

The trends mentioned above are accentuated as we change the penetration depth. Figure 5.8 shows that τ_{opt} values move away from 1 as the penetration depth increases for both APD and upstroke duration in simulations with and without a BZ. Differences between V^*_{opt} and V^*_m increase due to the optical signal averaging over a bigger volume for an increased penetration depth. Furthermore, the differences between τ_{opt} values with and without a BZ become more pronounced for both upstroke duration and APD calculations as the penetration depth increases. As we increase δ_{eff}, the differences between V^*_{opt} with and without a BZ are attenuated due to a larger scattering volume, such that more signal is acquired from the deeper ischaemic tissue, decreasing the relative contribution of the BZ. However, a large change remains in V^*_m with/without BZ (Figure 5.6b), thus leading to a larger difference in τ_{opt} as penetration depth increases.

Figure 5.8 Varying penetration depth effects, represented by τ_{opt}, for tissue with and without a BZ. (a) Upstroke duration and (b) APD, taken at different penetration depths (Low, Default, and High).

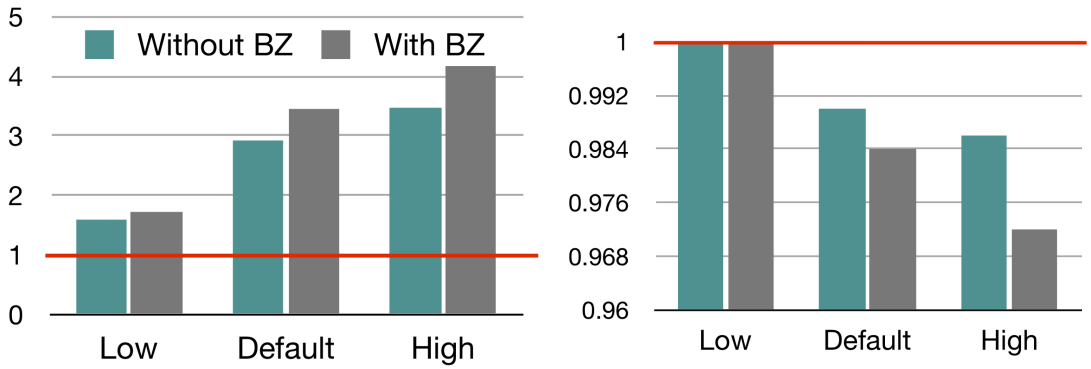

5.4 Conclusions

This chapter investigates the combined effects of ischaemia-induced transmural heterogeneities and photon scattering on epicardial optical mapping recordings in a globally ischaemic rabbit heart. We approach this with a combined experimental and simulation study. Preliminary dual-wavelength optical mapping experiments in globally ischaemic isolated hearts are performed. These show a clear difference in voltage-sensitive fluorescence emission between the two excitation wavelengths, which we attribute to the presence of transmural ischaemia-induced heterogeneities. We investigate this hypothesis with a model of global ischaemia, including transmural variation of electrophysiological parameters, combined with a model of photon density and excitation to simulate the optical signal at the surface of the heart. Simulations of V_m and V_{opt} are conducted on a model of ischaemic rabbit tissue with and without a BZ. This demonstrates that the ischaemia-induced electrophysiological heterogeneities affect the optical signal, resulting in a decrease in upstroke duration and an increase in APD compared to the optical signal from a homogeneously ischaemic slab of tissue. Furthermore, as the penetration depth of the optical signal increases, the differences between the epicardial V_{opt} and V_m are accentuated.

It is important to note that heterogeneities observed at the surface of the heart during global

ischaemia optical mapping experiments may be due to the air or bath surrounding the heart, however, it is not known if such heterogeneities exist *in vivo* at the surface of the heart. Studies have reported an epicardial border zone during myocardial infarction in dog [Pu and Boyden, 1997; Ursell et al., 1985; Peters et al., 1997; Aggarwal and Boyden, 1995; Costeas et al., 1997]. However, dogs have significant epicardial collateral flow compared to other species, which may play a role in maintaining the epicardial BZ [Maxwell et al., 1987]. Furthermore, the BZ of infarcted tissue is different to acutely ischaemic tissue due to various factors such as remodelling. Nonetheless, the heterogeneities observed in this study are similar to the well-reported spatial differences found between the well- and poorly-perfused tissue, described in Section 3.2 [Coronel, 1994; Janse et al., 1979; Schaapherder et al., 1990; Carmeliet, 1999].

Overall, this study shows that the electrophysiological heterogeneities that arise at the ventricle surface during ischaemia have a significant effect on optical mapping recordings. Furthermore, exciting fluorescent dyes with different wavelengths has an important impact on the resulting optical signal and may be used to investigate transmural heterogeneities. These findings provide new insights into optical mapping data interpretation when investigating the role of heterogeneity during global ischaemia. Furthermore, in this chapter we present a novel combined computational and experimental technique that can be used to investigate electrophysiological properties at the surface of the heart, such as ischaemia-induced heterogeneities. We can gain insight into spatio-temporal properties on the severity and degree of ischaemia through the extent of heterogeneities observed.

Due to ethical and practical limitations of carrying out experiments in human, there is significant uncertainty associated with the restricted data available. Therefore, there is a need for sensitivity analysis and computational investigations to improve our understanding of human electrophysiology during acute myocardial ischaemia, both of which are investigated in the following two chapters of this thesis.

Chapter 6

Electrophysiological properties under varied ischaemic conditions in human ventricular cell action potential models

The purpose of this chapter is to assess the applicability of recent human ventricular cell AP models to studies of ischaemia. In this chapter, we carry out a computational simulation study in single cell and tissue under normal and varied ischaemic conditions using 4 recent human models: ten Tusscher et al. 2006, Grandi et al. 2010, Carro et al. 2011, and O'Hara et al. 2011. We decrease the peak conductances of I_{Na} and I_{CaL} and varied the two ionic properties key to determine repolarisation during acute ischaemia: $[K^+]_o$ and peak conductance of $I_{K(ATP)}$. To evaluate the applicability of these models to simulate ischaemia, we analysed electrophysiological properties, such as ion current dynamics, APD, PRR, ERP and CV and compared them to human experimental data.

6.1 Introduction

In Section 2.5, we gave an overview of ischaemia and described how it is a dynamic and complex process that increases electrophysiological heterogeneities across the heart and the likelihood of developing arrhythmias, especially during the early phase of ischaemia (first 10 - 15 min) [Rodríguez et al., 2004a; Tice et al., 2007; Russell et al., 1984; Carmeliet, 1999]. The main physiological changes that occur were emphasised, namely hyperkalaemia, resulting in an increase in $[K^+]_o$, hypoxia, resulting in an opening of $I_{K(ATP)}$ channels, and acidosis, which decreases the conductances of I_{Na} and I_{CaL} currents [Carmeliet, 1999]. In Section 2.4 we introduced important electrophysiological properties (APD, ERP, PRR and CV) that are used to quantify arrhythmic risk, and in Section 3.3 we described how they are modulated by acute ischaemia. We showed how ischaemia induces a reduction in APD, a prolongation of PRR, a prolongation of ERP, and a reduction in conduction velocity, CV [Sutton et al., 2000; Taggart et al., 2001]. Therefore, heterogeneities between normal and ischaemic tissue occur and create a substrate for reentry [Pogwizd and Corr, 1987b; Janse and Wit, 1989; Coronel et al., 1991].

Most research on ischaemia has been carried out in animals, and data from human are scarce. Therefore, extrapolation of mechanisms from animal to human is challenging but it is facilitated by computational modelling. As argued in the introduction chapter of this thesis, they provide an essential platform within which parameters can be easily modified and their effects can be dissected to increase our understanding of ischaemia-induced arrhythmic mechanisms in human [Rodríguez et al., 2006]. However, most of the recent human models are created and validated with data from healthy cells. Their applicability for simulations of ischaemia is unknown. It is important to assess their behaviour under varied ischaemic conditions, as the ischaemic changes described above vary through time and space in and around an ischaemic area [Coronel et al., 1988; Wilensky et al., 1986; Fiolet et al., 1985; Schaapherder et al., 1990].

In this study we investigate the use of four recent computational human-specific ventricular

AP models under acute ischaemia. We now provide a brief summary of these models, as a detailed description was given in Sections 4.1.2 and 4.1.3. The most widely used and studied is the model developed by ten Tusscher et al. in 2006 (TP06) [ten Tusscher and Panfilov, 2006], which is based on a previous model from the same group [ten Tusscher et al., 2004]. A more recent human AP model is the Grandi et al. 2010 model (GPB) [Grandi et al., 2010], which is based on the 2004 rabbit cell model described by Shannon et al. [Shannon et al., 2004]. This model improved the AP response to frequency changes and offered a better performance during block of K^+ currents with respect to the TP06 model. However, the GPB model does not adequately reproduce APD restitution properties or APD rate adaptation dynamics [Carro et al., 2011]. Based on their analysis of these shortcomings, Carro *et al.* (CRLP) [Carro et al., 2011] modified and reformulated various currents, such as I_{CaL} and I_{K1}. The most recent human cell model is the O'Hara et al. 2011 (ORd) model [O'Hara et al., 2011], based on human data obtained from over 100 undiseased human hearts. The model incorporates the effects of Ca^{2+}/calmodulin-dependent protein kinase II (CaMKII) on known ionic currents.

Therefore, each model has its own strengths and weaknesses. The aim of this study is to provide an informed investigation of their response to varied ischaemic conditions by comparing electrophysiological properties in single cell and tissue simulations, in order to assess their utility for studying mechanisms of arrhythmogenesis in ischaemia.

6.2 Methods

6.2.1 Ischaemic electrophysiological changes

Models were initially compared under control conditions in order to better understand differences between ion current formulations. The comparison was then extended to ischaemia by modifying the following set of parameters: peak I_{Na} and I_{CaL} conductances were decreased by 25%, $[K^+]_o$ was increased from 5.4 mM (control value) to 8 mM and peak $I_{K(ATP)}$ conduc-

tance was increased by 5%. These values are within the range of parameters used in previous simulation studies of acute ischaemia (Section 4.1.5) and found experimentally (Section 3.1) [Tice et al., 2007; Heidenreich et al., 2012; Trénor et al., 2005; Yatani et al., 1984; Irisawa and Sato, 1986; Sato et al., 1985]. The $I_{K(ATP)}$ current formulation, based on [Michailova et al., 2005] and described in Equation (4.21), was added to the cell models using COR[1] [Garny et al., 2003].

Models were then compared by calculating important electrophysiological properties of arrhythmic risk (APD, PRR, ERP and CV). Hyperkalaemia and hypoxia, simulated through changes in $[K^+]_o$ and $I_{K(ATP)}$, are the two major ischaemic conditions affecting APD and PRR, therefore, they were varied in order to cover the range of values observed experimentally from control to ischaemic conditions (as shown in Section 3.1) [Coronel, 1994; Carmeliet, 1999; Weiss and Shine, 1982b; Van Wagoner and Lamorgese, 1994; Weiss et al., 1992]. In the first part of our study, $[K^+]_o$ = 5.4 mM and 8 mM defined the control and ischaemic conditions respectively however, experimental data has shown values of $[K^+]_o$ from 4 up to 9 mM, thus we extended the range of values investigated accordingly in our analysis. Therefore, $[K^+]_o$ was increased from 4 to 9 mM, in steps of 1 mM, and peak $I_{K(ATP)}$ conductance was increased from 0 to 20%, in steps of 2% in single cell and 4% in tissue. However, peak I_{Na} and I_{CaL} conductances were not varied from their ischaemic values (decreased by 25%). Therefore, in the second part of our study control conditions were defined by $[K^+]_o$ = 4 mM and peak $I_{K(ATP)}$ conductance = 0%, and ischaemic conditions by $[K^+]_o$ = 9 mM and peak $I_{K(ATP)}$ conductance = 20%.

6.2.2 Numerical methods

Single cell simulations were run in MATLAB for all models. Equations were solved using *ode15s* with a maximum time step of 1 ms, and a relative and absolute tolerance of 10^{-7} and

[1] http://cor.physiol.ox.ac.uk

10^{-9} respectively to ensure numerical convergence. Stimulus duration was set to 2 ms and the amplitude to 2 times the activation threshold. In order to assess whether differences observed between models were due to varying AP morphologies, we performed an AP clamp to the AP of the ORd model. This was done in the TP06, GPB and CRLP models by fixing the voltage at each time step to the one of the ORd model.

Tissue simulations were conducted using Chaste [Pitt-Francis et al., 2009] on a 5 cm long 1D strand of coupled cells. Tissue simulations were only carried out in the TP06, GPB and CRLP models due to limitations of the ORd model, as argued in this chapter. The space discretisation was 0.01 cm in all models. The ODE and PDE time steps were 0.005 ms and 0.01 ms for the CRLP and GPB models, and 0.001 ms and 0.01 ms for the TP06 model, which ensured convergence of results.

6.2.3 Data analysis

In single cell simulations, ERP was calculated once the cell was at steady state by applying a stimulus at progressively shorter coupling intervals (S2), with 10 ms precision. ERP was defined as the minimum S2 coupling interval (greater than the APD) that triggered an AP (defined as having a plateau phase above -20 mV). In tissue simulations, ERP was specified by the minimum S2 coupling interval that triggered excitation propagation along the strand. The tissue, at resting state, was stimulated with -10^6 $\mu\mathrm{A.cm}^{-3}$ for 0.5 ms at position $x = 0$ cm for 5 beats with an S1 period of 1000 ms, followed by decreasing S2 stimuli, with ERP calculated as the minimum S2 that triggered an AP in the cell at position $x = 3$ cm. In both single cell and tissue, the APD was calculated at 90% repolarisation and the PRR as the difference between ERP and APD.

6.3 Comparison of ionic current formulations

In order to assess these models under ischaemic conditions, we first need to understand their behaviour under control conditions. As shown in Figure 6.1a, all models display different AP morphologies with varying degrees of notch depth following depolarisation, length of the plateau phase, APD and resting V_m. The ORd displays the smallest notch and the shortest plateau phase and APD. Therefore, we clamp the other models to the AP of the ORd model, as shown in Figure 6.1b, in order to investigate how AP morphology modulates the behaviour of the ion currents.

The ionic currents investigated are: I_{Na} responsible for the upstroke, I_{CaL} responsible for the plateau phase, all three K^+ currents I_{Kr}, I_{Ks} and I_{K1} responsible for the repolarisation, I_{to} responsible for the initial small repolarisation following the upstroke, I_{NaCa} responsible for removing Ca^{2+} from the cell and I_{NaK} responsible for maintaining resting V_m.

6.3.1 Currents under control conditions

Fast inward sodium current I_{Na}

Figure 6.1c shows the time course of I_{Na} during the first 3 ms of the fast depolarisation upstroke. The TP06, GPB and CRLP models display similar I_{Na} dynamics with a similar peak amplitude and width. This is not surprising, as the formulations of I_{Na} in the 3 models are similar. The GPB and CRLP models do, however, divide the current into separate junctional cleft and subsarcolemmal components (as described earlier in Section 4.1.3). On the other hand, the peak of the I_{Na} current in the ORd model is shifted towards the right. This may be partly due to the ORd AP morphology, as is shown by the AP clamp (Figure 6.1d), where I_{Na} peak in all models is shifted towards the right. However, differences still remain in the amplitude and start of the I_{Na} current peak. These may be due to differences in formulation, the I_{Na} ORd model includes CaMKII effects and is composed of a fast and a late component (as described earlier

Figure 6.1 Comparing transmembrane voltage (V_m) fast sodium current (I_{Na}) and L-type calcium current (I_{CaL}) without and with ORd AP clamp for the TP06, GPB, CRLP and ORd models under normal conditions.

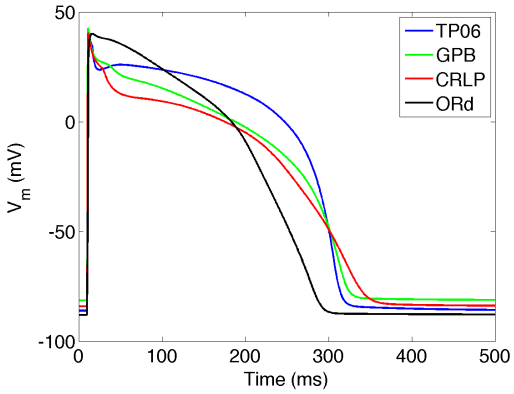

(a) V_m without ORd AP clamp

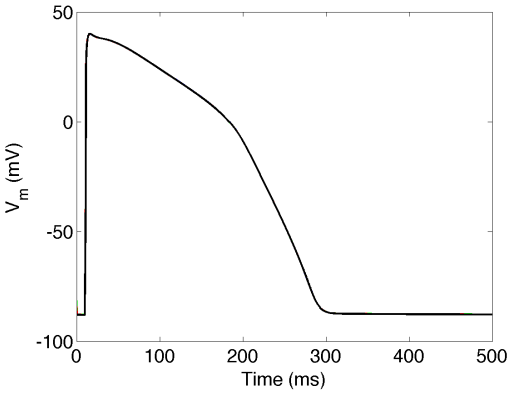

(b) V_m with ORd AP clamp

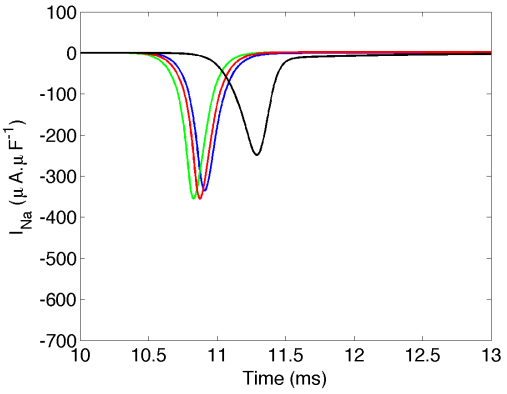

(c) I_{Na} without ORd AP clamp

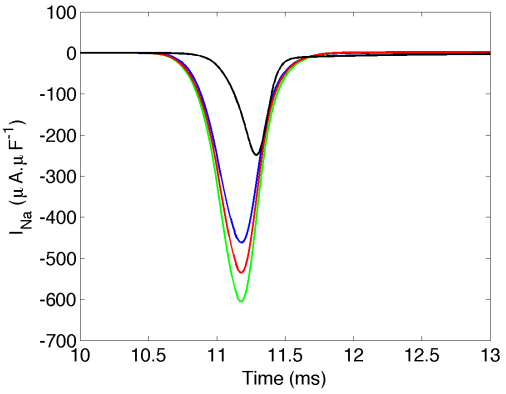

(d) I_{Na} with ORd AP clamp

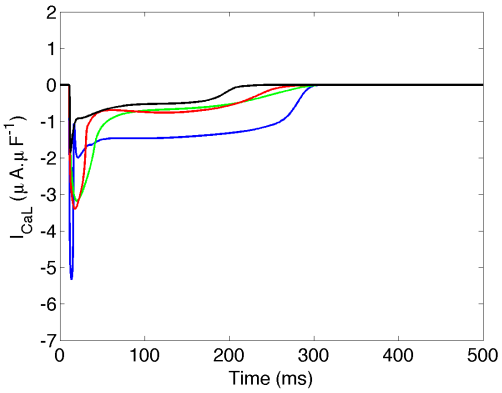

(e) I_{CaL} without ORd AP clamp

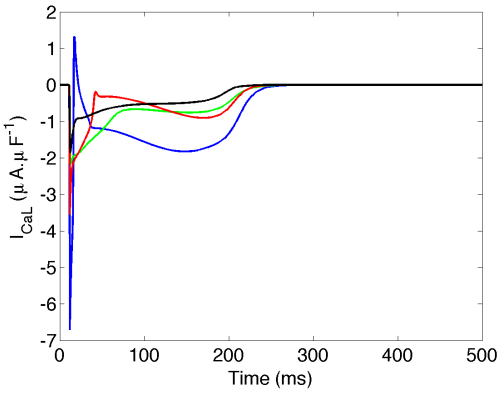

(f) I_{CaL} with ORd AP clamp

in Section 4.1.3).

As shown in Table 6.1, the I_{Na} formulation is based on different sets of experimental data in each model. The GPB and CRLP model are grouped in the same column as they both use the formulation of I_{Na} described in the GPB model apart from [Drouin et al., 1995], which the CRLP model use to better reproduce maximal upstroke velocity. The only set of data shared across the 4 models is [Nagatomo et al., 1998], which is used to calculate the temperature coefficient that converts parameters to physiological conditions. The rest are different, but mostly taken from human experiments, this may modulate the differences in I_{Na} amplitude observed.

L-type calcium current I_{CaL}

As shown in Figure 6.1e, the I_{CaL} current of the TP06 model has the highest peak amplitude while the ORd has the smallest, in line with the TP06 displaying the longest AP plateau phase. These differences are slightly modulated by AP morphology, mainly around the AP notch, as shown by the AP clamp in Figure 6.1f. As with the I_{Na} current, the formulation of the I_{CaL} in the TP06, GPB and CRLP models is similar. However, the GPB and CRLP models divide the current into separate junctional cleft and subsarcolemmal components and the ORd model formulation includes CAMKII effects (as described earlier in Section 4.1.3). As listed in Table 6.2, most of the data use to build the I_{CaL} current is from human, apart from some data used in the ORd model, to simulate the effects of CaMKII and the VDI and CDI components of I_{CaL}. The only set of data shared across the 4 models is [Magyar et al., 2000] and there is significant overlap between the data used in the TP06, GPB and CRLP models.

Rapid delayed rectifier potassium current I_{Kr}

Figure 6.2a shows the rapid delayed rectifier potassium current (I_{Kr}) which peaks as the cell completely repolarises, in line with the differences observed in APD (Figure 6.1a). Indeed, during the AP clamp the current peaks at similar times in all models, as shown in Figure 6.2b.

Table 6.1 Experimental data used to formulate I_{Na} in the 4 human ventricular AP models: TP06, GPB, CRLP and ORd showing information on the experimental setup: cell type, setup preparation and the temperature at which the experiments were performed.

Experimental Data	Cell Type	Preparation	Temp	TP06	GPB/ CRLP	ORd
[Nagatomo et al., 1998]	HEK-293 cells	Isolated cells	$23, 33°$	x	x	x
[Makita et al., 2000]	Xenopus oocytes	Isolated cells	$22°$	x		
[Sakakibara et al., 1992]	Human RA	Isolated cells	$37°$	x	x	
[Schneider et al., 1994]	Human atria	Isolated cells	$24°$	x		
[Viswanathan et al., 2001]	tsA-201 cells	Isolated cells	$21°$	x		
[Wan et al., 2001]	HEK-293 cells	Isolated cells	$37°$	x		
[Wang et al., 2000]	tsA-201 cells	Isolated cells	$32°$	x		
[Drouin et al., 1998]	Human LV	Tissue *in-vitro*	$37°$	x		
[Näbauer et al., 1996]	Human LV	Isolated cells	$35°$		x	
[Li et al., 1998]	Human RV	Isolated cells	$36°$		x	
[Li et al., 1999]	Human RV	Isolated cells	$36°$		x	
[Péréon et al., 2000]	Human ventricles/ COS-7 cells	Tissue *in-vitro* and Isolated cells	$37°$		x	
[Sakakibara et al., 1993]	Human ventricles	Isolated cells	$17°$			x
[Hanck and Sheets, 1992]	Dog Purkinje cells	Isolated cells	$37°$			x
[Wagner et al., 2006]	Rabbit/ Mouse ventricles	Isolated cells and *in vivo*	$37°$			x
[Spach et al., 2000]	Canine ventricles	Tissue *in-vitro*	$37°$			x
[Taggart, 2000]	Human ventricles	*in vivo*	$37°$			x
[Drouin et al., 1995]	Human LV	Tissue *in-vitro*	$37°$			x
[Maltsev et al., 1998]	Human LV	Isolated cells	$22 - 24°$			x
[Maltsev and Undrovinas, 2006]	Human ventricles	Isolated cells	$24°$			x

Table 6.2 List of experimental data used to formulate I_{CaL} in the 4 human ventricular AP models: TP06, GPB, CRLP and ORd. Information included on the experimental setup is defined in previous table.

Experimental Data	Cell Type	Preparation	Temp	TP06	GPB	CRLP	ORd
[Li and Nattel, 1997]	Human RA	Isolated cells	36°	x	x		
[Magyar et al., 2002]	Dog/Human LV	Isolated cells	12 – 14°	x			
[Pelzmann et al., 1998]	Human RV	Isolated cells	37°	x	x	x	
[Magyar et al., 2000]	Human LV	Isolated cells	37°	x	x	x	x
[Bénitah et al., 1992]	Human LV	Isolated cells	20 – 22°	x		x	
[Mewes and Ravens, 1994]	Human ventricles/atria	Isolated cells	21 – 23°	x		x	
[Beuckelmann et al., 1991]	Human ventricles	Isolated cells	37°			x	
[Sun et al., 1997]	Human RA	Isolated cells	23°			x	
[Li et al., 1999]	Human RV	Isolated cells	36°			x	
[Fülöp et al., 2004]	Human ventricles	Isolated cells	37°				x
[Aggarwal and Boyden, 1995]	Dog LV	Isolated cells	36°				x
[Kim et al., 2004]	Xenopus oocytes	Isolated cells	17 – 19°				x
[Dzhura et al., 2000]	Murine ventricles	Isolated cells	20 – 23°				x

Figure 6.2 Comparing rapid delayed rectifier potassium current (I_{Kr}) slow delayed rectifier potassium current (I_{Ks}) and inward rectifier potassium current (I_{K1}) with and without ORd AP clamp for the TP06 (blue), GPB (green), CRLP (red) and ORd (black) models under normal conditions.

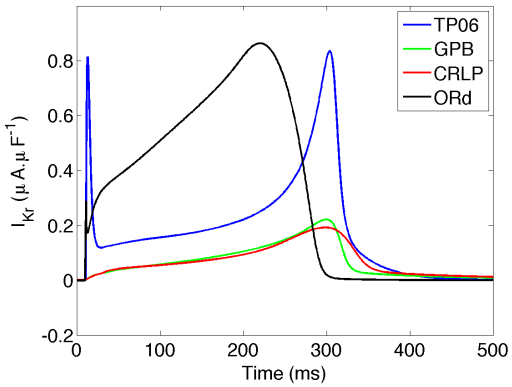

(a) I_{Kr} without ORd AP clamp

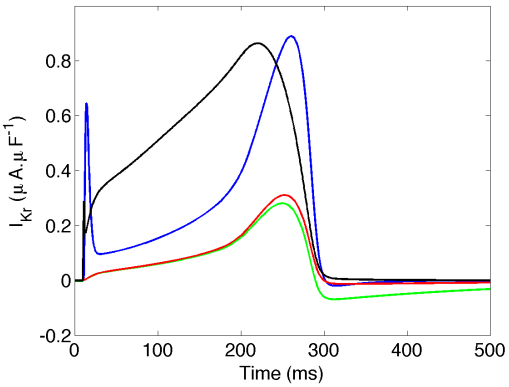

(b) I_{Kr} with ORd AP clamp

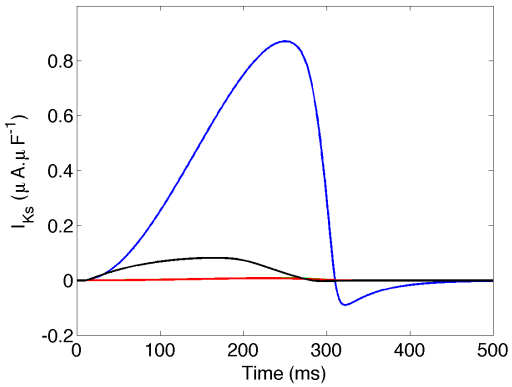

(c) I_{Ks} without ORd AP clamp

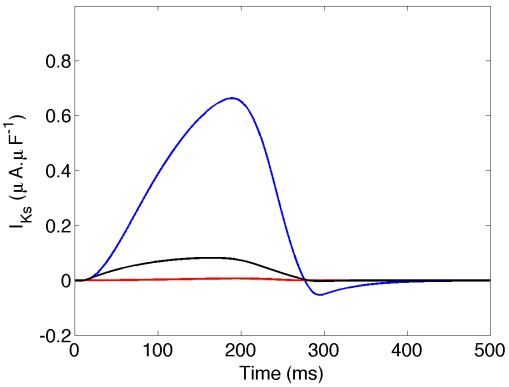

(d) I_{Ks} with ORd AP clamp

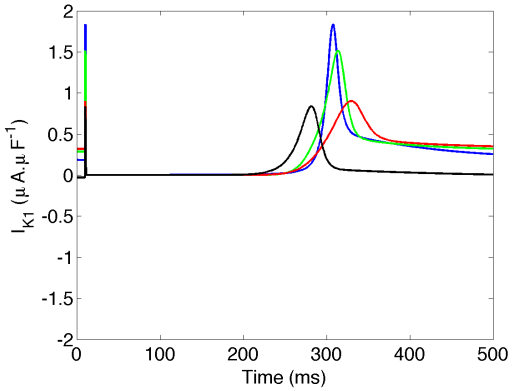

(e) I_{K1} without ORd AP clamp

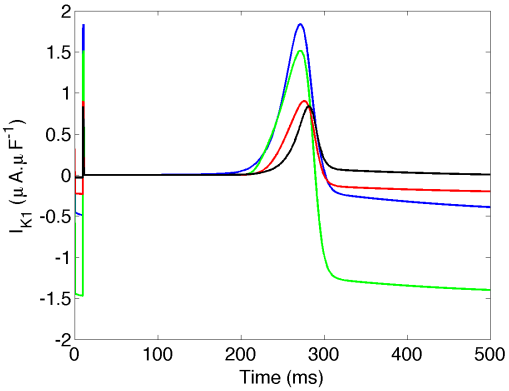

(f) I_{K1} with ORd AP clamp

Furthermore, the amplitudes of the current are quite different with the ORd and TP06 models displaying a much greater amplitude than the GPB and CRLP models. This behaviour may be due to the formulation of the current being similar in all 4 models, aside from the GPB and CRLP models not including the dependence on $[K^+]_o$ that is included in the TP06 and ORd models (as described earlier in Section 4.1.3). Despite the dissimilarities between the current of the TP06 and GPB/CRLP models, they use similar experimental data as shown in Table 6.3 [Zhou et al., 1998; Johnson et al., 1999; Iost et al., 1998]. On the other hand, O'Hara *et al.* carried out their own experiments to construct I_{Kr} in the ORd model.

Table 6.3 List of experimental data used to formulate I_{Kr} in the 4 human ventricular AP models: TP06, GPB, CRLP and ORd. Information included on the experimental setup is defined in previous table.

Experimental Data	Cell Type	Preparation	Temp	TP06	GPB/ CRLP	ORd
[Zhou et al., 1998]	HEK-293 cells	Isolated cells	$23, 35°$	x	x	
[Johnson et al., 1999]	CHO-K1 cells	Isolated cells	$20 - 25°$	x	x	
[Smith and Yellen, 2002]	Xenopus oocytes	Isolated cells and fluorescence	not specified	x		
[Li et al., 1996]	Human RV/ RA	Isolated cells	$36°$	x		
[Iost et al., 1998]	Human LV/ RV	Isolated cells	$12 - 14°$	x	x	
[Jost et al., 2008]	Human/Dog papillary muscles	Isolated cells	$37°$		x	
[O'Hara et al., 2011]	Human ventricles	Isolated cells	$37°$			x
[Jost et al., 2009]	Dog/ Human LV	Isolated cells	$37°$			x

Rapid delayed rectifier potassium current I_{Ks}

As shown in Figure 6.2c, the I_{Ks} current of the TP06 model displays the greatest peak amplitude followed by the ORd model. On the other hand, both the GPB and CRLP models display close to zero I_{Ks} activity. This behaviour is similar during AP clamp, apart from a slight decrease in I_{Ks} amplitude in the TP06 model, as is shown in Figure 6.2d. The TP06, GPB and CRLP models have similar I_{Ks} equations, apart from being divided into its subsarcolemmal

and junctional cleft components in the GPB and CRLP models. Furthermore, the ORd model displays a different formulation that depends on $[Ca^{2+}]_i$ (as described earlier in Section 4.1.3). As highlighted in Table 6.4, the 4 models share [Virág et al., 2001] as experimental data and the TP06 and ORd models share [Li et al., 1996]. However, the rest of the studies on which the formulation is based differ. The virtually non-existent I_{Ks} for the GPB and CRLP models may be due to the formulations in [Shannon et al., 2004] on which it is based.

Inward rectifier potassium current I_{K1}

As shown in Figure 6.2e the I_{K1} current, in all models, displays a brief initial peak at the time of depolarisation of the cell and then a wider one at the time of repolarisation, in line with the AP morphology shown in Figure 6.1a. This behaviour is similar during AP clamp, apart from a decrease in resting state, especially in the GPB model, as is shown in Figure 6.2f. The similar morphology of the current is in line with the similar formulation presented earlier in Section 4.1.3. However, as shown in Table 6.4, the current is fit to different experimental data in each model, which may explain the dissimilarities observed.

Transient outward potassium current I_{to}

As shown in Figure 6.3a, the I_{to} current of the TP06 model displays the greatest activity, while the current of the ORd model displays the smallest activity. As shown in Figure 6.3b, a similar I_{to} current behaviour is shown during the AP clamp, therefore, the differences observed are not dependent on AP morphology. The equations describing the current in each model are similar, but the GPB and CRLP models divide the current into a fast and slow component and the ORd model incorporates CAMKII effects, as presented earlier in Section 4.1.3. Table 6.4 shows that the TP06, GPB and CRLP models use data from [Näbauer et al., 1996; Wettwer et al., 1994] to parameterise their model while the ORd and the TP06 models only share the data from [Greenstein et al., 2000].

Sodium/calcium exchanger I_{NaCa}

Figure 6.3 Comparing transient outward potassium current I_{to}, sodium/calcium exchanger I_{NaCa} and sodium/potassium pump I_{NaK} with and without ORd AP clamp for the TP06, GPB, CRLP and ORd models under normal conditions.

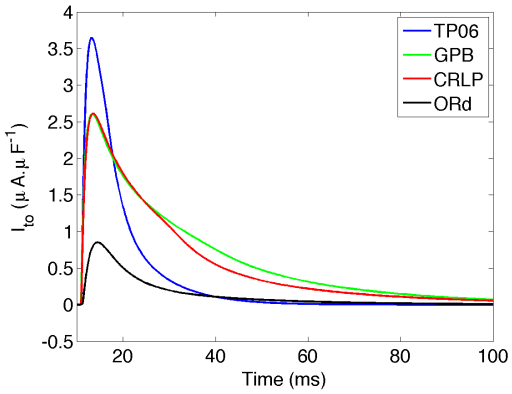

(a) I_{to} without ORd AP clamp

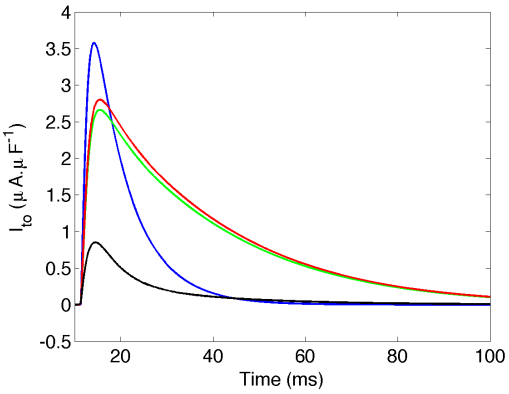

(b) I_{to} with ORd AP clamp

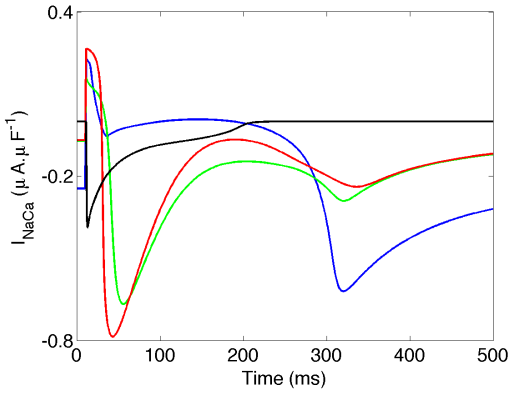

(c) I_{NaCa} without ORd AP clamp

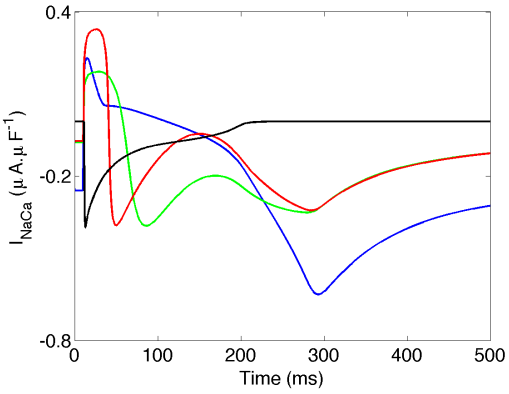

(d) I_{NaCa} with ORd AP clamp

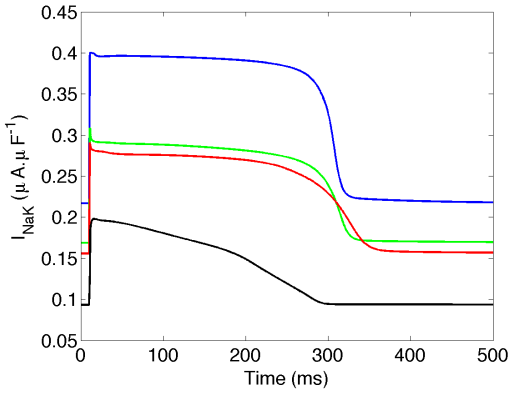

(e) I_{NaK} without ORd AP clamp

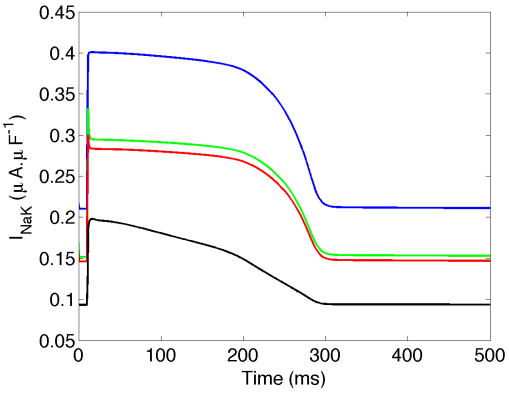

(f) I_{NaK} with ORd AP clamp

As shown in Figure 6.3c, the role of the exchanger is reversed during depolarisation in the TP06, GPB and CRLP models, but not the ORd model. Furthermore, the GPB and CRLP models display an additional inverted peak that follows the initial positive peak about 42 - 44 ms after depolarisation, which is not present in the TP06 model. The ORd model displays a single inverted peak at the time of depolarisation, and then slowly recovers back to its resting state. Figure 6.3d demonstrates this behaviour is not dependent on AP morphology as the currents display the same morphology during AP clamp with a decreased amplitude. The differences observed between the models are due to the varying equations and experimental data underlying the formulations used in each model. As shown in Table 6.4, the formulations are based on the Luo-Rudy model for the TP06 model, on the Shannon model for the GPB and CRLP models and on the Decker model for the ORd model [Luo and Rudy, 1994; Shannon et al., 2004; Decker et al., 2009]. However, the GPB, CRLP and ORd models do use the same experimental data from [Weber et al., 2003].

Sodium/potassium pump I_{NaK}

Figure 6.3e shows that, despite having a similar morphology in all models, I_{NaK} displays different maximum and resting amplitudes, with the TP06 and ORd models having the greatest and smallest amplitudes respectively. This behaviour is not dependent on AP morphology as demonstrated by the AP clamp in Figure 6.3f. As evidenced in Table 6.4, the current is based on different studies for each model, apart from the CRLP and GPB models. The formulation in the TP06 model is based on the Luo-Rudy, Priebe-Beuckelmann and Courtemanche models, while it is based on the Shannon 2004 model in the GPB and CRLP models, and the Smith and Crampin model in the ORd model [Luo and Rudy, 1994; Priebe and Beuckelmann, 1998; Courtemanche et al., 1998; Shannon et al., 2004; Smith and Crampin, 2004].

Table 6.4 List of studies used to inform the formulation of I_{Ks}, I_{K1}, I_{to}, I_{NaCa} and I_{NaK} formulations in the 4 human ventricular AP models: TP06, GPB, CRLP and ORd. Highlighted studies are shared across one or more models.

I_{Ks}	
TP06	[Virág et al., 2001; Li et al., 1996][Wang et al., 1994; Drouin et al., 1995; Li et al., 1998]
GPB/CRLP	[Virág et al., 2001] [Shannon et al., 2004]
ORd	[Virág et al., 2001][Li et al., 1996][Tohse, 1990]
I_{K1}	
TP06	[Courtemanche et al., 1998; Koumi et al., 1995]
GPB	[Magyar et al., 2000; Jost et al., 2008]
CRLP	[Fink et al., 2008]
ORd	[O'Hara et al., 2011; Bailly et al., 1998; Konarzewska et al., 1995; Jost et al., 2009]
I_{to}	
TP06	[Näbauer et al., 1996; Wettwer et al., 1994; Greenstein et al., 2000]
GPB/CRLP	[Näbauer et al., 1996; Wettwer et al., 1994] [Varro et al., 2006]
ORd	[Greenstein et al., 2000][O'Hara et al., 2011; Amos et al., 1996; Tessier et al., 1999; Wagner et al., 2009]
I_{NaCa}	
TP06	[Luo and Rudy, 1994; Noble et al., 1998]
GPB/CRLP	[Weber et al., 2003][Shannon et al., 2004]
ORd	[Weber et al., 2003][O'Hara et al., 2011; Kang and Hilgemann, 2004; Faber et al., 2007; Decker et al., 2009; Hund and Rudy, 2004]
I_{NaK}	
TP06	[Luo and Rudy, 1994; Priebe and Beuckelmann, 1998; Courtemanche et al., 1998]
GPB/CRLP	[Shannon et al., 2004]
ORd	[Smith and Crampin, 2004; Nakao and Gadsby, 1989; Pieske et al., 2002]

6.3.2 Currents under ischaemic conditions

We now investigate how the activity of these currents is modified under ischaemic conditions, as shown in Figure 6.4. We notice that the ischaemic AP displays the expected morphological changes in all models, namely an increase in resting V_m and a decrease in APD. This is driven by changes at the ionic level through a decrease in I_{Na}, I_{to}, I_{NaK} and I_{Ks}, and a earlier recovery of I_{CaL}, I_{NaCa} and all the repolarising potassium currents.

Under normal conditions, the CRLP and GPB models have a similar APD with a difference of just under 10 ms. This gap is, however, more than doubled under ischaemic conditions, with a difference in APD of more than 20 ms. The differences observed may be due to the changes introduced in the I_{K1} and I_{NaK} currents, as described in Section 4.1.3 in Chapter 4.

As shown in Figure 6.4b, the I_{Na} current of the GPB model is the most sensitive to ischaemia, as it displays the biggest decrease in peak amplitude of 81% compared to 56% for the TP06 model, 66% for the CRLP model and 76% for the ORd model. The amplitude of the I_{CaL} peak increases by 39%, 69%, 98% and 162% for the TP06, GPB, CRLP and ORd models, respectively, as shown in Figure 6.4c. Therefore, although the current of the TP06 model has the greatest amplitude, the I_{CaL} current of the ORd model displays the greatest sensitivity to ischaemia.

All of the repolarising currents (I_{Kr}, I_{Ks}, I_{K1}) recover earlier under ischaemic conditions due to the shorter APD and amplitudes are modified. As presented in Figure 6.4e, the I_{Ks} current amplitude is decreased by 38% and 63% in the TP06 and the ORd models respectively under ischaemia. Furthermore, the I_{K1} current (Figure 6.4f) in all models, apart from the ORd, is slightly upregulated during ischaemia, the amplitude of the repolarisation peak is increased by about 22% in the TP06, GPB and CRLP models, however it decreases by about 8% in the ORd model.

During ischaemia, peak I_{to} is shifted towards the right, its amplitude decreases and its width

increases, as can be seen in Figure 6.4g. The decrease in amplitude is of 41%, 53%, 41% and 59% for the TP06, GPB, CRLP and ORd models respectively. Therefore, the current of the ORd model displays the greatest change in amplitude under ischaemic conditions.

Under ischaemic conditions, the amplitudes of the depolarisation and repolarisation peaks of I_{NaCa} (Figure 6.4h) in the TP06 model are decreased by 77% and 32%. The two initial peaks of the GPB and CRLP models are decreased by 75% and 14% for the GPB model and 33% and 14% for the CRLP model respectively, however, the final peak is increased by 27% for the GPB model and by 31% for the CRLP model. The amplitude of the single peak in the ORd model is increased by 100% under ischaemic conditions. The maximal amplitude of the I_{NaK} current (Figure 6.4i) is decreased by approximately 33% in the TP06 and CRLP models, 29% in the GPB model, and 27% in the ORd model. The behaviour of these models under varying ischaemic conditions will be investigated further in the following section by investigating electrophysiological properties modulated by the ionic current dynamics described in this section.

6.4 Biomarkers under varying ischaemic conditions in single cell and 1D tissue simulations

We now investigate the behaviour of the models under varying $[K^+]_o$ and peak $I_{K(ATP)}$ conductance in single cell and 1D tissue simulations by comparing APD, ERP and PRR values (Tables 6.5 and 6.6). The study conducted in tissue also investigates effects on CV.

As shown in detail in the previous section, each model uses different current formulations and experimental data to describe the electrophysiological activity of a human ventricular cell. We have shown that the I_{Na} current of the ORd model is quite different from the other 3 models and the current of the GPB model is the most sensitive to ischaemia. This current is particularly important in modulating excitability of the cell, which is significantly compromised during ischaemia. These differences become more pronounced in this section, as shown in Section 6.4.3,

Figure 6.4 Comparing ischaemic (thick line) V_m, I_{Na}, I_{CaL}, I_{Kr}, I_{Ks}, I_{K1}, I_{to}, I_{NaCa} and I_{NaK} for the TP06, GPB, CRLP and ORd models (normal conditions shown in the thin dashed lines).

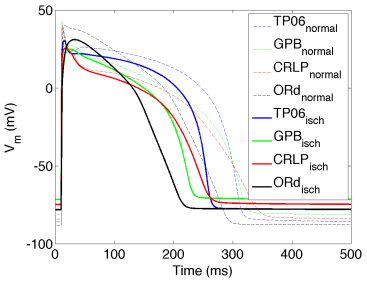

(a) Ischaemic V_m

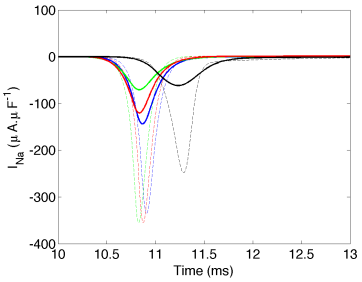

(b) Ischaemic I_{Na}

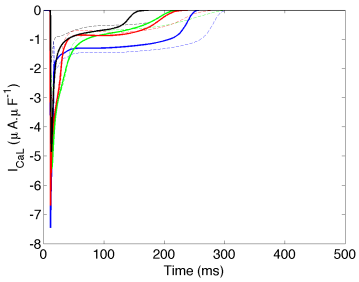

(c) Ischaemic I_{CaL}

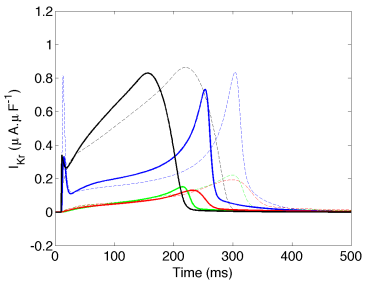

(d) Ischaemic I_{Kr}

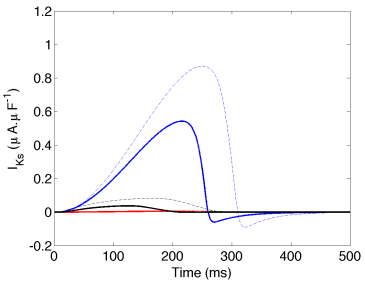

(e) Ischaemic I_{Ks}

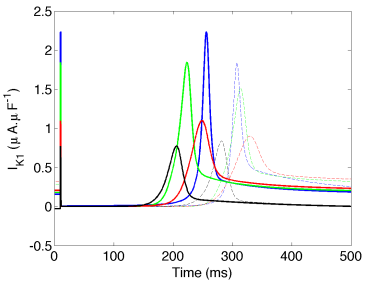

(f) Ischaemic I_{K1}

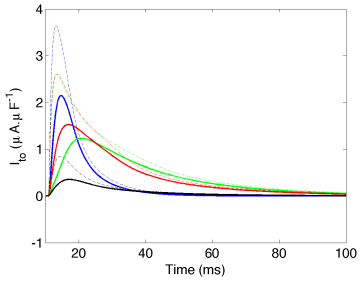

(g) Ischaemic I_{to}

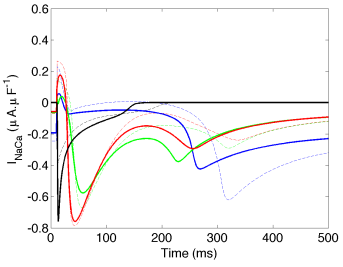

(h) Ischaemic I_{NaCa}

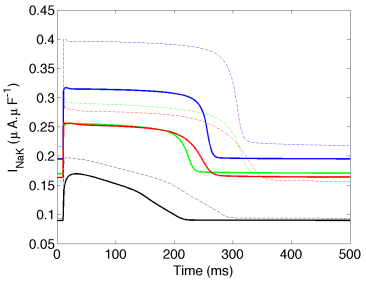

(i) Ischaemic I_{NaK}

as the ORd model does not reproduce the expected changes in PRR with ischaemia in the single cell simulations. Therefore, the model was not included in the tissue simulation investigation. Furthermore, all models were tested under maximum hyperkalaemic values of $[K^+]_o$ up to 9 mM, however, the GPB model demonstrated propagation failure in tissue for $[K^+]_o \geq 9$ mM, therefore, $[K^+]_o$ = 8 mM is used for this model.

In this section, to ease quantitative comparison between control and ischaemic conditions, *control conditions* are defined as $[K^+]_o$ = 4 mM and $f_{K(ATP)}$ = 0% and *ischaemic conditions* as $[K^+]_o$ = 9 mM and $f_{K(ATP)}$ = 20% (apart from the GPB model in tissue where maximum $[K^+]_o$ = 8 mM). This covers a wider range of values than the ones presented in the previous section, in order to better incorporate the range of values found experimentally (as described in Section 6.2.1).

6.4.1 APD under varying ischaemic conditions

The first column of Tables 6.5 and 6.6 shows APD values for varying peak $I_{K(ATP)}$ conductance (modulated by $f_{K(ATP)}$) and $[K^+]_o$ values for the models tested in single cell and tissue. In all models, as peak $I_{K(ATP)}$ and $[K^+]_o$ increase, the APD decreases.

In single cell simulations, there is a decrease in APD of 52%, 58%, 63% and 50% for the TP06, GPB, CRLP and ORd models respectively between control and ischaemic conditions. Therefore, the APD of the CRLP model is the most sensitive to changes in ischaemic parameters, as it displays the biggest % decrease in APD. In tissue simulations, as shown in the first column of Table 6.6, the APD displays a decrease of 48%, 83% and 57% for the TP06, GPB and CRLP models, respectively, between control and ischaemic conditions. We notice that the GPB model displays the biggest difference in APD as the model starts being unexcitable for $[K^+]_o$ = 8 mM and $f_{K(ATP)}$ = 20%, with an APD of 46.27 ms. As in the single cell simulations, the CRLP model is more sensitive to ischaemic changes than the TP06 model as it displays a bigger reduction in APD by almost 10%.

Table 6.5 Single cell results: comparison of APD, PRR and ERP of the TP06, GPB, CRLP, and ORd models to variations in $[K^+]_o$ and in peak $I_{K(ATP)}$ conductance scaling factor $f_{K(ATP)}$.

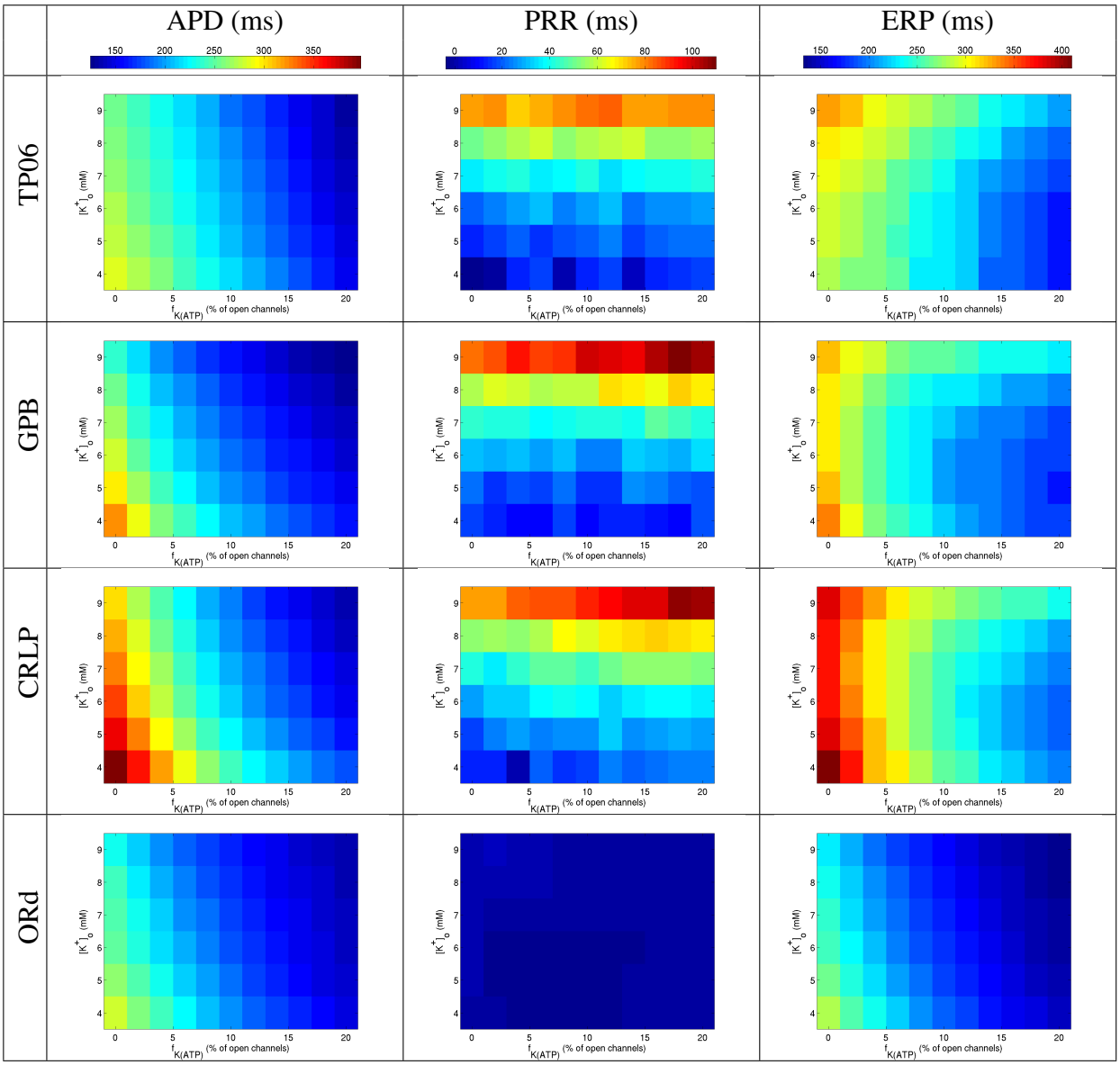

In single cell simulations, for $[K^+]_o$ = 4 mM, the increase in $f_{K(ATP)}$ from 0 to 20% induces a decrease in APD of 46%, 50%, 56% and 47% for the TP06, GPB, CRLP and ORd models respectively. In tissue, the decrease in APD is of 42%, 48% and 52% for the TP06, GPB and CRLP models, respectively. We notice that in both the single cell and tissue simulations, the CRLP model is the most sensitive to changes in $f_{K(ATP)}$. In single cell simulations, for $f_{K(ATP)}$ = 0%, the increase in $[K^+]_o$ from 4 mM to 9 mM, induces a decrease in APD of 11%, 26%, 24% and 18% for the TP06, GPB, CRLP and ORd models respectively. In tissue, the decrease in APD is of 9%, 26% and 28% for the TP06, GPB and CRLP models, respectively. Therefore, the GPB model is the most sensitive to changes in $[K^+]_o$, while at the tissue level the CRLP model is the most sensitive. In both single cell and tissue simulations, changes in $f_{K(ATP)}$ are responsible for a majority of the APD reduction as the % decrease in APD is more than doubled for changes in $f_{K(ATP)}$ compared to changes in $[K^+]_o$.

6.4.2 ERP under varying ischaemic conditions

The third column of Tables 6.5 and 6.6 shows ERP values for varying peak $I_{K(ATP)}$ conductance (modulated by $f_{K(ATP)}$) and $[K^+]_o$ values for the models tested. The ERP in all models, in single cell and tissue, decreases as peak $I_{K(ATP)}$ increases, while there is no clear correlation between ERP and $[K^+]_o$.

There is a decrease in ERP of 28%, 28%, 37% and 50% for the TP06, GPB, CRLP and ORd models, respectively, between control and ischaemic conditions. Excluding the ORd model (where ERP = APD), the ERP of the CRLP model is the most sensitive to changes in ischaemic parameters. At the tissue level, there is an ERP increase of 70% and 22% for the TP06 and CRLP models respectively and a decrease of 5% for the GPB model between control and ischaemic conditions. Therefore, the TP06 model displays the biggest increase in ERP.

In single cell simulations, for $[K^+]_o$ = 4 mM, the increase in $f_{K(ATP)}$ from 0 to 20% induces a decrease in ERP of 40%, 47%, 51% and 46% for the TP06, GPB, CRLP and ORd models,

respectively. In tissue, there is a decrease in ERP of 41%, 48% and 50% for the TP06, GPB and CRLP models, respectively. Both in single cell and tissue, the ERP of the CRLP model is the most sensitive to changes in $[K^+]_o$.

In single cell simulations, for $f_{K(ATP)}$ = 0%, the increase in $[K^+]_o$ from 4 to 9 mM, induces an increase in ERP of 17% for the TP06 model and a decrease of 6%, 7% and 11% for the GPB, CRLP and ORd models respectively. In tissue, there is an increase in ERP of 95%, 47% and 33% for the TP06, GPB and CRLP models, respectively. Therefore, the TP06 model is the most sensitive to changes in $[K^+]_o$. However, differences are observed in % between single cell and tissue, due to differences in ERP calculation described earlier (Section 6.2.3), therefore, the single cell ERP may be more sensitive to stimulus strength.

6.4.3 PRR under varying ischaemic conditions

The second column of Tables 6.5 and 6.6 shows PRR values, calculated as the APD subtracted from the ERP, for varying peak $I_{K(ATP)}$ (modulated by $f_{K(ATP)}$) and $[K^+]_o$ values for the models tested. The PRR of all the models, apart from the ORd model, increased as peak $I_{K(ATP)}$ and $[K^+]_o$ increased (with a relatively greater increase due to changes in $[K^+]_o$). There is an increase in PRR of 65.3 ms (495%), 82.6 ms (362%), 89.3 ms (566%) for the TP06, GPB, CRLP models and a decrease of 1.76 ms (332%) for the ORd model, respectively, between control and ischaemic conditions. The PRR of the CRLP model is the most sensitive to changes in ischaemic parameters, as it displays the largest increase in PRR. In tissue, there is an increase in PRR of 352 ms, 205 ms and 250 ms for the TP06, GPB and CRLP models, respectively, between control and ischaemic conditions. Therefore, the TP06 model displays the biggest increase in PRR.

In single cell simulations, for $[K^+]_o$ = 4 mM, the increase in $f_{K(ATP)}$ from 0 to 20% induces an increase in PRR of 19.4 ms, 1.33 ms, 11.67 ms for the TP06, GPB, CRLP models and a decrease of -0.18 ms for the ORd model. In tissue, there is a decrease in PRR of 9 ms, 16 ms and 13

ms for the TP06, GPB and CRLP models, respectively. Therefore, in single cell simulations the PRR of the TP06 model is the most sensitive to changes in $f_{K(ATP)}$, while in tissue, the GPB model is the most sensitive. This is due to the significant decrease in cell excitability in the GPB model for high $[K^+]_o$ values, as was shown in Section 6.3.2.

In single cell simulations, for $f_{K(ATP)}$ = 0%, the increase in $[K^+]_o$ from 4 to 9 mM, induces a decrease in PRR of 79.8 ms, 65.15 ms, 64.16 ms and 1.12 ms for the TP06, GPB, CRLP and ORd models, respectively. In tissue, there is an increase in PRR of 321 ms, 232 ms and 220 ms for the TP06, GPB and CRLP models, respectively. Therefore, both in single cell and tissue, the TP06 model is the most sensitive to changes in $[K^+]_o$.

Furthermore, both in single cell and tissue, changes in $[K^+]_o$ are responsible for a majority of the PRR increase observed. In single cell simulations, the ORd model does not display the expected increase in PRR under ischaemic conditions. This may be due to the differences in the formulations of the I_{Na} current, as described in the previous section. Furthermore, the GPB and CRLP models share the same h and j inactivation gates formulation as the TP06 model, while the ORd model displays a different formulation. These gates play an important role in modulating the recovery and availability of I_{Na} channels and may account for the differences observed in PRR.

6.4.4 CV under varying ischaemic conditions

The last column of Table 6.6 shows the CV for varying peak $I_{K(ATP)}$ (modulated by $f_{K(ATP)}$) and $[K^+]_o$ values for the three models tested. Results show that in all models, as $[K^+]_o$ increases, CV decreases. $I_{K(ATP)}$ does not play a role in modulating depolarisation, therefore, it does not affect CV, as shown in all models. An increase in $f_{K(ATP)}$ had little (decrease of 3% in the CRLP model) or no effect (in the TP06 and GPB models) on CV. There is a decrease in CV of 56%, 52% and 52% for the TP06, CRLP and GPB models, respectively, between control and ischaemic conditions. The TP06 model displays the biggest decrease in CV. For $f_{K(ATP)}$

= 0%, the increase in $[K^+]_o$ from 4 mM to 9 mM for the TP06 and CRLP models and up to 8 mM for the GPB model, induces a decrease in CV of 56%, 54% and 58% for the TP06, GPB and CRLP models, respectively. Therefore, the CRLP model is the most sensitive to changes in $[K^+]_o$.

6.4.5 Comparison to experimental data from human

Sutton *et al.* carried out epicardial electrogram recordings in human hearts during 3 min of simulated ischaemia [Sutton et al., 2000]. Their APD, PRR and ERP results are summarised in Figure 6.5, along with our results. Figure 6.5d also presents CV results from another electrogram recording study in human hearts carried out by Taggart *et al.* [Taggart, 2000]. The experimental ranges shown in the table take the values under control and ischaemic conditions, except for the ERP values, where we chose to take values for control and hyperkalaemic conditions ($[K^+]_o$ = 9 mM or 8 mM for the GPB model in tissue), as $[K^+]_o$ is the main factor influencing ERP. We chose these values as a comparison point as it has been shown that the $I_{K(ATP)}$ current activates only after the first few minutes of ischaemia [Zawar and Neumcke, 2000].

We simulate ischaemia up to 10-15 min post-occlusion, which covers the period of greatest arrhythmic risk, while the experimental results only simulate 3 min of ischaemia. We did not pick simulation results corresponding to 3 min of ischaemia as a comparison point due to the limited data available on electrophysiological values of $f_{K(ATP)}$ and $[K^+]_o$ at 3 min. Taking this into account, Figure 6.5 shows that the range of values observed in our simulations in single cell and tissue are comparable to the ones observed experimentally.

Results for the ORd model are only included in the APD results in single cell as the ERP was equal to the APD and the PRR was equal to 0 as described and shown in Table 6.6.

Figure 6.5a compares APD results from experiments to our single cell and tissue simulations.

Table 6.6: Tissue results: comparison of APD, PRR, ERP and CV of the TP06, GPB and CRLP models to variations in $[K^+]_o$ and in peak $I_{K(ATP)}$ conductance scaling factor $f_{K(ATP)}$.

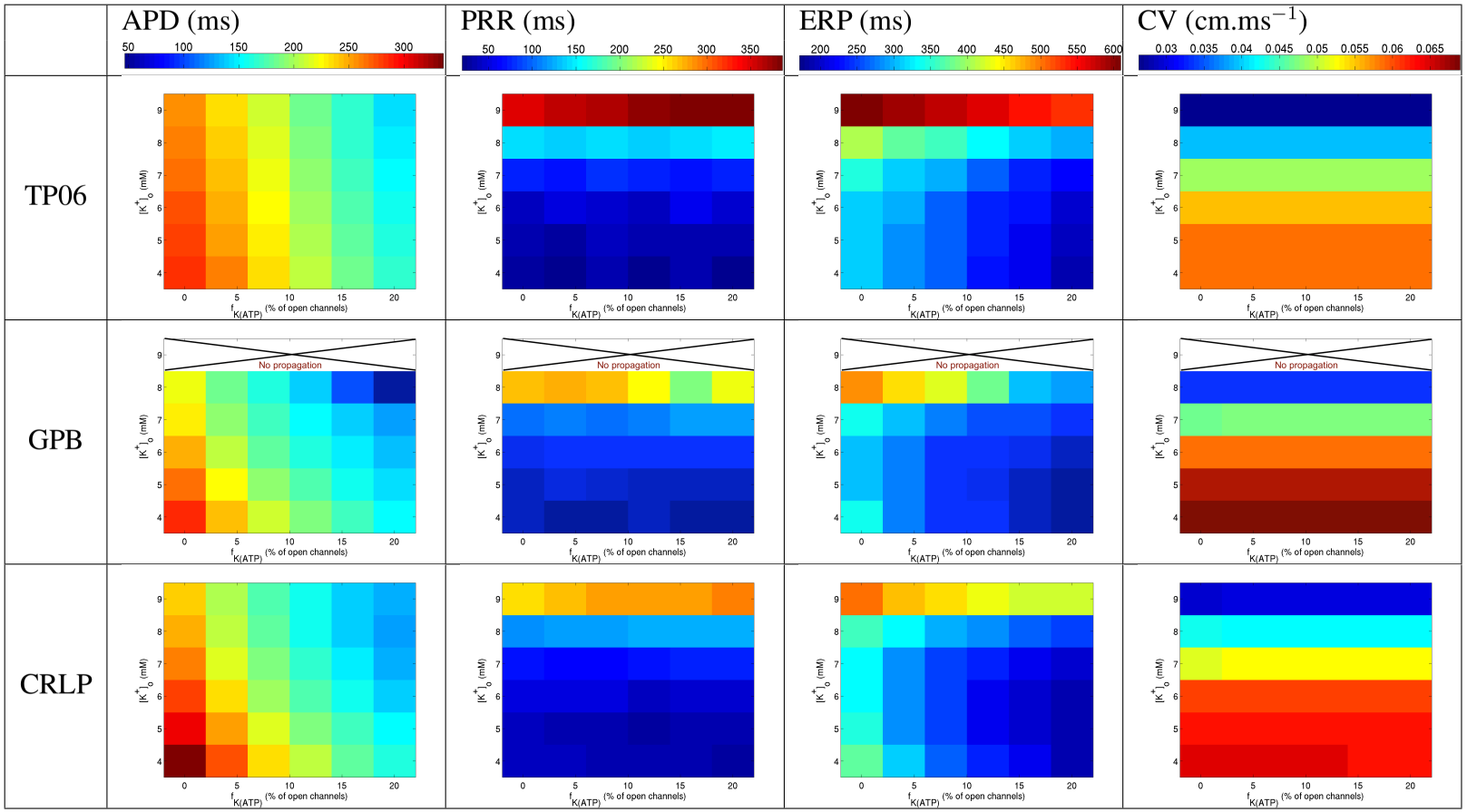

The minimum represents values after 3 min of ischaemia in the human experiments and the most ischaemic conditions in our simulations ($f_{K(ATP}$ = 20% and $[K^+]_o$ = 9 mM, or 8 mM for the GPB model in tissue). The maximum represents values before occlusion in the human experiments and under control conditions. In all models the minimum APD is lower by about 17% compared to experimental results, except for the GPB model in tissue. Furthermore, APD values under control conditions in all models are approximately 4% above experimental values apart from the GPB and CRLP model that display a much longer APD.

Figure 6.5b compares ERP results from experiments to our single cell and tissue simulations. The minimum represents values under control conditions, when the ERP is equal to the APD. The maximum represents values under ischaemic conditions, when excitability decreases and it takes longer to recover excitability. Simulation results overlap with experimental results for all models. In single cell simulations, the change in ERP is very small (TP06 model) or non-existent. Sutton *et al.* also found that for a larger stimulus, the ERP was unchanged during the first 3 min of ischaemia. A similar mechanism may be occurring in our simulations as the stimulus applied plays a more important role in single cell than in tissue, where the stimulus is provided by the neighbouring excited tissue. Therefore, in tissue, the models reproduce an increase in ERP, which was more than doubled for the TP06 model compared to the experimental data.

Figure 6.5c compares experimental PRR results and results from our single cell and tissue simulations. The minimum represents values under control conditions when the ERP is equal to the APD. The maximum represents values under ischaemic conditions when the cell's excitability decreases and takes longer to recover excitability. We notice that our simulation results overlap with experimental data, with minimum values being close to 0, as expected under control conditions. Maximum values are almost double those of experimental results for the TP06 model, however.

Figure 6.5d compares experimental CV results and results from our tissue simulations. The

minimum values represent decreased conduction under ischaemic conditions, while the maximum values represent control conduction. We notice that values shown are very similar to experimental data for all models. This suggests that there is no further decrease in CV between the 3 min of ischaemia measured experimentally and the 10 min simulated in our model.

Figure 6.5 Range of control to ischaemic APD, PRR, ERP and CV values from simulation results in single cell (gray rectangles), tissue (white rectangles) and experimental data (black rectangles) in human carried out by Sutton *et al.* [Sutton et al., 2000] and Taggart *et al.* [Taggart, 2000]. CV simulation results are only carried out in tissue.

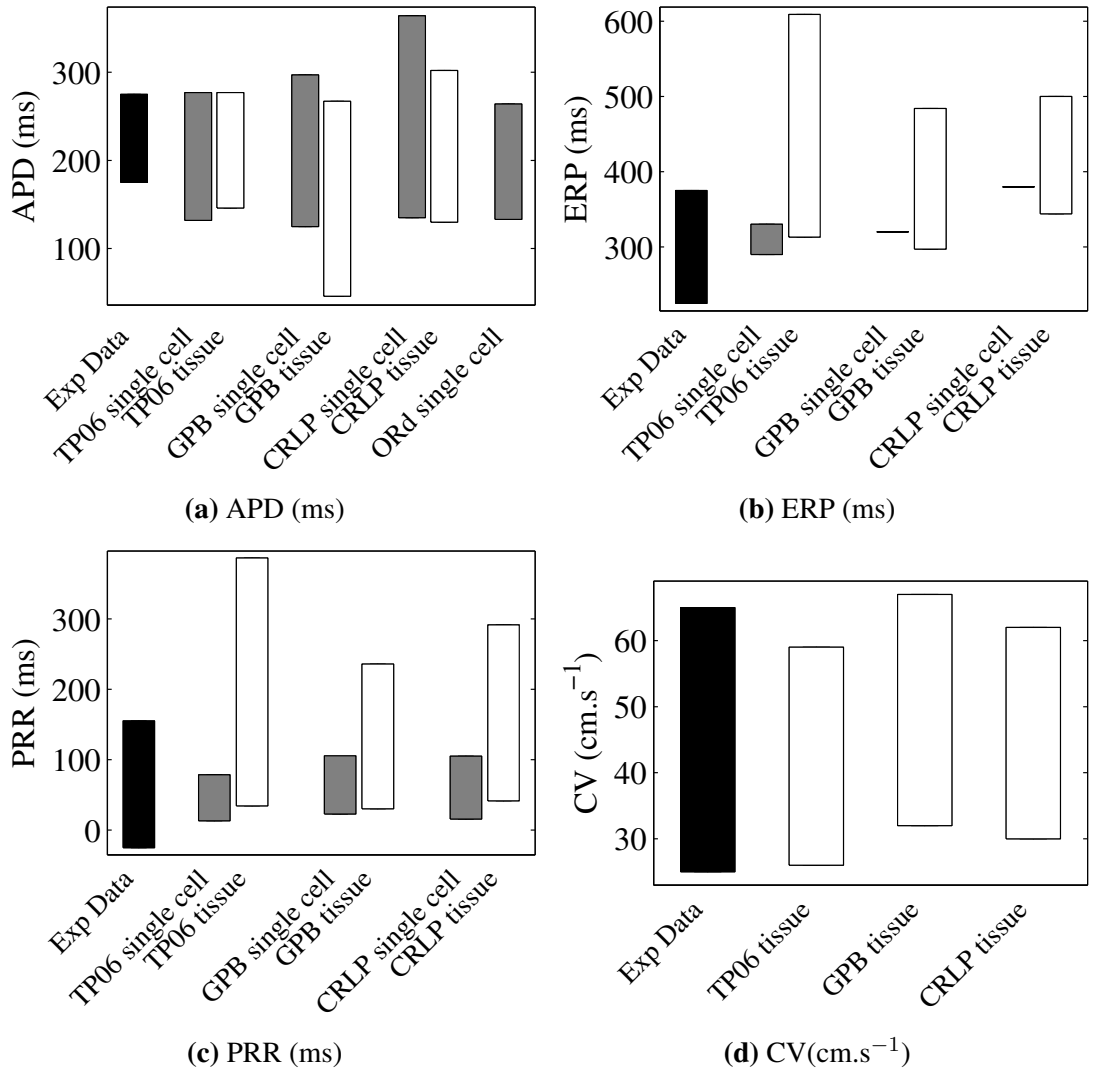

(a) APD (ms)

(b) ERP (ms)

(c) PRR (ms)

(d) CV(cm.s^{-1})

6.5 Discussion

This study investigated the behaviour of 4 recent human models (TP06, GPB, CRLP and ORd) under control and varying ischaemic conditions. This was done by comparing ionic current activity and biomarkers related to arrhythmic risk (APD, PRR, ERP and CV) in single cell and tissue by varying $[K^+]_o$ (4 - 9 mM) and peak $I_{K(ATP)}$ (0 - 20%). Here we analysed the sensitivity of each biomarker in turn and compared it to experimental data. Data in human is limited due to obvious practical and ethical reasons, therefore, whenever human data was not available we used data from animal experiments, such as when analysing ionic current dynamics. To the best of our knowledge, there is no human data available on the ionic effects of $[K^+]_o$ and peak $I_{K(ATP)}$ conductance on biomarkers such as APD, ERP, PRR and CV. However, we do use whole organ *in vivo* data from human carried out by Taggart *et al.* and Sutton *et al.* using electrograms during open chest surgery. In the following sections it is important to keep in mind that the ORd model was only tested in single cell and not in tissue due to its limitations. Furthermore, the GPB model did not reproduce results for $[K^+]_o$ = 9 mM in tissue due to propagation failure while the CRLP and ORd models did.

6.5.1 Limitations of the ORd and GPB models

As shown in Table 6.5 the ORd model did not display a PRR. This is due to differences in the I_{Na} current, which plays an important role in modulating the cell's excitability. As shown in Figure 6.1c the I_{Na} current showed a different morphology to the other 3 models, with a smaller peak that was shifted towards the right. Differences persisted with the ORd AP clamp, as shown in Figure 6.1d. O'Hara *et al.* are aware of this limitation and following a discussion with them, O'Hara added a note in the comments section of the publication on the PloS Computational Biology website, suggesting to replace their formulation of I_{Na} by the TP06 I_{Na} formulation.

The GPB model displayed propagation failure in tissue for $[K^+]_o$ = 9 mM, therefore cells did

not get excited, as labelled in the second row of Table 6.6. This behaviour is not reproduced in single cell simulations (see second row of Table 6.5), and may be due to coupling effects of tissue which create a more pronounced ischaemic environment due to neighbouring ischaemic cells. However, in the ionic current comparison (Section 6.3.2) we can already see that the GPB model is less excitable than the TP06 and CRLP models, with a lower I_{Na} amplitude under ischaemic conditions. The CRLP model, although it is based on the GPB model, does not reproduce the same limitation, as conductances of I_{Na} and I_{NaK}, which affect the cell excitability, were modified. $[K^+]_o$ values in animal experiments after 10-15 min of ischaemia reach values of up to 12 and 14 mM [Kleber, 1983; Watanabe et al., 1997]. However, no data is available on values reached in human hearts. Therefore, we can only assume that they reach similarly high values of $[K^+]_o$. Given the wide variability that exists within a population [Britton et al., 2013; Taneja et al., 2001; Gemmell et al., 2014] and the lack of data in human, it is not known if the propagation failure reproduced by the GPB model for $[\mathrm{K}^+]_\mathrm{o} \geq 9\mathrm{mM}$ is an accurate representation of ischaemia-induced effects in certain patients.

6.5.2 Inherent and ischaemia-induced variability

When discussing these findings, it is important to keep in mind the wide variability that exists at various levels: experimental study set up (such as solutions used and temperatures [Niederer et al., 2009; Quinn et al., 2011]), intra-subject (within the same individual or animal [Dangerfield et al., 2012; Jeyaraj et al., 2012]), inter-species (mice, guinea-pig, human [Harken et al., 1981; Fedorov et al., 2007; Panfilov, 2006]), and across individuals within the same species [Taneja et al., 2001]. Therefore, despite models producing different results, they may all accurately reproduce physiological behaviour.

Furthermore, during ischaemia there are many temporal and spatial heterogeneities that occur. As has been shown experimentally in animal studies, the increase in $[K^+]_o$ and peak $I_{K(ATP)}$ conductance is not always linear through time [Carmeliet, 1999]. Furthermore, the range of

ischaemic parameters simulated in our study reproduces some of the gradients that are observed at the border zone between the ischaemic central area and the healthy tissue. The border zone is a highly heterogeneous region that is prone to ectopic beats and plays an important role in arrhythmogenesis, as shown computationally and experimentally in pig hearts [Bernus et al., 2005b; Coronel et al., 1991]. As described in a pig and canine study carried out by Janse *et al.*, biomarkers can display very different properties in the border zone. For example, the ERP can be slightly shorter than the healthy tissue, compared to the central ischaemic zone, which will have a much longer ERP [Janse et al., 1985]. Shorter ERPs were observed in our simulations as peak $I_{K(ATP)}$ conductance increased.

6.5.3 APD decreases during ischaemia

Both the single cell and tissue results (first column of Tables 6.5 and 6.6) showed that all models reproduced the expected ischaemic APD behaviour. As $[K^+]_o$ and peak $I_{K(ATP)}$ increased, the APD became shorter, with the shortest APD occurring for the highest values of $[K^+]_o$ and peak $I_{K(ATP)}$.

The increased peak $I_{K(ATP)}$ current accelerates the repolarisation process due to an increased outward flux of K^+ ions, therefore decreasing the APD, as has been shown experimentally [Pandit et al., 2011; Carmeliet, 1999]. The single cell study shows that increased peak $I_{K(ATP)}$ conductance induced a decrease of 46%, 50%, 56% and 47% in APD for the TP06, GPB, CRLP and ORd models, respectively. In the tissue study, we saw a decrease of 42%, 48% and 52% for the TP06, GPB and CRLP models, respectively. The effect of varying peak $I_{K(ATP)}$ conductance is more pronounced in the GPB and CRLP models. This may be due to the decreased amplitudes of the repolarising currents I_{Kr}, I_{Ks} and I_{K1} compared to the TP06 and ORd models.

As $[K^+]_o$ increased, the activity of the repolarising currents increased, triggering a decrease in APD, as has been shown in previous animal studies [Coronel et al., 1988; Furukawa et al.,

1991]. The single cell study shows that increased $[K^+]_o$ induced a decrease of 11%, 26%, 24% and 18% in APD for the TP06, GPB, CRLP and ORd models, respectively. In the tissue study, we saw a decrease of 9%, 26% and 28% for the TP06, GPB and CRLP models respectively. Therefore, the APD of the GPB and CRLP models are more sensitive to changes in $[K^+]_o$, which may also be due to the decreased amplitudes of the repolarising currents. However, the TP06 model displays a % change in APD that is closer to the 4% change observed in whole pig hearts by Watanabe *et al.* [Watanabe et al., 1997].

The human study by Sutton *et al.* showed that APD can reach values of almost 180 ms after 3 min of ischaemia, these values are similar to the ones observed in our simulations, as shown in Figure 6.5. Their results show a decrease in APD of about 37% after 3 min of ischaemia. Taking into account the difference in simulated time of ischaemia, our results show a % decrease that is greater than the one observed experimentally after 3 min of ischaemia, both in single cell (52%, 58%, 63% and 50% for TP06, GPB, CRLP and ORd models) and tissue (48%, 83% and 57% for TP06, GPB and CRLP models).

The more pronounced decrease in APD of 83% reproduced by the GPB model in tissue is due to the lack of excitability of the cell, which prevents a full AP from being triggered, (Section 6.5.1) with an APD of just under 50 ms for $[K^+]_o$ = 8 mM and $f_{K(ATP)}$ = 20%. In fact, the GPB model does not propagate for values of $[K^+]_o \geq 9$ mM (as shown in the second row of Table 6.6). Coupling effects present in tissue may produce ischaemic conditions that are more pronounced due to the effect of neighbouring ischaemic cells, that are not present in the single cell study, where the GPB model does reproduce an AP for $[K^+]_o$ = 9 mM.

6.5.4 ERP increases during hyperkalaemia but decreases during hypoxia

In single cell, increased $[K^+]_o$ increased ERP by 17% for the TP06 model and decreased it by 6% and 7% for the GPB and CRLP models. In tissue, it increased ERP by 95%, 47% and 33% for the TP06, GPB and CRLP models. The ERP of the TP06 model is the most sensitive to

changes in $[K^+]_o$. However, hypoxia induced a decrease in ERP (Tables 6.5 and 6.6) as peak $I_{K(ATP)}$ increased due to the decrease in APD. In single cell and tissue there was a decrease of 40% and 41%, 28% and 48%, and 37% and 50% respectively in ERP for the TP06, GPB and CRLP models. These values are similar to the decrease observed in APD.

The differences between single cell and tissue results may be due to the way the ERP is calculated. ERP in single cell represents an S2 value for which the stimulus no longer triggers an AP, while in tissue it represents an S2 value for which the activation wave does not propagate until the end of the tissue. These two methods may explain some of the differences seen between the single cell and tissue ERP results, as the single cell study is highly dependent on the strength of the stimulus applied. Similar mechanisms were observed experimentally by Sutton *et al.*, where they showed no change in ERP during ischaemia for a stronger stimulus strength, the results shown in Figure 6.5b show ERP changes for the smaller stimulus strength. Furthermore, cells at the edge of the ischaemic region may display a reduced ERP [Coronel et al., 2012]. A study by Ma *et al.* on sheep hearts has shown that acute subendocardial ischaemia leads to a reduction in ERP [Ma and Wang, 2007]. Therefore, hyperkalaemia and hypoxia have opposing effects on ERP resulting in very small changes when the two conditions are combined.

6.5.5 PRR increases during ischaemia in all models apart from the ORd

Both the single cell and tissue results (second column of Tables 6.5 and 6.6) showed that all models, apart from the ORd, reproduced an increase in PRR as $[K^+]_o$ increased. The longest PRR occurs for the highest values of $[K^+]_o$ and peak $I_{K(ATP)}$. We will not describe the ORd model as it does not reproduce a PRR. Experimental data has shown that PRR increases significantly under ischaemic conditions, as is described in the review by Coronel *et al.* [Coronel et al., 2012] and in the experimental results carried out by Sutton *et al.*, presented in Figure 6.5 [Sutton et al., 2000].

The single cell study shows that increased peak $I_{K(ATP)}$ conductance induced an increase in

PRR of 19.4 ms, 1.33 ms and 11.7 ms for TP06, GPB and CRLP models, respectively. In the tissue study, we saw a decrease of 8.9 ms, 15.5 ms and 13.3 ms for the TP06, GPB and CRLP models, respectively. The differences between single cell and tissue results may be due to the way the ERP is calculated as it is defined as the smallest stimulus that triggers propagation in tissue rather than an AP in single cell.

As $[K^+]_o$ increases, the cell's excitability decreases, as has been described in human atrial cells by Taggart *et al.* [Taggart and Slater, 1971]. The single cell study shows that increased $[K^+]_o$ induced a decrease of 79.8 ms, 65.2 ms and 64.2 ms in APD for the TP06, GPB and CRLP models, respectively. In the tissue study, we saw an increase of 321 ms, 232 ms and 220 ms for the TP06, GPB and CRLP models, respectively. Therefore, both in single cell and tissue simulations, the PRR of the TP06 model is the most sensitive to changes in $[K^+]_o$. In all models, the PRR is more sensitive to changes in $[K^+]_o$ than changes in peak $I_{K(ATP)}$ conductance as $[K^+]_o$ has a greater effect on cell excitability.

6.5.6 CV changes during hyperkalaemia

CV was only calculated in tissue as it is a measure of how quickly the activation wave propagates from cell to cell. As shown in the last column of Table 6.6, CV is significantly slower for high values of $[K^+]_o$, reaching values close to 0.03 $\mathrm{cm.ms^{-1}}$. Experiments carried out by Taggart *et al.* in human showed CV control values ranging from 0.05 to just under 0.07 $\mathrm{cm.ms^{-1}}$ [Taggart, 2000]. After 3 min of ischaemia, Taggart *et al.* presented CV values of 0.027 $\mathrm{cm.ms^{-1}}$. As shown in Figure 6.5 results from our simulations are in agreement with their experimental results. This sensitivity analysis shows that CV is more sensitive to $[K^+]_o$ than to the repolarising current $I_{K(ATP)}$ (last column of Table 6.6); this is expected as CV is not directly affected by repolarisation.

6.6 Conclusions

In this chapter, a systematic analysis is performed to investigate the use of recent human AP models for studies of ischaemia. The results present the sensitivity of some important arrhythmic biomarkers (APD, ERP, PRR and CV) to variations in two of the main electrophysiological ischaemic parameters (an increase in $[K^+]_o$ and peak $I_{K(ATP)}$) in four recent human ventricular AP models (TP06, GPB, CRLP and ORd) using single cell and tissue simulations. We show that the TP06 and CRLP models show good agreement with experimental data, while the ORd and GPB models do not reproduce some experimentally observed ischaemic changes.

We observed that all models exhibited the expected decrease in APD under ischaemia in single cell and tissue, as well as an increase in PRR, apart from the ORd model. ERP decreased in all models as peak $I_{K(ATP)}$ increased due the decrease in APD, while this effect was counteracted by the increase in $[K^+]_o$, which makes the cell less excitable. Furthermore, CV decreased as $[K^+]_o$ increased in all models. These values lie within the physiological range taking into account the difference in time of simulated ischaemia (3 min in the experiments and 10 min in the simulations). The ORd model did not display the expected changes in PRR due to its I_{Na} specification. Secondly, the GPB did not show propagation for $[K^+]_o$ = 9 mM, due to the greater sensitivity of the GPB model to ischaemic conditions. This was reflected at the ionic current level as the decrease in I_{Na} amplitude under ischaemia was the greatest in the GPB model.

Results from this study are useful for the selection of a cell model to perform human-specific simulations of myocardial ischaemia. They demonstrate the importance of considering multiple biomarkers at both the single cell and tissue levels simulations to assess the applicability of cell models. Finally, this study provides important insights into the behaviour of the tested models under varied ischaemic conditions, expanding our knowledge of their greater utility. Overall, this work represents an important stepping stone in our pursuit to uncover arrhythmic mechanisms during ischaemia in human.

Chapter 7

Investigating anti- and pro-arrhythmic effects of hERG block in human regionally ischaemic ventricles

The purpose of this study is to investigate mechanisms underlying hERG block modulation of reentrant arrhythmias during regional acute ischaemia in a human whole ventricles model. Following our assessment of human ventricular models under varying ischaemic conditions in the previous chapter, we chose to use the TP06 model to extend our ischaemia investigation to drug cardiotoxicity in the human whole ventricles. Mechanisms underlying cases of increased mortality associated with hERG blockers in ischaemic patients are poorly understood. The lack of understanding results from the absence of high spatio-temporal experimental data on arrhythmic mechanisms in human due to practical and ethical limitations. In this chapter we present a biophysically-detailed human whole ventricles computational model of regional ischaemia built from the work presented in the previous chapters. Our results provide valuable insight into pro- and anti-arrhythmic mechanisms of hERG blockers.

7.1 Introduction

As introduced in Section 2.7, class III anti-arrhythmic drugs are first line therapy for patients suffering from abnormal atrial and ventricular rhythms [Wazni et al., 2005], often prescribed in combination with electrical therapy [Van Herendael et al., 2010]. Their anti-arrhythmic mode of action is known to be prolongation of repolarisation and increase of the wavelength for re-entry due to K^+ channel block [Williams, 1984; Nademanee et al., 1985]. However, as discussed in Section 3.4, recent studies have raised safety concerns in patients with coronary heart disease, as they show that class III drugs result in increased risk of longer-term hospitalisation and death in such patients [Steinberg et al., 2014]. Studies, such as Survival With ORal D-Sotalol (SWORD) trial, also demonstrate that administration of the hERG (human Ether-à-go-go Related Gene) blocker sotalol was associated with increased mortality in patients suffering from recent myocardial infarction, associated with ischaemic heart disease [Waldo et al., 1996]. Drug electrophysiological cardiotoxicity due to hERG block is a main concern and the most restricting factor in the development and application of both cardiac and non-cardiac drugs [Sanguinetti and Tristani-Firouzi, 2006]. Dissecting key underlying mechanisms, particularly in patients with an existing pro-arrhythmic substrate, is urgently needed to improve patient risk stratification, management, and development of improved anti-arrhythmic therapy.

The vast majority of sudden cardiac death patients suffer from coronary heart disease and myocardial ischaemia, i.e. a mismatch between oxygen supply and demand [Myerburg and Junttila, 2012]. In coronary heart disease patients, acute myocardial ischaemia can occur due to complete or partial coronary artery occlusion, or due to increased demand caused, for example, by exercise. As reviewed in Section 2.5, myocardial ischaemia alters the biophysical ionic processes of ventricular cells such as ionic currents and concentrations due to hyperkalaemia, hypoxia, and acidosis [Carmeliet, 1999]. At the tissue level these changes increase the spatio-temporal dispersion in refractoriness, repolarisation, and conduction velocity between healthy and ischaemic regions, which facilitates the onset of arrhythmias leading to sudden cardiac death

[Wilensky et al., 1986; Bernus et al., 2005a; Coronel et al., 1991]. Ischaemic pro-arrhythmic alterations have been investigated in a large number of studies (briefly reviewed in Section 3.5.2) [Wilensky et al., 1986; Coronel et al., 1991; Janse and Wit, 1989; Coronel et al., 1988; Sutton et al., 2000], but few have looked at how the changes are modulated by pharmacological action, and specifically hERG block [Wilhelms et al., 2012; Steinberg et al., 2014]. Furthermore, most studies have been conducted in animals and not human due to obvious ethical and practical reasons of experimental and clinical studies.

The aim of our study was to dissect the pro-arrhythmic and anti-arrhythmic mechanisms underlying hERG block modulation of the electrophysiological arrhythmic substrate induced by acute myocardial ischaemia in the human ventricles. Computer simulations have proven their ability to provide novel insights into mechanisms of electrophysiological arrhythmic events in ischaemia [Bernus et al., 2005a; Heidenreich et al., 2012; Rodríguez et al., 2006] and cardiotoxicity in non-ischaemic hearts [Moreno et al., 2011; Zemzemi et al., 2013], by generating high spatio-temporal resolution data not accessible using experimental methods alone. The present study extends this approach to the investigation of pharmacological action of hERG block in the human ischaemic ventricles.

7.2 Methods

7.2.1 Human whole ventricles model of acute regional myocardial ischaemia

An example of the code developed to run these simulations can be found in Appendix A.2. An anatomically-based, multi-scale model of human regionally-ischaemic ventricles was developed based on extensive experimental recordings from the literature [Spector et al., 1996; Carmeliet, 1999; Edvardsson et al., 1980; Glukhov et al., 2010; Wilensky et al., 1986; Coronel et al., 1988; Sutton et al., 2000; Durrer et al., 1970; Coronel et al., 1991; Lee et al., 1981], including biophysically detailed membrane kinetics, ischaemia induced heterogeneities, cell coupling,

electrotonic current flow, and fibre orientation (based on the Streeter method [Streeter et al., 1969]). The image-based human anatomical mesh contains 2.5 M nodes with 400 μm spatial discretisation, required for convergence of the numerical algorithms [Bernabeu et al., 2010b]. Intracellular conductivities were set to 5.25 mS/cm in the preferential direction and 0.57 mS/cm in the other directions. This induced a conduction velocity of about 60 cm/s in the normal tissue and a slowed conduction velocity of about 40 cm/s in the ischaemic region, these values are within experimental range [Taggart, 2000]. We apply zero flux Newmann boundary conditions [Pathmanathan et al., 2010b].

Human ventricular membrane kinetics were simulated with the ten Tusscher 2006 action potential model (TP06) [ten Tusscher and Panfilov, 2006], which has been extensively used in similar studies [Moreno et al., 2011; Zemzemi et al., 2013; Wilhelms et al., 2012]. The model choice was based on its suitability to simulate ischaemic electrophysiological alterations in human, as argued in Chapter 6 [Dutta et al., 2013]. The $I_{K(ATP)}$ current was included in the TP06 model, as defined in Equation (4.21) [Michailova et al., 2005].

Both clinical and experimental studies have shown the existence of transmural electrophysiological heterogeneities in APD ranging from 10 - 20 ms *in vivo* [Taggart et al., 2001] to 100 ms *in vitro* in human [Glukhov et al., 2010], which may have a pro-arrhythmic role [Kuo et al., 1983]. Transmural differences in I_{Ks} were therefore included as proposed in [Péréon et al., 2000; Xu et al., 2001], by applying a 6:4 ratio in I_{Ks} maximal conductance of 0.098 nS/nF and 0.392 nS/nF, as defined by the TP06 model [ten Tusscher and Panfilov, 2006]. As the existence of longer subendocardial APD remains controversial [Glukhov et al., 2010; Taggart et al., 2001; Péréon et al., 2000; Xu et al., 2001], a linear transmural APD gradient from endocardium to epicardium was imposed, with the longest APD at the endocardium [Glukhov et al., 2010; Taggart et al., 2001]. The APD gradient was 17% of the maximum APD, which is between values of 10% obtained by Taggart *et al.* from *in vivo* human studies [Taggart et al., 2001] and 24% obtained by Glukhov *et al.* from *in vitro* human wedge preparations [Glukhov et al., 2010]. The

gradient chosen led to the physiological inverse repolarisation time (RT) - activation time (AT) relationship described in *in vivo* human hearts [Franz et al., 1987] and intact dog hearts [Spach and Barr, 1975], and a physiological simulated pseudo-ECG, with a QT interval of $\sim$400 ms and a positive T-wave described *in vivo* human hearts and computational simulations [Gima and Rudy, 2002; Franz et al., 1987].

7.2.2 Biophysical model of the ischaemic region

Size and location of ischaemic regions vary from individual to individual. Lee *et al.* reported infarct size range values of 13 to 72% of the human LV [Lee et al., 1981]. Therefore, location and size of regional ischaemia in our model was chosen to affect $\sim$40% of the LV, in the middle of this range, and defined as an ellipsoid of radius 3 cm (Figure 7.1a). In agreement with [Wilensky et al., 1986; Coronel et al., 1991; Heidenreich et al., 2012; Rodríguez et al., 2006; Lee et al., 1981] and as reviewed in Section 3.2, heterogeneities in the ischaemic region due to diffusion between the ischaemic and normal tissue were also represented through the inclusion of a lateral ischaemic border zone (BZ) of width 0.5 cm and a layer of healthy endocardial cells of width 0.1 cm.

In the ischaemic central zone (ICZ), the ionic changes caused by the three main components of acute ischaemia (namely hyperkalaemia, hypoxia and acidosis) were introduced as in [Wilensky et al., 1986; Coronel et al., 1991; Heidenreich et al., 2012; Rodríguez et al., 2006]. Based on previous experimental and computational studies on the pro-arrhythmic mechanisms of acute ischaemia [Carmeliet, 1999; Janse and Wit, 1989; Rodríguez et al., 2006], we applied a degree of ischaemic severity that corresponds to highest arrhythmic risk, as examined in Section 2.5. Therefore, cells were assigned an increase in $[K^+]_o$ of 8.5 mM, an increase in peak conductance of $I_{K(ATP)}$ of 5% caused by hypoxia, and a decrease in peak conductance of I_{Na} and I_{CaL} of 25% due to acidosis [Wilensky et al., 1986; Coronel et al., 1988; Rodríguez et al., 2006]. The conditions applied reproduced expected changes in the human AP, namely increased resting

transmembrane potential, V_m, decreased V_m upstroke velocity, and shortened APD [Heidenreich et al., 2012; Rodríguez et al., 2006; Bernus et al., 2005a] (Figure 7.1). To approximate the gradients seen experimentally, the lateral BZ included a linear gradient in electrophysiological properties from the ICZ to the normal zone (NZ) [Wilensky et al., 1986; Coronel et al., 1988]. Given uncertainties surrounding the existence *in vivo* of the epicardial BZ, it was not included in our model, as in [Rodriguez et al., 2006; Heidenreich et al., 2012].

7.2.3 hERG block model

The effect of class III anti-arrhythmic drugs in the human regionally-ischaemic ventricles was simulated by decreasing the conductivity of I_{Kr} [Spector et al., 1996]. Using a simple pore block model [Brennan et al., 2009] with a Hill coefficient of 1, simulations were conducted using two simulated doses of I_{Kr} blocker corresponding to a drug concentration of 43% of IC50 (30% block) and 100% of IC50 (50% block).

7.2.4 Simulation protocol

Purkinje-like activation was simulated by stimulating regions of the endocardium shown by Durrer *et al.* in human to display the earliest activation [Durrer et al., 1970]. In agreement with their findings, our ventricles took 63 ms to fully depolarise. Two initial stimuli (S1) were applied with a cycle length of 800 ms. To trigger re-entry, a fully transmural premature excitation (S2) was applied to a region of 2 cm radius close to the apex covering NZ, BZ and ICZ, a region prone to premature excitation [Bernus et al., 2002; Coronel et al., 2002]. The vulnerability window (VW) of re-entry was the range of coupling intervals (CI) that resulted in re-entry (calculated with 1 ms precision around its boundaries). Over 150 simulations were conducted with the software Chaste [Mirams et al., 2013] using 1024 processors on HECToR, the UK's national supercomputer. It took approximately 6 h of supercomputing time to simulate 800 ms of cardiac electrical activity on the anatomically-accurate human whole ventricles mesh.

7.2.5 Data analysis

The electrical activity of the human ventricles was visualised both locally through V_m at each node and globally through the pseudo-ECG, as described below. Times labeled (in ms) in the figures showing the distribution of V_m are defined by setting 0 ms as the time of application of the premature S2 beat. The APD map, was calculated as the interval between activation of the node and the time at which it reached 90% repolarisation.

The pseudo-ECG is defined as the following integral over the mesh:

$$\phi(\mathbf{r}') = D \int \left(\nabla V_m \cdot \left(\nabla \frac{1}{||\mathbf{r} - \mathbf{r}'||} \right) \right) d\mathbf{r} \tag{7.1}$$

where **r**' = (x', y', z') are the electrode coordinates, **r** =(x, y, z) represent the source points and D is the diffusion tensor [Gima and Rudy, 2002]. As in the ECG (introduced in Section 2.8.1), the pseudo-ECG exhibited QRS complexes during ventricular activation and T waves during ventricular repolarisation, mimicking the ECG shape. The QT interval was calculated as the time interval between the earliest activation and the complete repolarisation of the ventricles.

7.3 Results

7.3.1 Sinus rhythm during regional ischaemia

Figure 7.1 illustrates the human anatomically-based electrophysiological model of regionally-ischaemic whole ventricles. Figure 7.1a shows the distribution of resting V_m on the LV epicardium with the ICZ exhibiting the highest resting V_m of about -70 mV due to increased $[K^+]_o$, in agreement with [Carmeliet, 1999]. The NZ has a normal resting V_m of -86 mV, with a gradient displayed in the BZ between the two regions. Figure 7.1b shows the APD map throughout the human ventricles after the second S1 stimulus, along with AP traces of epicardial cells from the ICZ and NZ. APDs in the ICZ are about 30% shorter than in the NZ, in agreement with a

35% difference reported in human *in vivo* measurements [Sutton et al., 2000], due to the effects of $I_{K(ATP)}$ activation and elevated $[K^+]_o$. The increase in resting V_m and shortened APD in the ICZ in the model therefore agree with previous *in vivo* human and *ex situ* animal studies [Carmeliet, 1999; Sutton et al., 2000; Wilensky et al., 1986; Taggart et al., 2001].

Figure 7.1c depicts the AT map in the human ventricles during sinus rhythm, along with the transmural RT - AT relationship in the NZ of the LV. The total activation time of 63 ms is in agreement with data in isolated human hearts [Durrer et al., 1970] and the inverse RT - AT relationship with data from *in vivo* human hearts and intact dog hearts [Spach and Barr, 1975; Franz et al., 1987]. The agreement of our simulation results with a variety of experimental reports lends credibility to our human regionally-ischaemic model and the simulation results reported below.

7.3.2 Effects of hERG block on sinus rhythm during regional ischaemia

Figure 7.2a shows the pseudo-ECG generated by the human regionally-ischaemic whole ventricles model for 0, 30 and 50% hERG block. The QT interval using the baseline human ischaemic ventricular model is 414 ms, in line with clinical reports [Browne et al., 1983; Yamaguchi et al., 2003], and it is prolonged by 5% for 30% hERG block and 9% for 50% hERG block. Therefore, in agreement with previous studies in non-ischaemic patients, hERG block increases the overall RT of the ventricles [Nademanee et al., 1985; Edvardsson et al., 1980]. Figure 7.2b shows the transmural APD gradient across the LV in the NZ, which is linear in all three scenarios, with the shortest APD in the epicardium and the longest APD in the endocardium, as has been shown in both *in vivo* and *ex situ* human studies [Glukhov et al., 2010; Taggart et al., 2001]. The APD transmural gradient in the NZ increases from 17% to 19% as the degree of hERG block increases to 30 and 50%, respectively.

The prolongation of the QT interval caused by hERG block is due to an overall prolongation of APD across the human regionally-ischaemic ventricles as illustrated in Figure 7.3 for the

Figure 7.1 Computational model of human regionally-ischaemic whole ventricles. Distribution of transmembrane voltage (V_m), on the epicardium of the LV and a cross section of the ventricles at resting state showing the ischaemic central zone (ICZ), the ischaemic lateral and endocardial border zone (BZ) and the normal zone (NZ) (a). Action potential duration (APD) map of a cross section of the ventricles and action potential (AP) traces from the ICZ and NZ (b). Activation time (AT) map of a cross section of the ventricles along with the transmural repolarisation time (RT) - AT relationship in the NZ (c).

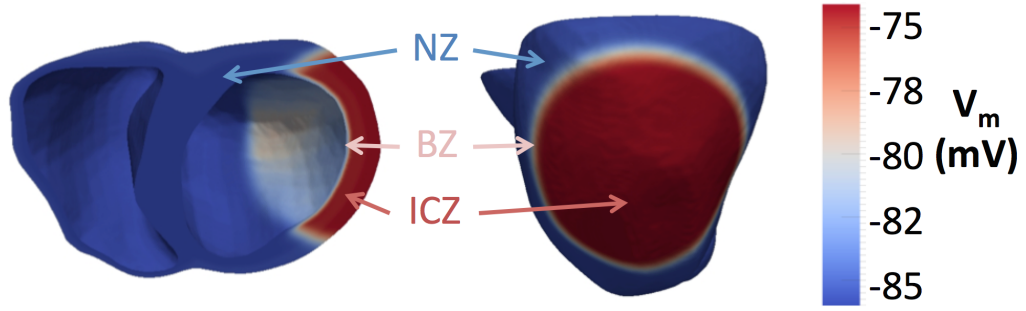

(a) Transmembrane voltage (mV)

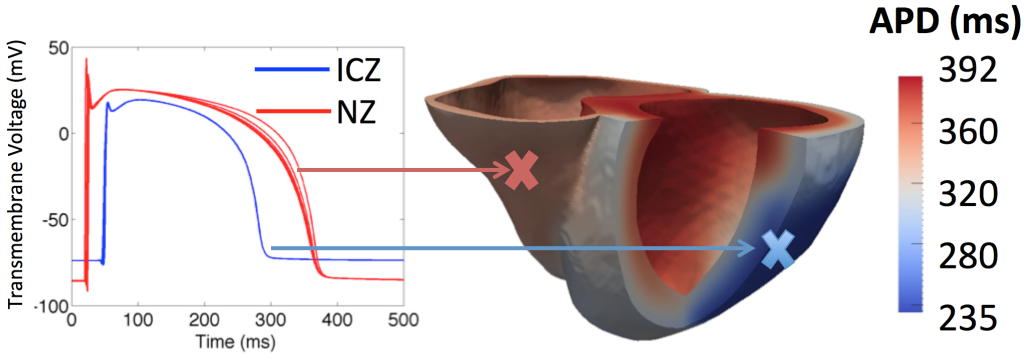

(b) APD (ms) map and AP trace from the ICZ and NZ

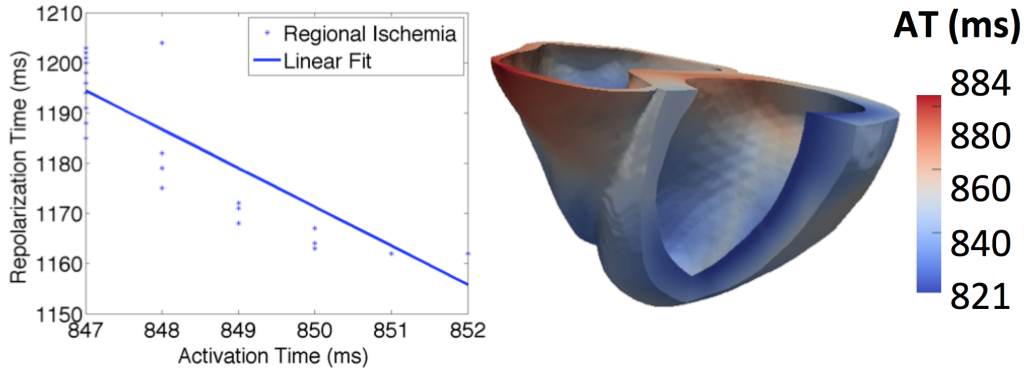

(c) AT (ms) map and RT-AT relationship in the NZ

different hERG doses. The average APD prolongation induced by hERG block is greater in the NZ (16 and 28 ms for 30 and 50% hERG block) than in the ICZ (12 and 20 ms).

Importantly, our results also show an increase in dispersion of APD as the degree of hERG block increases. The range of APD values increases from 156 ms in regional ischaemia to 175 ms with 50% hERG block. Therefore, hERG block further enhances the spatial dispersion of APD caused by regional ischaemia in the human ventricles. This may contribute to the substrate for reentry and may counteract the known anti-arrhythmic mechanism of APD prolongation caused by hERG block.

Figure 7.2 Effect of hERG block on the pseudo-ECG (a) and transmural action potential duration (APD) gradient in the normal zone (NZ) where the dots represent the simulation results and the solid line is the corresponding best fit (b) in our model of human regionally-ischaemic whole ventricles without hERG block (blue) and with 30% (green) and 50% (red) hERG block.

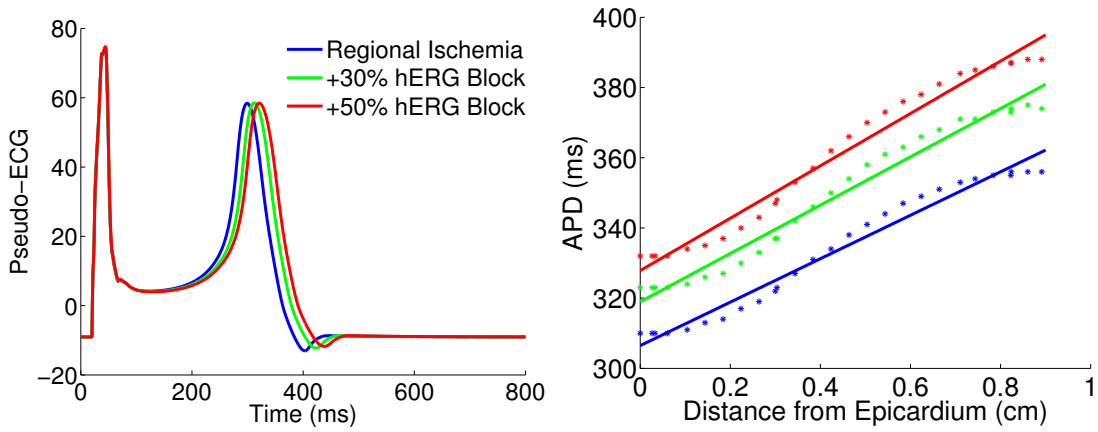

(a) Pseudo-ECG **(b)** Transmural APD gradient in the NZ

7.3.3 Anti-arrhythmic effects of hERG block decrease the VW

In order to evaluate modulation of arrhythmia propensity by hERG block in acute ischaemia, simulations were conducted to determine the VW for re-entry in the human regionally-ischaemic ventricles for increasing degrees of hERG block. Figure 7.3b shows that the VW is 85 ms in regional ischaemia, and it decreases by 24% to 65 ms with 30% hERG block, and then increases to 80 ms with 50% hERG block. Thus, the change in the VW with hERG block is biphasic and

dose-dependent. The reduction of the VW by 30% hERG block represents a cardio-protective mechanism, as the time frame for re-entry inducibility by extra stimulus is decreased. However, for 50% hERG block, VW is wider than for 30% hERG block (although 6% narrower than in control), indicating that additional pro-arrhythmic mechanisms may arise with further increase in hERG dose.

Figure 7.3 Action potential duration (APD) distribution and vulnerability window (VW) calculated in our model of human regionally-ischaemic whole ventricles without hERG block (blue) and with 30% (green) and 50% (red) hERG block, presented as a contour plot of the APD distribution histogram (a) and as a boxplot of APD and VW values (b).

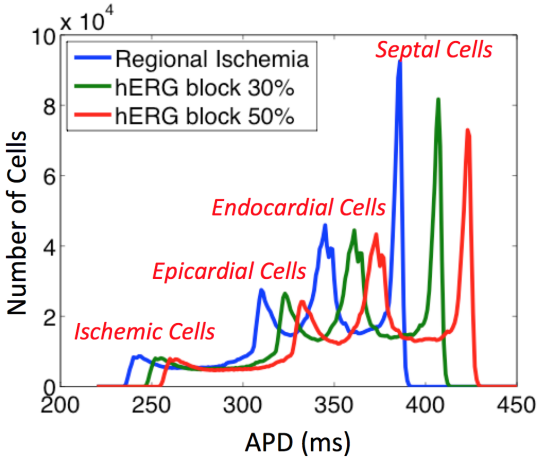

(a) Contour plot of the APD distribution histogram

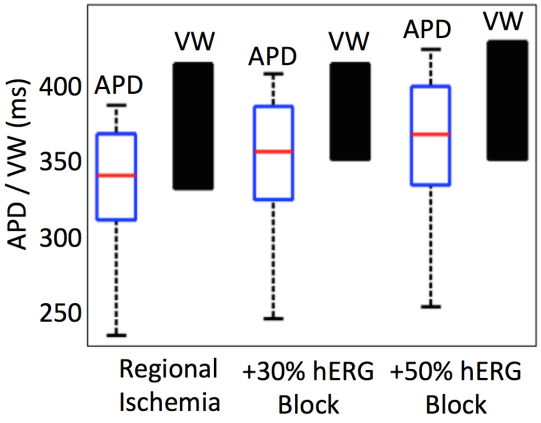

(b) Boxplot of APD distribution and VW

7.3.4 hERG block decreases likelihood of figure-of-eight re-entry during regional ischaemia

Figure-of-eight re-entry is established in the regionally-ischaemic human ventricles following premature excitation in the BZ during the VW, for all hERG block doses. The establishment of the re-entry includes 3 main phases, previously described in [Janse and Wit, 1989] and illustrated in Figure 7.4: (1) conduction block in the ICZ due to prolonged refractoriness and slow propagation through the BZ, (2) retrograde propagation through the ICZ following recovery, and (3) re-entry through the NZ. Figure 4 presents similar episodes of re-entry for 0 and 30% block (panels A and B, respectively). In both cases, conduction block occurs in the ICZ

Figure 7.4 Figure-of-eight re-entry in our model of human regionally-ischaemic whole ventricles without hERG block (a) and with 30% hERG block (b). Distribution of V_m on the LV epicardium and a diagram of the wavefront activity, at 100 ms intervals, 500 ms after a premature excitation with a coupling interval of 350 ms (a) and 360 ms (b). Corresponding pseudo-ECGs are shown. Times colored in grey are defined by setting 0 ms as the time of application of the premature excitation. Dashed gray lines surround the ICZ. The white arrows show the pathway of the excitation wave front. The colour scale is saturated, such that potentials above 20 mV and below -90 mV appear in red and blue, respectively.

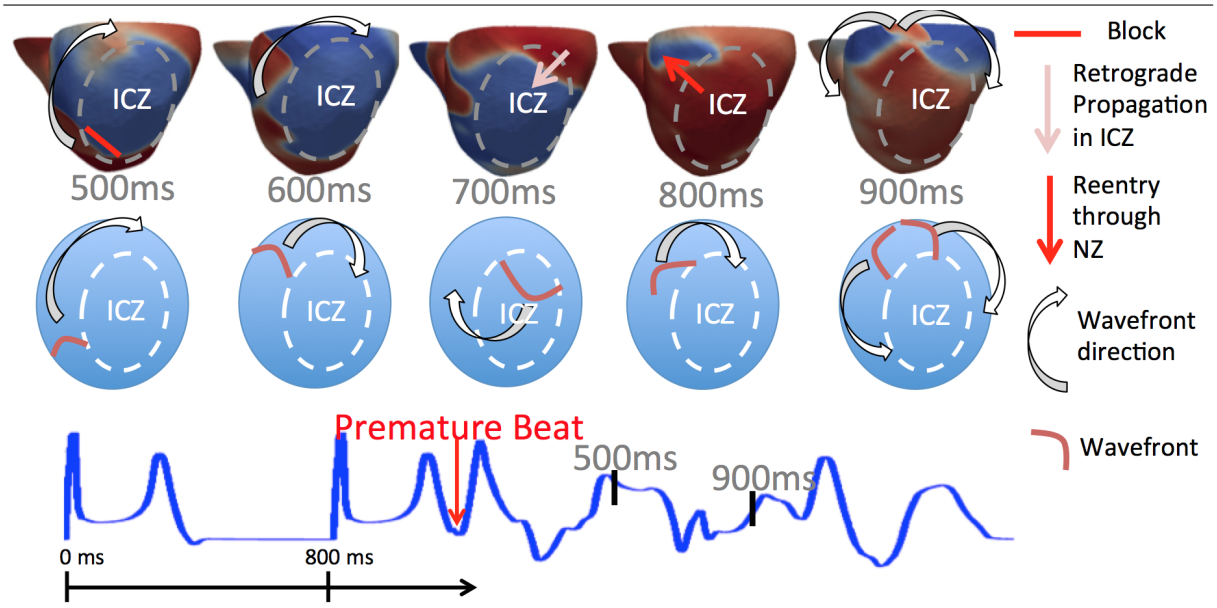

(a) Regional Ischaemia

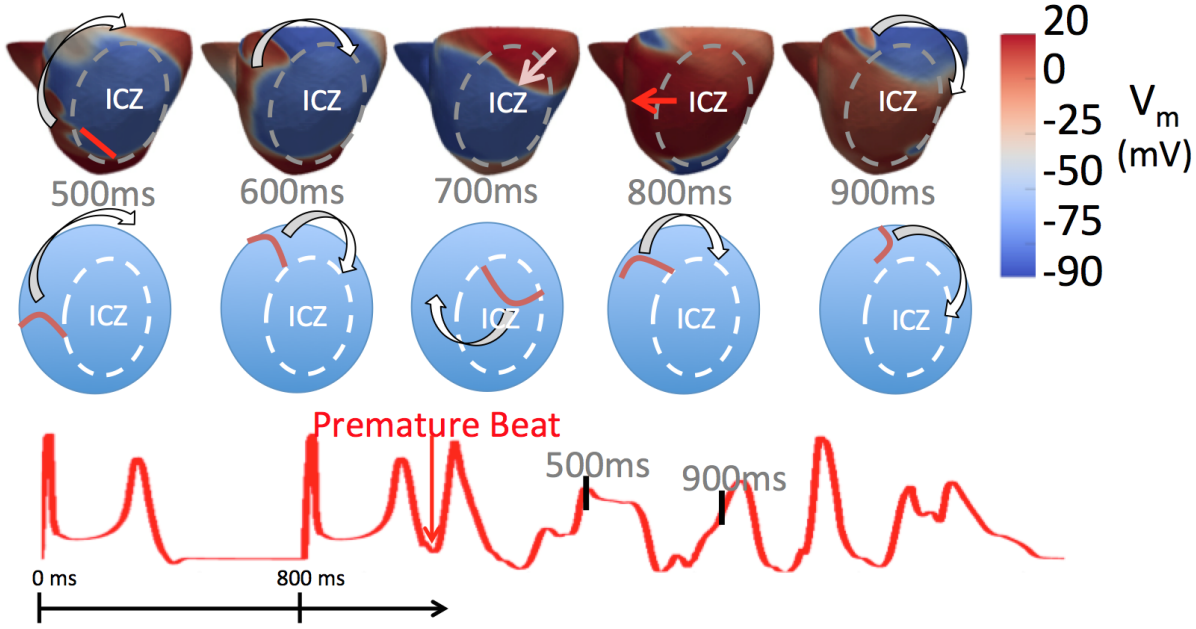

(b) +30% hERG Block

(snapshots 500 and 600 ms following premature stimulation, for 0 and 30% hERG block, respectively). Retrograde propagation occurs through the ICZ at similar locations close to the base of the ventricles (snapshot 700 ms following premature excitation), and establishment of re-entry through the BZ in both cases (snapshot 900 ms following premature excitation).

Figure 7.5 Anti-arrhythmic mechanisms of 30% hERG block in our model of human regionally-ischaemic whole ventricles. Distribution of V_m on the LV epicardium at different intervals ((a) 100 ms and (b) 60 ms) after two premature S2 beats applied at 350 ms (a) and 425 ms (b) after the previous S1.

(a) Reentry fails in the ICZ

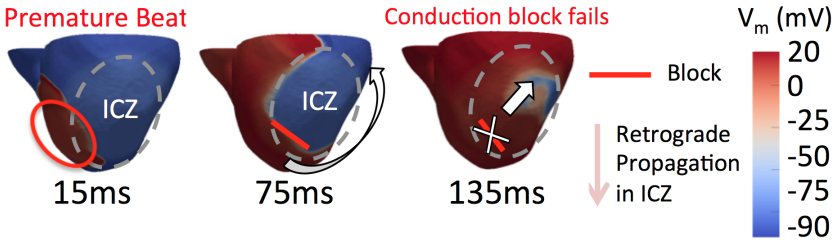

(b) Conduction block fails

Figure 7.5 illustrates the mechanisms by which the APD prolongation induced by hERG block both in the ICZ and NZ is responsible for decreasing the likelihood of establishment of re-entry, and therefore, for reducing the VW for 30% hERG block (Figure 7.3). Figure 7.5a shows the evolution of electrophysiological activity in the human regionally-ischaemic ventricles after a premature excitation applied at $\mathrm{CI} = 350$ ms (i.e. close to the lower bound of the VW). Following conduction block in the ICZ, propagation progresses around the ICZ (snapshot 110 ms). However, retrograde propagation through the ICZ fails, as ischaemic tissue is still refractory, and this is facilitated by prolongation of APD caused by hERG block (snapshot 210 ms). Figure 7.5b illustrates results of a similar simulation, but for premature excitation applied at long

$\mathrm{CI} = 425$ ms (i.e. close to the upper bound of the VW). Conduction block occurs initially (snapshot 75 ms), and leads to propagation around the ICZ. However, ICZ tissue recovers before the wave reaches the basal part of the ICZ. This mechanism was not observed without hERG block, therefore, results suggest this is due to the prolonged APD that allows more time for the ICZ to recover and be re-excited. Prolongation of repolarisation caused by hERG block in the NZ therefore reduces the probability of establishment of figure-of-eight reentry in the regionally-ischaemic ventricles for 30% hERG block.

7.3.5 hERG block generates pro-arrhythmic transmural pathways of re-entry

In order to investigate the increase in the VW with 50% compared to 30% hERG block, we further examined re-entry episodes as illustrated in Figure 7.6. While the main figure-of-eight re-entry around the ICZ is similar for all doses of hERG block, new pathways of transmural re-entry are observed at the BZ with 50% hERG block. As shown in Figure 7.6a, the epicardium is still refractory after the preceding figure-of-eight reentry cycle has completed, 1020 ms following premature excitation. However, the prolongation of APD in neighbouring endocardial tissue provides the stimulus required to sustain propagation and create a transmural pathway of re-entry. Our results show that an increase in transmural dispersion of APD of as little as 20 ms can facilitate the creation of new pathways for reentry. However, the transmural dispersion of APD that occurs with 30% or without hERG block does not provide a substrate for establishment of transmural re-entry. Figure 7.6b illustrates schematically the mechanisms by which increased dispersion in APD induced by 50% hERG block favour re-entry. The time course of APs for a site of early activation, represented in black, and a site of late activation, in red, show that the site of early activation is recovering when propagation attempts to reenter through the site of late activation. With low transmural dispersion in APD (such as for 0 and 30% hERG block, solid lines), the establishment of re-entry is prevented by the wave encountering refractory tissue. However, for increased repolarisation gradient, as for 50% hERG block (dashed

lines), long APD in the site of late activation provides the stimulus required for the area of early activation to recover and be stimulated again.

In support of the mechanisms described above, Figure 7.7a shows a cross section of the human model in which the difference in APD between 0 and 50% hERG block, ΔAPD50%-0%, is displayed throughout the ventricular tissue. The figure demonstrates an enhancement of the transmural dispersion of APD with increased hERG block. The increase in APD induced by hERG block is greater in the endocardial BZ (more than 30 ms) than in the ischaemic region (less than 20 ms). Defibrillation therapy studies in non-ischaemic hearts have also reported transmural reentry pathways induced by increased transmural dispersion of APD [Ashihara et al., 2008; Maharaj et al., 2008]. Similar mechanisms are observed in our study, where the increased dispersion is induced by hERG block instead of the shock-induced polarisation. Figure 7.7b shows that the transmural APD gradient in the BZ increases by 10 ms as the degree of hERG block increases from 0% to 50%. Therefore, hERG block contributes to further enhance the transmural gradient in repolarisation around the ischaemic border zone, thus facilitating the establishment of additional pathways for reentry.

7.4 Discussion

This computational study investigates anti- and pro-arrhythmic mechanisms of class III anti-arrhythmic agents in acute regional ischaemia using a biophysically-detailed anatomically-based model of the human whole ventricles. Our main findings are: (a) hERG block leads to anti-arrhythmic prolongation of APD, which reduces arrhythmia propensity in acute regional ischaemia, manifested in a decrease in the VW for re-entry, (b) hERG block however increases the inhomogeneities in APD in a dose dependent manner, (c) these heterogeneities contribute to the regional ischaemic pro-arrhythmic substrate, facilitating secondary transmural re-entrant pathways at the ischaemic border zone with higher doses of hERG block. The computational investigations presented in this study can be extended to explore mechanisms under different con-

Figure 7.6 Transmural pathways of re-entry generated by 50% hERG block in our model of human regionally-ischaemic whole ventricles. Distribution of V_m on the LV epicardium at 20 ms intervals after a premature excitation with a coupling interval of 361 ms (a). Times are defined by setting 0 ms as the time of application of the premature excitation. Schematic representation of mechanisms underlying hERG block induced transmural pathways of re-entry mediated by the dispersion of APD prolongation (b). The solid lines represent AP traces during regional ischaemia without hERG block and the dashed lines represent action potential traces with 50% hERG block.

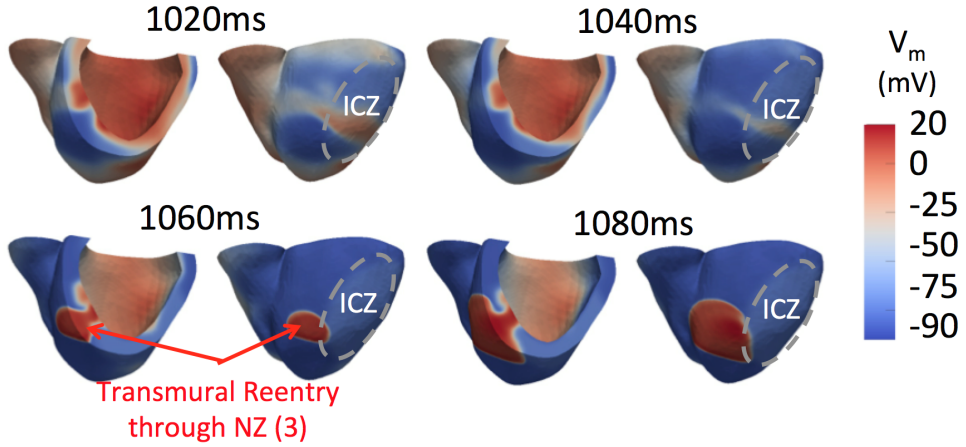

(a) Transmural reentry for +50% hERG block

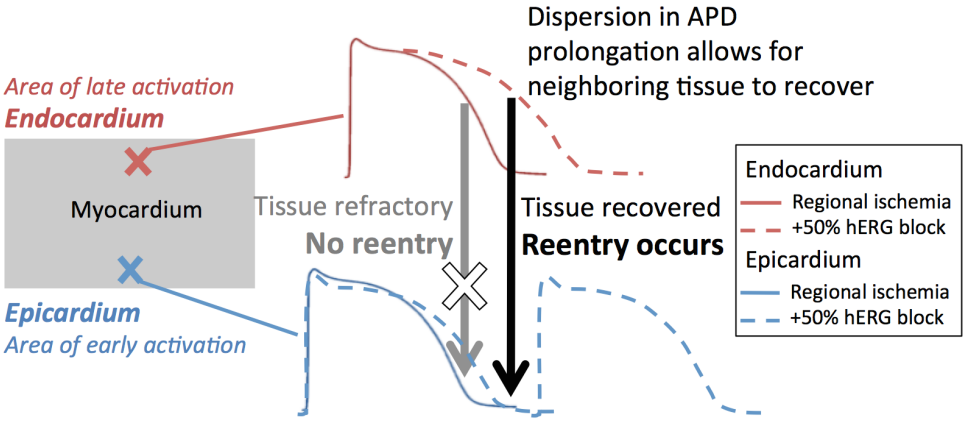

(b) Diagram of transmural reentry mechanism

Figure 7.7 Transmural dispersion of APD in our model of human regionally-ischaemic whole ventricles. Distribution of the difference in APD between 0 and 50% hERG block (ΔAPD50%-0%) (a). Dashed white lines surround the ICZ. The colour scale is saturated, such that values above 30 ms and below 20 ms appear in red and blue, respectively. Transmural gradient of APD in the border zone (BZ), where the dots represent the simulation results and the solid line is the corresponding best fit, without hERG block (blue) and with 30% (green) and 50% hERG block (red) (b).

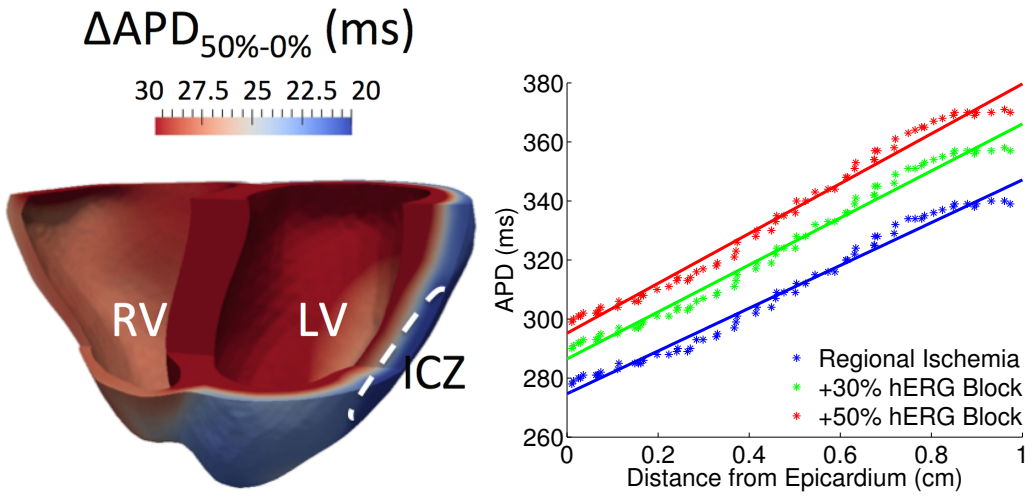

(a) Δ APD50%-0% **(b)** Transmural APD gradient in the BZ

ditions, such as varying sizes and locations of the ischaemic region, different drug compounds and their multi-channel effects, and inter-subject variability in ionic currents and repolarisation patterns. We expect the new insights provided here could help in the design of further experimental and clinical studies to improve patient risk stratification, using ECG-based biomarkers of transmural dispersion of APD derived from T-wave characteristics, and decisions about drug dose during management of anti-arrhythmic therapy.

7.4.1 Computational model of the human regionally-ischaemic ventricles and drug block

For this study, a novel human whole ventricle model was developed that includes representation of pro-arrhythmic alterations induced by acute regional myocardial ischaemia, which results in figure-of-eight re-entry. Simulation results using our model were compared against experimental data from the literature to evaluate and lend credibility to the model, and therefore support

our theoretical findings.

Simulations using the human ischaemic model reproduced the following physiological properties, reported in both *in vivo* and *ex situ* human studies: a transmural gradient in APD values (Figure 7.2b) [Glukhov et al., 2010; Taggart et al., 2001], an inverse RT-AT relationship (Figure 7.1c) [Spach and Barr, 1975; Franz et al., 1987], ischaemia-induced changes in AP morphology (Figure 7.1b) [Bernus et al., 2005a; Heidenreich et al., 2012; Rodríguez et al., 2006], size of the ischaemic region (Figure 7.1a) [Lee et al., 1981], and a pseudo-ECG with QT interval of 414 ms and a positive T-wave with a T-peak to T-end value of about 100ms (Figure 7.2b) [Browne et al., 1983; Yamaguchi et al., 2003]. Furthermore, in our simulations, figure-of-eight re-entry was established in the human ischaemic ventricles following ectopic excitations occurring during the VW, as demonstrated experimentally in pigs in the classical studies by Janse *et al.* and Coronel *et al.* [Janse and Wit, 1989; Coronel et al., 2002] and also computationally using the Luo Rudy dynamic model [Bernus et al., 2005a].

7.4.2 Prolongation of APD by hERG block is anti-arrhythmic in regional ischaemia

Our results agree with human studies showing an increase in APD and QT interval with hERG block [Waldo et al., 1996; Edvardsson et al., 1980; Suttorp et al., 1990; Nademanee et al., 1985]. An increase in monophasic APD of between 13-17% and in QT interval of about 10% with a sotalol drug dose of 40-100 mg and 160-480 mg has been reported in non-ischaemic patients [Nademanee et al., 1985; Edvardsson et al., 1980]. These values are similar to the 9% increase in APD and QT for 50% hERG block in our model (Figures 7.2 and 7.3).

Previous studies, which do not include ischaemic conditions, have shown that the protective mechanism of class III anti-arrhythmic agents act through increasing the APD [Edvardsson et al., 1980; Suttorp et al., 1990; Nademanee et al., 1985]. Few studies have investigated hERG block effects under ischaemic conditions. Wilhelms *et al.* carried out simulations showing how

amiodarone and cisapride increase QT interval in human ischaemic ventricles, however they do not investigate arrhythmic mechanisms [Wilhelms et al., 2012]. Our results show that an excitation wave is more likely to encounter refractory tissue in the ICZ when APD is increased by hERG block, as shown in Figure 7.5a. Furthermore, as shown in Figure 7.5b, in some cases increased APD in the NZ prevents conduction block in the ICZ from causing re-entry, as it allows more time for the neighbouring tissue to recover and be re-excited. This in turn reduces the VW in a drug dose-dependent manner, by 24% for 30% hERG block and 6% for 50% block. Therefore, the time frame within which re-entry can be triggered is shorter in the presence of hERG block, an anti-arrhythmic effect.

7.4.3 High degrees of hERG block favour transmural reentry by increasing APD heterogeneity in the ischaemic border zone

Class III anti-arrhythmic drugs are currently prescribed to ischaemic patients with coronary artery disease [Steinberg et al., 2014], in spite of the fact that they are associated with increased mortality rates [Waldo et al., 1996]. As was shown by the clinical trial carried out by Steinberg *et al.* in patients with coronary artery disease being prescribed amiodarone, sotalol and dofetilide [Steinberg et al., 2014]. As shown in Figure 7.6, prolongation of APD combined with increased dispersion of APD caused by 50% hERG block can in fact lead to new pathways of re-entry. APD prolongation increases the time interval during which depolarised tissue can provide the stimulus to excite neighbouring tissue through "the injury current" described in [Coronel et al., 1991]. Once a propagating wavefront is generated, APD heterogeneity favours the establishment of reentry close to the BZ, where the transmural gradient is the greatest. This mechanism is only observed in the presence of 50% hERG block, which leads to a sufficient increase in the transmural APD gradient. Similar transmural reentry pathways through intramural "tunnels" of propagation have been reported in rabbit studies of defibrillation shocks due to the enhanced transmural dispersion of APD caused by shock-induced polarisation [Ashihara et al., 2008; Maharaj et al., 2008].

The increased transmural dispersion of repolarisation induced by hERG block and its increased arrhythmic risk have previously been reported by van Opstal *et al.* in a study of dronedarone, a drug prolonging APD, in non-ischaemic dog hearts [van Opstal et al., 2001]. Figure 7.7a shows that the dispersion of APD is increased with 50% hERG block - the increase in APD compared to no hERG block is 20 ms in the ICZ, which contributes to further increase the gradient in refractoriness across the border zone. Furthermore, Figure 7.7b shows that there is an increase in the transmural gradient of repolarisation at the BZ from 21% in control to 23% with 50% hERG block, which corresponds to a 10 ms difference. Our results show that even a small increase of 10 ms in transmural gradient of repolarisation can play an important role in arrhythmogenesis. Thus, our results suggest that patients with a high baseline transmural dispersion of repolarisation are more sensitive to the pro-arrhythmic mechanisms of hERG blockers.

The pro-arrhythmic effects of hERG block are more pronounced with 50% than 30% block. In fact, 50% block results in greater dispersion of APD and a wider VW than 30% block. Our results are in agreement with a clinical study carried out by Suttorp *et al.* on the effect of increasing dose of sotalol on supraventricular tachyarrhythmias in patients undergoing coronary artery bypass operations [Suttorp et al., 1990]. Clinical findings show that less adverse effects were found for low-dose (40 mg) compared to high-dose (80 mg). Our simulation results provide a mechanistic explanation to the clinical studies showing that pro-arrhythmic effects of higher dose might be due to enhanced transmural dispersion of refractoriness at the ischaemic border zone and increased propensity for the establishment of transmural reentry. An evaluation of specific dose effects on both prolongation and heterogeneity of repolarisation (through biomarkers such as QT and T-peak to T-end intervals) might improve the evaluation of safety and efficacy of hERG block in ischaemic patients.

Chapter 8

Conclusions and future work

In this section we conclude this thesis by presenting its main achievements. We begin by summarising the motivation for this thesis and work carried out to achieve these goals. We focus on the key findings: a novel computational and experimental method to characterise ischaemia-induced heterogeneities, a thorough analysis of recent human AP ventricular models under varied ischaemic conditions and an investigation of the efficacy of class III anti-arrhythmic drugs during ischaemia. We then describe directions for future work and end with some concluding remarks.

8.1 Summary

Sudden cardiac death is a major killer in the western world and is usually preceded by arrhythmias, irregular heart beats. One of the main causes is ischaemia, *i.e.* mismatch between blood demand and supply. The greatest arrhythmic risk occurs during the acute phase (first 10 - 15 min), when the AP and excitability of the affected cells are altered through hyperkalaemia, acidosis and hypoxia. Ischaemia increases electrophysiological heterogeneities across the heart and the likelihood of developing cardiac arrhythmias. It is a complex and dynamic process that varies through time, as the duration of ischaemia progresses, and spatially, as a gradient in prop-

erties develops between the normal and ischaemic tissue. There is a need to develop better tools to measure and characterise the ischaemia-induced spatio-temporally varying pro-arrhythmic substrate.

Furthermore, acute ischaemia may be a possible risk factor for patients treated with anti-arrhythmic drugs. Clinical trials have shown that, despite anti-arrhythmic drugs being an effective first line therapy for many patients suffering from irregular heart beats, they may lead to increased mortality and rehospitalisation. Mechanisms underlying this paradox are not well understood due to the ethical and practical limitations of carrying out experiments in human. Therefore, most research is carried out in animal, especially rabbit hearts due to their similarities to human hearts. Computational models provide a powerful tool to extrapolate our understanding of mechanisms from animal to human. Therefore, we have used and investigated for the first time, the latest human computational models under ischaemic conditions. The goal of this thesis is to investigate pro-arrhythmic electrophysiological consequences of acute myocardial ischaemia in a multi-scale computational modelling and simulation framework.

In Chapter 2, we began by introducing the basic structure and function of the heart. We then focused on cardiac electrophysiology by explaining electrical conduction and the different ion channels that come into play during a cell's AP. An overview of ischaemia was then presented, namely the most important electrophysiological changes that occur during the acute phase. This provided the motivation and justification for the specific mechanisms and phase of ischaemia this thesis focused on. We then discussed the main types of arrhythmias and clinical treatments referred to in this thesis. Particular attention is paid to the pro-arrhythmic substrate created by ischaemia as well as anti-arrhythmic drugs, which set the context for the work presented in the final part of this thesis, presented in Chapter 7. Finally, we presented important clinical and experimental techniques, such as optical mapping, which played an integral role in the first study described in Chapter 5. Motivation for this initial study being carried out in rabbit is also described in this chapter.

In Chapter 3, we presented a thorough experimental and computational literature review of ischaemia-induced electrophysiological changes, the main focus throughout this thesis. We reviewed data on the main temporal and spatial electrophysiological changes that occur during ischaemia and their effect on important arrhythmogenic biomarkers. The complexity and range of uncertainty displayed in the experimental and clinical data is shown, therefore, demonstrating the powerful role of computational modelling. In the previous chapter, drug cardiotoxicity was briefly reviewed, but here particular attention was given to trials showing increased mortality in patients prone to ischaemia. This provided the motivation for the work presented in Chapter 7. Finally, we covered the major computational studies investigating ischaemia and arrhythmias that were used as stepping stones when building our models.

In Chapter 4, we described the mathematical and computational methods used in this thesis to simulate cardiac activity from the single cell level to the tissue and whole organ level. We began with a thorough review of cardiac cell electrophysiology models that have been developed over the past 60 years, beginning with the Nobel-prize winning work of Hodgkin and Huxley, right up to the most recent biophysically detailed human ventricular models. The equations that reproduce the activity of the main ionic currents were introduced, especially the most recent human ventricular models in order to reinforce the thorough model comparison argued in Chapter 6. Parameters used to simulate ischaemia by previous computational studies were also examined, as similar ones were used throughout this thesis. Finally, some of the solvers of ordinary differential equations describing the ionic current activity were presented. In the second part of this chapter, we turn our attention to the methods used to couple the ionic current models together into a mesh and simulate electrical propagation. We introduced the bidomain and monodomain equations that reproduce the electrical activity in the tissue simulations presented in Chapters 5, 6 and 7. We presented the methods used to approximate solutions to these equations, such as the finite element method. Finally, we provided an outline of the simulation software package Chaste within which most of the simulations presented in this thesis were run.

A more detailed description of the code development is shown in the Appendix.

In Chapter 5, we develop computational and experimental method to characterise ischaemia-induced heterogeneities in rabbit hearts. This study was carried out in rabbit given the similarity to human hearts and due to the limitations of carrying out such experiments in human. We showed how the state-of-the-art dual wavelength optical mapping technique in combination with our biophysically detailed computational model of ischaemic rabbit tissue can quantify and, therefore, improve our understanding of ischaemia-induced heterogeneities through space and time. We initially assessed computationally how photon scattering effects were modulated by the ischaemic border zone. We then demonstrated how a combined dual wavelength optical mapping and computational study could characterise the border zone thanks to differences in penetration depth of the illuminating light.

After having investigated ischaemia-induced changes in rabbit and developed a technique to characterise them, we aimed at extending our study computationally to human in Chapter 6. Therefore, we presented an analysis and comparison of the 4 most recent human AP ventricular models under control and varied ischaemic conditions. The applicability of most of these models to simulate ischaemia had not been investigated previously. We did this by carrying out a single cell and tissue level analysis of the changes in ionic currents and major electrophysiological properties under ischaemic conditions and discussing differences and similarities observed across the models. We initially compared ionic current activity in the 4 models under normal conditions in order to better understand the formulation differences across the models. We referred back to the equations described in Chapter 4 and compared the experimental data on which the models were based. We also performed an AP clamp in order to understand whether the differences were dependent on varying in AP morphology. We then focused on electrophysiological properties related to arrhythmogenesis, and we assessed whether the values reproduced lied within the physiological ranges observed clinically. Finally, we discussed the findings and argued the suitability of the models to simulate acute ischaemia.

Our findings from Chapter 6 informed our choice of human AP model in Chapter 7. We presented a novel biophysically detailed human whole ventricles model of regional ischaemia, which was closely compared to human experimental clinical data to lend credibility to the model. There is an urgent need to understand underlying mechanisms of the lethal side-effects of anti-arrhythmic drugs. For the first time, we computationally investigated how hERG blockers are modulated by regional ischaemia in human. As had been shown previously, our study demonstrated how computer simulations provide a high spatio-temporal resolution not possible through experiments alone, which is essential to investigate the dynamic and complex arrhythmic patterns. We simulated figure-of-eight reentry by applying a premature beat at varying coupling intervals. To assess arrhythmic risk, we calculated the vulnerability window as the time during which a reentry could be triggered. Results provided insights into the pro- and anti-arrhythmic mechanisms of hERG blockers during regional ischaemia. We discovered that arrhythmic risk was dose-dependent, as a higher dose increased the vulnerability window by creating new transmural reentry pathways.

8.2 Key findings

The first part of our work developed a novel method to characterise ischaemia-induced spatial heterogeneities using a combined computational and experimental approach. There is a need to improve recording techniques of the complex and dynamic differences induced by ischaemia as they play a pivotal role in arrhythmogenesis. Current experimental techniques suffer from numerous limitations, such as only being able to gather data from specific locations under the microelectrode. However, optical mapping can provide high spatio-temporal resolution. We showed that the red wavelength of light penetrates further into the tissue and contains more information on the deeper ischaemic tissue, while the blue wavelength of light has a more shallow penetration depth and contains mostly information on the healthier tissue at the surface of the heart. Therefore, our results show that combining this technique with computational models

of the dual wavelength optical mapping signal and ischaemia can lead to greater understanding of mechanisms occurring at the surface of the heart. This technique can provide important spatio-temporal information of ischaemia-induced electrophysiological changes not possible with current techniques.

The second part of this thesis provided an invaluable stepping stone in the computational study of ischaemia in human. Most recent human ventricular models have not been investigated under ischaemic conditions, therefore, our results are essential when choosing a model to investigate different degrees of ischaemia. We compared the 4 most recent human models under both normal and ischaemic conditions from the ion to the tissue level. Our results show that the TP06 and CRLP models are the most appropriate for studies of ischaemia. The ORd model is limited in its I_{Na} formulation and thus, does not display the expected ischaemic PRR, while the GPB is not able to reproduce electrical propagation for $[K^+]_o \geq 9$ mM. Therefore, we provided an overview of the strengths and weaknesses of each model when varying ischaemic parameters.

Finally, the third part of our thesis shows both the anti- and pro-arrhythmic effects of hERG blockers during regional ischaemia in a whole human ventricles computational model. The study is the first of its kind to investigate computationally the effects of hERG block during acute regional ischaemia. We show how hERG block modulates arrhythmic risk in a dose-dependent manner by simulating both 30% and 50% hERG block. Furthermore, higher hERG block leads to the creation of new transmural pathways of reentry, which increase the vulnerability to arrhythmias compared to 30% hERG block. Our results suggest the need for more dose-dependent clinical studies and better biomarkers of dispersion of repolarisation for improved patient risk stratification.

8.3 Future work

Many limitations of the work presented in this thesis could be investigated as future work. The whole ventricle study presented in Chapter 7 was carried out in a single geometry with specific initial conditions such as APD transmural dispersion and the cell model used. Many of these parameters could and should be varied or modified to investigate how they modulate the results found. Furthermore, apex-base and LV-RV differences should be incorporated. Mechanical effects could be included too through a fully coupled excitation-contraction model or more simply by incorporating stretch activated channel effects at the electrophysiological level [Trayanova et al., 2010; Trayanova, 2011]. Despite it being early stages of ischaemia (the first 10-15 min), the ischaemic tissue may nonetheless display a desynchronised pattern of contraction due to the slower conduction and shorter APD, which has been shown to affect the generation of premature beats [Jie et al., 2009; Horner et al., 1994]. This plays an important role in modulating the electro-mechanical feedback loop and the likelihood of generating arrhythmias [Li et al., 2004; Keldermann et al., 2009]. Furthermore, this interaction becomes very important during the later stages of ischaemia when the tissue starts become necrotic and unable to contract properly. This not only changes the mechanics of the ischaemic area but also of the surrounding tissue through changes in the stresses and strains applied to each cell.

Another possible extension of the hERG block study, could be to investigate the effect of varying properties of the ischaemic region, such as size, location and border zone, which can be modulated by many factors such as collateral blood flow [Miura and Downey, 1988; Bolli et al., 1986] and coronary artery occluded [Lee et al., 1981]. These properties can play an important role in modulating arrhythmogenesis, as has been shown by Bolli *et al.*, in open-chest dogs where VF did not develop when the ischaemic region represented less than 28% of the LV and the incidence of VF was inversely related to collateral perfusion. We estimate this study could take between 6 months and a year.

Furthermore, it would be interesting to investigate the effects of an epicardial BZ, as its existence *in vivo* remains uncertain. Some studies have reported it during myocardial infarction in dog hearts [Ursell et al., 1985; Pu and Boyden, 1997]. However, it cannot be investigated *in vivo* during acute ischaemia in human due to limitations of human experiments and current techniques. However, computer models provide a powerful framework to investigate the potential role of the epicardial BZ. It may interact with the underlying transmural heterogeneities, which we showed played an important role in modulating pathways of reentry during hERG block.

Finally, this model can also be used to investigate other drug compounds with specific- or multi-channel effects. Namely, other drugs that have been shown to display lethal side-effects, such as class I anti-arrhythmic drugs, sodium channel blockers, as was shown in the Cardiac Arrhythmia Suppression Trial (CAST) carried out in patients with myocardial infarction [Ruskin, 1989]. A similar study protocol to the one presented in Chapter 7 could be carried out with different levels of I_{Na} inhibition to simulate drug effects.

The combined computational and experimental optical mapping framework presented in Chapter 5 can be extended to help us understand the complex activation patterns that occur during arrhythmias and conduction block. Some preliminary simulation results are shown in Figure 8.1. Here we show an example of V_m on a rectangular piece of myocardial tissue to which we have applied a premature stimulus which caused a reentry and a conduction block in the ischaemic BZ. We expect that the difference between the two wavelengths will be more pronounced during the reentry and conduction block as the red light (deeper penetration) will gather information from the intramural wavefront, while the blue light will only gather information from the surface wavefront. As shown in 8.1b, we hypothesize that the simulated optical signal with a higher wavelength has a smaller amplitude than the one with the lower wavelength as it is gathering information from the tissue that is not excited too as opposed to only from the excited tissue at the surface. The next stage would be to carry out further simulations to test different stimula-

tion protocols and wavelength penetration depths before moving onto testing this hypothesis in optical mapping experiments.

This framework could help test the results from Chapter 7 experimentally by assessing transmural pathways of reentry, which is not possible with current experimental techniques. The combined computational and experimental approach could be used to investigate the existence of transmural pathways of reentry during regional ischaemia in the presence of hERG block.

Figure 8.1 Preliminary simulation results using our computational optical mapping framework described in Chapter 5 to investigate whether dual wavelength optical mapping experiments could be used to investigate transmural arrhythmic mechanisms.

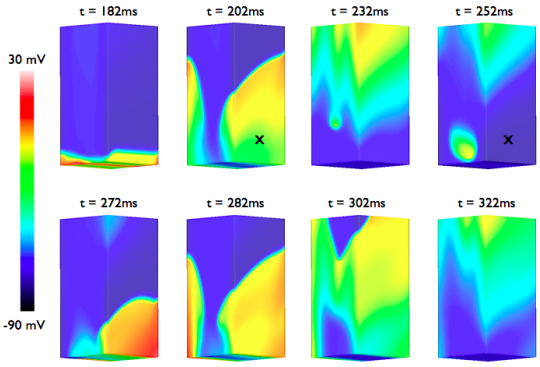

(a) Snapshots of V_m through time after the premature stimulus induces a reentry

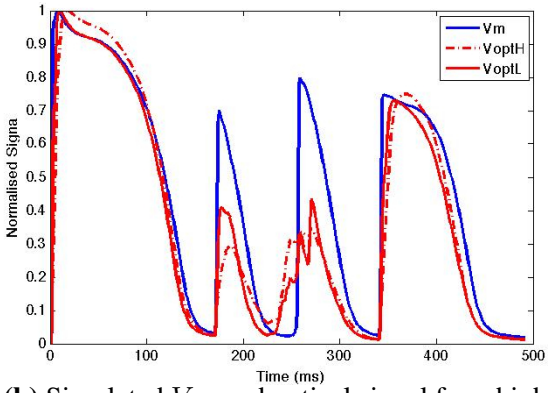

(b) Simulated V_m, and optical signal for a high (VoptH) and low (VoptL) penetration depth

Potential avenues for code improvement include parallelising the optical mapping code and incorporating it into the main Chaste repository. This would involve in depth knowledge of code parallelisation techniques, Chaste and the optical mapping model and we estimate it would take approximately 6 months to complete. Furthermore, Chaste functionality could be improved and extended, such as the postprocessing of simulation results, to include APD and AT maps during arrhythmias when each cell is likely to contain a different number of APDs and ATs. Currently it is only possible to get postprocessing maps during sinus rhythm. Finally, speed of the whole heart simulations could be improved by using the CVODE solver, instead of the backward Euler method, and the updated HDF5 reading and writing algorithm.

8.4 Concluding remarks

Since the first cardiac cell model was built 50 years ago by Denis Noble, computer models alongside experiments have provided invaluable insight into cardiac electrophysiology. This thesis is now part of the long series of milestones that demonstrate how computer modelling contributes to our increasing knowledge of cardiac electrophysiology, specifically acute ischaemia-induced changes and arrhythmic mechanisms. We presented three main novel contributions. Firstly, we built a combined dual wavelength optical mapping and computational rabbit tissue modelling framework to characterise ischaemia-induced heterogeneities with high spatio-temporal resolution, which is not possible with current techniques. Secondly, we investigated the applicability of the most important recent human computational models to simulate ischaemia. Finally, we constructed a human whole ventricles model of regional ischaemia in which we are able to dissect anti- and pro-arrhythmic mechanisms of anti-arrhythmic drugs.

Appendix A

Contributions to Chaste software

Here we describe some of the code we developed in order to run the simulations presented in this thesis. We first present some of the Chaste functionality we extended, improved and created as part of the *main Chaste repository*, which is freely available online. Most of the code we contributed to was developed during the Thursday pair programming sessions alongside one of the core developers. The code underlying all of the results presented in this thesis can be found in my *personal project repository* and calls many functions from the main Chaste repository. We give an overview of my personal project repository and present an example of one of the test functions that was developed as part of our project repository in order to run the whole ventricle simulation study presented in Chapter 7, most of the code development was carried out independently with the occasional help of the Chaste core developers and other members of the Computational Biology Group.

A.1 Main Chaste repository

An important feature we contributed to was outputting post processing maps, such as APD and AT maps (Figure 7.1), to CMGUI and VTK format. Previously, it was only possible to output them in Meshalyzer format. This involved restructuring the output pipeline in order write

all post-processing to the main HDF5 results file and remove all the hard-coded meshalyzer post-processing writer functionality. We then adapted the HDF5 converter class to write post-processing maps to any format requested (meshalyzer, cmgui or vtk). Furthermore, we created a python script in order to add time annotations to the vtk file. Previously Paraview, a visualisation software, treated each time step as a different data set, therefore it was not possible to use the animation functionality to visualise the data.

We also contributed to improving the Chaste archiving functionality. Chaste allows simulations to be archived and then run again from the same checkpoint in a separate simulation. Using this functionality, we discovered that the mesh partitioning was not archived properly when using the human whole ventricle mesh. Therefore, this was fixed by creating a minimum failing test and modifying the node partitioning pipeline with the help of the core Chaste developers.

Furthermore, we contributed to the creation of tutorials. These are used as guidelines with step by step commented instructions on the different stages of the simulation. We created a tutorial on running single cell simulations that explains how to run the model to steady state, what solver and parameters can be changed and how to calculate certain cell properties such as APD and upstroke velocity.

We also contributed to the Resource Description Framework (RDF) tagging process of CellML[1] files[2]. Chaste converts CellML files to C++ at compile time and RDF tags are used to define specific parameters to be modified, such as the conductance of a current. We developed a python script that automatically adds RDF tags to new CellML files. Finally, we were involved in adding support for new libraries such as PETSc 3.3 and ParMETIS, which play a role in parallelisation of the code.

[1] https://www.cellml.org

[2] https://chaste.cs.ox.ac.uk/trac/wiki/ChasteGuides/CodeGenerationFromCellML

A.2 Personal project repository

Within my own project repository, which isn't committed as part of the main Chaste repository, we developed all of the code that was used to run the simulations presented in Chapters 5, 6 and 7. For Chapter 5, we implemented Bishop's optical mapping signal synthesis code [Bishop et al., 2007b]. We also developed a model of ischaemia-induced heterogeneities in a 3D slab of ventricular tissue using the Mahajan 2008 rabbit model [Mahajan, 2008]. For Chapter 6, we developed code to analyse the 4 recent human ventricular models, and calculated properties such as APD, ERP and PRR. We developed our own method to calculate ERP and APD restitution curves. Finally for Chapter 7, we developed the stimulation protocol to generate arrhythmias in the whole ventricle geometry. We also created the ischaemic region, border zone, drug block and transmural heterogeneities with chosen properties.

We now describe the main components of a Chaste test function we developed independently using existing Chaste functionality to run the human whole ventricle simulations presented in Chapter 7.

A.2.1 Header

In the header section of the test function it is possible to include any cell model that is available in the CellML repository along with the ODE solver (forward or backward Euler or CVODE). For example in this test we used the ten Tusscher 2006 epicardial and midmyocardial cell models with an added $I_{K(ATP)}$ current using the backward Euler method. We also show some of the other headers that are included in a typical test function in Code A.1.

Code A.1 Header

```
#include <cxxtest/TestSuite.h>
#include <boost/assign.hpp>
#include <boost/shared_ptr.hpp>
#include "MonodomainProblem.hpp"
#include "PetscSetupAndFinalize.hpp"
#include "TetrahedralMesh.hpp"
```

```
7  #include "ten_tusscher_model_2006_epi_with_ikatp_rdfBackwardEuler.hpp"
   #include "ten_tusscher_model_2006_M_with_ikatp_rdfBackwardEuler.hpp"
9  #include "HeartGeometryInformation.hpp"
   #include "PseudoEcgCalculator.hpp"
11 #include "SimpleStimulus.hpp"
   #include "RegularStimulus.hpp"
13 #include "FileFinder.hpp"
   #include "CardiacSimulationArchiver.hpp"
15 #include "CommandLineArguments.hpp"
```

A.2.2 Defining stimulus and ischaemic region

We then create a cell factory, `BenchmarkCellFactory`, that defines the stimulus protocol and cellular heterogeneities, such as transmural differences and ischaemic regions. The first part of the class is shown in Code A.2. `HeartGeometryInformation`, defined on line 4, contains information on the distance of each cell to the different parts of the heart such as the endocardium and epicardium, therefore, the class is used to define the transmural heterogeneities of the heart and the endocardium stimulus regions. Distances are calculated in lines 24 to 26. Here we define a `RegularStimulus` with certain amplitude, duration, period and start time (lines 5 and 13). There are different types of stimulus and it is possible to define a premature stimulus too. The constructor of the cell factory is given a parameter, on line 11, that defines the amount by which the current should be blocked to simulate for example hERG block, an anti-arrhythmic drug.

Code A.2 `BenchmarkCellFactory` initial code defining stimulus and electrophysiological heterogeneities such as ischaemic, border zone regions and transmural differences

```
1  class BenchmarkCellFactory : public AbstractCardiacCellFactory<3>
   {
3    private:
       HeartGeometryInformation<3>* mpGeometryInfo;
5      boost::shared_ptr<RegularStimulus> mpStimulus1;
       std::vector<double> mEpiCellInitialConditions;
7      std::vector<double> mMCellInitialConditions;
       double ikr_scale;
9
     public:
11     BenchmarkCellFactory(double i_kr)
         : AbstractCardiacCellFactory<3>(),
```

```
13      mpStimulus1(new RegularStimulus(-70000.0, 1.5,800 ,20))//magnitude,
            duration,period, starttime
        {
15      ikr_scale=i_kr;
        }
17
        AbstractCardiacCellInterface* CreateCardiacCellForTissueNode(unsigned
            node)
19      {
        Cellten_tusscher_model_2006_M_with_ikatp_rdfFromCellMLBackwardEuler*
             M_cell;
21      Cellten_tusscher_model_2006_epi_with_ikatp_rdfFromCellMLBackwardEuler
            * epi_cell;

23      // distances
        double distance_epi = mpGeometryInfo->rGetDistanceMapEpicardium()[
            node];
25      double distance_lv = mpGeometryInfo->rGetDistanceMapLeftVentricle()[
            node];
        double distance_rv = mpGeometryInfo->rGetDistanceMapRightVentricle()
            [node];
```

Code A.3 defines the ellipsoid regions of stimulus (in the septum, LV and RV) and ischaemia as well as the ischaemic and normal electrophysiological parameters (lines 43-48). These are defined using `ChastePoint` and `ChasteEllipsoid`.

Code A.3 `BenchmarkCellFactory` class: defining regions of stimulus and ischaemic parameters

```
1       // Stimulus Regions - endocardial regions
        // -- Region 1 in Septum
3       ChastePoint<3> stim_septum_centre (4.0,5.0,3.2);
        ChastePoint<3> stim_septum_radius (2.0,1.0,2.0);
5       ChasteEllipsoid<3> stim_septum_region (stim_septum_centre,
            stim_septum_radius);
        bool cell_is_in_stim_septum_region = stim_septum_region.DoesContain(
            this->GetMesh()->GetNode(node)->rGetLocation());
7
        // -- Region 2 in LVtop
9       ChastePoint<3> stim_LVtop_centre (4.4,10.2,5.8);
        ChastePoint<3> stim_LVtop_radius (2.0,0.8,2.0);
11      ChasteEllipsoid<3> stim_LVtop_region (stim_LVtop_centre,
            stim_LVtop_radius);
        bool cell_is_in_stim_LVtop_region = stim_LVtop_region.DoesContain(
            this->GetMesh()->GetNode(node)->rGetLocation());
13
        // -- Region 3 in LVbottom
15      ChastePoint<3> stim_LVbottom_centre (4.8,8.8,3.2);
        ChastePoint<3> stim_LVbottom_radius (1.8,1.0,1.5);
```

```
17      ChasteEllipsoid<3> stim_LVbottom_region (stim_LVbottom_centre,
            stim_LVbottom_radius);
        bool cell_is_in_stim_LVbottom_region = stim_LVbottom_region.
            DoesContain(this->GetMesh()->GetNode(node)->rGetLocation());
19
        // -- Region 4 in RV
21      ChastePoint<3> stim_RV_centre (3.7,2.2,3.0);
        ChastePoint<3> stim_RV_radius (2.5,1.3,2.5);
23      ChasteEllipsoid<3> stim_RV_region (stim_RV_centre,stim_RV_radius);
        bool cell_is_in_stim_RV_region = stim_RV_region.DoesContain(this->
            GetMesh()->GetNode(node)->rGetLocation());
25
        // Ischaemic Region
27      double isch_r = 3.0;
        double isch_bz_r = 3.5;
29      double x_isch = 3.2;double y_isch = 10.3; double z_isch=3.6;
        ChastePoint<3> isch_centre (x_isch,y_isch,z_isch);
31      ChastePoint<3> isch_radius (isch_r,isch_r,isch_r);
        ChastePoint<3> isch_bz_radius (isch_bz_r,isch_bz_r,isch_bz_r);
33      ChasteEllipsoid<3> isch_region (isch_centre,isch_radius);
        ChasteEllipsoid<3> isch_bz_region (isch_centre,isch_bz_radius);
35      bool cell_is_in_ischReg = isch_region.DoesContain(this->GetMesh()->
            GetNode(node)->rGetLocation());
        bool cell_is_in_isch_bzReg = isch_bz_region.DoesContain(this->
            GetMesh()->GetNode(node)->rGetLocation());
37
        double x = this->GetMesh()->GetNode(node)->rGetLocation()[0];
39      double y = this->GetMesh()->GetNode(node)->rGetLocation()[1];
        double z = this->GetMesh()->GetNode(node)->rGetLocation()[2];
41
        // ---------- Ischaemic parameters
43      double k_n = 5.4;
        double k_i = 8.5;
45      double fkatp_n = 0;
        double fkatp_i = 0.05;
47      double ina_n = 1.0;
        double ina_i = 0.75;
```

We can define which cells will experience the stimulus by checking if they are within the region of stimulus, otherwise they are applied zero stimulus `mpZeroStimulus`. A series of `if-else` statements check which region the cell is in and apply the appropriate changes, such as the stimulus, the type of cell (epicardial or endocardial) and ischaemic parameters (set through the function `SetParameter`). Code A.4 defines the stimulus region in the septum.

Code A.4 `BenchmarkCellFactory` class: defining cells in the septum

```
        if (distance_epi >= distance_lv && distance_epi >= distance_rv)
```

```
2       {
          // Septum
4         double relative_position_septum = distance_rv / (distance_rv +
              distance_lv); // 0 if on RV and 1 if on LV

6         if(cell_is_in_stim_septum_region && relative_position_septum > 0.7)
          {
8           // stimulate region
            M_cell = new
                Cellten_tusscher_model_2006_M_with_ikatp_rdfFromCellMLBackwardEuler
                (this->mpSolver, this->mpStimulus1);
10        }
          else
12        {
            // don't stimulate
14          M_cell = new
                Cellten_tusscher_model_2006_M_with_ikatp_rdfFromCellMLBackwardEuler
                (this->mpSolver, this->mpZeroStimulus);
          }
16        double gkr = M_cell->GetParameter("
              membrane_rapid_delayed_rectifier_potassium_current_conductance"
              );
          M_cell->SetParameter("
              membrane_rapid_delayed_rectifier_potassium_current_conductance"
              ,gkr*ikr_scale);
18        return M_cell;
        }
20      else
```

Code A.5 defines the ischaemic region (lines 14-20) and the border zone (lines 24-46) in the epicardium as well as the level of drug block (lines 50-51). Similar code (not shown) is used to define the endocardial cells, which also includes stimulus and ischaemic regions.

Code A.5 `BenchmarkCellFactory` class: defining cells in the epicardium

```
          // left or right ventricle
2         double distance_endo = std::min(distance_lv, distance_rv);
          double relative_position = distance_endo / (distance_endo +
              distance_epi); // 0 if on endo and 1 if on epi
4
          if(relative_position > 0.6)
6         {
            // epicardial cell
8           epi_cell = new
                Cellten_tusscher_model_2006_epi_with_ikatp_rdfFromCellMLBackwardEuler
                (this->mpSolver, this->mpZeroStimulus);
            if(cell_is_in_isch_bzReg)
10          {
```

```
12          if(cell_is_in_ischReg)
            {
14            // Cell is in central ischaemic region
              epi_cell->SetParameter("extracellular_potassium_concentration"
                  ,k_i);
16            double gna = epi_cell->GetParameter("
                  membrane_fast_sodium_current_conductance");
              double gca = epi_cell->GetParameter("
                  membrane_L_type_calcium_current_conductance");
18            epi_cell->SetParameter("
                  membrane_fast_sodium_current_conductance",gna*ina_i);
              epi_cell->SetParameter("
                  membrane_L_type_calcium_current_conductance",gca*ina_i);
20            epi_cell->SetParameter("
                  membrane_atp_dependent_potassium_current_conductance",
                  fkatp_i);
            }
22          else
            {
24            // cell is in BZ area
              double distance_from_isch_centre = sqrt(pow((x-x_isch),2)+pow
                  ((y-y_isch),2)+pow((z-z_isch),2)); // distance from
                  ischaemic centre
26            // distance from central ischaemic zone
              // 0 if at central ischaemic zone
28            // 0.5 if at normal zone
              double distance_from_cz = distance_from_isch_centre - isch_r;
30            double bz_k = isch_bz_r-isch_r; // K+ border zone width

32            // linear ax+b equations, b=ischaemic value
              double a_k = (k_n-k_i)/bz_k;
34            double a_ina = (ina_n-ina_i)/bz_k;
              double a_fkatp = (fkatp_n-fkatp_i)/bz_k;
36
              // ----- calculate y
38            double y_k = a_k*distance_from_cz+k_i; // solution to ax+b=y
                  equation
              double y_ina = a_ina*distance_from_cz+ina_i;
40            double y_fkatp = a_fkatp*distance_from_cz+fkatp_i;
              epi_cell->SetParameter("extracellular_potassium_concentration"
                  ,y_k);
42            double gna = epi_cell->GetParameter("
                  membrane_fast_sodium_current_conductance");
              double gca = epi_cell->GetParameter("
                  membrane_L_type_calcium_current_conductance");
44            epi_cell->SetParameter("
                  membrane_fast_sodium_current_conductance",gna*y_ina);
              epi_cell->SetParameter("
                  membrane_L_type_calcium_current_conductance",gca*y_ina);
46            epi_cell->SetParameter("
                  membrane_atp_dependent_potassium_current_conductance",
                  y_fkatp);
```

```
48            }
            }
50          double gkr = epi_cell->GetParameter("
                membrane_rapid_delayed_rectifier_potassium_current_conductance
                ");
            epi_cell->SetParameter("
                membrane_rapid_delayed_rectifier_potassium_current_conductance
                ",gkr*ikr_scale);
52          return epi_cell;
          }
```

A.2.3 Running simulation and defining output

We then create a test function in which the simulation is initialised and run. The function initially gets certain parameters from the `CommandLineArguments` class that allows for arguments (I_{Kr} scaling factor and the duration of the simulation) to be passed from the command line and makes the use of automated scripts easier, as shown in Code A.6.

Code A.6 Test function that initialises and runs simulation: getting parameters

```
  class TestMeshBackwardEuler : public CxxTest::TestSuite
2 {
   public:
4  void Test3DMesh_IschBz_CommandLineArguments() throw(Exception)
   {
6
    //----- Get command line arguments - Ikr scaling factor and EndTime
8   unsigned endTime = 800;
    double ikr=1.0;
10  CommandLineArguments* p_args = CommandLineArguments::Instance();
    unsigned argc = *(p_args->p_argc); // has the number of arguments.
12  std::cout << "# " << argc-1 << " arguments supplied.\n" << std::flush;

14  bool ikr_Option = CommandLineArguments::Instance()->OptionExists("--
        ikr");
    if (ikr_Option == true) {
16    char* val = CommandLineArguments::Instance()->
          GetValueCorrespondingToOption("--ikr");
      ikr = atof(val);
18  }
    std :: cout << "IKr is " << ikr<< "ms \n";
20
    bool EndTime_Option = CommandLineArguments::Instance()->OptionExists("
        --duration");
22  if (EndTime_Option == true) {
```

```
        char* val = CommandLineArguments::Instance()->
            GetValueCorrespondingToOption("--duration");
24      endTime =atof(val);
      }
26    std :: cout << "Duration of simulation is " << endTime<< "ms \n";
```

Then the mesh is loaded along with the fibre orientation in lines 29-33 (Code A.7). It is also possible to generate meshes during compile time with given spatial dimensions and discretisation. We then set certain parameters such as the duration of the simulation and output directory path (lines 9-14).

Code A.7 Test function that initialises and runs simulation: loading the mesh

```
      //---- Load Mesh
2     TrianglesMeshReader<3,3> mesh_reader("../Mesh/UPF_human_0.4mm_NoBath")
          ;
      DistributedTetrahedralMesh<3,3> mesh;
4     mesh.ConstructFromMeshReader(mesh_reader);

6     HeartConfig::Instance()->SetMeshFileName("../Mesh/UPF_human_0.4
          mm_NoBath", cp::media_type::Orthotropic);
      std::stringstream ss;
8     ss << "
          Test_TrialStep7_WithFibres_Isch_BackwardEuler_EndoStim_NormalEndo0
          .1cm_lateralBZ_" << endTime << "_CL_800_K_8.5mM_Ikr" << ikr << "
          _Ecg_PostProcessingMaps";
      HeartConfig::Instance()->SetSimulationDuration(endTime); //ms
10    HeartConfig::Instance()->SetOutputDirectory(ss.str());
      HeartConfig::Instance()->SetOutputFilenamePrefix("results");
12    HeartConfig::Instance()->SetOdePdeAndPrintingTimeSteps(0.001, 0.01,
          1.0);
      unsigned scale = 3;
14    HeartConfig::Instance()->SetIntracellularConductivities(
          Create_c_vector(scale*1.75, scale*0.19, scale*0.19));
```

We then specify which post processing files should be outputted such as the pseudo ECG or APD maps, as shown in Code A.8. The output can be written in different formats: Meshalyzer, CMGUI or VTK[3] (lines 17-20).

Code A.8 Test function that initialises and runs simulation: post processing and output format

```
1     //---- ECG probes
      std::vector<std::pair<double,double> > pseudo_ecg_parameters;
```

[3] http://www.vtk.org

```
3     apd_maps_requested.push_back(4.3,3.3,2.4); // coordinates of electrode
      HeartConfig::Instance()->SetPseudoEcgElectrodePositions(
          pseudo_ecg_parameters);
5
      //---- Postprocessing maps
7     std::vector<std::pair<double,double> > apd_maps_requested;
      apd_maps_requested.push_back(std::make_pair(90,-20)); //percentage and
           threshold
9     HeartConfig::Instance()->SetApdMaps(apd_maps_requested);

11    std::vector<double> upstroke_time_maps_requested;
      upstroke_time_maps_requested.push_back(-20); // threshold
13    HeartConfig::Instance()->SetUpstrokeTimeMaps(
          upstroke_time_maps_requested);

15    HeartGeometryInformation<3> info(mesh, "../Mesh/UPF_human_0.4mm_NoBath
          .epi", "../Mesh/UPF_human_0.4mm_NoBath.rv", "../Mesh/UPF_human_0.4
          mm_NoBath.lv", true);

17    HeartConfig::Instance()->SetVisualizeWithMeshalyzer(true);
      HeartConfig::Instance()->SetVisualizeWithCmgui(false);
19    HeartConfig::Instance()->SetVisualizeWithVtk(false);
      HeartConfig::Instance()->SetVisualizeWithParallelVtk(false);
```

Finally, we run the monodomain simulation as shown in Code A.9 by giving it the cell factory (defined earlier) as an argument. We finally archive the simulation and save it (line 9) as a checkpoint to be loaded again later to continue the simulation from the time point at which it was saved.

Code A.9 Test function that initialises and runs simulation: running the simulation

```
      BenchmarkCellFactory cell_factory(ikr);
2     cell_factory.SetHeartGeometryInformation(&info);
      MonodomainProblem<3> monodomain_problem( &cell_factory );
4
      monodomain_problem.SetWriteInfo();
6     monodomain_problem.Initialise();
      monodomain_problem.Solve();
8
      CardiacSimulationArchiver<MonodomainProblem<3> >::Save(
          monodomain_problem, ss.str() + "/saved_simulation");
```

Bibliography

Aggarwal, R. and Boyden, P. A. (1995). Diminished Ca^{2+} and Ba^{2+} currents in myocytes surviving in the epicardial border zone of the 5-day infarcted canine heart. *Circulation Research*, 77(6):1180–1191.

Amos, G. J., Wettwer, E., Metzger, F., Li, Q., Himmel, H. M., and Ravens, U. (1996). Differences between outward currents of human atrial and subepicardial ventricular myocytes. *The Journal of Physiology*, 491 (Pt 1):31–50.

Antzelevitch, C., Sicouri, S., Litovsky, S. H., Lukas, A., Krishnan, S. C., Di Diego, J. M., Gintant, G. A., and Liu, D. W. (1991). Heterogeneity within the ventricular wall. Electrophysiology and pharmacology of epicardial, endocardial, and M cells. *Circulation Research*, 69(6):1427–1449.

Arora, R., Das, M. K., Zipes, D. P., and Wu, J. (2003). Optical mapping of cardiac arrhythmias. *Indian Pacing and Electrophysiology Journal*, 3(4):187–196.

Ashihara, T., Constantino, J., and Trayanova, N. A. (2008). Tunnel propagation of postshock activations as a hypothesis for fibrillation induction and isoelectric window. *Circulation Research*, 102(6):737–745.

Baartscheer, A. (1997). Small changes of cytosolic sodium in rat ventricular myocytes measured with SBFI in emission ratio mode. *Journal of Molecular and Cellular Cardiology*, 29(12):3375–3383.

Bailly, P., Mouchonière, M., Bénitah, J. P., Camilleri, L., Vassort, G., and Lorente, P. (1998). Extracellular K^+ dependence of inward rectification kinetics in human left ventricular cardiomyocytes. *Circulation*, 98(24):2753–2759.

Balke, C. W., Kaplinsky, E., Michelson, E. L., Naito, M., and Dreifus, L. S. (1981). Reperfusion ventricular tachyarrhythmias: correlation with antecedent coronary artery occlusion tachyarrhythmias and duration of myocardial ischemia. *American Heart Journal*, 101(4):449–456.

Banville, I. and Gray, R. A. (2002). Effect of action potential duration and conduction velocity restitution and their spatial dispersion on alternans and the stability of arrhythmias. *Journal of Cardiovascular Electrophysiology*, 13(11):1141–1149.

Baxter, W. T., Mironov, S. F., Zaitsev, A. V., Jalife, J., and Pertsov, A. M. (2001). Visualizing excitation waves inside cardiac muscle using transillumination. *Biophysical Journal*, 80(1):516–530.

Bénitah, J.-P., Bailly, P., D'Agrosa, M.-C., Ponte, J.-P., Delgado, C., and Lorente, P. (1992). Slow inward current in single cells isolated from adult human ventricles. *Pflügers Archiv*, 421(2-3):176–187.

Bernabeu, M., Pathmanathan, P., Pitt-Francis, J., and Kay, D. (2010a). Stimulus protocol determines the most computationally-efficient preconditioner for the bidomain equations. *IEEE Transactions on Bio-medical Engineering*.

Bernabeu, M. O., Southern, J., Wilson, N., Strazdins, P., Cooper, J., and Pitt-Francis, J. (2014). Chaste. *International Journal of High Performance Computing Applications*, 28(1):13–32.

Bernabeu, M. O., Wallman, M., and Rodriguez, B. (2010b). Shock-induced arrhythmogenesis in the human heart: A computational modelling study. *Conference proceedings : Annual International Conference of the IEEE Engineering in Medicine and Biology Society. IEEE Engineering in Medicine and Biology Society. Conference*, 2010:760–763.

Bernus, O., Wellner, M., Mironov, S. F., and Pertsov, A. M. (2005a). Simulation of voltage-sensitive optical signals in three-dimensional slabs of cardiac tissue: application to transillumination and coaxial imaging methods. *Physics in Medicine and Biology*, 50(2):215+.

Bernus, O., Wilders, R., Zemlin, C. W., Verschelde, H., and Panfilov, A. V. (2002). A computationally efficient electrophysiological model of human ventricular cells. *American Journal of Physiology - Heart and Circulatory Physiology*, 282(6):H2296–H2308.

Bernus, O., Zemlin, C. W., Zaritsky, R. M., Mironov, S. F., and Pertsov, A. M. (2005b). Alternating conduction in the ischaemic border zone as precursor of reentrant arrhythmias: A simulation study. *Europace*, 7(s2):S93–S104.

Bers, D. (1993). Control of Cardiac Contraction by SR Ca Release and Sarcolemmal Ca Fluxes. In *Excitation-Contraction Coupling and Cardiac Contractile Force*, volume 122 of *Developments in Cardiovascular Medicine*, pages 149–170. Springer Netherlands.

Bersohn, M. M., Philipson, K. D., and Fukushima, J. Y. (1982). Sodium-calcium exchange and sarcolemmal enzymes in ischemic rabbit hearts. *The American Journal of Physiology*, 242(5).

Beuckelmann, D. J., Näbauer, M., and Erdmann, E. (1991). Characteristics of calcium-current in isolated human ventricular myocytes from patients with terminal heart failure. *Journal of Molecular and Cellular Cardiology*, 23(8):929–937.

Bishop, M., Gavaghan, D., Trayanova, N., and Rodriguez, B. (2007a). Photon scattering effects in optical mapping of propagation and arrhythmogenesis in the heart. *Journal of Electrocardiology*, 40(6):S75–S80.

Bishop, M., Rodriguez, B., Eason, J., Whiteley, J., Trayanova, N., and Gavaghan, D. (2006). Synthesis of voltage-sensitive optical signals: Application to panoramic optical mapping. *Biophysical Journal*, 90(8):2938–2945.

Bishop, M., Rodriguez, B., Qu, F., Efimov, I., Gavaghan, D., and Trayanova, N. (2007b). The role of photon scattering in optical signal distortion during arrhythmia and defibrillation. *Biophysical Journal*, 93(10):3714–3726.

Bishop, M. J., Rowley, A., Rodriguez, B., Plank, G., Gavaghan, D. J., and Bub, G. (2011). The role of photon scattering in voltage-calcium fluorescent recordings of ventricular fibrillation. *Biophysical Journal*, 101(2):307–318.

Bolli, R., Fisher, D. J., and Entman, M. L. (1986). Factors that determine the occurrence of arrhythmias during acute myocardial ischemia. *American Heart Journal*, 111(2):261–270.

Bradley, C. P., Clayton, R. H., Nash, M. P., Mourad, A., Hayward, M., Paterson, D. J., and Taggart, P. (2011). Human ventricular fibrillation during global ischemia and reperfusion: paradoxical changes in activation rate and wavefront complexity. *Circulation. Arrhythmia and Electrophysiology*, 4(5):684–691.

Bray, M.-A. A. and Wikswo, J. P. (2003). Examination of optical depth effects on fluorescence imaging of cardiac propagation. *Biophysical Journal*, 85(6):4134–4145.

Brennan, T., Fink, M., and Rodriguez, B. (2009). Multiscale modelling of drug-induced effects on cardiac electrophysiological activity. *European Journal of Pharmaceutical Sciences*, 36(1):62–77.

Brennan, T., Fink, M., Rodriguez, B., and Tarassenko, L. T. (2007). Modelling effects of Sotalol on Action Potential morphology using a novel Markov model of the HERG channel. In Jarm, T., Kramar, P., and Zupanic, A., editors, *11th Mediterranean Conference on Medical and Biomedical Engineering and Computing 2007*, volume 16 of *IFMBE Proceedings*, pages 50–53. Springer Berlin Heidelberg.

Britton, O. J., Bueno-Orovio, A., Van Ammel, K., Lu, H. R., Towart, R., Gallacher, D. J., and Rodriguez, B. (2013). Experimentally calibrated population of models predicts and explains intersubject variability in cardiac cellular electrophysiology. *Proceedings of the National Academy of Sciences*, 110(23):E2098–E2105.

Brode, S. E., Schwartzman, D., Callans, D. J., Gottlieb, C. D., and Marchlinski, F. E. (1997). ICD-Antiarrhythmic Drug and ICD-Pacemaker Interactions. *Journal of Cardiovascular Electrophysiology*, 8(7):830–842.

Browne, K. F., Prystowsky, E., Heger, J. J., Chilson, D. A., and Zipes, D. P. (1983). Prolongation of the Q-T interval in man during sleep. *The American Journal of Cardiology*, 52(1):55–59.

Bueno-Orovio, A., Cherry, E. M., and Fenton, F. H. (2008). Minimal model for human ventricular action potentials in tissue. *Journal of Theoretical Biology*, 253(3):544–560.

Bueno-Orovio, A., Hanson, B. M., Gill, J. S., Taggart, P., and Rodriguez, B. (2012). In Vivo Human Left-to-Right Ventricular Differences in Rate Adaptation Transiently Increase Pro-Arrhythmic Risk following Rate Acceleration. *PloS ONE*, 7(12).

Bueno-Orovio, A., Pérez-García, V. M., and Fenton, F. H. (2006). Spectral methods for partial differential equations in irregular domains: The spectral smoothed boundary method. *SIAM Journal on Scientific Computing*, 28(3):886–900.

Cabrera, M. E., Zhou, L., Stanley, W. C., and Saidel, G. M. (2005). Regulation of cardiac energetics: role of redox state and cellular compartmentation during ischemia. *Annals of the New York Academy of Sciences*, 1047:259–270.

Caldwell, B. J., Trew, M. L., Sands, G. B., Hooks, D. A., LeGrice, I. J., and Smaill, B. H. (2009). Three Distinct Directions of Intramural Activation Reveal Nonuniform Side-to-Side Electrical Coupling of Ventricular Myocytes. *Circulation: Arrhythmia and Electrophysiology*, 2(4):433–440.

Camacho, S. A., Figueredo, V. M., Brandes, R., and Weiner, M. W. (1993). Ca(2+)-dependent fluorescence transients and phosphate metabolism during low-flow ischemia in rat hearts. *American Journal of Physiology - Heart and Circulatory Physiology*, 265(1):H114–H122.

Campbell, D. L., Giles, W. R., Hume, J. R., Noble, D., and Shibata, E. F. (1988). Reversal potential of the calcium current in bull-frog atrial myocytes. *The Journal of Physiology*, 403:267–286.

Cao, J.-M., Qu, Z., Kim, Y.-H., Wu, T.-J., Garfinkel, A., Weiss, J. N., Karagueuzian, H. S., and Chen, P.-S. (1999). Spatiotemporal Heterogeneity in the Induction of Ventricular Fibrillation by Rapid Pacing. *Circulation Research*, 84(11):1318–1331.

Carmeliet, E. (1999). Cardiac ionic currents and acute ischemia: from channels to arrhythmias. *Physiological Reviews*, 79(3):917–1017.

Carro, J., Rodríguez, J. F., Laguna, P., and Pueyo, E. (2011). A human ventricular cell model for investigation of cardiac arrhythmias under hyperkalaemic conditions. *Philosophical Transactions of the Royal Society A: Mathematical, Physical and Engineering Sciences*, 369(1954):4205–4232.

Carusi, A., Burrage, K., and Rodríguez, B. (2012). Bridging experiments, models and simulations: an integrative approach to validation in computational cardiac electrophysiology. *American Journal of Physiology - Heart and Circulatory Physiology*, 303(2):H144–H155.

Cascio, W. E. (2001). Myocardial ischemia: What factors determine arrhythmogenesis? *Journal of Cardiovascular Electrophysiology*, 12(6):726–729.

Cedilnik, A., Geveci, B., Moreland, K., Ahrens, J., and Favre, J. (2006). Remote large data visualization in the Paraview framework. In *Proceedings of the 6th Eurographics Conference on Parallel Graphics and Visualization*, EG PGV'06, pages 163–170, Aire-la-Ville, Switzerland, Switzerland. Eurographics Association.

Ch'en, F. F., Vaughan-Jones, R. D., Clarke, K., and Noble, D. (1998). Modelling myocardial ischaemia and reperfusion. *Progress in Biophysics and Molecular Biology*, 69(2-3):515–538.

Chen, P. S., Shibata, N., Dixon, E. G., Martin, R. O., and Ideker, R. E. (1986). Comparison of the defibrillation threshold and the upper limit of ventricular vulnerability. *Circulation*, 73(5):1022–1028.

Cheng, J., Kamiya, K., Liu, W., Tsuji, Y., Toyama, J., and Kodama, I. (1999). Heterogeneous distribution of the two components of delayed rectifier K^+ current: a potential mechanism of the proarrhythmic effects of methanesulfonanilideclass III agents. *Cardiovascular Research*, 43(1):135–147.

Cheong, W. F., Prahl, S. A., and Welch, A. J. (1990). A review of the optical properties of biological tissues. *IEEE Journal of Quantum Electronics*, 26(12):2166–2185.

Cherry, E. M. and Evans, S. J. (2008). Properties of two human atrial cell models in tissue: restitution, memory, propagation, and reentry. *Journal of Theoretical Biology*, 254(3):674–690.

Cherry, E. M. and Fenton, F. H. (2004). Suppression of alternans and conduction blocks despite steep APD restitution: electrotonic, memory, and conduction velocity restitution effects. *American Journal of Physiology - Heart and Circulatory Physiology*, 286(6):H2332–H2341.

Cherry, E. M. and Fenton, F. H. (2007). A tale of two dogs: analyzing two models of canine ventricular electrophysiology. *American Journal of Physiology - Heart and Circulatory Physiology*, 292(1):H43–H55.

Cherry, E. M. and Fenton, F. H. (2008). Visualization of spiral and scroll waves in simulated and experimental cardiac tissue. *New Journal of Physics*, 10(12):125016+.

Cherry, E. M., Greenside, H. S., and Henriquez, C. S. (2003). Efficient simulation of three-dimensional anisotropic cardiac tissue using an adaptive mesh refinement method. *Chaos: An Interdisciplinary Journal of Nonlinear Science*, 13(3):853–865.

Choi, B. R. and Salama, G. (2000). Simultaneous maps of optical action potentials and calcium transients in guinea-pig hearts: mechanisms underlying concordant alternans. *The Journal of Physiology*, 529 Pt 1:171–188.

Clark, R. B., Bouchard, R. A., Salinas-Stefanon, E., Sanchez-Chapula, J., and Giles, W. R. (1993). Heterogeneity of action potential waveforms and potassium currents in rat ventricle. *Cardiovascular Research*, 27(10):1795–1799.

Clarke, K., Stewart, L. C., Neubauer, S., Balschi, J. A., Smith, T. W., Ingwall, J. S., Nédélec, J. F., Humphrey, S. M., Kléber, A. G., and Springer, C. S. (1993). Extracellular volume and transsarcolemmal proton movement during ischemia and reperfusion: a 31P NMR spectroscopic study of the isovolumic rat heart. *NMR in Biomedicine*, 6(4):278–286.

Clayton, R. H. (2001). Computational models of normal and abnormal action potential propagation in cardiac tissue: linking experimental and clinical cardiology. *Physiological Measurement*, 22(3):R15–R34.

Clayton, R. H., Bernus, O., Cherry, E. M., Dierckx, H., Fenton, F. H., Mirabella, L., Panfilov, A. V., Sachse, F. B., Seemann, G., and Zhang, H. (2011a). Models of cardiac tissue electrophysiology: progress, challenges and open questions. *Progress in Biophysics and Molecular Biology*, 104(1-3):22–48.

Clayton, R. H., Nash, M. P., Bradley, C. P., Panfilov, A. V., Paterson, D. J., and Taggart, P. (2011b). Experiment-model interaction for analysis of epicardial activation during human ventricular fibrillation with global myocardial ischaemia. *Progress in Biophysics and Molecular Biology*.

Clerc, L. (1976). Directional differences of impulse spread in trabecular muscle from mammalian heart. *The Journal of Physiology*, 255(2):335–346.

Cobbe, S. M., Hoffman, E., Ritzenhoff, A., Brachmann, J., Kübler, W., and Senges, J. (1983). Action of sotalol on potential reentrant pathways and ventricular tachyarrhythmias in conscious dogs in the late postmyocardial infarction phase. *Circulation*, 68(4):865–871.

Cobbe, S. M. and Manley, B. S. (1987). The influence of ischaemia on the electrophysiological properties of amiodarone in chronically treated rabbit hearts. *European Heart Journal*, 8(11):1241–1248.

Cooper, J., Corrias, A., Gavaghan, D., and Noble, D. (2011). Considerations for the use of cellular electrophysiology models within cardiac tissue simulations. *Progress in Biophysics and Molecular Biology*, 107(1):74–80.

Cooper, J., McKeever, S., and Garny, A. (2006). On the application of partial evaluation to the optimisation of cardiac electrophysiological simulations. In *Proceedings of the 2006 ACM SIGPLAN Symposium on Partial Evaluation and Semantics-based Program Manipulation*, PEPM '06, pages 12–20, New York, NY, USA. ACM.

Coronel, R. (1994). Heterogeneity in extracellular potassium concentration during early myocardial ischaemia and reperfusion: implications for arrhythmogenesis. *Cardiovascular Research*, 28(6):770–777.

Coronel, R., Debakker, J., Wilmsschopman, F., Opthof, T., Linnenbank, A., Belterman, C., and Janse, M. (2006). Monophasic action potentials and activation recovery intervals as measures of ventricular action potential duration: Experimental evidence to resolve some controversies. *Heart Rhythm*, 3(9):1043–1050.

Coronel, R., Fiolet, J. W., Wilms-Schopman, F. J., Schaapherder, A. F., Johnson, T. A., Gettes, L. S., and Janse, M. J. (1988). Distribution of extracellular potassium and its relation to

electrophysiologic changes during acute myocardial ischemia in the isolated perfused porcine heart. *Circulation*, 77(5):1125–1138.

Coronel, R., Janse, M. J., Opthof, T., Wilde, A. A., and Taggart, P. (2012). Postrepolarization refractoriness in acute ischemia and after antiarrhythmic drug administration: action potential duration is not always an index of the refractory period. *Heart Rhythm*, 9(6):977–982.

Coronel, R., Wilms-Schopman, F. J., Opthof, T., van Capelle, F. J., and Janse, M. J. (1991). Injury current and gradients of diastolic stimulation threshold, TQ potential, and extracellular potassium concentration during acute regional ischemia in the isolated perfused pig heart. *Circ Res*, 68(5):1241–1249.

Coronel, R., Wilms-Schopman, F. J. G., and deGroot, J. R. (2002). Origin of ischemia-induced phase 1b ventricular arrhythmias in pig hearts. *J Am Coll Cardiol*, 39(1):166–176.

Coronel, R., Wilms-Schopman, F. J. G., Opthof, T., and Janse, M. J. (2009). Dispersion of repolarization and arrhythmogenesis. *Heart Rhythm*, 6(4):537–543.

Corr, P. B. and Witkowski, F. X. (1983). Potential electrophysiologic mechanisms responsible for dysrhythmias associated with reperfusion of ischemic myocardium. *Circulation*, 68(2 Pt 2).

Corrias, A., Jie, X., Romero, L., Bishop, M. J., Bernabeu, M., Pueyo, E., and Rodriguez, B. (2010). Arrhythmic risk biomarkers for the assessment of drug cardiotoxicity: from experiments to computer simulations. *Philosophical Transactions of the Royal Society A: Mathematical, Physical and Engineering Sciences*, 368(1921):3001–3025.

Costa, K. D., Takayama, Y., McCulloch, A. D., and Covell, J. W. (1999). Laminar fiber architecture and three-dimensional systolic mechanics in canine ventricular myocardium. *The American journal of physiology*, 276(2 Pt 2).

Costeas, C., Peters, N. S., Waldecker, B., Ciaccio, E. J., Wit, A. L., and Coromilas, J. (1997). Mechanisms causing sustained ventricular tachycardia with multiple QRS morphologies: results of mapping studies in the infarcted canine heart. *Circulation*, 96(10):3721–3731.

Courtemanche, M., Ramirez, R. J., and Nattel, S. (1998). Ionic mechanisms underlying human atrial action potential properties: insights from a mathematical model. *American Journal of Physiology - Heart and Circulatory Physiology*, 275(1):H301–H321.

Dangerfield, C. E., Kay, D., and Burrage, K. (2012). Modeling ion channel dynamics through reflected stochastic differential equations. *Physical Review E*, 85(5):051907+.

Darsee, J. R., Kloner, R. A., and Braunwald, E. (1981). Demonstration of lateral and epicardial border zone salvage by flurbiprofen using an in vivo method for assessing myocardium at risk. *Circulation*, 63(1):29–35.

Davies, M. J. (1990). A macro and micro view of coronary vascular insult in ischemic heart disease. *Circulation*, 82(3 Suppl).

Davies, M. J. and Thomas, A. (1984). Thrombosis and Acute Coronary-Artery Lesions in Sudden Cardiac Ischemic Death. *N Engl J Med*, 310(18):1137–1140.

de Lemos, J. A., Antman, E. M., Giugliano, R. P., McCabe, C. H., Murphy, S. A., Van de Werf, F., Gibson, C. M., and Braunwald, E. (2000). ST-segment resolution and infarct-related artery patency and flow after thrombolytic therapy. Thrombolysis in Myocardial Infarction (TIMI) 14 investigators. *The American Journal of Cardiology*, 85(3):299–304.

Dean, J. W. and Lab, M. J. (1990). Regional changes in ventricular excitability during load manipulation of the in situ pig heart. *The Journal of Physiology*, 429(1):387–400.

Deck, K. A., Kern, R., and Trautwein, W. (1964). Voltage clamp technique in mammalian cardiac fibres. *Pflügers Archiv European Journal of Physiology*, 280(1):50–62.

Decker, K. F., Heijman, J., Silva, J. R., Hund, T. J., and Rudy, Y. (2009). Properties and ionic mechanisms of action potential adaptation, restitution, and accommodation in canine epicardium. *American Journal of Physiology. Heart and Circulatory Physiology*, 296(4).

Dennis, S. (1991). Protons in ischemia: Where do they come from; Where do they go to? *Journal of Molecular and Cellular Cardiology*, 23(9):1077–1086.

DiMarco, J. P. (2003). Implantable CardioverterDefibrillators. *N Engl J Med*, 349(19):1836–1847.

DiMasi, J. A., Hansen, R. W., and Grabowski, H. G. (2003). The price of innovation: new estimates of drug development costs. *Journal of Health Economics*, 22(2):151–185.

Ding, L., Splinter, R., and Knisley, S. B. (2001). Quantifying spatial localization of optical mapping using Monte Carlo simulations. *IEEE Transactions on Biomedical Engineering*, 48(10):1098–1107.

Doering, A. E. and Lederer, W. J. (1993). The mechanism by which cytoplasmic protons inhibit the sodium-calcium exchanger in guinea-pig heart cells. *The Journal of Physiology*, 466:481–499.

Downar, E., Janse, M. J., and Durrer, D. (1977). The effect of acute coronary artery occlusion on subepicardial transmembrane potentials in the intact porcine heart. *Circulation*, 56(2):217–224.

Drouin, E., Charpentier, F., Gauthier, C., Laurent, K., and Le Marec, H. (1995). Electrophysiologic characteristics of cells spanning the left ventricular wall of human heart: Evidence for presence of M cells. *Journal of the American College of Cardiology*, 26(1):185–192.

Drouin, E., Lande, G., and Charpentier, F. (1998). Amiodarone reduces transmural heterogeneity of repolarization in the human heart. *Journal of the American College of Cardiology*, 32(4):1063–1067.

Durrer, D., Th, Freud, G. E., Janse, M. J., Meijler, F. L., and Arzbaecher, R. C. (1970). Total excitation of the isolated human heart. *Circulation*, 41(6):899–912.

Dutta, S., Bishop, M., Pathmanathan, P., Lee, P., Kohl, P., Quinn, T., and Rodriguez, B. (2011). Interpreting optical mapping recordings in the ischemic heart: A combined experimental and computational investigation functional imaging and modeling of the heart. volume 6666 of *Lecture Notes in Computer Science*, chapter 3, pages 20–27. Springer Berlin / Heidelberg, Berlin, Heidelberg.

Dutta, S., Minchole, A., Quinn, T. A., and Rodriguez, B. (2013). Recent human ventricular cell action potential models under varied ischaemic conditions. In *Computing in Cardiology Conference (CinC), 2013*, pages 695–698. IEEE.

Dzhura, I., Wu, Y., Colbran, R. J., Balser, J. R., and Anderson, M. E. (2000). Calmodulin kinase determines calcium-dependent facilitation of L-type calcium channels. *Nature Cell Biology*, 2(3):173–177.

Edvardsson, N., Hirsch, I., Emanuelsson, H., Pontén, J., and Olsson (1980). Sotalol-induced delayed ventricular repolarization in man. *European Heart Journal*, 1(5):335–343.

Efimov, I. R., Cheng, Y., Van Wagoner, D. R., Mazgalev, T., and Tchou, P. J. (1998). Virtual electrode-induced phase singularity : A basic mechanism of defibrillation failure. *Circ Res*, 82(8):918–925.

Efimov, I. R., Cheng, Y., Yamanouchi, Y., and Tchou, P. J. (2000). Direct Evidence of the Role of Virtual Electrode-Induced Phase Singularity in Success and Failure of Defibrillation. *Journal of Cardiovascular Electrophysiology*, 11(8):861–868.

Efimov, I. R., Huang, D. T., Rendt, J. M., and Salama, G. (1994). Optical mapping of repolarization and refractoriness from intact hearts. *Circulation*, 90(3):1469–1480.

Efimov, I. R., Nikolski, V. P., and Salama, G. (2004). Optical imaging of the heart. *Circulation Research*, 95(1):21–33.

Efimov, I. R., Sidorov, V., Cheng, Y., and Wollenzier, B. (1999). Evidence of three-dimensional scroll waves with ribbon-shaped filament as a mechanism of ventricular tachycardia in the isolated rabbit heart. *Journal of Cardiovascular Electrophysiology*, 10(11):1452–1462.

El-Sherif, N., Bub, G., and Lakireddy, V. (2009). The kinetics of intracellular calcium and arrhythmogenesis in ischemia/reperfusion: A calcium-centric mechanism of arrhythmia. pages 474–484.

Faber, G. M., Silva, J., Livshitz, L., and Rudy, Y. (2007). Kinetic properties of the cardiac L-type Ca2+ channel and its role in myocyte electrophysiology: a theoretical investigation. *Biophysical Journal*, 92(5):1522–1543.

Farid, T., Nair, K., Masse, S., Azam, M. A., Maguy, A., Lai, P. F. H., Umapathy, K., Dorian, P., Chauhan, V., Varró, A., Al-Hesayen, A., Waxman, M., Nattel, S., and Nanthakumar, K. (2011). Role of KATP Channels in the Maintenance of Ventricular Fibrillation in Cardiomyopathic Human Hearts. *Circulation Research*.

Fast, V. G. (2005). Simultaneous optical imaging of membrane potential and intracellular calcium. *Journal of Electrocardiology*, 38(4):107–112.

Fedida, D. and Giles, W. R. (1991). Regional variations in action potentials and transient outward current in myocytes isolated from rabbit left ventricle. *The Journal of Physiology*, 442(1):191–209.

Fedorov, V. V., Lozinsky, I. T., Sosunov, E. A., Anyukhovsky, E. P., Rosen, M. R., Balke, C. W., and Efimov, I. R. (2007). Application of blebbistatin as an excitation-contraction uncoupler for electrophysiologic study of rat and rabbit hearts. *Heart Rhythm*, 4(5):619–626.

Fenton, F. H., Cherry, E. M., Hastings, H. M., and Evans, S. J. (2002). Multiple mechanisms of spiral wave breakup in a model of cardiac electrical activity. *Chaos: An Interdisciplinary Journal of Nonlinear Science*, 12(3):852–892.

Ferrero, J. M., Sáiz, J., Ferrero, J. M., and Thakor, N. V. (1996). Simulation of action potentials from metabolically impaired cardiac myocytes. *Circulation Research*, 79(2):208–221.

Ferrero, J. M., Saiz, J., Ferrero, J. M., and Thakor, N. V. (1999). Postrepolarization refractoriness in ventricular cardiac cells: a simulation study. In *Computers in Cardiology, 1999*, pages 487–490. IEEE.

Ferrero, J. M., Trenor, B., and Romero, L. (2014). Multiscale computational analysis of the bioelectric consequences of myocardial ischaemia and infarction. *Europace*, 16(3):405–415.

Ferrero, J. M., Trenor, B., Saiz, J., Montilla, F., and Hernandez, V. (2003). Electrical activity and reentry in acute regional ischemia: insights from simulations. In *Engineering in Medicine and Biology Society, 2003. Proceedings of the 25th Annual International Conference of the IEEE*, volume 1, pages 17–20 Vol.1. IEEE.

Fink, M., Noble, D., Virag, L., Varro, A., and Giles, W. R. (2008). Contributions of HERG K^+ current to repolarization of the human ventricular action potential. *Progress in Biophysics and Molecular Biology*, 96(1-3):357–376.

Fiolet, J., Baartscheer, A., Schumacher, C., Terwelle, H., and Krieger, W. (1985). Transmural inhomogeneity of energy metabolism during acute global ischemia in the isolated rat heart: Dependence on environmental conditions. *Journal of Molecular and Cellular Cardiology*, 17(1):87–92.

Franz, M. R. (2003). The electrical restitution curve revisited. *Journal of Cardiovascular Electrophysiology*, 14:S140–S147.

Franz, M. R., Bargheer, K., Rafflenbeul, W., Haverich, A., and Lichtlen, P. R. (1987). Monophasic action potential mapping in human subjects with normal electrocardiograms: direct evidence for the genesis of the T wave. *Circulation*, 75(2):379–386.

Franz, M. R., Burkhoff, D., Spurgeon, H., Weisfeldt, M. L., and Lakatta, E. G. (1986). In vitro validation of a new cardiac catheter technique for recording monophasic action potentials. *European Heart Journal*, 7(1):34–41.

Fülöp, L., Bányász, T., Magyar, J., Szentandrássy, N., Varró, A., and Nánási, P. P. (2004). Reopening of L-type calcium channels in human ventricular myocytes during applied epicardial action potentials. *Acta physiologica Scandinavica*, 180(1):39–47.

Furukawa, T., Kimura, S., Furukawa, N., Bassett, A. L., and Myerburg, R. J. (1991). Role of cardiac ATP-regulated potassium channels in differential responses of endocardial and epicardial cells to ischemia. *Circ Res*, 68(6):1693–1702.

Garfinkel, A., Kim, Y.-H., Voroshilovsky, O., Qu, Z., Kil, J. R., Lee, M.-H., Karagueuzian, H. S., Weiss, J. N., and Chen, P.-S. (2000). Preventing ventricular fibrillation by flattening cardiac restitution. *Proceedings of the National Academy of Sciences*, 97(11):6061–6066.

Garny, A., Kohl, P., and Noble, D. (2003). Cellular open resource (cor): A public cellml based environment for modeling biological function. *International Journal of Bifurcation and Chaos*, 13(12):3579–3590.

Gasser, R. N. and Vaughan-Jones, R. D. (1990). Mechanism of potassium efflux and action potential shortening during ischaemia in isolated mammalian cardiac muscle. *The Journal of Physiology*, 431:713–741.

Gemmell, P., Burrage, K., Rodriguez, B., and Quinn, T. A. (2014). Population of computational rabbit-specific ventricular action potential models for investigating sources of variability in cellular repolarisation. *PLoS ONE*, 9(2):e90112+.

Gettes, L., Cascio, W., Johnson, T., and Fleet, W. (1991). Local Myocardial Biochemical and Ionic Alterations During Myocardial Ischaemia and Reperfusion. *Drugs*, 42(1):7–13.

Gilmour, R. F. and Zipes, D. P. (1980). Different electrophysiological responses of canine endocardium and epicardium to combined hyperkalemia, hypoxia, and acidosis. *Circulation Research*, 46(6):814–825.

Gima, K. and Rudy, Y. (2002). Ionic current basis of electrocardiographic waveforms. *Circulation Research*, 90(8):889–896.

Girouard, S. D., Laurita, K. R., and Rosenbaum, D. S. (1996). Unique properties of cardiac action potentials recorded with voltage-sensitive dyes. *Journal of Cardiovascular Electrophysiology*, 7(11):1024–1038.

Glukhov, A. V., Fedorov, V. V., Lou, Q., Ravikumar, V. K., Kalish, P. W., Schuessler, R. B., Moazami, N., and Efimov, I. R. (2010). Transmural dispersion of repolarization in failing and nonfailing human ventricle. *Circulation Research*, 106(5):981–991.

Grandi, E., Pasqualini, F. S., and Bers, D. M. (2010). A novel computational model of the human ventricular action potential and Ca transient. *Journal of Molecular and Cellular Cardiology*, 48(1):112–121.

Gray, R. A. (1999). What exactly are optically recorded "action potentials"? *Journal of Cardiovascular Electrophysiology*, 10(11):1463–1466.

Gray, R. A., Pertsov, A. M., and Jalife, J. (1998). Spatial and temporal organization during cardiac fibrillation. *Nature*, 392(6671):75–78.

Greenstein, J. L., Wu, R., Po, S., Tomaselli, G. F., and Winslow, R. L. (2000). Role of the calcium-independent transient outward current I_{to1} in shaping action potential morphology and duration. *Circulation Research*, 87(11):1026–1033.

Guarnieri, T., Levine, J. H., Veltri, E. P., Griffith, L. S. C., Watkins, L., Juanteguy, J., Mower, M. M., and Mirowski, M. (1987). Success of chronic defibrillation and the role of antiarrhythmic drugs with the automatic implantable cardioverter/defibrillator. *The American Journal of Cardiology*, 60(13):1061–1064.

Guo, D., Zhao, X., Wu, Y., Liu, T., Kowey, P. R., and Yan, g.-X. (2007). L-type calcium current reactivation contributes to arrhythmogenesis associated with action potential triangulation. *Journal of Cardiovascular Electrophysiology*, 18(2):196–203.

Haigney, M. C., Lakatta, E. G., Stern, M. D., and Silverman, H. S. (1994). Sodium channel blockade reduces hypoxic sodium loading and sodium-dependent calcium loading. *Circulation*, 90(1):391–399.

Hamill, O. P., Marty, A., Neher, E., Sakmann, B., and Sigworth, F. J. (1981). Improved patch-clamp techniques for high-resolution current recording from cells and cell-free membrane patches. *Pflügers Archiv European Journal of Physiology*, 391(2):85–100.

Hanck, D. A. and Sheets, M. F. (1992). Time-dependent changes in kinetics of Na+ current in single canine cardiac Purkinje cells. *American Journal of Physiology - Heart and Circulatory Physiology*, 262(4):H1197–H1207.

Hanson, B., Sutton, P., Elameri, N., Gray, M., Critchley, H., Gill, J. S., and Taggart, P. (2009). The interaction of activation-repolarisation coupling and restitution properties in humans. *Circulation: Arrhythmia and Electrophysiology*, pages CIRCEP.108.785352+.

Harken, A. H., Simson, M. B., Haselgrove, J., Wetstein, L., Harden, and Barlow, C. H. (1981). Early ischemia after complete coronary ligation in the rabbit, dog, pig, and monkey. *Am J Physiol Heart Circ Physiol*, 241(2):H202–210.

Hartmann, M., Decking, U. K., and Schrader, J. (1998). Cardioprotective actions of KC 12291. II. Delaying Na+ overload in ischemia improves cardiac function and energy status in reperfusion. *Naunyn-Schmiedeberg's archives of pharmacology*, 358(5):554–560.

Hasenfuss, G. (1998). Animal models of human cardiovascular disease, heart failure and hypertrophy. *Cardiovascular Research*, 39(1):60–76.

Heidenreich, E. A., Ferrero, J. M., and Rodríguez, J. F. (2012). *Modeling the Human Heart Under Acute Ischemia - Springer*.

Hestenes, M. R. and Stiefel, E. (1952). Methods of conjugate gradients for solving linear systems. *Journal of Research of the National Bureau of Standards*, 49(6):409+.

Hill, J. L. and Gettes, L. S. (1980). Effect of acute coronary artery occlusion on local myocardial extracellular K^+ activity in swine. *Circulation*, 61(4):768–778.

Himel, H. D., Bub, G., Yue, Y., and El-Sherif, N. (2009). Early voltage/calcium uncoupling predestinates the duration of ventricular tachyarrhythmias during ischemia/reperfusion. *Heart Rhythm*, 6(9):1359–1365.

Hirche, H., Franz, C., Bös, L., Bissig, R., Lang, R., and Schramm, M. (1980). Myocardial extracellular K^+ and H^+ increase and noradrenaline release as possible cause of early arrhythmias following acute coronary artery occlusion in pigs. *Journal of Molecular and Cellular Cardiology*, 12(6):579–593.

Hodgkin, A. L. and Huxley, A. F. (1952). A quantitative description of membrane current and its application to conduction and excitation in nerve. *The Journal of Physiology*, 117(4):500–544.

Hondeghem, L. M. (2006). Thorough QT/QTc not so thorough: removes torsadogenic predictors from the T-Wave, incriminates safe drugs, and misses profibrillatory drugs. *Journal of Cardiovascular Electrophysiology*, 17(3):337–340.

Hondeghem, L. M., Carlsson, L., and Duker, G. (2001). Instability and triangulation of the action potential predict serious proarrhythmia, but action potential duration prolongation is antiarrhythmic. *Circulation*, 103(15):2004–2013.

Hooks, D. A., Tomlinson, K. A., Marsden, S. G., LeGrice, I. J., Smaill, B. H., Pullan, A. J., and Hunter, P. J. (2002). Cardiac Microstructure. *Circulation Research*, 91(4):331–338.

Horacek, T., Neumann, M., Mutius, S., Budden, M., and Meesmann, W. (1984). Nonhomogeneous electrophysiological changes and the bimodal distribution of early ventricular arrhythmias during acute coronary artery occlusion. *Basic Research in Cardiology*, 79(6):649–667.

Horner, S. M., Lab, M. J., Murphy, C. F., Dick, D. J., Zhou, B., and Harrison, F. G. (1994). Mechanically induced changes in action potential duration and left ventricular segment length in acute regional ischaemia in the in situ porcine heart. *Cardiovascular Research*, 28(4):528–534.

Hu, H. (1997). Stretch-activated ion channels in the heart. *Journal of Molecular and Cellular Cardiology*, 29(6):1511–1523.

Huikuri, H. V., Castellanos, A., and Myerburg, R. J. (2001). Sudden death due to cardiac arrhythmias. *N Engl J Med*, 345(20):1473–1482.

Hund, T. J. and Rudy, Y. (2004). Rate dependence and regulation of action potential and calcium transient in a canine cardiac ventricular cell model. *Circulation*, 110(20):3168–3174.

Hwang, C., Swerdlow, C. D., Kass, R. M., Gang, E. S., Mandel, W. J., Peter, C. T., and Chen, P. S. (1994). Upper limit of vulnerability reliably predicts the defibrillation threshold in humans. *Circulation*, 90(5):2308–2314.

Hyatt, C. (2003). Synthesis of voltage-sensitive fluorescence signals from three-dimensional myocardial activation patterns. *Biophysical Journal*, 85(4):2673–2683.

Iost, N., Virág, L., Opincariu, M., Szécsi, J., Varró, A., and Papp, J. G. (1998). Delayed rectifier potassium current in undiseased human ventricular myocytes. *Cardiovascular Research*, 40(3):508–515.

Irisawa, H. and Sato, R. (1986). Intra- and extracellular actions of proton on the calcium current of isolated guinea pig ventricular cells. *Circulation Research*, 59(3):348–355.

Iwata, K., Hirai, M., Yoshida, Y., Iino, S., Kondo, T., Shimizu, A., Terazawa, M., Akahoshi, M., Inden, Y., Sugino, M., Tsuda, M., Tomita, Y., and Saito, H. (1999). Inverse relation of body-surface activation-recovery interval and recovery time to activation time in normal subjects: stronger correlation and more heterogeneous distribution in activation-recovery interval than in recovery time. *PACE*, 22(6 Pt 1):855–865.

Iyer, V., Mazhari, R., and Winslow, R. L. (2004). A computational model of the human left-ventricular epicardial myocyte. *Biophysical Journal*, 87(3):1507–1525.

Jalife, J. (2000). Ventricular fibrillation: Mechanisms of initiation and maintenance. *Annual Review of Physiology*, 62(1):25–50.

Janse, M., Kleber, A., Capucci, A., Coronel, R., and Wilmsschopman, F. (1986). Electrophysiological basis for arrhythmias caused by acute ischemia. Role of the subendocardium. *Journal of Molecular and Cellular Cardiology*, 18(4):339–355.

Janse, M. J., Capucci, A., Coronel, R., and Fabius, M. A. W. (1985). Variability of recovery of excitability in the normal canine and the ischaemic porcine heart. *European Heart Journal*, 6(suppl D):41–52.

Janse, M. J., Cinca, J., Moréna, H., Fiolet, J. W., Kléber, A. G., de Vries, G. P., Becker, A. E., and Durrer, D. (1979). The "border zone" in myocardial ischemia. An electrophysiological, metabolic, and histochemical correlation in the pig heart. *Circulation Research*, 44(4):576–588.

Janse, M. J. and Kléber, A. G. (1981). Electrophysiological changes and ventricular arrhythmias in the early phase of regional myocardial ischemia. *Circulation Research*, 49(5):1069–1081.

Janse, M. J., van Capelle, F. J., Morsink, H., Kléber, A. G., Wilms-Schopman, F., Cardinal, R., d'Alnoncourt, C. N., and Durrer, D. (1980). Flow of "injury" current and patterns of excitation during early ventricular arrhythmias in acute regional myocardial ischemia in isolated porcine and canine hearts. Evidence for two different arrhythmogenic mechanisms. *Circulation Research*, 47(2):151–165.

Janse, M. J. and Wit, A. L. (1989). Electrophysiological mechanisms of ventricular arrhythmias resulting from myocardial ischemia and infarction. *Physiological Reviews*, 69(4):1049–1169.

Jeyaraj, D., Haldar, S. M., Wan, X., McCauley, M. D., Ripperger, J. A., Hu, K., Lu, Y., Eapen, B. L., Sharma, N., Ficker, E., Cutler, M. J., Gulick, J., Sanbe, A., Robbins, J., Demolombe, S., Kondratov, R. V., Shea, S. A., Albrecht, U., Wehrens, X. H. T., Rosenbaum, D. S., and Jain, M. K. (2012). Circadian rhythms govern cardiac repolarization and arrhythmogenesis. *Nature*, 483(7387):96–99.

Jie, X., Gurev, V., and Trayanova, N. (2009). Mechanisms of mechanically induced spontaneous arrhythmias in acute regional ischemia. *Circ Res*, 106(1):192.

Jie, X., Rodriguez, B., and Trayanova, N. (2005). The ischemic heart: What causes ectopic beating? In *Engineering in Medicine and Biology Society, 2005. IEEE-EMBS 2005. 27th Annual International Conference of the*, pages 7194–7197.

Johnson, D. M., Heijman, J., Pollard, C. E., Valentin, J.-P. P., Crijns, H. J., Abi-Gerges, N., and Volders, P. G. (2010). I(Ks) restricts excessive beat-to-beat variability of repolarization during beta-adrenergic receptor stimulation. *Journal of Molecular and Cellular Cardiology*, 48(1):122–130.

Johnson, J. P., Mullins, F. M., and Bennett, P. B. (1999). Human ether-à-go-go-related gene K^+ channel gating probed with extracellular Ca^{2+}. Evidence for two distinct voltage sensors. *The Journal of General Physiology*, 113(4):565–580.

Jost, N., Acsai, K., Horváth, B., Bányász, T., Baczkó, I., Bitay, M., Bogáts, G., and Nánási, P. P. (2009). Contribution of I_{Kr} and I_{K1} to ventricular repolarization in canine and human myocytes: is there any influence of action potential duration? *Basic Research in Cardiology*, 104(1):33–41.

Jost, N., Varro, A., Szuts, V., Kovacs, P. P., Seprényi, G., Biliczki, P., Lengye, C., Prorok, J., Bitay, M., Ördög, B., Szabad, J., Varga-Orvos, Z., Puskas, L., Cotella, D., Papp, J. G., Virag, L., and Nattel, S. (2008). Molecular basis of repolarization reserve differences between dogs and man. *Circulation*, 118.

Ju, Y. K., Saint, D. A., and Gage, P. W. (1996). Hypoxia increases persistent sodium current in rat ventricular myocytes. *The Journal of Physiology*, 497 (Pt 2):337–347.

Kadish, A. (2004). What is a monophasic action potential? *Cardiovascular Research*, 63(4):580–581.

Kagiyama, Y., Hill, J. L., and Gettes, L. S. (1982). Interaction of acidosis and increased extracellular potassium on action potential characteristics and conduction in guinea pig ventricular muscle. *Circulation Research*, 51(5):614–623.

Kang, T. M. M. and Hilgemann, D. W. (2004). Multiple transport modes of the cardiac Na^+/Ca^{2+} exchanger. *Nature*, 427(6974):544–548.

Kaplinsky, E., Ogawa, S., Balke, C. W., and Dreifus, L. S. (1979). Two periods of early ventricular arrhythmia in the canine acute myocardial infarction model. *Circulation*, 60(2):397–403.

Karma, A. (1993). Spiral breakup in model equations of action potential propagation in cardiac tissue. *Physical Review Letters*, 71(7):1103–1106.

Keener, J. P. and Sneyd, J. (1998). *Mathematical Physiology*. 2nd edition.

Keldermann, R. H., Nash, M. P., Gelderblom, H., Wang, V. Y., and Panfilov, A. V. (2010). Electromechanical wavebreak in a model of the human left ventricle. *American Journal of Physiology - Heart and Circulatory Physiology*, 299(1):H134–H143.

Keldermann, R. H., Nash, M. P., and Panfilov, A. V. (2009). Modeling cardiac mechano-electrical feedback using reaction-diffusion-mechanics systems. *Physica D: Nonlinear Phenomena*, 238(11-12):1000–1007.

Kim, J., Ghosh, S., Nunziato, D. A., and Pitt, G. S. (2004). Identification of the components controlling inactivation of voltage-gated Ca^{2+} channels. *Neuron*, 41(5):745–754.

Kimura, S., Bassett, A. L., Furukawa, T., Cuevas, J., and Myerburg, R. J. (1990). Electrophysiological properties and responses to simulated ischemia in cat ventricular myocytes of endocardial and epicardial origin. *Circulation Research*, 66(2):469–477.

Kimura, S., Bassett, A. L., Kohya, T., Kozlovskis, P. L., and Myerburg, R. J. (1986). Simultaneous recording of action potentials from endocardium and epicardium during ischemia in the isolated cat ventricle: relation of temporal electrophysiologic heterogeneities to arrhythmias. *Circulation*, 74(2):401–409.

Kirkels, J. (1989). Intracellular magnesium during myocardial ischemia and reperfusion: Possible consequences for postischemic recovery. *Journal of Molecular and Cellular Cardiology*, 21(11):1209–1218.

Kleber, A. G. (1983). Resting membrane potential, extracellular potassium activity, and intracellular sodium activity during acute global ischemia in isolated perfused guinea pig hearts. *Circ Res*, 52(4):442–450.

Kléber, A. G. (1987). Conduction of the impulse in the ischemic myocardium–implications for malignant ventricular arrhythmias. *Experientia*, 43(10):1056–1061.

Kléber, A. G. (2000). ST-segment elevation in the electrocardiogram: a sign of myocardial ischemia. *Cardiovascular Research*, 45(1):111–118.

Kléber, A. G., Janse, M. J., van Capelle, F. J., and Durrer, D. (1978). Mechanism and time course of S-T and T-Q segment changes during acute regional myocardial ischemia in the pig heart determined by extracellular and intracellular recordings. *Circulation Research*, 42(5):603–613.

Knisley, S. B. (1995). Transmembrane voltage changes during unipolar stimulation of rabbit ventricle. *Circulation Research*, 77(6):1229–1239.

Knisley, S. B. and Smith, W. M. (1996). Experimental techniques for investigating cardiac electrical activity and response to electrical stimuli. *Proceedings of the IEEE*, 84(3):417–427.

Knopf, H., McDonald, F. M., Bischoff, A., Hirche, H., and Addicks, K. (1988). Effect of propranolol on early postischemia arrhythmias and noradrenaline and potassium release of ischemic myocardium in anesthetized pigs. *Journal of cardiovascular pharmacology*, 12 Suppl 1.

Kodama, I., Wilde, A., Janse, M. J., Durrer, D., and Yamada, K. (1984). Combined effects of hypoxia, hyperkalemia and acidosis on membrane action potential and excitability of guinea-pig ventricular muscle. *Journal of Molecular and Cellular Cardiology*, 16(3):247–259.

Komniski, M. S. S., Yakushev, S., Bogdanov, N., Gassmann, M., and Bogdanova, A. (2011). Interventricular heterogeneity in rat heart responses to hypoxia: the tuning of glucose metabolism, ion gradients, and function. *American Journal of Physiology. Heart and Circulatory Physiology*, 300(5).

Konarzewska, H., Peeters, G. A., and Sanguinetti, M. C. (1995). Repolarizing K^+ currents in nonfailing human hearts. Similarities between right septal subendocardial and left subepicardial ventricular myocytes. *Circulation*, 92(5):1179–1187.

Koumi, S.-i., Backer, C. L., and Arentzen, C. E. (1995). Characterization of inwardly rectifying K^+ channel in human cardiac myocytes. *Circulation*, 92(2):164–174.

Kuo, C. S., Munakata, K., Reddy, C. P., and Surawicz, B. (1983). Characteristics and possible mechanism of ventricular arrhythmia dependent on the dispersion of action potential durations. *Circulation*, 67(6):1356–1367.

Lakireddy, V., Baweja, P., Syed, A., Bub, G., Boutjdir, M., and El-Sherif, N. (2005). Contrasting effects of ischemia on the kinetics of membrane voltage and intracellular calcium transient underlie electrical alternans. *American Journal of Physiology - Heart and Circulatory Physiology*, 288(1):H400–H407.

Laurita, K. R. and Rosenbaum, D. S. (2008). Cellular mechanisms of arrhythmogenic cardiac alternans. *Progress in Biophysics and Molecular Biology*, 97(2-3):332–347.

Laurita, K. R. and Singal, A. (2001). Mapping action potentials and calcium transients simultaneously from the intact heart. *American Journal of Physiology - Heart and Circulatory Physiology*, 280(5):H2053–H2060.

Lawrence, C. L., Pollard, C. E., Hammond, T. G., and Valentin, J.-P. P. (2005). Nonclinical proarrhythmia models: predicting Torsades de Pointes. *Journal of pharmacological and toxicological methods*, 52(1):46–59.

Lee, C. O. and Fozzard, H. A. (1975). Activities of potassium and sodium ions in rabbit heart muscle. *The Journal of General Physiology*, 65(6):695–708.

Lee, J. T., Ideker, R. E., and Reimer, K. A. (1981). Myocardial infarct size and location in relation to the coronary vascular bed at risk in man. *Circulation*, 64(3):526–534.

Lee, P., Bollensdorff, C., Quinn, T. A., Wuskell, J. P., Loew, L. M., and Kohl, P. (2011). Single-sensor system for spatially resolved, continuous, and multiparametric optical mapping of cardiac tissue. *Heart Rhythm*.

LeGrice, I. J., Smaill, B. H., Chai, L. Z., Edgar, S. G., Gavin, J. B., and Hunter, P. J. (1995). Laminar structure of the heart: ventricular myocyte arrangement and connective tissue architecture in the dog. *The American Journal of Physiology*, 269(2 Pt 2):H571–H582.

Li, G.-R., Feng, J., Yue, L., and Carrier, M. (1998). Transmural heterogeneity of action potentials andI to1 in myocytes isolated from the human right ventricle. *American Journal of Physiology - Heart and Circulatory Physiology*, 275(2):H369–H377.

Li, G. R., Feng, J., Yue, L., Carrier, M., and Nattel, S. (1996). Evidence for two components of delayed rectifier K^+ current in human ventricular myocytes. *Circulation Research*, 78(4):689–696.

Li, G. R. and Nattel, S. (1997). Properties of human atrial I_{Ca} at physiological temperatures and relevance to action potential. *The American Journal of Physiology*, 272(1 Pt 2).

Li, G.-R., Yang, B., Feng, J., Bosch, R. F., Carrier, M., and Nattel, S. (1999). TransmembraneI Ca contributes to rate-dependent changes of action potentials in human ventricular myocytes. *American Journal of Physiology - Heart and Circulatory Physiology*, 276(1):H98–H106.

Li, W., Kohl, P., and Trayanova, N. (2004). Induction of ventricular arrhythmias following mechanical impact: A simulation study in 3D. *Journal of Molecular Histology*, 35(7):679–686.

Lloyd, C. M., Halstead, M. D., and Nielsen, P. F. (2004). CellML: its future, present and past. *Progress in Biophysics and Molecular Biology*, 85(2-3):433–450.

Lu, H. R., Vlaminckx, E., Van Ammel, K., and De Clerck, F. (2002). Drug-induced long QT in isolated rabbit Purkinje fibers: importance of action potential duration, triangulation and early afterdepolarizations. *European Journal of Pharmacology*, 452(2):183–192.

Lüderitz, B. (2009). Historical perspectives of cardiac electrophysiology. *Hellenic Journal of Cardiology*, 50(1):3–16.

Luo, C. H. and Rudy, Y. (1991). A model of the ventricular cardiac action potential. Depolarization, repolarization, and their interaction. *Circulation Research*, 68(6):1501–1526.

Luo, C. H. and Rudy, Y. (1994). A dynamic model of the cardiac ventricular action potential. II. Afterdepolarizations, triggered activity, and potentiation. *Circulation Research*, 74(6):1097–1113.

Ma, L. and Wang, L. (2007). Effect of acute subendocardial ischemia on ventricular refractory periods. *Experimental and Clinical Cardiology*, 12(2):63–66.

MacNeil, D. J. (1997). The side effect profile of class III antiarrhythmic drugs: focus on d,l-Sotalol. *The American Journal of Cardiology*, 80(8):90G–98G.

Magyar, J., Iost, N., Körtvély, A., Bányász, T., Virág, L., Szigligeti, P., Varró, A., Opincariu, M., Szécsi, J., Papp, J. G., and Nánási, P. P. (2000). Effects of endothelin-1 on calcium and

potassium currents in undiseased human ventricular myocytes. *Pflügers Archiv : European journal of physiology*, 441(1):144–149.

Magyar, J., Szentandrássy, N., Bányász, T., Fülöp, L., Varró, A., and Nánási, P. P. (2002). Effects of thymol on calcium and potassium currents in canine and human ventricular cardiomyocytes. *British Journal of Pharmacology*, 136(2):330–338.

Mahajan, A. (2008). Modifying L-Type calcium current kinetics: consequences for cardiac excitation and arrhythmia dynamics. *Biophysical Journal*, 94(2):411–423.

Maharaj, T., Blake, R., Trayanova, N., Gavaghan, D., and Rodriguez, B. (2008). The role of transmural ventricular heterogeneities in cardiac vulnerability to electric shocks. *Progress in Biophysics and Molecular Biology*, 96(1-3):321–338.

Maier, L. (2000). Differences in Ca^{2+}-handling and sarcoplasmic reticulum Ca^{2+}-content in isolated rat and rabbit myocardium. *Journal of Molecular and Cellular Cardiology*, 32(12):2249–2258.

Makita, N., Shirai, N., Wang, D. W., Sasaki, K., George, A. L., Kanno, M., and Kitabatake, A. (2000). Cardiac Na^+ channel dysfunction in Brugada syndrome is aggravated by β1-subunit. *Circulation*, 101(1):54–60.

Malloy, C. R., Buster, D. C., Margarida Castro, M. C. A., Geraldes, C. F. G. C., Jeffrey, and Sherry, A. D. (1990). Influence of global ischemia on intracellular sodium in the perfused rat heart. *Magn. Reson. Med.*, 15(1):33–44.

Maltsev, V. A., Sabbah, H. N., Higgins, R. S. D., Silverman, N., Lesch, M., and Undrovinas, A. I. (1998). Novel, ultraslow inactivating sodium current in human ventricular cardiomyocytes. *Circulation*, 98(23):2545–2552.

Maltsev, V. A. and Undrovinas, A. I. (2006). A multi-modal composition of the late Na^+ current in human ventricular cardiomyocytes. *Cardiovascular Research*, 69(1):116–127.

Manning, A. and Hearse, D. (1984). Reperfusion-induced arrhythmias: Mechanisms and prevention. *Journal of Molecular and Cellular Cardiology*, 16(6):497–518.

Marban, E., Kitakaze, M., Koretsune, Y., Yue, D. T., Chacko, V. P., and Pike, M. M. (1990). Quantification of $[Ca^{2+}]_i$ in perfused hearts. Critical evaluation of the 5F-BAPTA and nuclear magnetic resonance method as applied to the study of ischemia and reperfusion. *Circulation Research*, 66(5):1255–1267.

Maxwell, M. P., Hearse, D. J., and Yellon, D. M. (1987). Species variation in the coronary collateral circulation during regional myocardial ischaemia: a critical determinant of the rate of evolution and extent of myocardial infarction. *Cardiovascular Research*, 21(10):737–746.

Mazhari, R., Omens, J. H., Covell, J. W., and McCulloch, A. D. (2000). Structural basis of regional dysfunction in acutely ischemic myocardium. *Cardiovascular Research*, 47(2):284–293.

McDonald, F. M., Knopf, H., Hartono, S., Polwin, W., Bischoff, A., Hirche, H., and Addicks, K. (1986). Acute myocardial ischaemia in the anaesthetised pig: local catecholamine release and its relation to ventricular fibrillation. *Basic Research in Cardiology*, 81(6):636–645.

Mewes, T. and Ravens, U. (1994). L-type calcium currents of human myocytes from ventricle of non-failing and failing hearts and from atrium. *Journal of Molecular and Cellular Cardiology*, 26(10):1307–1320.

Michailova, A., Saucerman, J., Belik, M. E. E., and McCulloch, A. D. (2005). Modeling regulation of cardiac K_ATP and L-type Ca^{2+} currents by ATP, ADP, and Mg^{2+}. *Biophysical Journal*, 88(3):2234–2249.

Mirams, G. R., Arthurs, C. J., Bernabeu, M. O., Bordas, R., Cooper, J., Corrias, A., Davit, Y., Dunn, S.-J., Fletcher, A. G., Harvey, D. G., Marsh, M. E., Osborne, J. M., Pathmanathan, P., Pitt-Francis, J., Southern, J., Zemzemi, N., and Gavaghan, D. J. (2013). Chaste: an open source C++ library for computational physiology and biology. *PLoS Comput Biol*, 9(3):e1002970+.

Miura, T. and Downey, J. M. (1988). Collateral perfusion of ischemic myocardium is inversely related to the size of the ischemic zone. *Basic Research in Cardiology*, 83(2):128–136.

Mohabir, R., Lee, H. C., Kurz, R. W., and Clusin, W. T. (1991). Effects of ischemia and hypercarbic acidosis on myocyte calcium transients, contraction, and pH_i in perfused rabbit hearts. *Circulation Research*, 69(6):1525–1537.

Moréna, H., Janse, M. J., Fiolet, J. W., Krieger, W. J., Crijns, H., and Durrer, D. (1980). Comparison of the effects of regional ischemia, hypoxia, hyperkalemia, and acidosis on intracellular and extracellular potentials and metabolism in the isolated porcine heart. *Circulation Research*, 46(5):634–646.

Moreno, J. D., Zhu, Z. I., Yang, P.-C., Bankston, J. R., Jeng, M.-T., Kang, C., Wang, L., Bayer, J. D., Christini, D. J., Trayanova, N. A., Ripplinger, C. M., Kass, R. S., and Clancy, C. E. (2011). A computational model to predict the effects of class I anti-Arrhythmic drugs on ventricular rhythms. *Science Translational Medicine*, 3(98):98ra83.

Murphy, E., Steenbergen, C., Levy, L. A., Raju, B., and London, R. E. (1989). Cytosolic free magnesium levels in ischemic rat heart. *The Journal of Biological Chemistry*, 264(10):5622–5627.

Myburgh, D. P., Goldman, a. P., Cartoon, J., and Schamroth, J. M. (1979). The efficacy of sotalol in suppressing ventricular ectopic beats. *South African Medical Journal*, 56(8):295–298.

Myerburg, R. J. and Junttila, M. J. (2012). Sudden cardiac death caused by coronary heart disease. *Circulation*, 125(8):1043–1052.

Näbauer, M., Beuckelmann, D. J., Überfuhr, P., and Steinbeck, G. (1996). Regional differences in current density and rate-dependent properties of the transient outward current in subepicardial and subendocardial myocytes of human left ventricle. *Circulation*, 93(1):168–177.

Nademanee, K., Feld, G., Hendrickson, J., Singh, P. N., and Singh, B. N. (1985). Electrophysiologic and antiarrhythmic effects of sotalol in patients with life-threatening ventricular tachyarrhythmias. *Circulation*, 72(3):555–564.

Nagatomo, T., Fan, Z., Ye, B., Tonkovich, G. S., January, C. T., Kyle, J. W., and Makielski, J. C. (1998). Temperature dependence of early and late currents in human cardiac wild-type and long Q-T ΔKPQ Na^+ channels. *American Journal of Physiology - Heart and Circulatory Physiology*, 275(6):H2016–H2024.

Nakao, M. and Gadsby, D. C. (1989). [Na] and [K] dependence of the Na/K pump current-voltage relationship in guinea pig ventricular myocytes. *The Journal of General Physiology*, 94(3):539–565.

Nattel, S. (2002). New ideas about atrial fibrillation 50 years on. *Nature*, 415(6868):219–226.

Niederer, S. A., Fink, M., Noble, D., and Smith, N. P. (2009). A meta-analysis of cardiac electrophysiology computational models. *Experimental Physiology*, 94(5):486–495.

Niederer, S. A., Kerfoot, E., Benson, A. P., Bernabeu, M. O., Bernus, O., Bradley, C., Cherry, E. M., Clayton, R., Fenton, F. H., Garny, A., Heidenreich, E., Land, S., Maleckar, M., Pathmanathan, P., Plank, G., Rodríguez, J. F., Roy, I., Sachse, F. B., Seemann, G., Skavhaug, O., and Smith, N. P. (2011). Verification of cardiac tissue electrophysiology simulators using an N-version benchmark. *Philosophical Transactions of the Royal Society A: Mathematical, Physical and Engineering Sciences*, 369(1954):4331–4351.

Niederer, S. A. and Smith, N. P. (2007). A mathematical model of the slow force response to stretch in rat ventricular myocytes. *Biophysical Journal*, 92(11):4030–4044.

Noble, D. (1960). Cardiac action and pacemaker potentials based on the Hodgkin-Huxley equations. *Nature*, 188(4749):495–497.

Noble, D. (2002). Simulation of Na/Ca exchange activity during ischemia. *Annals of the New York Academy of Sciences*, 976:431–437.

Noble, D. and Rudy, Y. (2001). Models of cardiac ventricular action potentials: iterative interaction between experiment and simulation. *Mathematical, Physical and Engineering Sciences*, 359(1783):1127–1142.

Noble, D., Varghese, A., Kohl, P., and Noble, P. (1998). Improved guinea-pig ventricular cell model incorporating a diadic space, I_{Kr} and I_{Ks}, and length- and tension-dependent processes. *The Canadian Journal of Cardiology*, 14(1):123–134.

Noma, A. (1983). ATP-regulated K^+ channels in cardiac muscle. *Nature*, 305(5930):147–148.

O'Hara, T., Virág, L., Varró, A., and Rudy, Y. (2011). Simulation of the undiseased human cardiac ventricular action potential: model formulation and experimental validation. *PLoS Computational Biology*, 7(5):e1002061+.

Omichi, C., Lamp, S. T., Lin, S.-F. F., Yang, J., Baher, A., Zhou, S., Attin, M., Lee, M.-H. H., Karagueuzian, H. S., Kogan, B., Qu, Z., Garfinkel, A., Chen, P.-S. S., and Weiss, J. N. (2004). Intracellular Ca dynamics in ventricular fibrillation. *American Journal of Physiology. Heart and Circulatory Physiology*, 286(5).

Pandit, S. V., Clark, R. B., Giles, W. R., and Demir, S. S. (2001). A mathematical model of action potential heterogeneity in adult rat left ventricular myocytes. *Biophysical Journal*, 81(6):3029–3051.

Pandit, S. V. and Jalife, J. (2013). Rotors and the dynamics of cardiac fibrillation. *Circulation Research*, 112(5):849–862.

Pandit, S. V., Kaur, K., Zlochiver, S., Noujaim, S. F., Furspan, P., Mironov, S., Shibayama, J., Anumonwo, J., and Jalife, J. (2011). Left-to-right ventricular differences in I_{KATP} underlie epicardial repolarization gradient during global ischemia. *Heart Rhythm*, 8(11):1732–1739.

Pandit, S. V., Warren, M., Mironov, S., Tolkacheva, E. G., Kalifa, J., Berenfeld, O., and Jalife, J. (2010). Mechanisms underlying the antifibrillatory action of hyperkalemia in guinea pig hearts. *Biophysical Journal*, 98(10):2091–2101.

Panfilov, A. V. (2006). Is heart size a factor in ventricular fibrillation? Or how close are rabbit and human hearts? *Heart Rhythm*, 3(7):862–864.

Papadakis, M., Sharma, S., Cox, S., Sheppard, M. N., Panoulas, V. F., and Behr, E. R. (2009). The magnitude of sudden cardiac death in the young: a death certificate-based review in England and Wales. *Europace*, 11(10):1353–1358.

Papadatos, G. A., Wallerstein, P. M. R., Head, C. E. G., Ratcliff, R., Brady, P. A., Benndorf, K., Saumarez, R. C., Trezise, A. E. O., Huang, C. L. H., Vandenberg, J. I., Colledge, W. H., and

Grace, A. A. (2002). Slowed conduction and ventricular tachycardia after targeted disruption of the cardiac sodium channel gene Scn5a. *Proceedings of the National Academy of Sciences*, 99(9):6210–6215.

Pastore, J. M., Girouard, S. D., Laurita, K. R., Akar, F. G., and Rosenbaum, D. S. (1999). Mechanism linking T-Wave alternans to the genesis of cardiac fibrillation. *Circulation*, 99(10):1385–1394.

Pathmanathan, P., Bernabeu, M. O., Bordas, R., Cooper, J., Garny, A., Pitt-Francis, J. M., Whiteley, J. P., and Gavaghan, D. J. (2010a). A numerical guide to the solution of the bi-domain equations of cardiac electrophysiology. *Progress in Biophysics and Molecular Biology*, 102(2-3):136–155.

Pathmanathan, P., Chapman, S. J., Gavaghan, D. J., and Whiteley, J. P. (2010b). Cardiac electromechanics: The effect of contraction model on the mathematical problem and accuracy of the numerical scheme. *The Quarterly Journal of Mechanics and Applied Mathematics*, 63(3):375–399.

Pelzmann, B., Schaffer, P., Bernhart, E., Lang, P., Mächler, H., Rigler, B., and Koidl, B. (1998). L-type calcium current in human ventricular myocytes at a physiological temperature from children with tetralogy of Fallot. *Cardiovascular Research*, 38(2):424–432.

Penny, W. J. and Sheridan, D. J. (1983). Arrhythmias and cellular electrophysiological changes during myocardial ischaemia and reperfusion. *Cardiovascular Research*, 17(6):363–372.

Péréon, Y., Demolombe, S., Baró, I., Drouin, E., Charpentier, F., and Escande, D. (2000). Differential expression of KvLQT1 isoforms across the human ventricular wall. *American Journal of Physiology. Heart and Circulatory Physiology*, 278(6).

Peters, N. S., Coromilas, J., Severs, N. J., and Wit, A. L. (1997). Disturbed Connexin43 gap junction distribution correlates with the location of reentrant circuits in the epicardial border zone of healing canine infarcts that cause ventricular tachycardia. *Circulation*, 95(4):988–996.

Philipson, K. D., Bersohn, M. M., and Nishimoto, A. Y. (1982). Effects of pH on Na^+-Ca^{2+} exchange in canine cardiac sarcolemmal vesicles. *Circulation Research*, 50(2):287–293.

Pieske, B., Maier, L. S., Piacentino, V., Weisser, J., Hasenfuss, G., and Houser, S. (2002). Rate dependence of $[Na^+]_i$ and contractility in nonfailing and failing human myocardium. *Circulation*, 106(4):447–453.

Pitt-Francis, J., Bernabeu, M. O., Cooper, J., Garny, A., Momtahan, L., Osborne, J., Pathmanathan, P., Rodriguez, B., Whiteley, J. P., and Gavaghan, D. J. (2008). Chaste: using agile programming techniques to develop computational biology software. *Philosophical Transactions of the Royal Society A: Mathematical, Physical and Engineering Sciences*, 366(1878):3111–3136.

Pitt-Francis, J., Pathmanathan, P., Bernabeu, M. O., Bordas, R., Cooper, J., Fletcher, A. G., Mirams, G. R., Murray, P., Osborne, J. M., Walter, A., Chapman, S. J., Garny, A., van Leeuwen, I. M. M., Maini, P. K., Rodríguez, B., Waters, S. L., Whiteley, J. P., Byrne, H. M., and Gavaghan, D. J. (2009). Chaste: A test-driven approach to software development for biological modelling. *Computer Physics Communications*, 180(12):2452–2471.

Pogwizd, S. M. and Corr, P. B. (1987a). Electrophysiologic mechanisms underlying arrhythmias due to reperfusion of ischemic myocardium. *Circulation*, 76(2):404–426.

Pogwizd, S. M. and Corr, P. B. (1987b). Reentrant and nonreentrant mechanisms contribute to

arrhythmogenesis during early myocardial ischemia: results using three-dimensional mapping. *Circulation Research*, 61(3):352–371.

Pogwizd, S. M. and Corr, P. B. (1990). Mechanisms underlying the development of ventricular fibrillation during early myocardial ischemia. *Circulation Research*, 66(3):672–695.

Portaluppi, F. and Hermida, R. C. (2007). Circadian rhythms in cardiac arrhythmias and opportunities for their chronotherapy. *Advanced Drug Delivery Reviews*, 59(9-10):940–951.

Priebe, L. and Beuckelmann, D. J. (1998). Simulation study of cellular electric properties in heart failure. *Circulation Research*, 82(11):1206–1223.

Pu, J. and Boyden, P. A. (1997). Alterations of Na+ Currents in Myocytes From Epicardial Border Zone of the Infarcted Heart. *Circulation Research*, 81(1):110–119.

Pueyo, E., Corrias, A., Virág, L., Jost, N., Szél, T., Varró, A., Szentandrássy, N., Nánási, P. P., Burrage, K., and Rodríguez, B. (2011). A multiscale investigation of repolarization variability and its role in cardiac arrhythmogenesis. *Biophysical Journal*, 101(12):2892–2902.

Qu, Z., Weiss, J. N., and Garfinkel, A. (1999). Cardiac electrical restitution properties and stability of reentrant spiral waves: a simulation study. *American Journal of Physiology - Heart and Circulatory Physiology*, 276(1):H269–H283.

Quinn, T. A., Granite, S., Allessie, M. A., Antzelevitch, C., Bollensdorff, C., Bub, G., Burton, R. A., Cerbai, E., Chen, P. S., Delmar, M., Difrancesco, D., Earm, Y. E., Efimov, I. R., Egger, M., Entcheva, E., Fink, M., Fischmeister, R., Franz, M. R., Garny, A., Giles, W. R., Hannes, T., Harding, S. E., Hunter, P. J., Iribe, G., Jalife, J., Johnson, C. R., Kass, R. S., Kodama, I., Koren, G., Lord, P., Markhasin, V. S., Matsuoka, S., McCulloch, A. D., Mirams, G. R., Morley, G. E., Nattel, S., Noble, D., Olesen, S. P., Panfilov, A. V., Trayanova, N. A., Ravens, U., Richard, S., Rosenbaum, D. S., Rudy, Y., Sachs, F., Sachse, F. B., Saint, D. A., Schotten, U., Solovyova, O., Taggart, P., Tung, L., Varró, A., Volders, P. G., Wang, K., Weiss, J. N., Wettwer, E., White, E., Wilders, R., Winslow, R. L., and Kohl, P. (2011). Minimum Information about a Cardiac Electrophysiology Experiment (MICEE): standardised reporting for model reproducibility, interoperability, and data sharing. *Progress in Biophysics and Molecular Biology*, 107(1):4–10.

Quinn, T. A. and Kohl, P. (2013). Combining wet and dry research: experience with model development for cardiac mechano-electric structure-function studies. *Cardiovascular Research*, 97(4):601–611.

Ramanathan, C., Jia, P., Ghanem, R., Ryu, K., and Rudy, Y. (2006). Activation and repolarization of the normal human heart under complete physiological conditions. *Proceedings of the National Academy of Sciences*, 103(16):6309–6314.

Rang, H. P., Dale, M. M., Ritter, J. M., and Moore, P. K. (2003). *Pharmacology*.

Reimer, K. A., Lowe, J. E., Rasmussen, M. M., and Jennings, R. B. (1977). The wavefront phenomenon of ischemic cell death. 1. Myocardial infarct size vs duration of coronary occlusion in dogs. *Circulation*, 56(5):786–794.

Riccio, M. L., Koller, M. L., and Gilmour, R. F. (1999). Electrical Restitution and Spatiotemporal Organization During Ventricular Fibrillation. *Circulation Research*, 84(8):955–963.

Roberts, D. E., Hersh, L. T., and Scher, A. M. (1979). Influence of cardiac fiber orientation on wavefront voltage, conduction velocity, and tissue resistivity in the dog. *Circulation Research*, 44(5):701–712.

Roberts, D. E. and Scher, A. M. (1982). Effect of tissue anisotropy on extracellular potential fields in canine myocardium in situ. *Circulation Research*, 50(3):342–351.

Rodríguez, B., Ferrero, J. M., and Trénor, B. (2002). Mechanistic investigation of extracellular K^+ accumulation during acute myocardial ischemia: a simulation study. *American Journal of Physiology. Heart and Circulatory Physiology*, 283(2).

Rodriguez, B., Tice, B., Blake, R., Gavaghan, D., and Trayanova, N. (2006). Vulnerability to electric shocks in the regionally-ischemic ventricles. In *Engineering in Medicine and Biology Society, 2006. EMBS '06. 28th Annual International Conference of the IEEE*, pages 2280–2283. IEEE.

Rodríguez, B., Tice, B. M., Eason, J. C., Aguel, F., Ferrero, J. M., and Trayanova, N. (2004a). Effect of acute global ischemia on the upper limit of vulnerability: a simulation study. *American Journal of Physiology - Heart and Circulatory Physiology*, 286(6):H2078–H2088.

Rodríguez, B., Tice, B. M., Eason, J. C., Aguel, F., and Trayanova, N. (2004b). Cardiac vulnerability to electric shocks during phase 1A of acute global ischemia. *Heart Rhythm*, 1(6):695–703.

Rodríguez, B. and Trayanova, N. (2003). Upper limit of vulnerability in a defibrillation model of the rabbit ventricles. *Journal of Electrocardiology*, 36 Suppl:51–56.

Rodríguez, B., Trayanova, N., and Noble, D. (2006). Modeling cardiac ischemia. *Annals of the New York Academy of Sciences*, 1080(Interactive and Integrative Cardiology):395–414.

Romero, L., Carbonell, B., Trenor, B., Rodríguez, B., Saiz, J., and Ferrero, J. M. (2011). Systematic characterization of the ionic basis of rabbit cellular electrophysiology using two ventricular models. *Progress in Biophysics and Molecular Biology*, 107(1):60–73.

Rosenbaum, D. S., Jackson, L. E., Smith, J. M., Garan, H., Ruskin, J. N., and Cohen, R. J. (1994). Electrical alternans and vulnerability to ventricular arrhythmias. *N Engl J Med*, 330(4):235–241.

Rosenbaum, D. S. and Jalife, J. (2001). *Optical mapping of cardiac excitation and arrhythmias*.

Rumsey, W. L., Pawlowski, M., Lejavardi, N., and Wilson, D. F. (1994). Oxygen pressure distribution in the heart in vivo and evaluation of the ischemic "border zone". *American Journal of Physiology - Heart and Circulatory Physiology*, 266(4):H1676–H1680.

Ruskin, J. N. (1989). The cardiac arrhythmia suppression trial (CAST). *The New England Journal of Medicine*, 321(6):386–388.

Russell, D. C., Lawrie, J. S., Riemersma, R. A., and Oliver, M. F. (1984). Mechanisms of phase 1a and 1b early ventricular arrhythmias during acute myocardial ischemia in the dog. *The American Journal of Cardiology*, 53(2):307–312.

Russell, D. C. and Oliver, M. F. (1978). Ventricular refractoriness during acute myocardial ischaemia and its relationship to ventricular fibrillation. *Cardiovascular Research*, 12(4):221–227.

Saad, Y. and Schultz, M. H. (1986). GMRES: A generalized minimal residual algorithm for solving nonsymmetric linear systems. *SIAM Journal on Scientific and Statistical Computing*, 7(3):856–869.

Saffitz, J. E., Kanter, H. L., Green, K. G., Tolley, T. K., and Beyer, E. C. (1994). Tissue-specific determinants of anisotropic conduction velocity in canine atrial and ventricular myocardium. *Circulation Research*, 74(6):1065–1070.

Sager, P. T., Gintant, G., Turner, J. R., Pettit, S., and Stockbridge, N. (2014). Rechanneling the cardiac proarrhythmia safety paradigm: a meeting report from the Cardiac Safety Research Consortium. *American heart journal*, 167(3):292–300.

Sakakibara, Y., Furukawa, T., Singer, D. H., Jia, H., Backer, C. L., Arentzen, C. E., and Wasserstrom, J. A. (1993). Sodium current in isolated human ventricular myocytes. *The American Journal of Physiology*, 265(4 Pt 2).

Sakakibara, Y., Wasserstrom, J. A., Furukawa, T., Jia, H., Arentzen, C. E., Hartz, R. S., and Singer, D. H. (1992). Characterization of the sodium current in single human atrial myocytes. *Circulation Research*, 71(3):535–546.

Sands, G. B., Gerneke, D. A., Hooks, D. A., Green, C. R., Smaill, B. H., and Legrice, I. J. (2005). Automated imaging of extended tissue volumes using confocal microscopy. *Microsc. Res. Tech.*, 67(5):227–239.

Sanguinetti, M. C. and Tristani-Firouzi, M. (2006). hERG potassium channels and cardiac arrhythmia. *Nature*, 440(7083):463–469.

Sano, T., Takayama, N., and Shimamoto, T. (1959). Directional Difference of Conduction Velocity in the Cardiac Ventricular Syncytium Studied by Microelectrodes. *Circulation Research*, 7(2):262–267.

Sarkar, A. X. and Sobie, E. A. (2011). Quantification of repolarization reserve to understand interpatient variability in the response to proarrhythmic drugs: a computational analysis. *Heart Rhythm*, 8(11):1749–1755.

Sato, R., Noma, A., Kurachi, Y., and Irisawa, H. (1985). Effects of intracellular acidification on membrane currents in ventricular cells of the guinea pig. *Circulation Research*, 57(4):553–561.

Scarborough, P., Bhatnagar, P., Wickramasinghe, K., Smolina, K., and Mitchell, C. (2010). Coronary heart disease statistics 2010 edition. Technical report.

Schaapherder, A. F. M., Schumacher, C. A., Coronel, R., and Fiolet, J. W. T. (1990). Transmural inhomogeneity of extracellular $[K^+]$ and pH and myocardial energy metabolism in the isolated rat heart during acute global ischemia; dependence on gaseous environment. *Basic Research in Cardiology*, 85(1):33–44.

Schang, S. J. and Pepine, C. J. (1977). Transient asymptomatic S-T segment depression during daily activity. *The American Journal of Cardiology*, 39(3):396–402.

Schneider, M., Proebstle, T., Hombach, V., Hannekum, A., and Rüdel, R. (1994). Characterization of the sodium currents in isolated human cardiocytes. *Pflügers Archiv*, 428(1):84–90.

Schreur, J. (1993). Post-ischemic contractile dysfunction does not correlate with an elevated intracellular free $[Mg^{2+}]$: A 31P-NMR study on isolated rat and rabbit hearts. *Journal of Molecular and Cellular Cardiology*, 25(9):1015–1024.

Schroeder, W. J., Avila, L. S., and Hoffman, W. (2000). Visualizing with VTK: a tutorial. *Computer Graphics and Applications, IEEE*, 20(5):20–27.

Shannon, T. R., Wang, F., Puglisi, J., Weber, C., and Bers, D. M. (2004). A mathematical treatment of integrated Ca dynamics within the ventricular myocyte. *Biophysical Journal*, 87(5):3351–3371.

Shattock, M. J. and Bers, D. M. (1989). Rat vs. rabbit ventricle: Ca flux and intracellular Na assessed by ion-selective microelectrodes. *American Journal of Physiology - Cell Physiology*, 256(4):C813–C822.

Shaw, R. M. and Rudy, Y. (1997a). Electrophysiologic effects of acute myocardial ischemia. A mechanistic investigation of action potential conduction and conduction failure. *Circulation Research*, 80(1):124–138.

Shaw, R. M. and Rudy, Y. (1997b). Electrophysiologic effects of acute myocardial ischemia: a theoretical study of altered cell excitability and action potential duration. *Cardiovascular Research*, 35(2):256–272.

Shivkumar, K., Deutsch, N. A., Lamp, S. T., Khuu, K., Goldhaber, J. I., and Weiss, J. N. (1997). Mechanism of hypoxic K loss in rabbit ventricle. *Journal of Clinical Investigation*, 100(7):1782–1788.

Skouibine, K., Trayanova, N., and Moore, P. (2000). Success and failure of the defibrillation shock: insights from a simulation study. *Journal of Cardiovascular Electrophysiology*, 11(7):785–796.

Smith, G. L. and Allen, D. G. (1988). Effects of metabolic blockade on intracellular calcium concentration in isolated ferret ventricular muscle. *Circulation Research*, 62(6):1223–1236.

Smith, N. P. and Crampin, E. J. (2004). Development of models of active ion transport for whole-cell modelling: cardiac sodiumpotassium pump as a case study. *Progress in Biophysics and Molecular Biology*, 85(2-3):387–405.

Smith, P. L. and Yellen, G. (2002). Fast and slow voltage sensor movements in HERG potassium channels. *The Journal of General Physiology*, 119(3):275–293.

Smith, W. T., Fleet, W. F., Johnson, T. A., Engle, C. L., and Cascio, W. E. (1995). The Ib phase of ventricular arrhythmias in ischemic in situ porcine heart is related to changes in cell-to-cell electrical coupling. *Circulation*, 92(10):3051–3060.

Spach, M. S. and Barr, R. C. (1975). Ventricular intramural and epicardial potential distributions during ventricular activation and repolarization in the intact dog. *Circulation Research*, 37(2):243–257.

Spach, M. S. and Dolber, P. C. (1986). Relating extracellular potentials and their derivatives to anisotropic propagation at a microscopic level in human cardiac muscle. Evidence for electrical uncoupling of side-to-side fiber connections with increasing age. *Circulation Research*, 58(3):356–371.

Spach, M. S., Heidlage, J. F., Dolber, P. C., and Barr, R. C. (2000). Electrophysiological effects of remodeling cardiac gap junctions and cell size. *Circulation Research*, 86(3):302–311.

Spector, P. S., Curran, M. E., Keating, M. T., and Sanguinetti, M. C. (1996). Class III antiarrhythmic drugs block HERG, a human cardiac delayed rectifier K^+ channel. Open-channel block by methanesulfonanilides. *Circulation Research*, 78(3):499–503.

Sporton, S. C., Taggart, P., Sutton, P. M., Walker, J. M., and Hardman, S. M. (1997). Acute ischaemia: a dynamic influence on QT dispersion. *The Lancet*, 349(9048):306–309.

Steinberg, B. A., Broderick, S. H., Lopes, R. D., Shaw, L. K., Thomas, K. L., DeWald, T. A., Daubert, J. P., Peterson, E. D., Granger, C. B., and Piccini, J. P. (2014). Use of antiarrhythmic drug therapy and clinical outcomes in older patients with concomitant atrial fibrillation and coronary artery disease. *Europace*, pages euu077+.

Stern, M. D., Song, L. S., Cheng, H., Sham, J. S., Yang, H. T., Boheler, K. R., and Ríos, E. (1999). Local control models of cardiac excitation-contraction coupling. A possible role for allosteric interactions between ryanodine receptors. *The Journal of General Physiology*, 113(3):469–489.

Streeter, D. D., Spotnitz, H. M., Patel, D. P., Ross, J., and Sonnenblick, E. H. (1969). Fiber orientation in the canine left ventricle during diastole and systole. *Circulation Research*, 24(3):339–347.

Sun, H., Leblanc, N., and Nattel, S. (1997). Mechanisms of inactivation of L-type calcium channels in human atrial myocytes. *American Journal of Physiology - Heart and Circulatory Physiology*, 272(4):H1625–H1635.

Sutton, P. M., Taggart, P., Opthof, T., Coronel, R., Trimlett, R., Pugsley, W., and Kallis, P. (2000). Repolarisation and refractoriness during early ischaemia in humans. *Heart (British Cardiac Society)*, 84(4):365–369.

Suttorp, M. J., Kingma, Peels, H. O. J., Koomen, E. M., Tijssen, J. G. P., van Hemel, N. M., Defauw, J. A. M., and Ernst, S. M. P. G. (1991). Effectiveness of sotalol in preventing supraventricular tachyarrhythmias shortly after coronary artery bypass grafting. *The American Journal of Cardiology*, 68(11):1163–1169.

Suttorp, M. J., Kingma, J. H., Tjon Joe Gin, R. M., van Hemel, N. M., Koomen, E. M., Defauw, J. A., Adan, A. J., and Ernst, S. M. (1990). Efficacy and safety of low- and high-dose sotalol versus propanalol in the prevention of supraventricular tachyarrhythmias early after coronary artery bypass operations. *The Journal of Thoracic and Cardiovascular Surgery*, 100(6):921–926.

Tacker, W. A., Niebauer, M. J., Babbs, C. F., Combs, W. J., Hahn, B. M., Barker, M. A., Seipel, J. F., Bourland, J. D., and Geddes, L. A. (1980). The effect of newer antiarrhythmic drugs on defibrillation threshold. *Critical Care Medicine*, 8(3):177–180.

Taggart, P. (2000). Inhomogeneous transmural conduction during early ischaemia in patients with coronary artery disease. *Journal of Molecular and Cellular Cardiology*, 32(4):621–630.

Taggart, P., Carruthers, M., Joseph, S., Kelly, H. B., Marcomichelakis, J., Noble, D., O'Neill, G., and Somerville, W. (1979). Electrocardiographic changes resembling myocardial ischaemia in asymptomatic men with normal coronary arteriograms. *British Heart Journal*, 41(2):214–225.

Taggart, P. and Slater, J. D. (1971). Significance of potassium in genesis of arrhythmias in induced cardiac ischaemia. *British Medical Journal*, 4(5781):195–198.

Taggart, P., Sutton, P. M. I., Opthof, T., Coronel, R., Trimlett, R., Pugsley, W., and Kallis, P. (2001). Transmural repolarisation in the left ventricle in humans during normoxia and ischaemia. *Cardiovascular Research*, 50(3):454–462.

Taneja, T., Windhagen Mahnert, B., Passman, R., Goldberger, J., and Kadish, A. (2001). Effects of sex and age on electrocardiographic and cardiac electrophysiological properties in adults. *Pacing and Clinical Electrophysiology*, 24(1):16–21.

Tani, M. and Neely, J. R. (1989). Role of intracellular Na^+ in Ca^{2+} overload and depressed recovery of ventricular function of reperfused ischemic rat hearts. Possible involvement of H^+-Na^+ and Na^+-Ca^{2+} exchange. *Circulation Research*, 65(4):1045–1056.

ten Tusscher, K., Bernus, O., Hren, R., and Panfilov, A. (2006). Comparison of electrophysiological models for human ventricular cells and tissues. *Progress in Biophysics and Molecular Biology*, 90(1-3):326–345.

ten Tusscher, K. H., Hren, R., and Panfilov, A. V. (2007). Organization of ventricular fibrillation in the human heart. *Circulation Research*, 100(12).

ten Tusscher, K. H., Noble, D., Noble, P. J., and Panfilov, A. V. (2004). A model for human ventricular tissue. *American Journal of Physiology. Heart and Circulatory Physiology*, 286(4):H1573–H1589.

ten Tusscher, K. H. W. J. and Panfilov, A. V. (2006). Alternans and spiral breakup in a human ventricular tissue model. *American Journal of Physiology - Heart and Circulatory Physiology*, 291(3):H1088–H1100.

Terkildsen, J. R., Crampin, E. J., and Smith, N. P. (2007). The balance between inactivation and activation of the Na^+-K^+ pump underlies the triphasic accumulation of extracellular K^+ during myocardial ischemia. *American Journal of Physiology - Heart and Circulatory Physiology*, 293(5):H3036–H3045.

Tessier, S., Karczewski, P., Krause, E.-G., Pansard, Y., Acar, C., Lang-Lazdunski, M., Mercadier, J.-J., and Hatem, S. N. (1999). Regulation of the transient outward K^+ current by Ca^{2+}/calmodulin-dependent protein kinases II in human atrial myocytes. *Circulation Research*, 85(9):810–819.

Thygesen, K., Alpert, J. S., White, H. D., and Joint ESC/ACCF/AHA/WHF Task Force for the Redefinition of Myocardial Infarction (2007). Universal definition of myocardial infarction. *European Heart Journal*, 28(20):2525–2538.

Tice, B. M., Rodríguez, B., Eason, J., and Trayanova, N. (2007). Mechanistic investigation into the arrhythmogenic role of transmural heterogeneities in regional ischaemia phase 1A. *Europace*, 9(suppl 6):vi46–vi58.

Tohse, N. (1990). Calcium-sensitive delayed rectifier potassium current in guinea pig ventricular cells. *The American Journal of Physiology*, 258(4 Pt 2).

Trayanova, N. (2006). Defibrillation of the heart: insights into mechanisms from modelling studies. *Experimental Physiology*, 91(2):323–337.

Trayanova, N., Eason, J., and Aguel, F. (2002). Computer simulations of cardiac defibrillation: a look inside the heart. *Computing and Visualization in Science*, 4(4):259–270.

Trayanova, N. A. (2011). Whole-heart modeling. *Circulation Research*, 108(1):113–128.

Trayanova, N. A., Constantino, J., and Gurev, V. (2010). Models of stretch-activated ventricular arrhythmias. *Journal of Electrocardiology*, 43(6):479–485.

Trénor, B., Ferrero, J. M., Rodríguez, B., and Montilla, F. (2005). Effects of pinacidil on reentrant arrhythmias generated during acute regional ischemia: a simulation study. *Annals of Biomedical Engineering*, 33(7):897–906.

Ursell, P. C., Gardner, P. I., Albala, A., Fenoglio, J. J., and Wit, A. L. (1985). Structural and electrophysiological changes in the epicardial border zone of canine myocardial infarcts during infarct healing. *Circulation Research*, 56(3):436–451.

Valderrabano, M. (2007). Influence of anisotropic conduction properties in the propagation of the cardiac action potential. *Progress in Biophysics and Molecular Biology*, 94(1-2):144–168.

Van Herendael, H., Pinter, A., Ahmad, K., Korley, V., Mangat, I., and Dorian, P. (2010). Role of antiarrhythmic drugs in patients with implantable cardioverter defibrillators. *Europace*, 12(5):618–625.

van Opstal, J. M., Schoenmakers, M., Verduyn, S. C., de Groot, S. H. M., Leunissen, J. D. M., van der Hulst, F. F., Molenschot, M. M. C., Wellens, H. J. J., and Vos, M. A. (2001). Chronic

amiodarone evokes no Torsade de Pointes arrhythmias despite QT lengthening in an animal model of acquired Long-QT syndrome. *Circulation*, 104(22):2722–2727.

Van Wagoner, D. R. and Lamorgese, M. (1994). Ischemia potentiates the mechanosensitive modulation of atrial ATP-sensitive potassium channels. *Annals of the New York Academy of Sciences*, 723(1):392–395.

Vandenberg, J. I., Metcalfe, J. C., and Grace, A. A. (1993). Mechanisms of pH_i recovery after global ischemia in the perfused heart. *Circulation Research*, 72(5):993–1003.

Varro, A., Virag, L., Acsai, K., Jost, N., Lengyel, C., and Papp, J. G. (2006). P6-2: Role of the slowly inactivating transient outward potassium current in cardiac repolarization. *Heart Rhythm*, 3(5, Supplement). Heart Rhythm 2006 27th Annual Scientific Sessions of Heart Rhythm Society.

Verduyn, S. C., Vos, M. A., van der Zande, J., van der Hulst, F. F., and Wellens, H. J. (1997). Role of interventricular dispersion of repolarization in acquired torsade-de-pointes arrhythmias: reversal by magnesium. *Cardiovascular Research*, 34(3):453–463.

Vermeulen, J. (1996). Electrophysiologic and extracellular ionic changes during acute ischemia in failing and normal rabbit myocardium. *Journal of Molecular and Cellular Cardiology*, 28(1):123–131.

Vigmond, E. J., Weber dos Santos, R., Prassl, A. J., Deo, M., and Plank, G. (2008). Solvers for the cardiac bidomain equations. *Progress in Biophysics and Molecular Biology*, 96(1-3):3–18.

Virág, L., Iost, N., Opincariu, M., Szolnoky, J., Szécsi, J., Bogáts, G., Szenohradszky, P., Varró, A., and Papp, J. G. (2001). The slow component of the delayed rectifier potassium current in undiseased human ventricular myocytes. *Cardiovascular Research*, 49(4):790–797.

Viswanathan, P. C., Bezzina, C. R., George, A. L., Roden, D. M., Wilde, A. A. M., and Balser, J. R. (2001). Gating-dependent mechanisms for flecainide action in SCN5A-linked arrhythmia syndromes. *Circulation*, 104(10):1200–1205.

Volders, P. G. A., Sipido, K. R., Carmeliet, E., Spätjens, R. L. H. M. G., Wellens, H. J. J., and Vos, M. A. (1999). Repolarizing K^+ currents I_{TO1} and I_{Ks} are larger in right than left canine ventricular midmyocardium. *Circulation*, 99(2):206–210.

Wagner, S., Dybkova, N., Rasenack, E. C., Jacobshagen, C., Fabritz, L., Kirchhof, P., Maier, S. K., Zhang, T., Hasenfuss, G., Brown, J. H. H., Bers, D. M., and Maier, L. S. (2006). Ca^{2+}/calmodulin-dependent protein kinase II regulates cardiac Na^+ channels. *The Journal of Clinical Investigation*, 116(12):3127–3138.

Wagner, S., Hacker, E., Grandi, E., Weber, S. L., Dybkova, N., Sossalla, S., Sowa, T., Fabritz, L., Kirchhof, P., Bers, D. M., and Maier, L. S. (2009). Ca/calmodulin kinase II differentially modulates potassium currents. *Circulation. Arrhythmia and Electrophysiology*, 2(3):285–294.

Wagner, S., Wu, S. T., Parmley, W. W., and Wikman-Coffelt, J. (1990). Influence of ischemia on [Ca2+]i transients following drug therapy in hearts from aortic constricted rats. *Cell Calcium*, 11(6):431–444.

Waldo, A. L., Camm, A. J., deRuyter, H., Friedman, P. L., MacNeil, D. J., Pauls, J. F., Pitt, B., Pratt, C. M., Schwartz, P. J., and Veltri, E. P. (1996). Effect of d-sotalol on mortality in patients with left ventricular dysfunction after recent and remote myocardial infarction. The SWORD Investigators. Survival With Oral d-Sotalol. *Lancet*, 348(9019):7–12.

Walton, R. D., Benoist, D., Hyatt, C. J., Gilbert, S. H., White, E., and Bernus, O. (2010). Dual excitation wavelength epifluorescence imaging of transmural electrophysiological properties in intact hearts. *Heart Rhythm*, 7(12):1843–1849.

Wan, X., Chen, S., Sadeghpour, A., Wang, Q., and Kirsch, G. E. (2001). Accelerated inactivation in a mutant Na^+ channel associated with idiopathic ventricular fibrillation. *American Journal of Physiology - Heart and Circulatory Physiology*, 280(1):H354–H360.

Wang, D. W., Makita, N., Kitabatake, A., Balser, J. R., and George, A. L. (2000). Enhanced Na^+ channel intermediate inactivation in Brugada syndrome. *Circulation Research*, 87(8):e37–e43.

Wang, Z., Fermini, B., and Nattel, S. (1994). Rapid and slow components of delayed rectifier current in human atrial myocytes. *Cardiovascular Research*, 28(10):1540–1546.

Watanabe, I., Kanda, A., Engle, C. L., and Gettes, L. S. (1997). Comparison of the effects of regional ischemia and hyperkalemia on the membrane action potentials of the in situ pig heart. *Journal of Cardiovascular Electrophysiology*, 8(11):1229–1236.

Watanabe, M. A., Fenton, F. H., Evans, S. J., Hastings, H. M., and Karma, A. (2001). Mechanisms for discordant alternans. *Journal of Cardiovascular Electrophysiology*, 12(2):196–206.

Watson, R. M., Markle, D. R., Ro, Y. M., Goldstein, S. R., McGuire, D. A., Peterson, J. I., and Patterson, R. E. (1984). Transmural pH gradient in canine myocardial ischemia. *The American Journal of Physiology*, 246(2 Pt 2).

Wazni, O. M., Marrouche, N. F., Martin, D. O., Verma, A., Bhargava, M., Saliba, W., Bash, D., Schweikert, R., Brachmann, J., Gunther, J., Gutleben, K., Pisano, E., Potenza, D., Fanelli, R., Raviele, A., Themistoclakis, S., Rossillo, A., Bonso, A., and Natale, A. (2005). Radiofrequency ablation vs antiarrhythmic drugs as first-line treatment of symptomatic atrial fibrillation: a randomized trial. *JAMA : the journal of the American Medical Association*, 293(21):2634–2640.

Weber, C. R., Piacentino, V., Houser, S. R., and Bers, D. M. (2003). Dynamic regulation of sodium/calcium exchange function in human heart failure. *Circulation*, 108(18):2224–2229.

Weidmann, S. (1970). Electrical constants of trabecular muscle from mammalian heart. *The Journal of Physiology*, 210(4):1041–1054.

Weiss, J. and Shine, K. I. (1982a). Extracellular K^+ accumulation during myocardial ischemia in isolated rabbit heart. *The American Journal of Physiology*, 242(4):H619–628.

Weiss, J. and Shine, K. I. (1982b). $[K^+]_o$ accumulation and electrophysiological alterations during early myocardial ischemia. *The American Journal of Physiology*, 243(2):H318–327.

Weiss, J. and Shine, K. I. (1986). Effects of heart rate on extracellular $[K^+]$ accumulation during myocardial ischemia. *The American Journal of Physiology*, 250(6 Pt 2).

Weiss, J. N., Chen, p.-S., Qu, Z., Karagueuzian, H. S., Lin, s.-F., and Garfinkel, A. (2002). Electrical Restitution and Cardiac Fibrillation. *Journal of Cardiovascular Electrophysiology*, 13(3):292–295.

Weiss, J. N., Garfinkel, A., Karagueuzian, H. S., Qu, Z., and Chen, P. S. (1999). Chaos and the transition to ventricular fibrillation: a new approach to antiarrhythmic drug evaluation. *Circulation*, 99(21):2819–2826.

Weiss, J. N., Venkatesh, N., and Lamp, S. T. (1992). ATP-sensitive K^+ channels and cellular K^+ loss in hypoxic and ischaemic mammalian ventricle. *The Journal of Physiology*, 447:649–673.

Wettwer, E., Amos, G. J., Posival, H., and Ravens, U. (1994). Transient outward current in human ventricular myocytes of subepicardial and subendocardial origin. *Circulation Research*, 75(3):473–482.

Wichter, T., Borggrefe, M., Haverkamp, W., Chen, X., and Breithardt, G. (1992). Efficacy of antiarrhythmic drugs in patients with arrhythmogenic right ventricular disease. Results in patients with inducible and noninducible ventricular tachycardia. *Circulation*, 86(1):29–37.

Wilde, A. A., Escande, D., Schumacher, C. A., Thuringer, D., Mestre, M., Fiolet, J. W., and Janse, M. J. (1990). Potassium accumulation in the globally ischemic mammalian heart. A role for the ATP-sensitive potassium channel. *Circulation Research*, 67(4):835–843.

Wilde, A. A., Peters, R. J., and Janse, M. J. (1988). Catecholamine release and potassium accumulation in the isolated globally ischemic rabbit heart. *Journal of Molecular and Cellular Cardiology*, 20(10):887–896.

Wilde, A. A. M. and Aksnes, G. (1995). Myocardial potassium loss and cell depolarisation in ischaemia and hypoxia. *Cardiovascular Research*, 29(1):1–15.

Wilensky, R. L., Tranum-Jensen, J., Coronel, R., Wilde, A. A., Fiolet, J. W., and Janse, M. J. (1986). The subendocardial border zone during acute ischemia of the rabbit heart: an electrophysiologic, metabolic, and morphologic correlative study. *Circulation*, 74(5):1137–1146.

Wilhelms, M., Dossel, O., and Seemann, G. (2011). In silico investigation of electrically silent acute cardiac ischemia in the human ventricles. *Biomedical Engineering, IEEE Transactions on*, 58(10):2961–2964.

Wilhelms, M., Rombach, C., Scholz, E. P., Dössel, O., and Seemann, G. (2012). Impact of amiodarone and cisapride on simulated human ventricular electrophysiology and electrocardiograms. *Europace*, 14(suppl 5):v90–v96.

Williams, E. M. V. (1984). A classification of antiarrhythmic actions reassessed after a decade of new drugs. *The Journal of Clinical Pharmacology*, 24(4):129–147.

Wu, S., Weiss, J. N., Chou, c.-C., Attin, M., Hayashi, H., and Lin, s.-F. (2005). Dissociation of membrane potential and intracellular calcium during ventricular fibrillation. *Journal of Cardiovascular Electrophysiology*, 16(2):186–192.

Xu, X., Rials, S. J., Wu, Y., Salata, J. J., Liu, T., Bharucha, D. B., Marinchak, R. A., and Kowey, P. R. (2001). Left ventricular hypertrophy decreases slowly but not rapidly activating delayed rectifier potassium currents of epicardial and endocardial myocytes in rabbits. *Circulation*, 103(11):1585–1590.

Yamaguchi, M., Shimizu, M., Ino, H., Terai, H., Uchiyama, K., Oe, K., Mabuchi, T., Konno, T., Kaneda, T., and Mabuchi, H. (2003). T wave peak-to-end interval and QT dispersion in acquired long QT syndrome: a new index for arrhythmogenicity. *Clinical science (London, England : 1979)*, 105(6):671–676.

Yan, G. X., Chen, J., Yamada, K. A., Kléber, A. G., and Corr, P. B. (1996). Contribution of shrinkage of extracellular space to extracellular K^+ accumulation in myocardial ischaemia of the rabbit. *The Journal of Physiology*, 490 (Pt 1):215–228.

Yang, Z., Zhang, H., Kong, S., Yue, X.-F. F., Jin, Y.-B. B., Jin, J., and Huang, Y.-C. C. (2007). Study for relevance of the acute myocardial ischemia to arrhythmia by the optical mapping method. *Physiological Measurement*, 28(5):481–488.

Yao, A., Su, Z., Nonaka, A., Zubair, I., Lu, L., Philipson, K. D., Bridge, J. H. B., and Barry,

W. H. (1998). Effects of overexpression of the Na^{+}-Ca^{2+} exchanger on $[Ca^{2+}]_i$ transients in murine ventricular myocytes. *Circulation Research*, 82(6):657–665.

Yatani, A., Brown, A. M., and Akaike, N. (1984). Effect of extracellular pH on sodium current in isolated, single rat ventricular cells. *The Journal of Membrane Biology*, 78(2):163–168.

Yellon, D. M. and Hausenloy, D. J. (2007). Myocardial Reperfusion Injury. *N Engl J Med*, 357(11):1121–1135.

You, B., Pu, J., Liu, N., Yu, R., Ruan, Y., Li, Y., and Wang, L. (2005). Effect of lidocaine and amiodarone on transmural heterogeneity of ventricular repolarization in isolated rabbit hearts model of sustained global ischemia. *Journal of Huazhong University of Science and Technology*, 25(4):400–403.

Young, A. A., Legrice, I. J., Young, M. A., and Smaill, B. H. (1998). Extended confocal microscopy of myocardial laminae and collagen network. *Journal of microscopy*, 192(Pt 2):139–150.

Zaitsev, A. V., Guha, P. K., Sarmast, F., Kolli, A., Berenfeld, O., Pertsov, A. M., de Groot, J. R., Coronel, R., and Jalife, J. (2003). Wavebreak formation during ventricular fibrillation in the isolated, regionally ischemic pig heart. *Circulation Research*, 92(5):546–553.

Zawar, C. and Neumcke, B. (2000). Differential activation of ATP-sensitive potassium channels during energy depletion in CA1 pyramidal cells and interneurones of rat hippocampus. *Pflügers Archiv*, 439(3):256–262.

Zemzemi, N., Bernabeu, M. O., Saiz, J., Cooper, J., Pathmanathan, P., Mirams, G. R., Pitt-Francis, J., and Rodriguez, B. (2013). Computational assessment of drug-induced effects on the electrocardiogram: from ion channel to body surface potentials. *Br J Pharmacol*, 168(3):718–733.

Zeng, J., Laurita, K. R., Rosenbaum, D. S., and Rudy, Y. (1995). Two Components of the Delayed Rectifier K^{+} Current in Ventricular Myocytes of the Guinea Pig Type. *Circulation Research*, 77(1):140–152.

Zhou, L., Salem, J. E., Saidel, G. M., Stanley, W. C., and Cabrera, M. E. (2005). Mechanistic model of cardiac energy metabolism predicts localization of glycolysis to cytosolic subdomain during ischemia. *American Journal of Physiology. Heart and Circulatory Physiology*, 288(5).

Zhou, Z., Gong, Q., Ye, B., Fan, Z., Makielski, J. C., Robertson, G. A., and January, C. T. (1998). Properties of HERG channels stably expressed in HEK 293 cells studied at physiological temperature. *Biophysical Journal*, 74(1):230–241.

Zicha, S., Xiao, L., Stafford, S., Cha, T. J., Han, W., Varro, A., and Nattel, S. (2004). Transmural expression of transient outward potassium current subunits in normal and failing canine and human hearts. *The Journal of Physiology*, 561(3):735–748.